

# **AEROSOL COAGULATION AND NUCLEATION**

**Thesis by**

**David Da-Teh Huang**

**In Partial Fulfillment of the Requirements**

**for the Degree of**

**Doctor of Philosophy**

**California Institute of Technology**

**Pasadena, California**

**1991**

**(Submitted August 21, 1990)**

**To My Parents and Chaoyin**

## ACKNOWLEDGEMENTS

First and foremost, I would like to forward my deepest gratitude to my advisor, Professor John H. Seinfeld, for his continuous support, encouragement, and advice throughout these years. I also extend thanks for the trust and freedom he gave me in my research at Caltech. To work with John is both an honor and a great pleasure.

The following professors kindly served on my committee: John F. Brady, Richard C. Flagan, George R. Gavalas, and Kikuo Okuyama. I thank them for their time and help through my course of study. In particular, I am grateful to Kikuo and Richard; I have enjoyed sharing and discussing ideas with them.

The financial support from the National Science Foundation (Grants no. ATM-8503103 and ATM-9003186), Environmental Protection Agency, and Mobil Fund are gratefully acknowledged.

Appreciation also goes to my friends and colleagues; I wish to thank Ken Wolfenbarger, Yong P. Kim, and Chak Chan for being such wonderful officemates. I thank Ken, in particular, for his support and understanding. The friendship of my former roommates, John Brewer, Scott King, and Todd Przybycien are greatly valued. I also thank Shih-Chen Wang and Yu-Sheng Zhang for their help.

I want to dedicate this dissertation to my family and my family-in-law whose love and devotion always encouraged me during my study. I thank my brother, Eric, for his continuous support of this work. I am especially indebted to my wife, Chaoyin; this thesis would never have come out without her patience and encouragement.

## ABSTRACT

For aerosol Brownian coagulation in the transition regime of Knudsen number in the presence of an interparticle potential, the Fokker-Planck equation is solved by using the Grad's 13-moment method. The mass and energy accommodation coefficients that are used to describe the results of collisional processes are appropriately defined and interfaced with the Fokker-Planck moment equations. Analytical and numerical solutions of the number and energy flux profiles for the potential-free, power-law potential, van der Waals potential, and Coulombic potential situations are obtained. The results are in good agreement with those predicted by the flux-matching method of Fuchs. The present fundamental approach, therefore, provides theoretical support of the coagulation coefficient expression obtained by the empirical flux-matching method.

For coagulation between ultrafine particles, we solved the BGK equation for large but finite Knudsen number situations by taking into account the van der Waals potential and/or the Coulombic/image potential. We present closed form best-fit equations for data calculated from the theory. The conditions where either Coulombic, image, or van der Waals forces predominate are determined.

A new expression of the image potential between a charged particle and an uncharged particle is obtained. We calculate the coagulation rate between the particles and are able to determine the enhancement of coagulation rate due to the interparticle potential in all size regimes.

An aerosol coagulation process is applied to the formation of aerosol particles in the semiconductor thin film preparation. In the CVD reactor, we consider simultaneous aerosol coagulation, diffusion, and generation of aerosol monomers by chemical reaction. The mass and number concentration of monomers and particles are computed as functions of temperature, pressure, input vapor concentration, and position in the reactor. The thin film growth rate can be subsequently evaluated. It is found that under certain circumstances, aerosol particle generation may



significantly suppress the film growth due to monomers.

The formulation of the homogeneous nucleation free energy change of aerosol clusters is reexamined. It is shown that the inclusion of the cluster translational and rotational motion in the cluster formation free energy change is appropriate. The classical and statistical thermodynamics are shown to be consistent.

The cell model of liquids of statistical mechanics is employed to reevaluate the free energy change of cluster formation in aerosol nucleation. We provide a new molecular level theory that is applicable in the larger cluster size range where liquid-like properties begin to emerge and a cluster surface is present. The microcluster surface tension can be appropriately defined. The cluster rotational contribution to the free energy change, though it must be accounted for, is shown to be insignificant for liquid-like clusters.

---

---

## TABLE OF CONTENTS

---

---

Acknowledgements . . . . .	iv
Abstract . . . . .	v
Table of Contents . . . . .	vii
 Chapter 1. Introduction . . . . .	 1
 Chapter 2. On Mass, Momentum, and Energy Accommodation Coefficients . . . . .	 5
 Chapter 3. Fokker-Planck Equation Solution of Aerosol Brownian Coagulation with an Interparticle Potential . . . . .	 24
 Chapter 4. BGK Equation Solution of Coagulation for Large Knudsen Number Aerosols with a Singular Attractive Contact Potential . . . . .	 91
 Chapter 5. Image Potential Between a Charged Particle and an Uncharged Particle in Aerosol	

Coagulation — Enhancement in all Size Regimes and Interplay with van der Waals Forces . . . . .	143
Chapter 6. Aerosol Formation by Rapid Nucleation in the Preparation of SiO <sub>2</sub> Thin Film from SiCl <sub>4</sub> and O <sub>2</sub> Gases Using the CVD Process . . . . .	165
Chapter 7. Reexamination of Homogeneous Nucleation Free Energy Change . . . . .	218
Chapter 8. Prediction of Homogeneous Nucleation Free Energy Change from the Cell Model of Liquids . . . . .	239
Chapter 9. Summary and Concluding Remarks . . . . .	312
Appendix On the Relation Between Binary Diffusivity and Mean Free Path . . . . .	315

## **CHAPTER 1**

### **INTRODUCTION**

Brownian coagulation and homogeneous nucleation are two of the major research topics in aerosol science. The issues involved in these two topics are now briefly described.

*Brownian Coagulation* — Aerosol particles of a few micrometers or less undergo Brownian motion and coagulate. The actual coagulation rate between the aerosol particles is governed by Brownian motion, a stochastic behavior, and is described by an equation for the particle velocity distribution function, the Boltzmann equation. There are two approximate equations, the Fokker-Planck equation (FPE) and the Batnager-Gross-Krook equation (BGK), which greatly simplify the collision term in the Boltzmann equation and can be used to determine the rate of coagulation. These equations must be solved, for the coagulation problems, with boundary conditions that are associated with mass, momentum, and energy accommodation at the two particles' contact point. Also in the presence of an interparticle potential, the particle concentration, as well as the particle trajectory close to the two-particle contact, will be different from those at large separations. Therefore, different forms of interparticle potential may produce different coagulation rates. For highly nonlinear interparticle potentials such as the van der Waals potential and the electric image potential, numerical solutions for the FPE or BGK equations are necessary.

Chapters 2-6 are devoted to the subject of aerosol coagulation. Chapter 2 discusses the surface boundary conditions for solving either the FPE or the BGK equation, that is, to appropriately and microscopically define the mass, momentum, and energy accommodation coefficients and to show how these coefficients can interface with the governing equations. In Chapter 3, we solve the FPE for Brownian coagulation of both large and small particles in the presence of an interparticle potential; the potentials considered are the power-law potential, the van

der Waals potential, and the Coulombic potential. In Chapter 4, we solve the BGK equation in a range of very large but finite Knudsen numbers, that is, for particles or clusters close to the free molecule range. The interparticle potentials considered are the van der Waals potential and the electric Coulombic and/or image potential. Chapter 4 provides information on the coagulation process in aerosol nucleation, since the latter involves clusters of free molecule sizes. In Chapter 5, we obtain a new expression for the electric image potential between two finite-sized particles. The coagulation rate under such a potential over the entire range of Knudsen number will be calculated. We will also consider a situation of simultaneous van der Waals and interparticle image potentials. The size range over which each of the potential components predominates is determined. In Chapter 6, we use an overall coagulation and growth model to describe the  $\text{SiO}_2$  particles' behavior in the gas phase of a chemical vapor deposition reactor. This model shows that  $\text{SiO}_2$  particles generated from the subcluster coagulation process may substantially influence the final  $\text{SiO}_2$  thin film growth rate. The relation between the gas-phase particle mean free path and the aerosol particle binary diffusivity is important in determining the coagulation rate between particles. This relation is necessary in Chapters 2-6 and is discussed in theoretical terms in the Appendix of this thesis.

*Nucleation* — Nucleation is the first stage of a phase transition. In aerosol nucleation, molecular-sized clusters coagulate and dissociate in the gas phase to form larger particles. The rate of coagulation of monomers and clusters must be obtained from the Brownian coagulation analysis. On the other hand, the dissociation of clusters is related to the free energy change of cluster formation. The classical approach to obtain the cluster formation free energy change is to use macroscopic classical thermodynamics, and a relation between cluster surface tension and the free energy change of cluster formation can be obtained. The surface

tension, however, is ill-defined for microscopic molecular clusters. Therefore, a molecular level theory for the cluster formation free energy change is necessary, and the theory should address the issue of microcluster surface tension.

The last two chapters of the thesis are devoted to the free energy change of cluster formation in nucleation. In Chapter 7, we reexamine the inclusion of translational and rotational motion in the free energy change, a controversial issue in the field of homogeneous nucleation theory. Then, in Chapter 8, we employ a statistical mechanical model, the cell model of liquids, to rederive the cluster partition function which can be further related to the free energy change of cluster formation in a nucleation process. This approach provides a new theory for the evaluation of the free energy change, and the microcluster surface tension can be appropriately defined and calculated.

## **CHAPTER 2**

### **ON MASS, MOMENTUM, AND ENERGY ACCOMMODATION COEFFICIENTS**

**Appeared in Journal of Colloid and Interface Science**

**Vol. 130, No. 1, pp. 275-280, June 1989**



## INTRODUCTION

Ambiguity frequently arises in defining sticking probability (condensation coefficients) and accommodation coefficients of mass, momentum, and energy. In this note, we draw a clear distinction among these various parameters that are used to describe the results of collisional processes between molecules and surfaces.

### REFLECTION PROBABILITY DENSITY, $R(\mathbf{v}', \mathbf{v})$

Close to a boundary  $S$ , one can define  $R(\mathbf{v}', \mathbf{v})d\mathbf{v}$  as the probability that an incident molecule with velocity in the range  $(\mathbf{v}', \mathbf{v}' + d\mathbf{v}')$  leaves the surface with velocity in the range  $(\mathbf{v}, \mathbf{v} + d\mathbf{v})$ . The function  $R(\mathbf{v}', \mathbf{v})$  obeys the so-called *thermostat condition* (1):

$$|\mathbf{v} \cdot \mathbf{i}| f(\mathbf{v}) d\mathbf{v} = d\mathbf{v} \int_{\mathbf{v}' \cdot \mathbf{i} < 0} R(\mathbf{v}', \mathbf{v}) f(\mathbf{v}') |\mathbf{v}' \cdot \mathbf{i}| d\mathbf{v}' \quad (\text{on } S), \quad [1]$$

where  $f(\mathbf{v})$  is the molecular distribution function;  $\mathbf{i}$  is the normal unit vector directed from the surface, and  $\mathbf{v} \cdot \mathbf{i} > 0$ ,  $\mathbf{v}' \cdot \mathbf{i} < 0$ . The physical meaning of Eq. [1] is that the emerging flux of molecules with velocity  $\mathbf{v}$  is just equal to the impinging flux of molecules with velocity  $\mathbf{v}'$  multiplied by the probability  $R(\mathbf{v}', \mathbf{v}) d\mathbf{v}$  and integrated over all possible  $\mathbf{v}'$ .

If one integrates  $R(\mathbf{v}', \mathbf{v})$  over all possible emerging velocities  $\mathbf{v}$ , the result represents the probability that an incident molecule with velocity in the range  $(\mathbf{v}', \mathbf{v}' + d\mathbf{v}')$  will eventually leave the surface. Thus we write

$$\int_{\mathbf{v} \cdot \mathbf{i} > 0} R(\mathbf{v}', \mathbf{v}) d\mathbf{v} = 1 - \beta_s(\mathbf{v}'), \quad [2]$$

where  $\beta_s(\mathbf{v}')$  stands for the probability of sticking of an incident molecule with velocity in the range  $(\mathbf{v}', \mathbf{v}' + d\mathbf{v}')$ . This factor is a function of  $\mathbf{v}'$  since, for example,

a faster striking molecule has less chance of sticking than a slower molecule. Also a normally-incident molecule is expected to stick more easily than those that graze the surface.

Denoting the incoming and emerging number fluxes in the normal direction as  $J_i^-$  and  $J_i^+$ ,

$$\begin{aligned} J_i^- &= \int_{\mathbf{v}' \cdot \mathbf{i} < 0} f(\mathbf{v}') |\mathbf{v}' \cdot \mathbf{i}| d\mathbf{v}' \\ J_i^+ &= \int_{\mathbf{v} \cdot \mathbf{i} > 0} f(\mathbf{v}) |\mathbf{v} \cdot \mathbf{i}| d\mathbf{v} , \end{aligned} \quad [3]$$

the *sticking probability*,  $\alpha_s$ , is defined such that

$$J_i^+ = J_i^- (1 - \alpha_s) . \quad [4]$$

It follows from Eqs. [1] through [4] that

$$\alpha_s = \frac{\int_{\mathbf{v}' \cdot \mathbf{i} < 0} \beta_s(\mathbf{v}') f(\mathbf{v}') |\mathbf{v}' \cdot \mathbf{i}| d\mathbf{v}'}{\int_{\mathbf{v}' \cdot \mathbf{i} < 0} f(\mathbf{v}') |\mathbf{v}' \cdot \mathbf{i}| d\mathbf{v}'} , \quad [5]$$

The physical significance of Eq. [5] is that the sticking probability,  $\alpha_s$ , is an overall parameter that accounts for a distribution of all possible incident  $\mathbf{v}'$ , hence it is equal to the average over  $\beta_s(\mathbf{v}')$ . The sticking probability may also be termed the *condensation coefficient* or *mass accommodation coefficient*. Values of  $\alpha_s$  are difficult to calculate theoretically since a full understanding of the surface and the intermolecular potential is necessary. Therefore,  $\alpha_s$  values are generally obtained by experiment.

For those impinging molecules that ultimately leave the surface, there should exist a certain correlation between the incoming and outgoing molecular velocities. In this regard, Maxwell (2) proposed a phenomenological relation that is often

employed. It states that a nonsticking incoming molecule is presumed either to be trapped on the surface momentarily and then emitted in all directions according to an isotropic Maxwellian velocity distribution, or to bounce off immediately as a billiard ball. The former situation is known as *diffusive reflection* and the latter as *specular reflection*. We call the probability that an emitted molecule is reflected diffusively the *Maxwellian coefficient*,  $\alpha_M(\mathbf{v}')$ .  $\alpha_M$  is also a function of  $\mathbf{v}'$  since one expects, for example, that it is more difficult for faster molecules to reside on the surface temporarily. Maxwell's relation corresponds to choosing

$$\frac{R(\mathbf{v}', \mathbf{v})}{1 - \beta_s(\mathbf{v}')} = \alpha_M(\mathbf{v}') \mathcal{F}(\mathbf{v}) + [1 - \alpha_M(\mathbf{v}')] \delta(\mathbf{v}' - \mathbf{v} + 2(\mathbf{v} \cdot \mathbf{i})\mathbf{i}) , \quad [6]$$

where  $\delta$  is the Kronecker delta defined in the velocity space. Following the definition of  $R(\mathbf{v}', \mathbf{v})$  and  $\beta_s(\mathbf{v}')$ , the left-hand side of Eq. [6] represents the probability density that a reemitted molecule has a velocity in the range  $(\mathbf{v}, \mathbf{v} + d\mathbf{v})$  provided its incident velocity is in the range  $(\mathbf{v}', \mathbf{v}' + d\mathbf{v}')$ . The situations of diffusive and specular reflection are represented by the first and second terms on the right-hand side of Eq. [6], respectively. One sees that the second term would be nonzero merely when  $\mathbf{v} - 2(\mathbf{v} \cdot \mathbf{i})\mathbf{i} = \mathbf{v}'$  (i.e., with a change only in the normal component of the velocity). The function  $\mathcal{F}(\mathbf{v})$  in the first term is independent of  $\mathbf{v}'$ , that is, in a sense the molecule forgets its incident velocity.  $\mathcal{F}(\mathbf{v})$  can be determined by using Eqs. [1] and [6] at the surface equilibrium condition (i.e.,  $f = f_{0,s}$  and  $\beta_s(\mathbf{v}') = 0$ ) to yield (1)

$$\mathcal{F}(\mathbf{v}) = \frac{\alpha_M(\mathbf{v} - 2(\mathbf{v} \cdot \mathbf{i})\mathbf{i}) |\mathbf{v} \cdot \mathbf{i}| f_{0,s}(\mathbf{v})}{\int_{\mathbf{v}' \cdot \mathbf{i} < 0} \alpha_M(\mathbf{v}') |\mathbf{v}' \cdot \mathbf{i}| f_{0,s}(\mathbf{v}') d\mathbf{v}'} , \quad [7]$$

where  $f_{0,s}(\mathbf{v})$  is the equilibrium molecular distribution function at surface conditions,

$$f_{0,s}(\mathbf{v}) = n \left( \frac{m}{2\pi k T_s} \right)^{3/2} \exp \left( -\frac{mv^2}{2k T_s} \right), \quad [8]$$

in which  $n$  is the gas phase density, and  $T_s$  is the surface temperature. Finally, combining Eqs. [6] and [7], one obtains

$$R(\mathbf{v}', \mathbf{v}) = (1 - \beta_s(\mathbf{v}')) \left\{ \frac{\alpha_M(\mathbf{v} - 2(\mathbf{v} \cdot \mathbf{i})\mathbf{i}) \alpha_M(\mathbf{v}') |\mathbf{v} \cdot \mathbf{i}| f_{0,s}(\mathbf{v})}{\int_{\mathbf{v}'' \cdot \mathbf{i} < 0} \alpha_M(\mathbf{v}'') |\mathbf{v}'' \cdot \mathbf{i}| f_{0,s}(\mathbf{v}'') d\mathbf{v}''} + [1 - \alpha_M(\mathbf{v}')] \delta(\mathbf{v}' - \mathbf{v} + 2(\mathbf{v} \cdot \mathbf{i})\mathbf{i}) \right\} \quad [9]$$

in which  $\mathbf{v} \cdot \mathbf{i} > 0$ ,  $\mathbf{v}' \cdot \mathbf{i} < 0$ , and  $\mathbf{v}'' \cdot \mathbf{i} < 0$ .

## THE ACCOMMODATION COEFFICIENTS

In order to seek appropriate definitions of accommodation coefficients of momentum and energy, it is convenient to define the half-range distribution functions

$$\begin{aligned} f^+(\mathbf{v}) &= f(\mathbf{v}) H(\mathbf{v} \cdot \mathbf{i} > 0) \\ f^-(\mathbf{v}) &= f(\mathbf{v}) H(\mathbf{v} \cdot \mathbf{i} < 0), \end{aligned} \quad [10]$$

where  $H$  is the heaviside function which is unity if its argument is true and zero otherwise. Upon substituting Eq. [9] into Eq. [1], the half-range distribution functions at the surface obey

$$\begin{aligned} f^+(\mathbf{v}) &= \frac{\alpha_M(\mathbf{v} - 2(\mathbf{v} \cdot \mathbf{i})\mathbf{i}) f_{0,s}(\mathbf{v}) \int_{\mathbf{v}' \cdot \mathbf{i} < 0} [1 - \beta_s(\mathbf{v}')] \alpha_M(\mathbf{v}') f^-(\mathbf{v}') |\mathbf{v}' \cdot \mathbf{i}| d\mathbf{v}'}{\int_{\mathbf{v}'' \cdot \mathbf{i} < 0} \alpha_M(\mathbf{v}'') |\mathbf{v}'' \cdot \mathbf{i}| f_{0,s}(\mathbf{v}'') d\mathbf{v}''} \\ &+ [1 - \beta_s(\mathbf{v} - 2(\mathbf{v} \cdot \mathbf{i})\mathbf{i})] [1 - \alpha_M(\mathbf{v} - 2(\mathbf{v} \cdot \mathbf{i})\mathbf{i})] f^-(\mathbf{v} - 2(\mathbf{v} \cdot \mathbf{i})\mathbf{i}) \quad (\text{on } S). \end{aligned} \quad [11]$$

The accommodation coefficient of a quantity  $\phi(\mathbf{v})$  is defined as (3)

$$\alpha(\phi) = \frac{\int_{\mathbf{v}' \cdot \mathbf{i} < 0} \phi(\mathbf{v}') |\mathbf{v}' \cdot \mathbf{i}| f^-(\mathbf{v}') d\mathbf{v}' - \int_{\mathbf{v} \cdot \mathbf{i} > 0} \phi(\mathbf{v}) |\mathbf{v} \cdot \mathbf{i}| f^+(\mathbf{v}) d\mathbf{v}}{\int_{\mathbf{v}' \cdot \mathbf{i} < 0} \phi(\mathbf{v}') |\mathbf{v}' \cdot \mathbf{i}| f^-(\mathbf{v}') d\mathbf{v}' - \int_{\mathbf{v} \cdot \mathbf{i} > 0} \phi(\mathbf{v}) |\mathbf{v} \cdot \mathbf{i}| f_0^+(\mathbf{v}) d\mathbf{v}} \quad (\text{on } S), \quad [12]$$

where  $f_0^+(\mathbf{v})$  is  $f^+(\mathbf{v})$  evaluated at  $\alpha_M = 1$ ; from Eqs. [5], [8], and [11],

$$f_0^+(\mathbf{v}) = (1 - \alpha_s) \frac{m^2 J_i^-}{2\pi k^2 T_s^2} \exp\left(-\frac{mv^2}{2kT_s}\right), \quad [13]$$

On the right-hand side of Eq. [12], the first term of the numerator (and the denominator) is the incoming  $\phi$  flux; the second term in the numerator is the emerging  $\phi$  flux; and the second term in the denominator is the emerging  $\phi$  flux provided that all the nonsticking incident molecules are equilibrated with the surface and thus reflected diffusively. By setting  $\phi(\mathbf{v})$  equal to  $|\mathbf{v} \cdot \mathbf{i}|$ ,  $\mathbf{v} \times \mathbf{i}$ , and  $v^2/2$ , one obtains  $\alpha(\phi)$  as the *normal momentum*, *tangential momentum*, and *energy* (or *thermal*) accommodation coefficients. We denote these quantities as  $\alpha_{n.m.}$ ,  $\alpha_{t.m.}$ , and  $\alpha_e$ , respectively. The *mass* accommodation coefficient,  $\alpha_s$ , can also be defined from Eq. [12] by setting  $\phi = 1$  and neglecting the second term in the denominator. That is, the *mass* of molecules that *accommodates* with the surface will *not be reflected diffusively*. This definition of mass accommodation coefficient is in agreement with Eq. [4].

The half-range incoming  $\phi$  fluxes are denoted by the symbols listed in Table I. The equilibrium emerging fluxes (*i.e.*, the second term in the denominator in Eq. [12]) can be evaluated by integrating Eq. [13] over  $\mathbf{v} \cdot \mathbf{i} > 0$ . These expressions are also listed in Table I in terms of the half-range incoming fluxes. On the other hand, the emerging fluxes (*i.e.*, the second term in the numerator in Eq. [12]) can be expressed, by using Eq. [11], as

$$\begin{aligned} \int_{\mathbf{v} \cdot \mathbf{i} > 0} \phi(\mathbf{v}) |\mathbf{v} \cdot \mathbf{i}| f^+(\mathbf{v}) d\mathbf{v} &= \frac{\int_{\mathbf{v}' \cdot \mathbf{i} < 0} [1 - \beta_s(\mathbf{v}')] \alpha_M(\mathbf{v}') f^-(\mathbf{v}') |\mathbf{v}' \cdot \mathbf{i}| d\mathbf{v}'}{\int_{\mathbf{v}'' \cdot \mathbf{i} < 0} \alpha_M(\mathbf{v}'') |\mathbf{v}'' \cdot \mathbf{i}| f_{0,s}(\mathbf{v}'') d\mathbf{v}''} \times \\ &\quad \int_{\mathbf{v} \cdot \mathbf{i} > 0} \phi(\mathbf{v}) |\mathbf{v} \cdot \mathbf{i}| \alpha_M(\mathbf{v} - 2(\mathbf{v} \cdot \mathbf{i})\mathbf{i}) f_{0,s}(\mathbf{v}) d\mathbf{v} \\ &\quad + \int_{\mathbf{v}' \cdot \mathbf{i} < 0} \phi(\mathbf{v}') |\mathbf{v}' \cdot \mathbf{i}| [1 - \beta_s(\mathbf{v}')] [1 - \alpha_M(\mathbf{v}')] f^-(\mathbf{v}') d\mathbf{v}' . \end{aligned} \quad [14]$$

From this equation, we realize that once the functional forms of  $\beta_s(\mathbf{v}')$  and  $\alpha_M(\mathbf{v}')$  are known, the emerging fluxes given by Eq. [14] can be further related to the half-range incoming fluxes. Because the surface condition is generally unknown, information on  $\beta_s(\mathbf{v}')$  must be obtained from measurements of the sticking probability,  $\alpha_s$  (recall Eq. [5]). To a first approximation, we can assume henceforth that all incident molecules have the same probability of sticking regardless of their velocities, *i.e.*,

$$\beta_s(\mathbf{v}'_1) = \beta_s(\mathbf{v}'_2) = \dots = \alpha_s \quad [15]$$

Under this assumption, we present models of  $\alpha_M(\mathbf{v}')$  in the following two sections by Maxwell (2) and Epstein (4) and their ensuing results, respectively.

### MAXWELL'S PRESCRIPTION OF $\alpha_M$

In Maxwell's original work,  $\alpha_M(\mathbf{v}')$  was taken to be a constant. Values of  $\alpha_M$  can be arbitrarily chosen and/or determined by data fitting from experiment. Equation [11] becomes, in this case,

$$\begin{aligned} f^+(\mathbf{v}) &= (1 - \alpha_s) \left\{ \frac{\alpha_M m^2}{2\pi k^2 T_s^2} J_i^- \exp\left(-\frac{mv^2}{2kT_s}\right) \right. \\ &\quad \left. + (1 - \alpha_M) f^-(\mathbf{v} - 2(\mathbf{v} \cdot \mathbf{i})\mathbf{i}) \right\} \quad (\text{on } S) . \end{aligned} \quad [16]$$

Consequently, the emerging  $\phi$  fluxes and their corresponding accommodation coefficients are evaluated in terms of the incoming  $\phi$  fluxes as shown in Table II. For the situations where  $\alpha_s = 0$ , we find

$$\alpha_{n.m.} = \alpha_{t.m.} = \alpha_e = \alpha_M \quad (\alpha_s = 0) . \quad [17]$$

Thus a constant Maxwellian coefficient is equal to constant accommodation coefficients of both momentum and energy when the surface is a perfect reflector. For the cases where  $\alpha_s = 1$ , all the accommodation coefficients have the value of unity, since no molecule can leave the surface. The tangential momentum accommodation coefficient, in particular, does not depend on the incoming  $\phi$  fluxes and is a constant. This is because its equilibrium emerging flux is zero (recall Table I) due to symmetry and the incoming fluxes cancel identically in both the numerator and denominator in Eq. [12].

### EPSTEIN'S PRESCRIPTION OF $\alpha_M$

Taking into account the velocity dependence of  $\alpha_M(\mathbf{v}')$ , Epstein (4) proposed the model

$$\alpha_M(\mathbf{v}') = \exp\left(-\frac{mv'^2}{2kT_1}\right) + B\left[1 - \exp\left(-\frac{mv'^2}{2kT_2}\right)\right] , \quad [18]$$

where  $T_1 < T_2$ ;  $T_1$ ,  $T_2$ , and  $B$  are parameters determined from curve fitting with experimental data under the conditions that the gas phase is in equilibrium with the surface. The first term in Eq. [18] predicts the speed dependence of  $\alpha_M$  at low temperatures. That is, the larger the kinetic energy of the incident molecules, the smaller the value of  $\alpha_M$ . The second term in Eq. [18], on the contrary, dominates the behavior of  $\alpha_M$  at higher temperatures. At high temperature conditions, there

is always a nonnegligible fraction, the parameter  $B$ , of incident molecules that will be scattered diffusively. Maxwell's constant  $\alpha_M$  is therefore realized as a limiting case of Epstein's model at high temperature and has the value  $B$ .

Substituting Eqs. [18] and [15] into Eq. [14], one can express the emerging  $\phi$  fluxes as functions of the incoming  $\phi$  fluxes. These relations are given in Table IIIa. Table IIIb shows the momentum and energy accommodation coefficients as functions of  $T_1$ ,  $T_2$ ,  $B$ , and the incoming fluxes (*i.e.*,  $J_i^-$ ,  $J_{i,\alpha_M}^-$ ,  $p_{im}^-$ ,  $p_{im,\alpha_M}^-$ ,  $q_i^-$ , and  $q_{i,\alpha_M}^-$  defined in Table IIIa). All the accommodation coefficients, again, become unity when the surface becomes a perfect absorber ( $\alpha_s = 1$ ).

## BOUNDARY CONDITIONS

The main purpose of finding expressions of accommodation coefficients is to relate them to boundary conditions of mass, momentum, and energy. The latter are necessary in solving governing equations of interest for transport of molecules to surfaces (*e.g.*, the Boltzmann, Fokker-Plank, or BGK equations). We give an example of finding boundary conditions of a heat and mass transfer problem.

The mass boundary condition follows directly from the definition of the mass accommodation coefficient, Eq. [4]. The full-range number flux on the surface is accordingly found to be

$$J_i = J_i^+ - J_i^- = -\alpha_s J_i^- \quad (\text{on } S) . \quad [19]$$

Likewise, the thermal boundary condition is found from the definition of the energy accommodation coefficient (Eq. [12] by setting  $\phi = \mathbf{v}^2/2$ ),



$$\alpha_e = \frac{q_i^- - q_i^+}{q_i^- - 2(1 - \alpha_s)J_i^- kT_s/m} \quad (\text{on } S) . \quad [20]$$

It follows that

$$q_i = q_i^+ - q_i^- = 2(1 - \alpha_s) \frac{\alpha_e kT_s}{m} J_i^- - \alpha_e q_i^- \quad (\text{on } S) , \quad [21]$$

where  $q_i$  is the full-range energy flux and  $\alpha_e$  is a function of  $J_i^-$ ,  $q_i^-$ ,  $J_{i,\alpha_M}^-$ , and  $q_{i,\alpha_M}^-$  (recall Tables II and III). These incoming fluxes can be further related to the full-range fluxes once a functional form of the distribution function  $f$  is available. We illustrate this by using the form of  $f$  proposed by Grad (5, 6),

$$\begin{aligned} f = & \left( \frac{h}{\sqrt{2\pi}} \right)^3 \exp\left(-\frac{C^2}{2}\right) \left\{ n + \frac{h}{2} \sum_l J_l C_l (7 - C^2) \right. \\ & + \frac{h^2}{2} \sum_l \sum_m \left( p_{lm} - \frac{n}{h^2} \delta_{lm} \right) (C_l C_m - \delta_{lm}) \\ & \left. + h^3 \sum_l q_l C_l \left( \frac{C^2}{5} - 1 \right) \right\} , \quad l, m = i, j, k , \end{aligned} \quad [22]$$

in which  $h = \sqrt{m/kT}$ ;  $C_i = h(\mathbf{v} \cdot \mathbf{i})$ ; and  $\delta_{lm}$  is the Kronecker delta in the normal sense.  $J_l$  denotes the full-range number flux in the  $l$ th direction; and  $p_{lm}$  and  $q_l$  are the full-range ( $lm$ th direction) momentum flux and the ( $l$ th direction) energy flux per unit mass, respectively. The results of half-range integration over  $\mathbf{v}' \cdot \mathbf{i} < 0$  are

$$J_i^- = \frac{n}{h\sqrt{2\pi}} - \frac{J_i}{2} + \frac{h}{2\sqrt{2\pi}} \left( p_{ii} - \frac{n}{h^2} \right) \quad [23]$$

$$q_i^- = \frac{2n}{h^3\sqrt{2\pi}} - \frac{q_i}{2} + \frac{1}{2h\sqrt{2\pi}} \left( 4p_{ii} + p_{jj} + p_{kk} - \frac{6n}{h^2} \right) \quad [24]$$

$$\begin{aligned} J_{i,\alpha_M}^- = & \frac{n}{h\sqrt{2\pi}} A^{(2)} - \frac{J_i}{4} [7A^{(5/2)} - 5A^{(7/2)}] - \frac{h^2 q_i}{2} [A^{(7/2)} - A^{(5/2)}] \\ & + \frac{h}{2\sqrt{2\pi}} \left\{ \left( p_{ii} - \frac{n}{h^2} \right) A^{(3)} + \left( p_{ii} + p_{jj} + p_{kk} - \frac{3n}{h^2} \right) (A^{(3)} - A^{(2)}) \right\} \end{aligned} \quad [25]$$

and

$$q_{i,\alpha_M}^- = \frac{2n}{h^3\sqrt{2\pi}} A^{(3)} - \frac{35}{8} \frac{J_i}{h^2} [A^{(7/2)} - A^{(9/2)}] - \frac{q_i}{4} [7A^{(9/2)} - 5A^{(7/2)}] \\ + \frac{1}{2h\sqrt{2\pi}} \left\{ 3\left(p_{ii} - \frac{n}{h^2}\right) A^{(4)} + \left(p_{ii} + p_{jj} + p_{kk} - \frac{3n}{h^2}\right) (3A^{(4)} - 2A^{(3)}) \right\}, \quad [26]$$

where

$$A^{(n)} = \left(\frac{T_1}{T_1 + T}\right)^n - B \left(\frac{T_2}{T_2 + T}\right)^n + B. \quad [27]$$

For the mass boundary condition, we can substitute Eq. [23] into Eq. [19] and recognize  $T = T_s$  at the surface to obtain

$$J_i = \frac{\alpha_s}{(\alpha_s - 2)h_s\sqrt{2\pi}} (n + h_s^2 p_{ii}) \quad (\text{on } S), \quad [28]$$

where  $h_s = \sqrt{m/kT_s}$ . Similarly, one can substitute Eqs. [23]–[26] into the expressions of  $\alpha_e$  in either Table II or Table IIIb to evaluate the thermal boundary condition. Maxwell's constant  $\alpha_M$  model (from Table II) yields a simpler result,

$$q_i = \frac{1}{(2 + \epsilon)h_s^3\sqrt{2\pi}} \left\{ (\gamma - 2\epsilon - \eta)n \right. \\ \left. + h_s^2\epsilon \left[ \left(4 + \frac{\gamma}{\epsilon} - \frac{\eta}{\epsilon}\right) p_{ii} + p_{jj} + p_{kk} \right] \right\} \quad (\text{on } S), \quad [29]$$

where  $\epsilon = \alpha_M\alpha_s - \alpha_M - \alpha_s$ ;  $\gamma = 2(1 - \alpha_s)\alpha_M$ ; and  $\eta = \gamma\alpha_s/(\alpha_s - 2)$ . The thermal boundary condition found by using Epstein's model is considerably more complicated and thus is not presented in this note.

## DISCUSSION

A major assumption in this work is the validity of Eq. [15], where the probability of the sticking of an incident molecule with velocity in the range  $(\mathbf{v}', \mathbf{v}' + d\mathbf{v}')$ ,

$\beta_s(\mathbf{v}')$  was approximated as equal to the overall sticking probability,  $\alpha_s$ . This situation can be realized for the following two reasons:

- (A) The calculation of the accommodation coefficients where  $\beta_s(\mathbf{v}')$  is involved (Eq. [14]) contains integrations over all possible incident velocities weighted by the incident  $\phi(\mathbf{v}')$  flux. The distribution function  $f$  is customarily expressed as the sum of its equilibrium value,  $f_0$ , and higher-order perturbation terms (e.g., Eq. [22]). If the system is not highly departed from the equilibrium condition, the leading term  $f_0$  dominates the higher-order terms. Because  $f_0$  behaves as a Maxwellian-type exponential decay in the high velocity range,  $\beta_s(\mathbf{v}')$  can be approximated as a constant by substituting the nominal value of  $\mathbf{v}'$ .
- (B) The molecules in a transport process tend to follow the direction of the mean velocity. If this direction, for example, is perpendicular to the boundary surface, one expects that the number of grazing molecules should be much less than the number of normally incident molecules. Furthermore, because values of  $f_0$  do not depend on the velocity direction, the influence of velocity direction on the integrations of  $\beta_s(\mathbf{v}')$  enters only into the perturbation terms of  $f$ . Therefore, it is reasonable to assume that  $\beta_s(\mathbf{v}')$  is independent of the velocity direction and is a constant.

We would also like to remark that many articles (for example, see Ivchenko (7)) define the mass accommodation coefficient,  $\alpha_s$ , from Eq. [12] by setting  $\phi = 1$  without neglecting the second term in the denominator in Eq. [12]. This is not appropriate because by saying *mass accommodation* we mean that the trapped molecules on the surface will not be scattered by any mechanism. The theoretical calculation by Narsimhan and Ruckenstein (8) of aerosol coagulation is a special result that corresponds to choosing  $\alpha_s = 0$  and  $\alpha_M = 1$  ( $\alpha_M$  was named the

“momentum accommodation coefficient”). These authors proposed that the coagulation may occur even when  $\alpha_s = 0$  because of the capture of particles in the interaction potential well which is located some distance from the collision surface. In consequence, the calculated “sticking probability” is in fact the probability that the two associating particles form a doublet. Mork *et al.* (9) and Sitarski and Seinfeld (10) used the thermal boundary condition in which  $\alpha_M = 0$ , though it was not mentioned explicitly.

## CONCLUSION

Here we present definitions of the sticking probability (Eqs. [4] and [5]) and the accommodation coefficients (Eq. [12]). The sticking probability is defined as the fraction of the total incident molecules that will not leave the surface. The accommodation coefficient of a quantity  $\phi$  is defined as the ratio of the net  $\phi$  flux to the  $\phi$  flux when all the molecules accommodate with the surface before they leave. We show that when  $\alpha_s = 0$ , the momentum and energy accommodation coefficients are equal to the constant phenomenological Maxwellian coefficient,  $\alpha_M$ . For cases where  $\alpha_s = 1$ , all the accommodation coefficients have the value of unity. The tangential momentum, due to its symmetry, has the accommodation coefficient independent of the fluxes for Maxwell's constant  $\alpha_M$  model. We also show the mass and energy boundary conditions that are calculated from the corresponding accommodation coefficients. In general, accommodation coefficients are functions of the full-range mass, momentum and energy fluxes. In consequence, the boundary conditions will be altered if the transport process is changing. Finally, accommodation coefficients of momentum and energy will always be greater than the sticking probability, since at least an  $\alpha_s$  portion of the total incident molecules is fully accommodated with the surface.

## ACKNOWLEDGEMENT

This work was supported by the National Science Foundation under Grant ATM-8503103.

## REFERENCES

1. Ferziger, J. H., and Kaper, H. G., "Mathematical Theory of Transport Processes in Gases," North-Holland, Amsterdam, 1972.
2. Maxwell, J. C., *Philos. Trans. R. Soc. London* **157**, 49 (1867).
3. Cercignani, C., "The Boltzmann Equation and Its Applications," Springer-Verlag, Berlin, 1988.
4. Epstein, M., *AIAA* **5**, 1797 (1967).
5. Grad, H., *Commun. Pure Appl. Math.* **2**, 325 (1949).
6. Grad, H., *Commun. Pure Appl. Math.* **2**, 331 (1949).
7. Ivchenko, I., *J. Colloid Interface Sci.* **120**, 1 (1987).
8. Narsimhan, G., and Ruckenstein, E., *J. Colloid Interface Sci.* **104**, 344 (1985).
9. Mork, K. J., Razi Naqvi, K., and Waldenstrøm, S., *J. Colloid Interface Sci.* **98**, 103 (1984).
10. Sitarski, M., and Seinfeld, J. H., *J. Colloid Interface Sci.* **61**, 261 (1977).

**Table I**  
**Equilibrium Emerging Fluxes as Functions**  
**of the Incoming Fluxes in Eq. [12]**

$\phi(\mathbf{v})$	Incoming Flux <sup>a</sup>	Equilibrium Emerging Flux
1	$J_i^-$	$(1 - \alpha_s) J_i^-$
$ \mathbf{v} \cdot \mathbf{i} $	$p_{ii}^-$	$(1 - \alpha_s) J_i^- \sqrt{\pi k T_s / 2m}$
$\mathbf{v} \times \mathbf{i}$	$p_{ij}^- \mathbf{k} - p_{ik}^- \mathbf{j}$	0
$v^2/2$	$q_i^-$	$2(1 - \alpha_s) J_i^- k T_s / m$

a.  $J_i^- \equiv \int_{\mathbf{v}' \cdot \mathbf{i} < 0} |\mathbf{v}' \cdot \mathbf{i}| f^-(\mathbf{v}') d\mathbf{v}';$

$q_i^- \equiv \frac{1}{2} \int_{\mathbf{v}' \cdot \mathbf{i} < 0} v'^2 |\mathbf{v}' \cdot \mathbf{i}| f^-(\mathbf{v}') d\mathbf{v}';$  and

$p_{im}^- \equiv \int_{\mathbf{v}' \cdot \mathbf{i} < 0} |\mathbf{v}' \cdot \mathbf{i}| |\mathbf{v}' \cdot \mathbf{m}| f^-(\mathbf{v}') d\mathbf{v}',$  where  $\mathbf{m} = \mathbf{i}, \mathbf{j},$  or  $\mathbf{k}.$

**Table II**  
**Accommodation Coefficients and Emerging Fluxes as Functions**  
**of the Incoming Fluxes by Maxwell's Prescription of  $\alpha_M$**

$\phi(\mathbf{v})$	Emerging Flux	Accommodation Coefficient, $\alpha(\phi)$
1	$(1 - \alpha_s) J_i^-$	$\alpha_s^a$
$ \mathbf{v} \cdot \mathbf{i} $	$\alpha_M (1 - \alpha_s) J_i^- \sqrt{\pi k T_s / 2m}$  $+(1 - \alpha_s)(1 - \alpha_M) p_{ii}^-$	$\alpha_M + \frac{(1 - \alpha_M) \alpha_s p_{ii}^-}{p_{ii}^- - (1 - \alpha_s) J_i^- \sqrt{\pi k T_s / 2m}}$
$\mathbf{v} \times \mathbf{i}$	$(1 - \alpha_s)(1 - \alpha_M) \times$  $(p_{ij}^- \mathbf{k} - p_{ik}^- \mathbf{j})$	$\alpha_M + \alpha_s - \alpha_s \alpha_M$
$v^2/2$	$2(1 - \alpha_s) \alpha_M J_i^- k T_s / m$  $+(1 - \alpha_s)(1 - \alpha_M) q_i^-$	$\alpha_M + \frac{(1 - \alpha_M) \alpha_s q_i^-}{q_i^- - 2(1 - \alpha_s) J_i^- k T_s / m}$

*a.* Definition of  $\alpha_s$



Table IIIa

Emerging Fluxes as Functions of the Incoming Fluxes  
by Epstein's Prescription of  $\alpha_M$

$\phi(\mathbf{v})$	Emerging Flux $a, b, c$
1	$(1 - \alpha_s) J_i^-$
$ \mathbf{v} \cdot \mathbf{i} $	$(1 - \alpha_s) J_{i, \alpha_M}^- A_s^{(5/2)} \sqrt{\pi k T_s} / \sqrt{2m} A_s^{(2)}$ $+ (1 - \alpha_s) p_{ii}^- - (1 - \alpha_s) p_{ii, \alpha_M}^-$
$\mathbf{v} \times \mathbf{i}$	$(1 - \alpha_s) (p_{ij}^- - p_{ij, \alpha_M}^-) \mathbf{k}$ $- (1 - \alpha_s) (p_{ik}^- - p_{ik, \alpha_M}^-) \mathbf{j}$
$v^2/2$	$2(1 - \alpha_s) J_{i, \alpha_M}^- k T_s A_s^{(3)} / m A_s^{(2)}$ $+ (1 - \alpha_s) q_i^- - (1 - \alpha_s) q_{i, \alpha_M}^-$

a.  $J_i^-$ ,  $q_i^-$ , and  $p_{im}^-$  ( $m = i, j, k$ ) are defined in Table I.

b.  $J_{i, \alpha_M}^- \equiv \int_{\mathbf{v}' \cdot \mathbf{i} < 0} \alpha_M(\mathbf{v}') |\mathbf{v}' \cdot \mathbf{i}| f^-(\mathbf{v}') d\mathbf{v}'$ ;

$q_{i, \alpha_M}^- \equiv \frac{1}{2} \int_{\mathbf{v}' \cdot \mathbf{i} < 0} \alpha_M(\mathbf{v}') v'^2 |\mathbf{v}' \cdot \mathbf{i}| f^-(\mathbf{v}') d\mathbf{v}'$ ; and

$p_{im, \alpha_M}^- \equiv \int_{\mathbf{v}' \cdot \mathbf{i} < 0} \alpha_M(\mathbf{v}') |\mathbf{v}' \cdot \mathbf{m}| |\mathbf{v}' \cdot \mathbf{i}| f^-(\mathbf{v}') d\mathbf{v}'$ ,

where  $\mathbf{m} = \mathbf{i}, \mathbf{j}$  or  $\mathbf{k}$ .

c.  $A_s^{(n)} = \left( \frac{T_1}{T_1 + T_s} \right)^n - B \left( \frac{T_2}{T_2 + T_s} \right)^n + B$ .

Table IIIb

Accomodation Coefficients as Functions of the Incoming  
Fluxes by Epstein's Prescription of  $\alpha_M$

$\phi(\mathbf{v})$	Accomodation Coefficient, $\alpha(\phi)$
1	$\alpha_s$
$ \mathbf{v} \cdot \mathbf{i} $	$\frac{\alpha_s p_{ii}^- / (1 - \alpha_s) + p_{ii, \alpha_M}^- - J_{i, \alpha_M}^- A_s^{(5/2)} \sqrt{\pi k T_s} / \sqrt{2m} A_s^{(2)}}{p_{ii}^- / (1 - \alpha_s) - J_i^- \sqrt{\pi k T_s} / 2m}$
$\mathbf{v} \times \mathbf{i}$	$\left[ (\alpha_s p_{ij}^- + p_{ij, \alpha_M}^- - \alpha_s p_{ij, \alpha_M}^-) \mathbf{k} - (\alpha_s p_{ik}^- + p_{ik, \alpha_M}^- - \alpha_s p_{ik, \alpha_M}^-) \mathbf{j} \right] / (p_{ij}^- \mathbf{k} - p_{ik}^- \mathbf{j})$
$v^2/2$	$\frac{\alpha_s q_i^- / (1 - \alpha_s) + q_{i, \alpha_M}^- - 2J_{i, \alpha_M}^- k T_s A_s^{(3)} / m A_s^{(2)}}{q_i^- / (1 - \alpha_s) - 2J_i^- k T_s / m}$

## **CHAPTER 3**

# **FOKKER-PLANCK EQUATION SOLUTION OF AEROSOL BROWNIAN COAGULATION WITH AN INTERPARTICLE POTENTIAL**

**Accepted for publication in  
Journal of Colloid and Interface Science, 1990**

## ABSTRACT

For the Brownian coagulation of aerosol particles in the transition regime of Knudsen number in the presence of an interparticle potential, the Fokker-Planck equation is solved by using Grad's 13-moment method. Mass and energy accommodation coefficients are interfaced with the Fokker-Planck moment equations through the use of half-range fluxes. Analytical solutions of the potential-free situation are obtained for arbitrary values of the accommodation coefficients. Numerical solutions of the number and energy flux profiles for a repulsive or an attractive interparticle potential of power-law form are obtained by a two-dimensional shooting scheme. This numerical algorithm is further applied to calculate the coagulation coefficient between two transition regime particles under either a van der Waals potential or a Coulombic potential. The results are in good agreement with those predicted by the flux-matching method of Fuchs. The present fundamental approach, therefore, provides theoretical support of the coagulation coefficient expression obtained by the empirical flux-matching method in the presence of an interparticle potential.

## INTRODUCTION

Predicting the rate of Brownian coagulation between particles has long been of major interest. While the limiting cases of free-molecule and continuum regime coagulation are well established, coagulation in the transition regime of Knudsen number ( $Kn \sim O(1)$ ) has remained an elusive problem. There are generally two approaches to obtain expressions for coagulation coefficients in the transition regime: the flux-matching method and solution of the Fokker-Planck equation (FPE). Table I summarizes available solutions for transition regime coagulation classified by approach and by the absence or presence of interparticle potentials.

For coagulation in the absence of interparticle potentials, Fuchs (1) proposed the so-called limiting sphere flux-matching method that interpolates between the solutions for  $Kn \ll 1$  and  $Kn \gg 1$ . Dahneke (2) used the same method by an analogy to the condensation problem. Sitarski and Seinfeld (3) were apparently the first to use the FPE and the Grad's 13-moment method (4, 5) to derive expressions for the particle coagulation rate. That approach was further pursued by Mork *et al.* (6). Harris (7) used the Lees two-stream distribution function method to solve the three-dimensional FPE. Sahni (8, 9) solved the FPE by expanding the distribution function in terms of Legendre polynomials and Burnett functions. In a similar approach Kumar and Menon (10) carried the Burnett expansion up to the seventh order. Loyalka (11) applied a variational method of solving the Bhatnager-Gross-Krook (BGK) equation for condensation (12) to the problem of potential-free coagulation.

In actual practice, particle coagulation rarely occurs in the absence of interparticle forces. For example, there is a Coulombic interparticle potential between two charged colliding particles, and there may exist instantaneous van der Waals forces

between two uncharged particles. Therefore, to obtain an expression for the coagulation rate in the presence of an interparticle potential in the transition regime of Knudsen number is a natural extension of the earlier work in the potential-free case. There are several papers that use various flux-matching methods to obtain the coagulation rate in the presence of an interparticle potential. In the Appendix, we present the most popular method of Fuchs (13) and show how it reduces to the Fuchs potential-free situation (1). Narsimhan and Ruckenstein (14) considered the influence of interparticle forces acting within a short distance of the collision surface and matched the heat and mass fluxes with the solution of Mork *et al.* (6). They found the lower bound (for two small particles) and the upper bound (for two large particles) of the particle collision rate. However, their final expression does not give the well-known correction factor in the presence of a potential in the continuum regime, because it was assumed that the potential-free solution of Mork *et al.* is valid over the far field. Alam (15) used the interparticle potential free-molecule collision rate expression obtained by Marlow (16) and matched it with the solution of continuum theory by the limiting sphere method. The expression of Marlow itself, however, is only valid for situations of monotonic attractive potentials.

It is useful at this point to make some remarks on the flux-matching method. First, the transition regime rate obtained by the flux-matching method depends, of course, on the coagulation rates in both the continuum and free-molecule regimes. The proper coagulation rate expression in the free-molecule regime in the presence of an interparticle potential is, however, still controversial. For example, the expressions of Fuchs and Sutugin (17) and Graham and Homer (18) were criticized by Marlow (16) for employing the assumption that all the particles possess equal kinetic energy. Marlow's expression was obtained first by an integration over the

incident trajectories, then by an average over the Maxwellian velocity distribution. Brock and Hidy (19), who solved the linearized Boltzmann equation, also obtained an approximate formula for free-molecule coagulation with an interparticle force. In a recent paper of the authors (20), Marlow's approach (16) has been pursued in solving the BGK equation to evaluate the coagulation rate at large but finite Knudsen numbers in the presence of either a monotonic or nonmonotonic singular attractive contact potential. Because of the empirical interpolation of the two limiting regimes, information on the moment profiles (*i.e.*, mass and energy fluxes as well as concentration as functions of radial distance) supplied by the flux-matching method in the transition regime is less accurate than the more fundamental solutions obtained by solving the FPE.

In the FPE approach to interparticle potential situations, Sceats and co-workers (21-23) projected the three-dimensional FPE into one dimension; the elimination of coordinates is equivalent to assuming that the particles are rapidly thermalized. The rate expression was then obtained by adopting a one-dimensional Kramers reaction model (24). That is, two free-molecule particles coagulate as if there is a one-dimensional diffusion of the quantity  $n(r)r^2$  along the two-particle reaction path. Burschka and Titulaer (25-27) considered the situations of a uniform (constant) potential by solving the one-dimensional FPE.

The reduction of the 3-D FPE to the 1-D FPE, *i.e.*, the average of the Boltzmann factors of the centrifugal potential (or the tangential kinetic energy), is less appropriate in the free-molecule regime because the relaxation time scale is relatively large in comparison to that of the transition regime. The advantage of the 1-D approach, on the other hand, is that it is simple to describe coagulation between high density particles in which particles are rapidly thermalized. A drawback of the FPE approach, in general, is that the solutions do not approach

the correct limiting coagulation rate in the free-molecule regime. For example, in the potential-free situation there is a factor of  $2/3$  offset by using Grad's 13-moment method (6, 9) and a factor of 0.881 offset by using the Lees two-stream method (10). These deviations are inherent in the reduction of Eq. [1] (FPE of 12-dimensions in the phase space) to Eq. [9] (FPE of 6-dimensions in the phase space) of this paper; an exact reduction must give a nonlocal FPE corresponding to an equation of motion of a non-Markovian system. The free-molecule solution deviations may also arise from the truncation of the infinite number of moment equations. A strength of the FPE method, on the other hand, is that the solutions of the transition regime coagulation rate do not depend on the *a priori* knowledge of the free-molecule regime; all the information on the continuum-transition regime can be obtained through a first principle analysis of the particle Brownian motion, rather than on empirical interpolation.

As indicated in Table I, the goal of the present paper is to consider Brownian coagulation in the presence of an interparticle potential through a three-dimensional FPE approach. We start by using Grad's 13-moment method (4, 5) to expand the distribution function and then evaluate the Fokker-Planck moment equations. By the spherical symmetry assumption, we obtain three equations governing the concentration, number and energy fluxes. The boundary conditions of these differential equations are further interfaced with mass and energy accommodation coefficients (28). In the potential-free situation, analytical solutions of the governing equations are available. The coagulation coefficient (Eq. [55]) reduces to the previous potential-free result of Mork *et al.* (6). Comparisons of the potential-free expressions by various theories are tabulated in Table II. For situations in the presence of a potential, owing to the correlations of the boundary conditions and the highly nonlinear expressions of most interparticle potentials, one needs to



seek numerical solutions. In this regard, we construct a two-dimensional shooting scheme for solving the governing equations. Influences of both repulsive and attractive potentials on the moment profiles are illustrated by assuming a power-law potential form. Finally, we give a comparison between the predicted coagulation coefficients of the present work with that of the Fuchs flux-matching method for situations of equal-sized particle coagulation in the presence of either a Coulombic or a van der Waals interparticle potential.

### THE FOKKER-PLANCK EQUATION (FPE)

In describing the motion of two colliding aerosol particles that undergo Brownian motion, we denote  $f^{(2)}(\mathbf{r}_1, \mathbf{c}_1; \mathbf{r}_2, \mathbf{c}_2) d\mathbf{r}_1 d\mathbf{c}_1 d\mathbf{r}_2 d\mathbf{c}_2$  as the probability of finding the first particle in volume element  $d\mathbf{r}_1$  with velocities in  $d\mathbf{c}_1$  and the second particle in volume element  $d\mathbf{r}_2$  with velocities in  $d\mathbf{c}_2$ . This two-particle distribution function satisfies the Fokker-Planck equation (29),

$$\begin{aligned} \frac{\partial f^{(2)}}{\partial t} + \mathbf{c}_1 \cdot \nabla_{\mathbf{r}_1} f^{(2)} + \mathbf{c}_2 \cdot \nabla_{\mathbf{r}_2} f^{(2)} + \frac{\mathbf{X}_1}{m_1} \cdot \nabla_{\mathbf{c}_1} f^{(2)} + \frac{\mathbf{X}_2}{m_2} \cdot \nabla_{\mathbf{c}_2} f^{(2)} \\ = \zeta_1 \nabla_{\mathbf{c}_1} \cdot \left[ (\mathbf{c}_1 - \mathbf{u}(\mathbf{r}_1)) f^{(2)} + \frac{kT}{m_1} \nabla_{\mathbf{c}_1} f^{(2)} \right] \\ + \zeta_2 \nabla_{\mathbf{c}_2} \cdot \left[ (\mathbf{c}_2 - \mathbf{u}(\mathbf{r}_2)) f^{(2)} + \frac{kT}{m_2} \nabla_{\mathbf{c}_2} f^{(2)} \right] , \end{aligned} \quad [1]$$

where  $m_i$  is the mass of the  $i$ th particle ( $i=1$  or  $2$ );  $\mathbf{X}_i$  is the total force acting upon the  $i$ th particle;  $\mathbf{u}(\mathbf{r}_i)$  is the local mean velocity of the fluid at the position  $\mathbf{r}_i$ ; and  $\zeta_i = 6\pi\mu_g R_i / m_i C_{c,i}$  is the friction coefficient of the  $i$ th particle, in which  $\mu_g$  is the bath gas viscosity,  $R_i$  is the  $i$ th particle radius, and  $C_{c,i}$  is the  $i$ th particle slip correction factor. The quantity  $\mathbf{c}_i - \mathbf{u}(\mathbf{r}_i)$  is known as the *peculiar velocity* of particle  $i$  and will be denoted as  $\mathbf{C}_i$ . The fluid velocity is defined as the mass average velocity of all background gas molecules and particle  $i$  at the position  $\mathbf{r}_i$ ,

(30),

$$\mathbf{u}(\mathbf{r}_i) = \frac{n_g m_g \sum_j \mathbf{c}_{g,j} + n_i m_i \mathbf{c}_i}{n_g m_g + n_i m_i}, \quad [2]$$

where  $n_g$  and  $n_i$  are the number densities of the bath gas molecules and the  $i$ th particle, respectively.  $m_g$  is the mass of a gas molecule.  $\mathbf{c}_{g,j}$  is the  $j$ th gas molecule velocity. In general, the background gas has a much higher concentration than that of aerosol particles, so  $n_g \gg n_i$ . If we assume the gas molecules do not stick to the surface of particles, there is no sink in the space for the gas molecules. Therefore,  $\sum_j \mathbf{c}_{g,j} = 0$  since there is no directional preference of the gas molecule velocities. Equation [2] leads to  $\mathbf{u}(\mathbf{r}_i) \simeq \mathbf{c}_i n_i m_i / n_g m_g \simeq 0$ , and thus the  $i$ th particle velocity  $\mathbf{c}_i$  can be regarded as the same as its peculiar velocity  $\mathbf{C}_i$ .

The relaxation time scale for the aerosol Brownian motion ( $1/\zeta_1$  or  $1/\zeta_2$ ) is typically about  $10^{-11}$  s. This scale is much shorter than the monomer-monomer coagulation time scale, which is commonly around  $10^{-8}$  s at STP. Thus, the FPE can be written in its steady-state form,

$$\begin{aligned} & \mathbf{C}_1 \cdot \nabla_{\mathbf{r}_1} f^{(2)} + \mathbf{C}_2 \cdot \nabla_{\mathbf{r}_2} f^{(2)} + \frac{\mathbf{X}_1}{m_1} \cdot \nabla_{\mathbf{C}_1} f^{(2)} + \frac{\mathbf{X}_2}{m_2} \cdot \nabla_{\mathbf{C}_2} f^{(2)} \\ &= \zeta_1 \nabla_{\mathbf{C}_1} \cdot \left[ \mathbf{C}_1 f^{(2)} + \frac{kT}{m_1} \nabla_{\mathbf{C}_1} f^{(2)} \right] + \zeta_2 \nabla_{\mathbf{C}_2} \cdot \left[ \mathbf{C}_2 f^{(2)} + \frac{kT}{m_2} \nabla_{\mathbf{C}_2} f^{(2)} \right]. \end{aligned} \quad [3]$$

In the absence of external forces, the only force acting upon both particles is the interparticle force along the line joining the centers of the particles,  $\mathbf{X}_1 = -\mathbf{X}_2$ . Introducing the center-of-mass coordinates of distance  $\mathcal{R}$  and velocity  $\mathcal{C}$

$$\mathcal{R} = \frac{m_1 \mathbf{r}_1 + m_2 \mathbf{r}_2}{m_1 + m_2}; \quad \mathcal{C} = \frac{m_1 \mathbf{u}_1 + m_2 \mathbf{u}_2}{m_1 + m_2}, \quad [4]$$

and the relative coordinates  $\mathbf{r}$  and  $\mathbf{C}$

$$\mathbf{r} = \mathbf{r}_1 - \mathbf{r}_2; \quad \mathbf{C} = \mathbf{C}_1 - \mathbf{C}_2, \quad [5]$$

one can transform Eq. [3] in terms of  $\mathcal{R}$ ,  $\mathcal{C}$ ,  $\mathbf{r}$ , and  $\mathbf{C}$  (8). If the two colliding particles are exactly equal in size, the resulting equation permits a separable solution that allows the relative motion to be decoupled from the center-of-mass coordinates (8), i.e.,

$$f^{(2)}(\mathbf{r}_1, \mathbf{C}_1; \mathbf{r}_2, \mathbf{C}_2) = f_c(\mathcal{R}, \mathcal{C}) f(\mathbf{r}, \mathbf{C}) , \quad [6]$$

which yields

$$\mathbf{C} \cdot \nabla_{\mathcal{R}} f_c = \zeta \nabla_{\mathcal{C}} \cdot \left[ \mathcal{C} f_c + \frac{kT}{2m} \nabla_{\mathcal{C}} f_c \right] \quad [7]$$

and

$$\mathbf{C} \cdot \nabla_{\mathbf{r}} f + \frac{\mathbf{X}}{m/2} \cdot \nabla_{\mathbf{C}} f = \zeta \nabla_{\mathbf{C}} \cdot \left[ \mathbf{C} f + \frac{kT}{m/2} \nabla_{\mathbf{C}} f \right] , \quad [8]$$

where  $\zeta = \zeta_1 = \zeta_2$ ,  $m = m_1 = m_2$ , and  $\mathbf{X} = \mathbf{X}_1 = -\mathbf{X}_2$ . The simultaneous movement of the two colliding particles is described by Eq. [7]. For coagulation, the appropriate equation is Eq. [8] since it governs the relative motion between the particles. The distribution function  $f^{(2)}$  is not separable for two particles of different sizes because the friction coefficients as well as the particle masses are different. However, for two particles of slightly different sizes, such as in a monodisperse aerosol, and in nucleation processes where all the clusters have about the same size, one can still approximate a separable solution of Eq. [3] and obtain an equation similar to Eq. [8] that governs the relative motion of the colliding particles,

$$\mathbf{C} \cdot \nabla_{\mathbf{r}} f + \frac{\mathbf{X}}{\mu} \cdot \nabla_{\mathbf{C}} f \simeq \xi \nabla_{\mathbf{C}} \cdot \left[ \mathbf{C} f + \frac{kT}{\mu} \nabla_{\mathbf{C}} f \right] , \quad [9]$$

where  $\mu = m_1 m_2 / (m_1 + m_2)$  is the reduced mass, and  $\xi = \zeta_1 \zeta_2 (m_1 + m_2) / (m_1 \zeta_1 + m_2 \zeta_2)$  is the effective friction coefficient (8). The latter expression is in agreement with the additivity of the two particle Brownian diffusivities ( $\mathcal{D} = \mathcal{D}_1 + \mathcal{D}_2$ ) with the Einstein relation ( $\mathcal{D}_i = kT / \zeta_i m_i$ ).

A typical example of the "collision" of two particles with quite different sizes is molecular condensation onto a droplet. In such a case, one can simply assume that the larger particle (#1) is fixed relative to the smaller one (#2). Hence in that case we need only to solve the FPE governing the *singlet* distribution function  $f^{(1)}$ . This, again, reduces to Eq. [9] if  $m_1 \gg m_2$ , and  $|C_1| \ll |C_2|$ . For the situations that the two particles are of different sizes but not extremely unequal, Eq. [9] is still approximately valid since it is the limiting form for the two situations discussed above. Therefore, Eq. [9] will be used as a starting point even when the two particles are of different sizes.

## THE MOMENT EQUATIONS

Equation [9] can be written in the form (3)

$$h^2 \mathbf{F} \cdot \nabla_{\mathbf{v}} g + \mathbf{v} \cdot \nabla_{\mathbf{r}} g = h \xi \nabla_{\mathbf{v}} \cdot [\omega \nabla_{\mathbf{v}} (g/\omega)] , \quad [10]$$

in which the following change of variables has been employed,

$$\begin{aligned} \mathbf{v} &= h \mathbf{C} \quad ; \quad h = \sqrt{\mu/kT} \\ g(\mathbf{r}, \mathbf{v}) &= f(\mathbf{r}, \mathbf{C})/h^3 \quad ; \quad \mathbf{F} = \mathbf{X}/\mu = -\nabla \Phi \\ \omega(\mathbf{r}, \mathbf{v}) &= \exp(-v^2/2 - \Phi(\mathbf{r})h^2)/(2\pi)^{3/2} . \end{aligned} \quad [11]$$

$\mathbf{F}$  and  $\Phi$  are the interparticle force and potential per unit reduced mass, respec-

tively. Grad (4, 5) expressed the distribution function as an expansion of the Hermite polynomials and truncated it at the third order,

$$g(\mathbf{r}, \mathbf{v}) = \omega(\mathbf{r}, \mathbf{v}) n_{\infty} \left[ a^{(0)}(\mathbf{r}) H^{(0)}(\mathbf{v}) + \sum_i a_i^{(1)}(\mathbf{r}) H_i^{(1)}(\mathbf{v}) + \frac{1}{2} \sum_i \sum_j a_{ij}^{(2)}(\mathbf{r}) H_{ij}^{(2)}(\mathbf{v}) + \frac{1}{10} \sum_i a_i^{(3)}(\mathbf{r}) H_i^{(3)}(\mathbf{v}) \right] , \quad [12]$$

where

$$\begin{aligned} H^{(0)} &= 1 & ; & \quad a^{(0)} = n(\mathbf{r}) \exp(\Phi h^2) / n_{\infty} \\ H_i^{(1)} &= v_i & ; & \quad a_i^{(1)} = h j_i(\mathbf{r}) \exp(\Phi h^2) / n_{\infty} \\ H_{ij}^{(2)} &= v_i v_j - \delta_{ij} & ; & \quad a_{ij}^{(2)} = h^2 p_{ij}(\mathbf{r}) \exp(\Phi h^2) / n_{\infty} \\ H_i^{(3)} &= v_i (v^2 - 5) & ; & \quad a_i^{(3)} = [2h^3 q_i(\mathbf{r}) - 5h j_i(\mathbf{r})] \exp(\Phi h^2) / n_{\infty} \end{aligned} \quad [13]$$

and

$$\begin{aligned} n(\mathbf{r}) &= \int_{\mathbf{C}} f d\mathbf{C} = \int_{\mathbf{v}} g d\mathbf{v} \\ j_i(\mathbf{r}) &= \int_{\mathbf{C}} f C_i d\mathbf{C} = \frac{1}{h} \int_{\mathbf{v}} g v_i d\mathbf{v} \\ p_{ij}(\mathbf{r}) &= \int_{\mathbf{C}} f C_i C_j d\mathbf{C} - \frac{\delta_{ij} n(\mathbf{r})}{h^2} = \frac{1}{h^2} \left[ \int_{\mathbf{v}} g v_i v_j d\mathbf{v} - \delta_{ij} n(\mathbf{r}) \right] \\ q_i(\mathbf{r}) &= \int_{\mathbf{C}} f \frac{C_i^2}{2} d\mathbf{C} = \frac{1}{h^3} \int_{\mathbf{v}} g \frac{v^2}{2} v_i d\mathbf{v} . \end{aligned} \quad [14]$$

The summation terms in Eq. [12] are performed over the Cartesian coordinates,  $i, j = x, y, \text{ or } z$ . The relative motion of the two particles can be viewed as that of a fictitious particle of mass  $\mu$  moving toward a massless target particle whose radius is the sum of the two particle radii. Consequently, the physical meaning of the parameters in Eq. [14] can be related to the fictitious particle as follows:  $n(\mathbf{r})$  is the number density;  $j_i(\mathbf{r})$  is the  $i$ th direction number flux;  $q_i(\mathbf{r})$  is the  $i$ th direction energy flux per unit mass; and the first term in the  $p_{ij}$  expression,  $\int_{\mathbf{C}} f C_i C_j d\mathbf{C}$ , is the  $ij$ -th direction momentum flux per unit mass. The function  $n_{\infty}$  in Eq. [13] is the number density at a distance far from the collision surface,  $n_{\infty} = n(\mathbf{r} \rightarrow \infty)$ . Grad's expansion (Eq. [12]) is sometimes referred to as the *13-moment method*

because 13 distinct moments of the distribution function  $f$  are involved (*i.e.*, one moment in the  $n$  scalar, three in the  $j$  vector, six in the  $p$  tensor, and three in the  $q$  vector).

The Hermite polynomials obey the following recursive formulas (4),

$$\begin{aligned} v_k H^{(0)} &= H_k^{(1)} \\ v_k H_i^{(1)} &= H_{ik}^{(2)} + \delta_{ik} H^{(0)} \\ v_k H_{ij}^{(2)} &= H_{ijk}^{(3)} + \delta_{jk} H_i^{(1)} \\ v_k H_{ijl}^{(3)} &= H_{ijkl}^{(4)} + \delta_{ik} H_{jl}^{(2)} + \delta_{jk} H_{il}^{(2)} + \delta_{lk} H_{ij}^{(2)} \end{aligned} \quad [15]$$

in which

$$\begin{aligned} H_{ijk}^{(3)} &= v_i v_j v_k - (v_i \delta_{jk} + v_j \delta_{ik} + v_k \delta_{ij}) \\ H_{ijkl}^{(4)} &= v_i v_j v_k v_l - (v_i v_j \delta_{kl} + v_i v_k \delta_{jl} + v_i v_l \delta_{jk} \\ &\quad + v_j v_k \delta_{il} + v_j v_l \delta_{ik} + v_k v_l \delta_{ij}) + \delta_{ij} \delta_{kl} + \delta_{ik} \delta_{jl} + \delta_{il} \delta_{jk} \end{aligned} \quad [16]$$

are the third- and fourth-order Hermite polynomials. The function  $H_i^{(3)}$  in Eq. [13] is a truncated third-order Hermite polynomial;  $H_i^{(3)} = \sum_j H_{ijj}^{(3)} = v_i(v^2 - 5)$ . Because the Hermite polynomials are the eigenfunctions of the so-called Fokker-Planck operator,  $\nabla_v \cdot [\omega \nabla_v (\cdot)]$ ,

$$\nabla_v \cdot [\omega \nabla_v H^{(m)}] = -m \omega H^{(m)}, \quad [17]$$

one can use Eqs. [12], [15], and [17] to transform Eq. [10] into

$$\begin{aligned} h \sum_k F_k &\left[ a_k^{(1)} H^{(0)} + \sum_i a_{ki}^{(2)} H_i^{(1)} + \frac{a_k^{(3)}}{10} \left( \sum_i H_{ii}^{(2)} - 2H^{(0)} \right) \right. \\ &\quad \left. + \frac{1}{5} \sum_i a_i^{(3)} (H_{ik}^{(2)} + \delta_{ik} H^{(0)}) \right] + \frac{1}{h} \sum_k \frac{\partial}{\partial r_k} (\chi_k) \\ &= -\xi \left( \sum_i a_i^{(1)} H_i^{(1)} + \sum_i \sum_j a_{ij}^{(2)} H_{ij}^{(2)} + \frac{3}{10} \sum_i a_i^{(3)} H_i^{(3)} \right), \end{aligned} \quad [18]$$

in which

$$\begin{aligned} \chi_k(\mathbf{r}, \mathbf{v}) = & a^{(0)} H_k^{(1)} + \sum_i a_i^{(1)} (H_{ik}^{(2)} + \delta_{ik} H^{(0)}) \\ & + \frac{1}{2} \sum_i \sum_j a_{ij}^{(2)} (H_{ijk}^{(3)} + \delta_{ik} H_j^{(1)} + \delta_{jk} H_i^{(1)}) \\ & + \frac{1}{10} \sum_i a_i^{(3)} \left[ \sum_j (H_{ijjk}^{(4)} + \delta_{ik} H_{jj}^{(2)} + 2\delta_{jk} H_{ij}^{(2)}) \right] . \end{aligned} \quad [19]$$

The orthogonality of the Hermite polynomials can be expressed as (4)

$$\int_{\mathbf{v}} \exp(-\frac{v^2}{2}) H_i^{(n)} H_j^{(m)} d\mathbf{v} = \delta_{mn} \delta_{ij} (2\pi)^{3/2} m! , \quad [20]$$

where  $\delta_{ij}$  is unity if  $i = (i_1, i_2, \dots, i_n)$  is a permutation of  $j = (j_1, j_2, \dots, j_m)$  and zero otherwise. The *moment equations* can be deduced by multiplying both sides of Eq. [18] by  $\omega H^{(m)}$ , where  $m = 0, 1, 2$ , or  $3$ , and integrating over  $\mathbf{v}$ . Using the orthogonality, one finds

$$\sum_k \frac{\partial j_k}{\partial r_k} = 0 \quad [21]$$

$$\left( \frac{\partial n}{\partial r_l} - n h^2 F_l \right) + h^2 \sum_k \frac{\partial p_{lk}}{\partial r_k} = -\xi h^2 j_l \quad [22]$$

$$-\frac{1}{2} (j_l F_m + F_l j_m) + \frac{1}{5} \left( \frac{\partial q_l}{\partial r_m} + \frac{\partial q_m}{\partial r_l} \right) + \frac{\delta_{lm}}{5} \sum_k \frac{\partial q_k}{\partial r_k} = -\xi p_{lm} \quad [23]$$

$$\begin{aligned} 2 \sum_k \frac{\partial p_{lk}}{\partial r_k} - 2h^2 \sum_k p_{lk} F_k + \frac{\partial}{\partial r_l} \left( \sum_k p_{kk} \right) - h^2 F_l \sum_k p_{kk} \\ = -3\xi (2h^2 q_l - 5j_l) . \end{aligned} \quad [24]$$

Eqs. [21]–[24] compose a set of 13 equations that can be solved for the 13 unknown moments subject to appropriate boundary conditions.

Instead of solving for the 13 moments simultaneously, one notes that the pressure terms in Eqs. [22] and [24] can be eliminated by substituting Eq. [23]. The

resulting equations, together with Eq. [21], can be used to solve for the seven moments  $n$ ,  $\mathbf{j}$ , and  $\mathbf{q}$  independently. These equations in vector form are

$$\nabla \cdot \mathbf{j} = 0 \quad (\nabla \equiv \nabla_{\mathbf{r}}) , \quad [25]$$

$$\begin{aligned} \nabla n - h^2 n \mathbf{F} + \frac{h^2}{2\xi} [\mathbf{j}(\nabla \cdot \mathbf{F}) + \mathbf{F} \cdot \nabla \mathbf{j} + \mathbf{j} \cdot \nabla \mathbf{F}] \\ - \frac{h^2}{5\xi} \{ 3 \nabla^2 \mathbf{q} + 2 [\nabla \times (\nabla \times \mathbf{q})] \} = -\xi h^2 \mathbf{j} , \end{aligned} \quad [26]$$

and

$$\begin{aligned} h^2 \left[ 2\mathbf{F}(\mathbf{j} \cdot \mathbf{F}) - \frac{7}{5}\mathbf{F}(\nabla \cdot \mathbf{q}) + \mathbf{j}(\mathbf{F} \cdot \mathbf{F}) - \frac{2}{5} \sum_j F_j \nabla q_j - \frac{2}{5}(\mathbf{F} \cdot \nabla \mathbf{q}) \right] \\ - [\nabla(\mathbf{j} \cdot \mathbf{F}) + \mathbf{j}(\nabla \cdot \mathbf{F}) + \mathbf{F} \cdot \nabla \mathbf{j} + \mathbf{j} \cdot \nabla \mathbf{F}] \\ + \frac{11}{5} \nabla^2 \mathbf{q} + \frac{9}{5} [\nabla \times (\nabla \times \mathbf{q})] = 3\xi (2h^2 \mathbf{q} - 5\mathbf{j}) , \end{aligned} \quad [27]$$

in which the  $l$ th components of vectors  $\mathbf{j}$ ,  $\mathbf{q}$ , and  $\mathbf{F}$  are  $j_l$ ,  $q_l$ ,  $F_l$ , respectively. In the next section, these equations are nondimensionalized and are further simplified by assuming spherical symmetry.

## SPHERICAL SYMMETRY AND NONDIMENSIONALIZATION

For aerosol collision processes, we can assume that the fictitious massless particle is spherical and the interparticle potential as well as the moments (i.e.,  $n$ ,  $\mathbf{j}$ , and  $\mathbf{q}$ ) are functions only of the radial distance between the particle centers,  $r$ . Let us denote

$$\mathbf{j} = j \frac{\mathbf{r}}{r} ; \quad \mathbf{q} = q \frac{\mathbf{r}}{r} ; \quad \mathbf{F} = F \frac{\mathbf{r}}{r} . \quad [28]$$

If collision is considered to occur once the distance between the two particle



centers is less than a certain range  $R$  (i.e., the *collision surface*), the dimensionless group  $\kappa = (h\xi R)^{-1}$  has the significance of an *effective* Knudsen number,

$$\kappa = \frac{1}{h\xi R} = \frac{\left(\frac{1}{h}\right)\left(\frac{1}{\xi}\right)}{R} = \frac{\left(\frac{\text{thermal speed}}{\text{collision surface distance}}\right)\left(\frac{\text{relaxation time in background gas}}{\text{collision surface distance}}\right)}{\left(\frac{\text{particle mean free path}}{\text{particle radius}}\right)} \propto \frac{\left(\frac{\text{particle-background gas}}{\text{mean free path}}\right)}{\left(\frac{\text{particle}}{\text{radius}}\right)}.$$

The characteristic length scale for the Brownian motion Fokker-Planck moment equations [25]–[27] (or [21]–[24]) is  $\kappa R$ . The physical significance of the latter is the effective mean free path of the fictitious incident particle. The time scale is the Brownian motion relaxation time,  $1/\xi$ . The determination of the location of the collision surface  $R$  is addressed in a later section. We can nondimensionalize the moment equations according to the above characteristic scales. The dimensionless moments, force, and potential are, therefore,

$$\begin{aligned} \hat{n} &= nR^3\kappa^3 & ; & & \hat{j} &= jR^2\kappa^2/\xi \\ \hat{q} &= q/\xi^3 & ; & & \kappa &= (h\xi R)^{-1} \\ \hat{r} &= r/R\kappa & ; & & \hat{F} &= F/R\kappa\xi^2 = -d\hat{\Phi}/d\hat{r} \\ \hat{\Phi} &= \Phi h^2 \end{aligned} \tag{29}$$

and the moment equations [25] to [27] become

$$\frac{d\hat{j}}{d\hat{r}} + \frac{2\hat{j}}{\hat{r}} = 0 \tag{30}$$

$$\frac{d\hat{n}}{d\hat{r}} + \hat{n}\frac{d\hat{\Phi}}{d\hat{r}} - \hat{j}\frac{d^2\hat{\Phi}}{d\hat{r}^2} - \frac{3}{5}\left(\frac{d^2\hat{q}}{d\hat{r}^2} + \frac{2}{\hat{r}}\frac{d\hat{q}}{d\hat{r}} - \frac{2\hat{q}}{\hat{r}^2}\right) = -\hat{j} \tag{31}$$

$$\begin{aligned} \frac{d^2\hat{q}}{d\hat{r}^2} + \frac{2}{\hat{r}}\frac{d\hat{q}}{d\hat{r}} - \frac{2\hat{q}}{\hat{r}^2} + \frac{1}{11}\frac{d\hat{\Phi}}{d\hat{r}}\left(15\hat{j}\frac{d\hat{\Phi}}{d\hat{r}} + 11\frac{d\hat{q}}{d\hat{r}} + 14\frac{\hat{q}}{\hat{r}}\right) \\ + \frac{5}{11}\left(\frac{d\hat{\Phi}}{d\hat{r}}\frac{d\hat{j}}{d\hat{r}} + 3\hat{j}\frac{d^2\hat{\Phi}}{d\hat{r}^2}\right) = \frac{15}{11}(2\hat{q} - 5\hat{j}) . \end{aligned} \tag{32}$$

Equation [30] has the solution  $\hat{j} = A/\hat{r}^2$ , where  $A$  is a constant. At the collision

surface  $r = R$ ,  $\hat{r} = 1/\kappa$  and  $\hat{j} = \hat{j}_s = A\kappa^2$ . If the concentration at infinity ( $\hat{n}_\infty$ ) is known, the coagulation coefficient is then determined from

$$K = -\frac{4\pi R^2}{n_\infty} j|_R = -\frac{4\pi}{h^3 \xi^2} \frac{A}{\hat{n}_\infty} = -4\pi R D \kappa \frac{A}{\hat{n}_\infty} , \quad [33]$$

where  $D = kT/\xi\mu = 1/\xi h^2$  is the Einstein relation for the Brownian diffusivity. The value of  $A$  is correlated with other surface quantities (*i.e.*, surface concentration  $\hat{n}_s$ , and surface heat flux  $\hat{q}_s$ ) through the accommodation conditions at the collision surface. Therefore, in the next section we discuss the mass and energy accommodation conditions and show how they interface with the governing equations [30]–[32]. In the subsequent section, we present a numerical scheme that can determine the value of  $A$  by solving Eqs. [31] and [32] simultaneously with the use of the accommodation coefficients.

## MASS AND ENERGY ACCOMMODATION

In a coagulation process, the incoming number or energy flux is different from the corresponding outgoing flux depending on the surface conditions. Therefore, to discuss the mass and energy accommodation at the collision surface, we need to introduce the concept of “half-range fluxes” (28), in which only half of the velocity space (*i.e.*, all particles with velocities that have the same sign in one specific direction) is considered. In our present work the corresponding half-range distribution functions are, therefore, defined as  $f^\pm(\mathbf{C}) = f(\mathbf{C})H(C_r = \pm)$ ; where  $C_r = \mathbf{C} \cdot \mathbf{r}$ , and  $H$  is the Heaviside function. If one focuses on the collision surface,  $f^-$  and  $f^+$  represent the distribution functions of the incoming and outgoing particles, respectively. Consequently, the half-range number and energy fluxes are defined as the first and third moments of the half-range distribution functions (recall Eq.

[14]); i.e.,

$$j^{\pm} \equiv \int_{\mathbf{C}} C_r f^{\pm}(\mathbf{C}) d\mathbf{C} \quad [34]$$

$$q^{\pm} \equiv \frac{1}{2} \int_{\mathbf{C}} C^2 C_r f^{\pm}(\mathbf{C}) d\mathbf{C} , \quad [35]$$

where in both equations the integrations are carried out over the entire speed range,  $-\infty < |\mathbf{C}| < \infty$ . Upon using the Grad expansion of the distribution function, these half-range fluxes can be evaluated analytically in terms of the full-range moments,

$$j^{\pm} = \frac{n}{h\sqrt{2\pi}} \pm \frac{j}{2} + \frac{h}{2\sqrt{2\pi}} p_{rr} \quad [36]$$

$$q^{\pm} = \frac{2n}{h^3\sqrt{2\pi}} + \frac{1}{2h\sqrt{2\pi}} \left( 3p_{rr} + \sum_k p_{kk} \right) \pm \frac{q}{2} . \quad [37]$$

Equations [36] and [37] give  $j = j^+ - j^-$  and  $q = q^+ - q^-$ , which are in agreement with the definition of half-range fluxes.

For mass accommodation, there is a fraction of the incident particles that will permanently stick onto the collision surface. Energy accommodation occurs when a portion of the outgoing energy flux has fully equilibrated with the collision surface. We can illustrate these phenomena by considering the "stickiness" and "stiffness" of the collision surface. For example, a stickier surface can withhold more impinging particles and thus has a higher mass accommodation. A stiffer surface is expected to have less ability in equilibrating with the incoming fluxes and should have a lower energy accommodation. Since microscopic surface properties are generally unknown, phenomenological models are often employed to represent the energy and mass accommodation. For example, we can assume that all incoming particles have the same probability of sticking regardless of their incident velocity directions (28). This assumption permits using only one single-valued mass accommodation

coefficient (*i.e.*, the sticking probability),  $\alpha_S$ , to specify the degree of "stickiness." The most commonly used model for particle reflection (*i.e.*, the degree of "stiffness") at the collision surface is one proposed by Maxwell (31), who assumed that a nonsticking incoming particle is either trapped on the surface momentarily and then emitted in all directions (*i.e.*, diffusive reflection), or bounces off immediately like a billiard ball (*i.e.*, specular reflection). The probability of diffusive reflection is called the *Maxwellian coefficient* and is denoted as  $\alpha_M$ . Assuming that  $\alpha_M$  does not depend on the incoming particle velocity, one obtains the following relation between the half-range distribution functions ( $f^+$  and  $f^-$ ) at the surface (28),

$$f^+(\mathbf{v}) = (1 - \alpha_S) \left\{ \frac{\alpha_M h^4}{2\pi} j^- \exp\left(-\frac{v^2}{2}\right) + (1 - \alpha_M) f^-(\mathbf{v} - 2v_r \mathbf{r}) \right\} , \quad [38]$$

where we have used  $\mathbf{v} = h\mathbf{C}$  (Eq. [11]). The two terms on the right-hand side represent contributions from diffusive and specular reflection, respectively. The assumption that the collision surface temperature,  $T_s$ , is equal to that of the background gas,  $T$ , is implicit in Eq. [38].

Physically, the accommodation coefficient is the ratio of the net flux of a quantity to that of the equilibrium (fully accommodated) situation. Therefore, the mass and thermal accommodation coefficients,  $\alpha_S$  and  $\alpha_e$ , are defined as

$$\alpha_S \equiv \frac{j^- - j^+}{j^-} ; \quad \alpha_e \equiv \frac{q^- - q^+}{q^- - q^0} \quad (\text{on } S) , \quad [39a, b]$$

in which  $q^0 = 2(1 - \alpha_S)j^-/h^2$  is the equilibrium emergent energy flux from the surface; it is found by setting  $\alpha_M = 1$  in Eq. [38], multiplying  $v^2/2$ , and integrating over  $\mathbf{v}$ . Note that when all the particles stick to the surface, there is no equilibrium emergent number flux. Therefore, the denominator of the  $\alpha_S$  definition in Eq.

[39a], which represents the equilibrium net number flux, is just  $j^-$ . Figures 1 and 2 schematically interpret both accommodation coefficients.

Due to the difficulty in measuring the thermal accommodation coefficient, Eq. [39b] provides a relation between  $\alpha_e$  and the Maxwellian coefficient,  $\alpha_M$ . For arbitrary  $\alpha_M$ , we can again take the second moment on both sides of Eq. [38] and obtain  $q^+ = 2(1 - \alpha_S)\alpha_M j^-/h^2 + (1 - \alpha_S)(1 - \alpha_M)q^-$ . This leads to

$$\alpha_e = \alpha_M + \frac{(1 - \alpha_M)\alpha_S q^-}{q^- - 2(1 - \alpha_S)j^-/h^2} . \quad [40]$$

The number and energy surface boundary conditions are the corresponding full-range fluxes evaluated at the collision surface ( $r = R$ ),

$$j_s = j_s^+ - j_s^- = -\alpha_S j_s^- \quad [41]$$

$$q_s = q_s^+ - q_s^- = 2(1 - \alpha_S)\frac{\alpha_e j_s^-}{h^2} - \alpha_e q_s^- , \quad [42]$$

in which the subscript "s" denotes the surface quantities. The half-range fluxes on the right-hand sides of Eqs. [41] and [42] can be replaced with the full-range fluxes from Eqs. [36] and [37]. However, the pressure terms in the latter two equations need to be further related to  $j$  and  $q$ . From Eq. [23],

$$p_{rr} = \frac{1}{\xi} \left( jF - \frac{3}{5} \frac{dq}{dr} - \frac{2q}{5r} \right) \quad [43]$$

$$\sum_k p_{kk} = \frac{1}{\xi} \left( jF - \frac{dq}{dr} - \frac{2q}{r} \right) . \quad [44]$$

Upon combining Eqs. [36], [37], and [40]–[44], and nondimensionalizing according to Eq. [29], the surface boundary conditions become

$$B_{n1}\hat{n}_s + B_{n2}\hat{q}_s + B_{n3}\frac{d\hat{q}}{d\hat{r}}\Big|_s = B_{n4}\hat{j}_s = A\kappa^2 B_{n4} \quad [45]$$

$$B_{e1}\hat{n}_s + B_{e2}\hat{q}_s + B_{e3}\frac{d\hat{q}}{d\hat{r}}\Big|_s = B_{e4}\hat{j}_s = A\kappa^2 B_{e4} , \quad [46]$$

where

$$\begin{aligned} B_{n1} &= 2\alpha_S/(2 - \alpha_S) & ; & & B_{n2} &= -B_{n1}\kappa/5 \\ B_{n3} &= -3B_{n1}/10 & ; & & B_{n4} &= -\sqrt{2\pi} + \frac{1}{2}B_{n1}\frac{d\hat{\Phi}}{d\hat{r}}\Big|_s \end{aligned} \quad [47]$$

and

$$\begin{aligned} B_{e1} &= \alpha_S/\pi \\ B_{e2} &= \frac{1}{\sqrt{2\pi}}\left(1 - \frac{1}{2}\alpha_S - \frac{1}{2}\alpha_M + \frac{1}{2}\alpha_S\alpha_M\right) - \frac{\kappa}{5\pi}\left(3\alpha_M + 4\alpha_S - 3\alpha_S\alpha_M\right) \\ B_{e3} &= \frac{1}{10\pi}\left(4\alpha_S\alpha_M - 7\alpha_S - 4\alpha_M\right) \\ B_{e4} &= \frac{1}{\sqrt{2\pi}}\alpha_M(\alpha_S - 1) + \frac{1}{2\pi}\left(\alpha_M + 2\alpha_S - \alpha_S\alpha_M\right)\frac{d\hat{\Phi}}{d\hat{r}}\Big|_s . \end{aligned} \quad [48]$$

The coefficients in Eqs. [45] and [46] with subscripts “n” and “e” denote the number and energy accommodation conditions, respectively.

## TWO-DIMENSIONAL SHOOTING SCHEME

In this section, we first summarize the governing equations and boundary conditions. Then a two-dimensional shooting algorithm is presented for obtaining the numerical solutions of number and energy fluxes in the presence of an interparticle potential. Finally, we will discuss the appropriate definitions of the collision surface for different situations.

*Governing equations and boundary conditions.* Our governing moment equations are Eqs. [30]–[32]. The solution of Eq. [30] is  $\hat{j} = A/\hat{r}^2$  with an undetermined constant  $A$ . The boundary condition of the first-order ODE [31] is that  $\hat{n}(\hat{r} \rightarrow \infty) = \hat{n}_\infty$ . The boundary conditions of the second-order ODE [32] are that

at  $\hat{r} = 1/\kappa$ ,  $\hat{q} = \hat{q}_s$ , and that  $\hat{q}$  is finite when  $\hat{r}$  approaches infinity. The solutions of Eqs. [31] and [32] need also to satisfy the surface accommodation conditions, Eqs. [45] and [46]. In general, since only the concentration at infinity ( $\hat{n}_\infty$ ) and the  $\kappa$  value are given, one needs to guess the initial conditions for Eqs. [31] and [32] and iterate to shoot for correct solutions.

*Two-dimensional shooting scheme.* In order to calculate the coagulation coefficient (recall Eq. [33]), the  $A$  value must be determined by simultaneously solving the governing equations [31] and [32]. For a given  $\kappa$  and an initial guess of the  $\hat{n}_s$  and  $A$  values, Eqs. [45] and [46] give the values of  $\hat{q}_s$  and  $d\hat{q}/d\hat{r}|_s$ . The latter are used to solve Eq. [32] by checking whether  $\hat{q}$  is finite at large  $\hat{r}$ , in order to obtain an appropriate value of  $A$  at a given guess of  $\hat{n}_s$ . This is the first shooting (i.e., find  $A$  at a fixed  $\hat{n}_s$ ). To shoot the next guess of the  $\hat{n}_s$  value, we take advantage of Eq. [31] which gives the relation

$$\hat{n}_s = \exp(-\hat{\Phi}_s) \left\{ \hat{n}_\infty - \int_{1/\kappa}^{\infty} e^{\hat{\Phi}} \left[ \frac{A}{\hat{r}^2} \left( \frac{d^2 \hat{\Phi}}{d\hat{r}^2} - 1 \right) + \frac{3}{5} \left( \frac{d^2 \hat{q}}{d\hat{r}^2} + \frac{2}{\hat{r}} \frac{d\hat{q}}{d\hat{r}} - \frac{2\hat{q}}{\hat{r}^2} \right) \right] d\hat{r} \right\} . \quad [49]$$

With a newly calculated  $\hat{n}_s$ , surface boundary conditions [45] and [46] yield new values of  $\hat{q}_s$  and  $d\hat{q}/d\hat{r}|_s$ , and the entire procedure can be iterated until both  $\hat{n}_s$  and  $A$  converge. Therefore, for a known potential  $\hat{\Phi}$  and a given effective Knudsen number  $\kappa$ , a two-dimensional shooting method is necessary to solve the moment equations [31] and [32].

*Definition of the collision surface.* The choice of an appropriate collision surface should take into account the effect of the interparticle potential. In the free-molecule regime, an appropriate definition of the collision surface is where the maximum of an effective potential occurs; the effective potential is a combination of the interparticle potential with the centrifugal potential (16, 20). When colli-

sions between particles become more frequent, particles may relax in the angular direction, and the thermal average of the centrifugal potential can also define a unique barrier that serves to determine the flux (21-23). In this paper, however, we assume that radial symmetry is valid three-dimensionally in order to obtain moment equations [30]–[32]; that is, the particle collision frequency is assumed to be sufficiently high that the centrifugal potential contribution to the energy barrier can be neglected. As a result, the collision surface location can be uniquely determined from only the interparticle potential.

For situations of monotonic attractive potential or monotonic finite repulsive potential, the closest distance that the two colliding particles can approach occurs at the sum of the two particle radii,  $R_{12} = R_1 + R_2$ . The location of the collision surface, therefore, is where  $r = R_{12}$ . On the other hand, for situations involving a nonmonotonic potential that has an attractive part and a repulsive part, the location of collision surface can be characterized as where  $d\Phi/dr = 0$ . For example, the Coulombic potential between two particles carrying unipolar charges is repulsive in the long range. However, when the distance between the two particle radii becomes shorter, the electrical image force between the two particles is attractive and it may overwhelm the repulsive Coulombic force. Therefore, in this situation, the collision surface should be determined by setting  $d\Phi/dr = 0$  in order to evaluate the effect of long-range repulsive potential to the Brownian coagulation. Another example of nonmonotonic potential is the van der Waals potential that is attractive in the long range but repulsive in the very short range. To evaluate the enhancement of the Brownian coagulation rate by the long-range van der Waals attractive potential, again, the collision surface should be set at where  $d\Phi/dr = 0$ . Doing so, the effect of short-range repulsive van der Waals potential to the Brownian coagulation rate is not considered; instead, the phenomenological sticking probability,  $\alpha_s$ , takes into



account any possible reflection by the short-range repulsive potential.

## POTENTIAL-FREE SOLUTIONS

In the absence of interparticle forces, the number and energy fluxes as well as the coagulation coefficient can be obtained analytically from Eqs. [31] and [32]. The collision surface  $R$  is just the sum of the two hard sphere particle radii. We use the notation  $R_{12}$  and  $\kappa_{12}(=1/h\xi R_{12})$  instead of  $R$  and  $\kappa$ , in the present case, in order to distinguish from interparticle potential situations where  $R \neq R_{12}$ . Equation [32], in this case, reduces to the modified spherical Bessel equation (32). The solutions, subject to Eqs. [45] and [46], are

$$\frac{\hat{n}}{\hat{n}_\infty} = 1 - \frac{1}{\hat{r}\kappa_{12}} \left[ P + \frac{3}{5} Q \kappa_{12} \exp\left(\frac{1}{X\kappa_{12}} - \frac{\hat{r}}{X}\right) \right] \quad [50]$$

$$\frac{\hat{j}}{\hat{n}_\infty} = -\frac{P}{\kappa_{12}\hat{r}^2} \quad [51]$$

$$\frac{\hat{q}}{\hat{n}_\infty} = -\frac{5}{2} \frac{P}{\kappa_{12}\hat{r}^2} + Q \frac{X}{\hat{r}} \left(1 + \frac{X}{\hat{r}}\right) \exp\left(\frac{1}{X\kappa_{12}} - \frac{\hat{r}}{X}\right), \quad [52]$$

where

$$P = \frac{c_n b_e - c_e b_n}{a_n b_e - a_e b_n}; \quad Q = \frac{c_n a_e - c_e a_n}{b_n a_e - b_e a_n}; \quad X = \sqrt{\frac{11}{30}} \quad [53]$$

$$\begin{aligned} a_n &= -B_{n1} - \frac{5}{2} \kappa_{12} B_{n2} + 5\kappa_{12}^2 B_{n3} + \kappa_{12} B_{n4} \\ a_e &= -B_{e1} - \frac{5}{2} \kappa_{12} B_{e2} + 5\kappa_{12}^2 B_{e3} + \kappa_{12} B_{e4} \\ b_n &= -\frac{3}{5} \kappa_{12} B_{n1} + \kappa_{12} X B_{n2} + \kappa_{12}^2 X^2 B_{n2} - \kappa_{12} B_{n3} \\ &\quad - 2X \kappa_{12}^2 B_{n3} - 2X^2 \kappa_{12}^3 B_{n3} \\ b_e &= -\frac{3}{5} \kappa_{12} B_{e1} + \kappa_{12} X B_{e2} + \kappa_{12}^2 X^2 B_{e2} - \kappa_{12} B_{e3} \\ &\quad - 2X \kappa_{12}^2 B_{e3} - 2X^2 \kappa_{12}^3 B_{e3} \\ c_n &= -B_{n1}; \quad c_e = -B_{e1} \end{aligned} \quad [54]$$

and the  $B$ s are given in Eqs. [47] and [48] with  $\kappa = \kappa_{12}$  and  $\hat{\Phi} = 0$ . From Eq. [33], the coagulation coefficient is

$$K = 4\pi R_{12} \mathcal{D} P \quad (\hat{\Phi} = 0) . \quad [55]$$

For situations of  $\alpha_M = 0$  and arbitrary  $\alpha_S$ , Eq. [55] reduces to

$$\begin{aligned} K = \pi R_{12} \mathcal{D} \Big\{ & \left( \frac{X}{2Y} + \frac{2}{5} \right) + X \left( \frac{1}{5} + \frac{X}{2Y} \right) \kappa_{12} + \frac{X^2}{5} \kappa_{12}^2 \Big\} / \\ & \Big\{ \left( \frac{X}{2Y} + \frac{2}{5} \right) + \left( \frac{19}{40Y} + \frac{X}{2Y^2} + \frac{X^2}{2Y} + \frac{X}{5} \right) \kappa_{12} \\ & + \left( \frac{11}{20} + \frac{3X}{5Y} + \frac{X^2}{2Y^2} + \frac{X^2}{5} \right) \kappa_{12}^2 + \frac{3X^2}{5Y} \kappa_{12}^3 \Big\} \quad (\hat{\Phi} = 0) , \end{aligned} \quad [56]$$

where  $X = \sqrt{11/30}$  (same as in Eq. [53]) and  $Y = 2\alpha_S / [(2 - \alpha_S)\sqrt{2\pi}]$ . This result further reduces to the solutions of Mork *et al.* (6) in the case of  $\alpha_S = 1$ .

Figure 3 shows the dimensionless concentration,  $\hat{n}/\hat{n}_\infty$ , as a function of the dimensionless radial distance,  $\hat{r}\kappa_{12}(= r/R_{12})$ , from Eq. [50]. The collision surface is at  $\hat{r}\kappa_{12} = 1$ . We note that the higher the sticking probability ( $\alpha_S$ ) the lower the concentration at a given radial distance. Also because particles that have larger mean free paths have more uniformity in radial concentration profiles, we note in Figure 3 that the higher the effective Knudsen number, the closer the ratio  $\hat{n}/\hat{n}_\infty$  is to unity.

Figures 4–6 show the dimensionless surface moments ( $\hat{n}_s$ ,  $\hat{j}_s$ , and  $\hat{q}_s$ ) as functions of the effective Knudsen number,  $\kappa_{12}$ . Equations [50]–[54] were used in the calculation and the surface moments are obtained by setting  $\hat{r} = 1/\kappa_{12}$ . As expected, for a given value of  $\kappa_{12}$ , the higher the sticking probability  $\alpha_S$ , the lower the surface concentration and the higher the surface number and energy fluxes. The

stiffness parameter  $\alpha_M$  (recall that  $\alpha_M = 1$  and 0 represent the perfect diffusive reflection and perfect specular reflection, respectively), however, does not significantly influence the surface concentration and fluxes because  $\alpha_M$  only determines how the nonsticking particles are reflected from the surface. The surface number flux,  $\hat{j}_s$ , can be related to the coagulation coefficient by equating Eqs. [51] and [55]; one has

$$\frac{|\hat{j}_s|}{\hat{n}_\infty} = \frac{K}{4\pi R_{12}\mathcal{D}} \kappa_{12} . \quad [57]$$

As  $\kappa_{12}$  increases, the Brownian diffusivity  $\mathcal{D}$  may also increase substantially because the friction force on particles becomes smaller; as a result, from Eq. [57] the surface number flux is smaller. On the other hand, Eq. [57] predicts that the surface number concentration is small at low  $\kappa_{12}$  values. This explains the decrease of the surface number flux at both high and low Knudsen numbers as shown in Figure 5. For the same reason, Figure 6 shows that the surface energy flux also decreases at both ends of the Knudsen number.

Figure 7 shows the coagulation coefficient calculated from Eq. [55] as a function of the effective Knudsen number  $\kappa_{12}$  with the sticking probability  $\alpha_s$  as a parameter. The Maxwellian coefficient,  $\alpha_M$ , was set to be unity. We note that a smaller sticking probability will result in a smaller value of the coagulation coefficient. Also larger particles are less sensitive to the value of sticking probability than smaller particles. For example, one can compare the values of coagulation coefficient of a larger particle with  $\kappa_{12} = 0.1$  and a smaller particle with  $\kappa_{12} = 1$ ; a decrease in  $\alpha_s$  from 1.0 to 0.5 may result in a 17.9% decrease in the coagulation coefficient for the larger particle ( $K/4\pi R_{12}\mathcal{D}$  is reduced from 0.871 to 0.715) and a 44.1% decrease for the smaller particle ( $K/4\pi R_{12}\mathcal{D}$  is reduced from 0.313 to 0.175). The reason for this behavior is that the scavenging of incoming particles by the

larger surface area of a larger particle somewhat compensates for the decrease in sticking probability.

Figure 8 shows the influence of the Maxwellian coefficient,  $\alpha_M$ , on the value of the coagulation coefficient over the entire range of  $\alpha_S$ . For a given sticking probability  $\alpha_S$  and a Knudsen number  $\kappa_{12}$ , a change in the mechanism of reflection (from  $\alpha_M = 0$  to 1, specular to diffusive reflection) may only result in a coagulation coefficient change within 0.4%. At  $\alpha_S = 0$ , all the incoming particles are reflected and thus  $K(\alpha_M = 1) = K(\alpha_M = 0) = 0$ . On the other hand, at  $\alpha_S = 1$ , all the incoming particles are captured at the surface; the value of  $\alpha_M$  has no meaning in this situation, and therefore  $K(\alpha_M = 1) = K(\alpha_M = 0)$ . For any intermediate  $\alpha_S$  value,  $K(\alpha_M = 1)$  is always higher than  $K(\alpha_M = 0)$ . This phenomenon can be intuitively explained as follows: A higher value of  $\alpha_M$  indicates that a larger portion of the incoming particles can accommodate with the collision surface. In other words, the surface is less stiff (or softer) and is able to trap more particles in the coagulation process.

## SOLUTIONS OF POWER-LAW POTENTIAL

To see the qualitative influence on the moments profiles ( $\hat{n}$ ,  $\hat{j}$ , and  $\hat{q}$ ), we consider a potential of the form

$$\hat{\Phi} = \frac{\lambda}{\hat{r}^\nu} . \quad [58]$$

With this power-law potential, we solve Eqs. [31] and [32] simultaneously subject to the surface boundary conditions Eqs. [45] and [46]. In Eq. [58], values of  $\nu$  and  $\lambda$  determine the shape and magnitude of the power-law potential, respectively. For

$\lambda > 0$ , the potential is repulsive; for  $\lambda < 0$ , the potential is attractive. In either case, the potential is monotonic and the location of collision surface is  $r = R_{12}$ .

Figure 9 shows the predicted dimensionless concentration profile ( $\hat{n}/\hat{n}_\infty$ ) for five values of  $\alpha_S$ . The collision surface is at  $\hat{r}\kappa = 1$ . In the calculation, we chose  $\lambda = -1$  (attractive potential),  $\nu = 6$ ,  $\kappa = 1$ , and  $\alpha_M = 0$ . For the same reason as that in Figure 3, we note that the higher the value of sticking probability the lower the concentration profile. For situations that  $\alpha_S = 0.3, 0.5$ , and  $0.7$ , the concentrations near the collision surface are enhanced because of the simultaneous short-range reflection by the collision surface and the thermalization of particles in the attractive potential well. As the sticking probability  $\alpha_S$  increases, the surface sink effect overwhelms the potential thermalization and thus greatly reduces the surface concentration, as shown by the  $\alpha_S = 0.9$  and  $1.0$  curves.

Figure 10 shows the concentration profiles of three different values of  $\lambda$ . We used  $\alpha_S = 1$ ,  $\nu = 6$ , and  $\kappa = 1$ . The value of  $\alpha_M$  does not influence the calculation results when  $\alpha_S = 1$ , since the latter represents that all the incoming particles are captured. The solid line shows the potential-free solution ( $\lambda = 0$ ), where the concentration monotonically decreases to a minimum at the collision surface. For  $\lambda = 1$ , the potential is repulsive; the concentration profile is higher than that of the potential-free situation ( $\lambda = 0$ ) in the range  $\hat{r}\kappa > 1.2$ , because particles are barricaded by the potential in the far field. The concentration decreases fast near the collision surface for  $\lambda = 1$  because of the higher potential and the surface sink. In the case of an attractive potential ( $\lambda = -1$ ), particles are trapped and thermalized in a short range near the collision surface; however, the enhancement of concentration due to the potential trapping is compensated by the surface sink and, in this example, the concentration profile does not exceed that of the potential-free case near the surface.

In some attractive potential situations, enhancement of particle concentration near the collision surface by potential trapping is not influenced by the surface sink, and as a result, the concentration profiles in a short range may exceed that of the potential-free situation. We demonstrate this point by varying the power-law shape from  $\nu = 6$  to  $\nu = 2$ . For a constant negative  $\lambda$ , the higher the  $\nu$  value the stronger the attractive potential. Figure 11 shows the concentration profiles for different values of  $\nu$  at  $\alpha_s = 1$  (perfect sink),  $\lambda = -1$ , and  $\kappa = 1$ . At  $\nu = 2$ , for example, the potential is stronger than that of higher values of  $\nu$ ; the incoming particles can be easily trapped and exhibit a higher concentration than in the potential-free situation (*i.e.*, solid line in Figure 9) irrespective of the perfect surface sink.

Figure 12 shows the normalized surface number flux,  $|\hat{j}_s|/\hat{n}_\infty$ , as a function of the power-law potential order,  $\nu$ , for  $\alpha_s = 1$  and  $\kappa = 1$ . When  $\lambda > 0$ ,  $|\hat{j}_s| \approx$  constant, because a potential barrier always exists at the collision surface. For  $\lambda = 0, 1$ , and  $2$ , the corresponding constant values of  $|\hat{j}_s|/\hat{n}_\infty$  are  $0.313, 0.120$ , and  $0.042$ , respectively. On the other hand, for  $\lambda < 0$ , the smaller the  $\nu$  value the stronger the potential, and therefore, the stronger the surface number flux.

Figure 13 shows the isopleths of the ratio of coagulation coefficient to that of the potential-free situation,  $K/K(\Phi = 0)$ , as functions of both the Knudsen number  $\kappa$  and the power-law coefficient  $\lambda$ . In the calculation, the potential power  $\nu = 6$ , and the sticking probability  $\alpha_s = 1$ . The isopleths values are chosen as  $0.377$  (retardation by repulsive potential) and  $1.530$  (enhancement by attractive potential) such that both isopleths curves pass the point ( $\kappa = 1, |\lambda| = 1$ ). It is seen that for a constant retardation or enhancement in the coagulation rate, an increase in Knudsen number from  $1$  to  $9$  requires a decrease in  $|\lambda|$  from  $1$  to  $10^{-6}$ . In other words, if the interparticle potential is of the power-law form as given by Eq. [58], a small magnitude of the potential may greatly enhance or decrease the

coagulation rate between particles of sizes near the free-molecule regime.

Finally, we discuss a measure of the nonequilibrium phenomenon. For a true equilibrium situation (*i.e.*, the distribution function is Boltzmann), from Eq. [12], the Hermite polynomial coefficients  $a_i^{(1)}$ ,  $a_i^{(2)}$ , and  $a_i^{(3)}$  should be zero. Since the  $a_i^{(3)}$  term in Eq. [12] represents the highest order perturbation of the distribution function from equilibrium in the Grad's 13-moment method, therefore, to examine whether  $a_i^{(3)}$  is zero or not is equivalent to examining whether the distribution function is close to equilibrium such that the third-order Hermite polynomial perturbation term in Eq. [12] can be ignored. To justify this point, Eq. [13] requires  $5\hat{j} = 2\hat{q}$  when  $a_i^{(3)} = 0$ . The physical meaning of  $5\hat{j} = 2\hat{q}$  is that the constant pressure heat capacity has the value  $5/2$ , which corresponds to the ideal gas (equilibrium) situation. In consequence, the deviation of the quantity  $5\hat{j}/2\hat{q}$  from unity can be regarded as a measure of the deviation of the distribution function from equilibrium. Figure 14 shows the calculated  $5\hat{j}/2\hat{q}$  as a function of  $\hat{r}\kappa$  for the conditions  $\kappa = 1$ ,  $\alpha_M = 0$ , and  $\nu = 6$ . For  $\hat{r} \geq 5$ ,  $5\hat{j}/2\hat{q} \approx 1$  in all the situations. For the range  $1 \leq \hat{r} \leq 5$ , the potential-free ( $\lambda = 0$ ) curve slightly increases close to the collision surface due to the fact that the  $\hat{j}$  flux is enhanced by the surface sink. This nonequilibrium phenomenon is more emphasized for the  $\lambda = -1$  cases since, in these cases, not only the surface sink but also the attractive potential itself increases the  $\hat{j}$  value. In the short range from the collision surface, however, the  $\lambda = -1$  curves sharply decrease because the surface sink may attract particles and thus reduce the nonequilibrium phenomenon caused by the over-populated particles. For  $\alpha_S = 0.1$ , the nonequilibrium situation is more serious than that of  $\alpha_S = 1$  because the collision surface reflects more particles in the potential well and, hence, increases nonequilibrium. The contrary result is found for the repulsive potential curves ( $\lambda = 1$  and  $2$ ). Values of  $5\hat{j}/2\hat{q}$  are less than unity because

$\hat{j}$  is decreased by the repulsive potential. These curves achieve minima owing to the fact that  $\hat{j}$  is again enhanced by the surface sink. Because an increase in  $\lambda$  represents a stronger repulsive force and a lower particle concentration, the curve of  $\lambda = 2$  shows a larger deviation of  $5\hat{j}/2\hat{q}$  from unity than that of the  $\lambda = 1$  curve in Figure 14.

## SOLUTIONS OF THE COULOMBIC POTENTIAL

Situations involving an interparticle Coulombic potential are considered in this section. We will focus on the calculation of coagulation coefficient between particles by the method of FPE with the shooting scheme. The calculated results are compared with that predicted by the limiting sphere flux-matching method of Fuchs (1, 13).

If  $z_{pi}$  denotes the elementary charge on the  $i$ th particle, the Coulombic potential between two charged particles is

$$V = \frac{z_{p1} z_{p2} e^2}{4\pi\epsilon_{\text{air}} r} \quad , \quad [59]$$

in which  $e = 1.602 \times 10^{-19} \text{C}$ ;  $\epsilon_{\text{air}} \approx 8.854 \times 10^{-12} \text{Cm}^{-1}\text{V}^{-1}$  is the air permittivity. In Eq. [59], for simplicity the image force effect is omitted. The collision surface in this situation, therefore, is the sum of the two colliding particle radii. The dimensionless potential  $\hat{\Phi}$  is related to  $V$  by  $\hat{\Phi} = V/kT$  and can be further written in the form

$$\hat{\Phi} = \frac{Z}{\hat{r}} \quad ; \quad Z = \frac{z_{p1} z_{p2} e^2 h \xi}{4\pi\epsilon_{\text{air}} kT} \quad . \quad [60]$$

Equation [60] is just of the power-law potential form, Eq. [58], with  $\lambda = Z$  and



$$\nu = 1.$$

For equal-sized particle coagulation, the coagulation coefficient computed by the FPE method with a potential given by Eq. [60] is shown by the solid lines in Figure 15. Results predicted by the Fuchs limiting sphere flux-matching method (1) (see Appendix) are shown by the dashed lines. In the flux-matching calculation, the original Fuchs free-molecule coagulation coefficient in the presence of a potential was used (13) (recall also Table I). The conditions used in the calculation are  $\alpha_S = 1$ ,  $\rho_p = 1000 \text{ kg m}^{-3}$ ,  $l_{\text{air}} = 6.86 \times 10^{-8} \text{ m}$ ,  $\mu_{\text{air}} = 1.83 \times 10^{-5} \text{ kg m}^{-1}\text{s}^{-1}$ , and  $T = 298 \text{ K}$ . One notes that these two different approaches agree well with each other over a broad range of particle sizes.

Figure 16 shows the ratio of the coagulation coefficient to that of the potential-free situation as a function of the absolute value of charge product,  $|z_{p1}z_{p2}|$ . Because the particles cannot carry fractional charges, the portion of  $0.1 < |z_{p1}z_{p2}| < 1$  in Figure 16 can be realized as the probability that the particles carry integer charges. For example,  $z_{p1}z_{p2} = 0.5$  may represent a group of coagulating particles, 50% of which carry positive one charge. The coagulation coefficient  $K$  is normalized with respect to the potential-free solution of the Fuchs flux-matching method. The dashed lines are the result using the Fuchs method, and the solid lines are that of the FPE method. Again, the two theories are in good agreement for particles of sizes greater than  $0.03 \text{ }\mu\text{m}$ . Differences between the results of the two theories become significant for particles of sizes smaller than  $0.01 \text{ }\mu\text{m}$ . This may be due to the empirical nature of the flux-matching theory, the uncertainty of the Fuchs expression of coagulation coefficient in the presence of a potential, or the failure of prediction of free-molecule regime coagulation by the FPE method. The Fuchs method, for example, may give the results that in case of  $z_{p1}z_{p2} > 0$  (repulsion),  $K$  can be negative for sufficiently small particle size and sufficiently large charge

product; *e.g.*, for particles of size  $0.01 \mu\text{m}$  in diameter,  $K$  predicted by the Fuchs theory is negative for any  $z_{p1}z_{p2} > 1$ . One expects, however, that there should always be at least an extremely small amount of coagulation due to an occasionally high kinetic energy in the Brownian motion.

## SOLUTIONS OF THE VAN DER WAALS POTENTIAL

We now consider the presence of an interparticle van der Waals potential in coagulation. Again, we will focus on the calculation of coagulation coefficient and the comparison with the results predicted by the limiting sphere flux-matching method.

The van der Waals potential between an  $i$ -mer (that contains  $i$  molecules) and a  $j$ -mer (that contains  $j$  molecules) can be deduced from the intermolecular Lennard-Jones 6-12 potential,

$$\phi(r) = 4\epsilon \left[ \left( \frac{\sigma}{r} \right)^{12} - \left( \frac{\sigma}{r} \right)^6 \right] , \quad [61]$$

where  $\epsilon$  and  $\sigma$  are the Lennard-Jones parameters;  $r$  is the distance between two molecules. Upon assuming a pairwise additivity of all the individual intermolecular interactions, the interparticle potential can be evaluated from the double integration over the volumes of both particles. One obtains

$$\begin{aligned} \hat{\Phi} = & \frac{1}{kT} \int_{v_i} \int_{v_j} \frac{\phi(r)}{v_m^2} dv_j dv_i = \\ & \frac{H}{2520} \left\{ \frac{\tilde{r}_i \tilde{r}_j}{\tilde{r}} \left[ (\tilde{r} + \tilde{r}_i + \tilde{r}_j)^{-7} + (\tilde{r} + \tilde{r}_i - \tilde{r}_j)^{-7} + (\tilde{r} - \tilde{r}_i + \tilde{r}_j)^{-7} + (\tilde{r} - \tilde{r}_i - \tilde{r}_j)^{-7} \right] \right. \\ & - \frac{1}{6} \left[ (\tilde{r} + \tilde{r}_i + \tilde{r}_j)^{-6} - (\tilde{r} + \tilde{r}_i - \tilde{r}_j)^{-6} - (\tilde{r} - \tilde{r}_i + \tilde{r}_j)^{-6} + (\tilde{r} - \tilde{r}_i - \tilde{r}_j)^{-6} \right] \\ & + \frac{1}{5\tilde{r}} \left[ (\tilde{r} + \tilde{r}_i + \tilde{r}_j)^{-5} - (\tilde{r} + \tilde{r}_i - \tilde{r}_j)^{-5} - (\tilde{r} - \tilde{r}_i + \tilde{r}_j)^{-5} + (\tilde{r} - \tilde{r}_i - \tilde{r}_j)^{-5} \right] \Big\} \\ & - \frac{H}{6} \left\{ \frac{2\tilde{r}_i \tilde{r}_j}{\tilde{r}^2 - (\tilde{r}_i + \tilde{r}_j)^2} + \frac{2\tilde{r}_i \tilde{r}_j}{\tilde{r}^2 - (\tilde{r}_i - \tilde{r}_j)^2} + \ln \frac{\tilde{r}^2 - (\tilde{r}_i + \tilde{r}_j)^2}{\tilde{r}^2 - (\tilde{r}_i - \tilde{r}_j)^2} \right\} , \end{aligned} \quad [62]$$

where

$$\begin{aligned} \tilde{r}_i &= \frac{R_i}{r^*} ; \quad \tilde{r}_j = \frac{R_j}{r^*} ; \quad \tilde{r} = \frac{r}{r^*} ; \\ r^* &= 2^{1/6} \sigma ; \quad H = 4\pi \frac{\epsilon}{kT} \frac{\sigma^6}{v_m^2} . \end{aligned} \quad [63]$$

In Eqs. [62] and [63],  $v_m$  is the volume of a molecule;  $r^*$  is the distance corresponding to the maximum depth of the interparticle potential in Eq. [61].  $H$  is the dimensionless Hamaker constant (*i.e.*, Hamaker constant divided by  $kT$ ). Equation [62] reduces to the expression by Narsimhan and Ruckenstein (14) for the situation of equal-sized particle coagulation.

Equation [62] can be differentiated with respect to the radial distance and set to zero to find the location of the collision surface. The collision surface corresponds to the distance where the van der Waals potential is at its minimum.

Figure 17 shows the ratio of the coagulation coefficient to that of the potential-free situation (*i.e.*, the coagulation enhancement) as a function of the dimensionless Hamaker constant; the coagulation enhancement is due to the long-range attractive part of the van der Waals potential. The conditions of this calculation are the same as those in the Coulombic potential case. The results from using the present FPE method are compared with those predicted by the Fuchs flux-matching method (1)

at three different particle sizes. This time, the more elaborate expression for free-molecule regime coagulation in the presence of an interparticle potential of Marlow (16) was used in the flux-matching calculation (see Appendix and recall Table I). The matching is henceforth referred to as the "generalized Fuchs flux-matching." In Figure 17, the solid and dashed lines are obtained by the FPE method and the generalized Fuchs flux-matching, respectively. It is seen that the results are in good agreement; small differences occur for  $H < 1$  and at reduced particle size. The predictions made by the FPE method are in general higher than those predicted by the generalized Fuchs flux-matching.

## CONCLUDING REMARKS

In this paper, the Brownian coagulation of aerosol particles with an interparticle potential is analyzed through the use of the Fokker-Planck equation. The particle velocity distribution function is expanded in terms of the Hermite polynomials. Grad's 13-moment method is used to truncate the distribution function at the third-order Hermite polynomial and to obtain the moment equations. The moment equations are interfaced with appropriate collision surface conditions in terms of the sticking probability,  $\alpha_s$ , and the Maxwellian coefficient,  $\alpha_M$ . A two-dimensional shooting method is used to solve the simultaneous moment equations to obtain profiles of number concentration, number, and energy fluxes for situations with and without an interparticle potential.

The influences of the sticking probability, potential magnitude, and potential shape on the concentration profile were elucidated by using a power-law potential. The incoming particles may possess a high concentration in a short range near the target particle due to the attractive potential thermalization and/or the short-range reflection by a low sticking probability collision surface. The enhancement of particle concentration by the thermalization effect may be compensated for by the collision surface sink for a higher sticking probability. For repulsive potential situations, particles may be reflected into the far field due to the higher potential energy near the collision surface.

Coagulation coefficients calculated from the FPE method by using a Coulombic potential or a van der Waals potential are in good agreement with those predicted by the Fuchs flux-matching method over a broad range of particle sizes in the transition regime. Because the matching method solution depends upon the free-molecule regime coagulation rate expression, we used both the Fuchs and the

Marlow correction factors for coagulation in the free-molecule regime with an interparticle potential. In either case, differences with the results of FPE method are small. The free-molecule expression by Fuchs may result in a negative coagulation rate for sufficiently small particles in a repulsive potential situation. Solutions of the transition regime particle coagulation rate in the presence of an interparticle potential by the FPE approach should be, therefore, regarded as more accurate than the empirical matching predictions.

### ACKNOWLEDGMENTS

This work was supported by National Science Foundation Grant ATM-8503103.

## APPENDIX

### The Fuchs Flux-Matching Method with an Interparticle Potential

Fuchs (1, 13) assumed that around the fictitious target particle, there is an inner region of length  $\delta$  in which kinetic theory situations prevail and an outer region in which continuum transport theory dominates. The actual coagulation rate can be deduced from the matching of the number fluxes obtained from the two theories. This method shall, in general, be referred to as the Fuchs flux-matching method.

Table III lists the matching conditions used by different authors with or without an interparticle potential in the Fuchs flux-matching method. Dahneke (2) and Alam (15) chose  $r = R$  as the matching surface; Fuchs (1, 13) and Marlow (16), on the other hand, chose  $r = \delta$  as the matching surface. The right- and left-hand sides of the equations in Table III represent the particle incoming rates obtained by continuum transport theory and by gas kinetic theory, respectively. In the presence of an interparticle potential,  $E^{\text{fm}}$  and  $E^{\text{c}}$  in Table III stand for the correction factor of the coagulation rate in the free-molecule regime and continuum regime, respectively. The matching conditions of  $\Phi \neq 0$  of Marlow (16) and Alam (15) are analogous to that of Fuchs (1) and Dahneke (2) of the potential-free situation; the factors  $E^{\text{fm}}$  and  $E^{\text{c}}$  are introduced to account for the interparticle potential. However, this analogy is not appropriate because the continuum regime particle infusion rate in the presence of a potential is different from the potential-free solution multiplied by the factor  $E^{\text{c}}$ . The correct expression obtained by solving the Fick's first law in the presence of a potential was given by Fuchs (13) as shown in the last row in Table III. In this appendix, we shall briefly derive this result and its subsequent coagulation coefficient expression. We will then discuss the expressions

of the correction factor  $E^{\text{fm}}$  by Fuchs (13) and Marlow (16), respectively.

At the outer region, the Fick's first law and equation of continuity are

$$-\mathcal{D}\left(\frac{dn}{dr} + \frac{n}{kT}\frac{dV}{dr}\right) = j \quad [A1]$$

$$\frac{dj}{dr} + \frac{2j}{r} = 0 \quad , \quad [A2]$$

in which  $V$  is the interparticle potential;  $\mathcal{D}$  is the Brownian diffusivity ( $\mathcal{D} = \mathcal{D}_1 + \mathcal{D}_2$ ).

Eqs. [A1] and [A2] give the solution

$$n_\infty - n(r) \exp(\hat{\Phi}(r)) = \frac{-jr^2}{\mathcal{D}} \int_r^\infty \frac{\exp(\hat{\Phi}(r))}{r^2} dr \quad (\delta \leq r \leq \infty) \quad , \quad [A3]$$

where  $\hat{\Phi}(r) = V/kT$  is the dimensionless potential. The incoming particle rate (number of particles per unit time) at the inner-outer boundary is thus

$$4\pi\delta^2|j|_{r=\delta} = \left[ \delta \int_\delta^\infty \frac{\exp(\hat{\Phi}(r))}{r^2} dr \right]^{-1} 4\pi\mathcal{D}\delta \{ n_\infty - n_\delta \exp(\hat{\Phi}_\delta) \} \quad . \quad [A4]$$

The bracket term in Eq. [A4] is the well-known correction factor of the continuum regime coagulation rate (33),  $E^c$ . The left-hand side of Eq. [A4] is to be matched with the result obtained from gas kinetic theory.

In the inner region the incoming particle flux at  $r = \delta$ , from kinetic theory, is  $n_\delta \bar{c}/4$ ; where  $\bar{c} = \sqrt{8kT/\pi\mu}$  is the mean velocity. With  $\alpha_s$  as the sticking probability, the net coagulation rate at the collision surface  $r = R$  is  $E^{\text{fm}}\alpha_s\pi R^2 n_\delta \bar{c}$ , in which  $E^{\text{fm}}$  is the free-molecule regime correction factor for the interparticle potential situations. The net particle incoming rate at  $r = R$  is equal to that at  $r = \delta$ . The matching condition by Fuchs (13) in Table III was obtained by



equating this free-molecule rate with the one given by Eq. [A4]. Doing so, one further obtains

$$\frac{n_\delta}{n_\infty} = \left[ \exp(\hat{\Phi}_\delta) + \frac{E^{\text{fm}}}{E^c} \frac{\alpha_S R^2 \bar{c}}{4\mathcal{D}\delta} \right]^{-1} . \quad [\text{A5}]$$

The coagulation coefficient is given by  $E^{\text{fm}} \alpha_S \pi R^2 n_\delta \bar{c} / n_\infty$ ,

$$K = \frac{E^{\text{fm}} E^c \alpha_S R^2 \pi \bar{c}}{E^c \exp(\hat{\Phi}_\delta) + E^{\text{fm}} \frac{\alpha_S R^2 \bar{c}}{4\mathcal{D}\delta}} . \quad [\text{A6}]$$

In the remainder of this appendix, we will show two different expressions of  $E^{\text{fm}}$  by Fuchs (13) and Marlow (16). Fuchs (13) analyzed the conservation of energy and momentum of the two colliding particles and obtained an equation that relates the impact parameter,  $b$ , with the closest approach,  $\rho_m$ , and the inner-outer boundary distance,  $\delta$  (see Figure 18). With an assumption by Fuchs that all the incoming particles possess equal kinetic energy,  $3kT/2$ , the equation is

$$b^2 = \rho_m^2 \left[ 1 + \frac{2}{3} (\hat{\Phi}_\delta - \hat{\Phi}_{\rho_m}) \right] . \quad [\text{A7}]$$

Figure 18 shows a physical interpretation of particle deflections in an attractive force field. With a decrease in the impact parameter  $b$  from  $\delta$  to  $b_m$ , the incoming particles are deflected without collision with the target particle. For the impact parameter  $b$  of values smaller than  $b_m$ , the incoming particles are captured by the target particle. Therefore, in this situation, the collision surface area is enhanced. On the other hand, for a repulsive potential the collision surface area is decreased. In either case, one can define the correction factor as

$$E^{\text{fm}} = \left( \frac{b_m}{R} \right)^2 \quad (\text{Fuchs}) . \quad [\text{A8}]$$

For some functional forms of attractive potential,  $b_m$  should be obtained from the differentiation of Eq. [A7],  $db/d\rho_m = 0$ . However, Fuchs (13) did not mention that for the repulsive potential and some forms of attractive potential,  $b_m$  can be found by directly substituting  $\rho_m = R$  in Eq. [A7]. We illustrate this by using the Coulombic potential given by Eq. [59] as an example. Eq. [A7] in this situation becomes

$$b^2 = \rho_m^2 \left[ 1 + \frac{z_{p1} z_{p2} e^2}{6\pi\epsilon_{\text{air}} kT} \left( \frac{1}{\delta} - \frac{1}{\rho_m} \right) \right] \quad [\text{A9}]$$

If one sets  $db/d\rho_m = 0$ , there is no positive real value of  $b$  available. This means that the  $b_m$  value always occurs at  $\rho_m = R$  for both  $z_{p1} z_{p2} < 0$  and  $z_{p1} z_{p2} > 0$  situations. Consequently, from Eq. [A9], we have

$$\left( \frac{b_m}{R} \right)^2 = 1 + \frac{z_{p1} z_{p2} e^2}{6\pi\epsilon_{\text{air}} kT} \left( \frac{1}{\delta} - \frac{1}{R} \right) . \quad [\text{A10}]$$

One notes for  $(b_m/R)^2 > 1$  (i.e., enhancement of capture cross-sectional area) for  $z_{p1} z_{p2} < 0$  (attractive force);  $(b_m/R)^2 < 1$  (i.e., decrease of capture cross-sectional area) for  $z_{p1} z_{p2} > 0$  (repulsive force).

The coagulation coefficient (Eq. [A6]), in the presence of a Coulombic potential, becomes

$$K = 4\pi R \mathcal{D} \times \left\{ \frac{4\mathcal{D}}{\alpha_S R \bar{c}} \frac{\exp(z_{p1} z_{p2} e^2 / 4\pi\epsilon_{\text{air}} kT \delta)}{\left[ \left( \frac{1}{\delta} - \frac{1}{R} \right) z_{p1} z_{p2} e^2 / 6\pi\epsilon_{\text{air}} kT + 1 \right]} + \frac{4\pi\epsilon_{\text{air}} kT R}{z_{p1} z_{p2} e^2} \left[ \exp\left( \frac{z_{p1} z_{p2} e^2}{4\pi\epsilon_{\text{air}} kT \delta} \right) - 1 \right] \right\}^{-1} . \quad [\text{A11}]$$

The expression of  $E^{\text{fm}}$  by Marlow (16), on the other hand, accounts for the distribution of the incoming particle kinetic energy. The result is

$$E^{\text{fm}} = -\frac{1}{2R^2} \int_R^\delta r^2 \frac{d}{dr} \left( r \frac{d\hat{\Phi}}{dr} \right) \exp\left(-\hat{\Phi} - \frac{r}{2} \frac{d\hat{\Phi}}{dr}\right) dr - \frac{\delta^2}{2R^2} \int_\delta^\infty \frac{d}{dr} \left( r \frac{d\hat{\Phi}}{dr} \right) \exp\left(-\hat{\Phi} - \frac{r}{2} \frac{d\hat{\Phi}}{dr}\right) dr \quad (\text{Marlow}) \quad [A12]$$

Equations [A12] and [A6] were used in the calculation of the coagulation coefficient in situations involving a van der Waals interparticle potential (Figure 17).

Finally, we would like to point out that Eq. [A6] reduces to the Fuchs potential-free solution (1) given in Table II by setting both  $E^c$  and  $E^{\text{fm}}$  to unity and  $\hat{\Phi} = 0$ .

## REFERENCES

1. Fuchs, N. A., "Mechanics of Aerosols." Pergamon, New York, 1964.
2. Dahneke, B., in "Theory of Dispersed Multiphase Flow" (R. E. Meyer Ed.), p. 97. Academic Press, New York, 1983.
3. Sitarski, M., and Seinfeld, J. H., *J. Colloid Interface Sci.* **61**, 261 (1977).
4. Grad, H., *Commun. Pure Appl. Math.* **2**, 325 (1949).
5. Grad, H., *Commun. Pure Appl. Math.* **2**, 331 (1949).
6. Mork, K. J., Razi Naqvi, K., and Waldenstrøm, S., *J. Colloid Interface Sci.* **98**, 103 (1984).
7. Harris, S., *J. Chem. Phys.* **77**, 934 (1982).
8. Sahni, D. C., *J. Colloid Interface Sci.* **91**, 418 (1983).
9. Sahni, D. C., *Phys. Rev. A* **30**, 2056 (1984).
10. Kumar, V., and Menon, V. G., *J. Chem. Phys.* **82**, 917 (1985).
11. Loyalka, S. K., *J. Colloid Interface Sci.* **57**, 578 (1976).
12. Loyalka, S. K., *J. Chem. Phys.* **58**, 354 (1973).
13. Fuchs, N. A., *Geofis. Pura Appl.* **56**, 185 (1963).
14. Narsimhan, G., and Ruckenstein, E., *J. Colloid Interface Sci.* **104**, 344 (1985).
15. Alam, M. K., *Aerosol Sci. Technol.* **6**, 41 (1987).
16. Marlow, W. H., *J. Chem. Phys.* **73**, 6284 (1980).
17. Fuchs, N. A., and Sutugin, A. G., *J. Colloid Sci.* **20**, 492 (1965).
18. Graham, S. C., and Homer, J. B., *Faraday Symp.* **7**, 85 (1973).
19. Brock, J. R., and Hidy, G. M., *J. Appl. Phys.* **36**, 1857 (1965).
20. Huang, D. D., Seinfeld, J. H., and Marlow, W. H., *J. Colloid Interface Sci.*, in press.
21. Sceats, M. G., *J. Chem. Phys.* **84**, 5206 (1986).
22. Roger, P. M., and Sceats, M. G., *J. Chem. Phys.* **83**, 3558 (1985).

23. Sceats, M. G., *J. Colloid Interface Sci.* **129**, 101 (1989).
24. Kramers, H. A., *Physica* **7**, 284 (1940).
25. Burschka M. A., and Titulaer, U. M., *J. Stat. Phys.* **25**, 569 (1981).
26. Burschka M. A., and Titulaer, U. M., *J. Stat. Phys.* **26**, 59 (1981).
27. Burschka M. A., and Titulaer, U. M., *Physica A* **112**, 315 (1982).
28. Huang, D. D., and Seinfeld, J. H., *J. Colloid Interface Sci.* **130**, 275 (1989).
29. Mazo, R. M., "Statistical Mechanical Theories of Transport Processes." Oxford, Pergamon, 1967.
30. McQuarrie, D. A., "Statistical Mechanics." Harper and Row, New York, 1976.
31. Maxwell, J. C., *Philos. Trans. R. Soc. London* **157**, 49 (1867).
32. Abramowitz, M., and Stegun, I. A., "Handbook of Mathematical Functions." Dover Publications, New York, 1972.
33. Seinfeld, J. H., "Atmospheric Chemistry and Physics of Air Pollution." Wiley, New York, 1986.

Table I. Summary of Prior Work on Brownian Coagulation in the Transition Regime

Method Case	Flux-Matching (Limiting-Sphere)	Fokker-Planck Equation (FPE)	
		1-dimensional	3-dimensional
Potential-free ( $\Phi = 0$ )	Fuchs (1) Dahneke (2)	Sceats and coworkers (21-23)	Sitarski-Seinfeld (3) Mork et al. (6) Harris (7) Sahni (8, 9) Kumar-Menon (10) Loyalka (11)
Inter-particle potential ( $\Phi \neq 0$ )	Fuchs (13) Narsimhan and Ruckenstein (14) Alam (15) Marlow (16)	Burschka and Titulaer (25-27)	Present Work
Remarks	Solution depends on the continuum and free-molecule coagulation rates.	Averaging over the centrifugal potential in the free-molecule regime is less appropriate.	Usually fails to yield correct result in the free-molecule regime.

Table II  
Summary of the Potential-Free Coagulation Coefficient Expressions

Reference	$K/4\pi R_{12}D$	Remarks
Fuchs (1)	$\left[ \frac{R_{12}}{R_{12} + g_{12}} + \frac{\sqrt{2\pi}}{\alpha_S \kappa_{12}} \right]^{-1}$	$g_{12} = (g_1^2 + g_2^2)^{1/2}$ ; $g_i = \frac{1}{6R_i l_i} \left[ (2R_i + l_i)^3 - (4R_i^2 + l_i^2)^{1.5} \right] - 2R_i$ ; $l_i = \frac{8D_i}{\pi \bar{c}_i}$ ; $\bar{c}_i = \sqrt{\frac{8kT}{\pi m_i}}$
Dahneke (2)	$\frac{1 + \kappa_D}{1 + 2\kappa_D (1 + \kappa_D^2)}$	$\kappa_D = \sqrt{\frac{\pi}{2}} \kappa_{12}$ ; $\alpha_S = 1$
Sitarski and Seinfeld (3)	$\sum_{i=1}^2 \frac{D_i}{D} \left\{ \frac{1 + 0.2 z \kappa_{SS,i}}{1 + \left( 0.68 z + \frac{0.1\pi}{z} \right) \kappa_{SS,i} + 0.06 \pi \kappa_{SS,i}^2} \right\}$	$\kappa_{SS,i} = \frac{10D_i h_i}{\sqrt{2\pi} R_{12}}$ ; $h_i = \sqrt{\frac{8}{\pi}} \frac{1}{\bar{c}_i}$ ; $z = \frac{\alpha_S}{2 - \alpha_S}$
Mork <i>et al.</i> (6)	Eq. [55] with $\alpha_S = 1$ and $\alpha_M = 0$	$\alpha_S = 1$ ; $\alpha_M = 0$

(Continued...)

(Table II continued)

Harris (7)	$\frac{4}{3\pi\kappa_H} \left( 1 + \frac{1.85}{\kappa_H} \right) \frac{3.16}{\kappa_H^2} + \frac{4.7}{\kappa_H} + 2.27$	$\kappa_H = \frac{2}{3} \sqrt{\frac{2}{\pi}} \kappa_{12} ; \quad \alpha_S = 1$
Sahni (8)	$\left[ 1 + \left( \frac{1}{\alpha_S} - \frac{1}{2} \right) \frac{\sqrt{\pi}}{x} + \frac{\sqrt{\pi}}{2x} \exp(x^2) \operatorname{erfc}(x) \right]^{-1}$	$x = \frac{1}{\sqrt{2}\kappa_{12}} ; \quad \alpha_S \text{ arbitrary}$
Kumar and Menon (10)	Values in Table I of Ref. (10)	$a = \frac{\kappa_{12}}{\sqrt{2}} ; \quad \alpha_S = 1$
Loyalka (11)	$f(\operatorname{Kn}_p)$ in Table I of Ref. (11)	$\operatorname{Kn}_p = \kappa_{12} ; \quad \alpha_S = 1$
Sceats (23)	$\frac{t\sqrt{4+t^2} - t^2}{2}$	$t = \frac{\bar{c}R_{12}}{4D} = \frac{\kappa_{12}}{\sqrt{2\pi}} ; \quad \alpha_S = 1$
Present FPE Solution	Eq. [55]	$\alpha_S \text{ and } \alpha_M \text{ arbitrary}$



Table III. Prior Matching Conditions used in the Fuchs Flux-Matching Method

Works	Matching Conditions	Remarks
Dahneke (2)	$\bar{c}\pi R^2(n_\delta - n'_R) = 4\pi RD(n_\infty - n'_R)$	match at $R$ ; $n_R = 0$
Fuchs (1)	$\alpha_s \bar{c}\pi R^2(n_\delta - n'_R) = 4\pi\delta D(n_\infty - n_\delta)$	match at $\delta$ ; $n_R = 0$
Marlow (16)	$\alpha_s E^{\text{fm}} \bar{c}\pi R^2(n_\delta - n'_R) = E^c 4\pi\delta D(n_\infty - n_\delta)$	match at $\delta$ ; $n_R = 0$
Alam (15)	$E^{\text{fm}} \bar{c}\pi R^2 n_R = E^c 4\pi RD(n_\infty - n_R)$	match at $R$ ; $n_R \neq 0$
Fuchs (13)	$\alpha_s E^{\text{fm}} \bar{c}\pi R^2(n_\delta - n'_R) = E^c 4\pi\delta D$ $\times (n_\infty - n_\delta \exp(\hat{\Phi}_\delta))$	match at $\delta$ ; $n_R = 0$

## LIST OF FIGURES

- Figure 1. Physical interpretation of the mass accommodation coefficient.  $j^-$ ,  $j^+$ , and  $j$  are the incoming, outgoing, and net outgoing number fluxes, respectively.
- Figure 2. Physical interpretation of the energy accommodation coefficient.  $q^-$ ,  $q^+$ ,  $q^{\text{spec}}$ ,  $q^{\text{diff}}$ ,  $q$  and  $q^0$  are the incoming, outgoing, specular outgoing, diffusive outgoing, net outgoing, and equilibrium emergent energy fluxes per unit reduced mass, respectively.  $q^0$  is defined as  $q^+$  with  $q^{\text{spec}} = 0$ .
- Figure 3. Dimensionless concentration,  $\hat{n}/\hat{n}_\infty$ , as a function of the dimensionless radial distance,  $\hat{r}\kappa_{12}$ , for the potential-free situation.
- Figure 4. Dimensionless surface concentration,  $\hat{n}_s/\hat{n}_\infty$ , as a function of the effective Knudsen number,  $\kappa_{12}$ , for the potential-free situation.
- Figure 5. Dimensionless surface number flux,  $|\hat{j}_s|/\hat{n}_\infty$ , as a function of the effective Knudsen number,  $\kappa_{12}$ , for the potential-free situation.
- Figure 6. Dimensionless surface energy flux,  $|\hat{q}_s|/\hat{n}_\infty$ , as a function of the effective Knudsen number,  $\kappa_{12}$ , for the potential-free situation.
- Figure 7. Dimensionless coagulation coefficient,  $K/4\pi R_{12}\mathcal{D}$ , as a function of the effective Knudsen number,  $\kappa_{12}$ , for the potential-free situation.
- Figure 8. Influence of the Maxwellian coefficient,  $\alpha_M$ , on the value of the dimensionless coagulation coefficient,  $K/4\pi R_{12}\mathcal{D}$ , over the entire range of  $\alpha_S$  for the potential-free situation.
- Figure 9. Dimensionless concentration,  $\hat{n}/\hat{n}_\infty$ , as a function of the dimensionless radial distance,  $\hat{r}\kappa$ , for a power-law potential with  $\alpha_S$  as a parameter.
- Figure 10. Dimensionless concentration,  $\hat{n}/\hat{n}_\infty$ , as a function of the dimensionless

radial distance,  $\hat{r}\kappa$ , for a power-law potential with  $\lambda$  as a parameter.

Figure 11. Dimensionless concentration,  $\hat{n}/\hat{n}_\infty$ , as a function of the dimensionless radial distance,  $\hat{r}\kappa$ , for a power-law potential with  $\nu$  as a parameter.

Figure 12. Normalized surface number flux,  $|\hat{j}_s|/\hat{n}_\infty$ , as a function of the power-law potential order,  $\nu$ , with  $\lambda$  as a parameter.

Figure 13. Power-law potential coefficient,  $|\lambda|$ , as a function of the effective Knudsen number,  $\kappa$ , at two values of  $K/K(\Phi = 0)$ .

Figure 14. Measure of the deviation from equilibrium ( $5\hat{j}/2\hat{q}$ ) as a function of the dimensionless radial distance  $\hat{r}\kappa$  for three situations:  $\lambda = -1$  (attractive potential), 0 (potential-free), and 1 (repulsive potential).

Figure 15. Coagulation coefficient for equal-sized particles with a Coulombic potential as a function of the particle size and charge product.

Figure 16. Coagulation coefficient for equal-sized particles with a Coulombic potential normalized with respect to the potential-free solution of Fuchs as a function of the particle size and charge product. Solid lines and dashed lines are calculated from the FPE method and the Fuchs matching method, respectively.

Figure 17. Enhancement of the coagulation coefficient for equal-sized particles with a van der Waals potential as a function of the dimensionless Hamaker constant,  $H$ , at three different particle sizes.

Figure 18. Fuchs flux-matching limiting sphere and the physical interpretation of the increase in capture surface area in the presence of an attractive interparticle force. For  $b \leq b_m$ , incoming particles are captured.

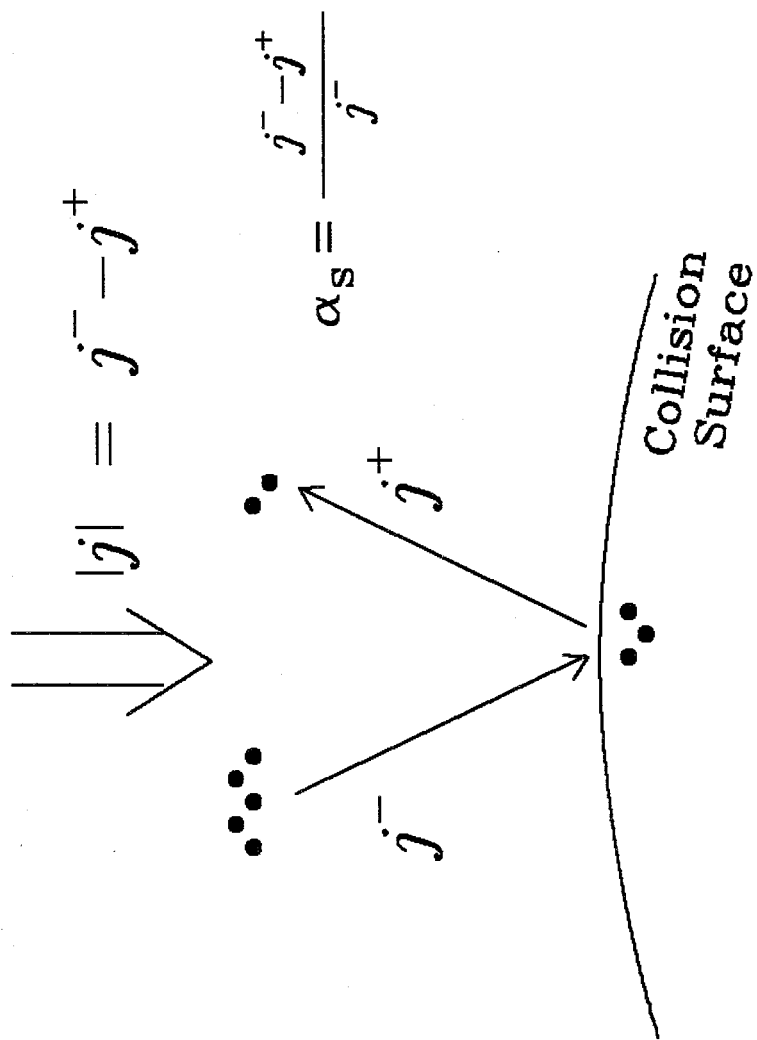


Figure 1

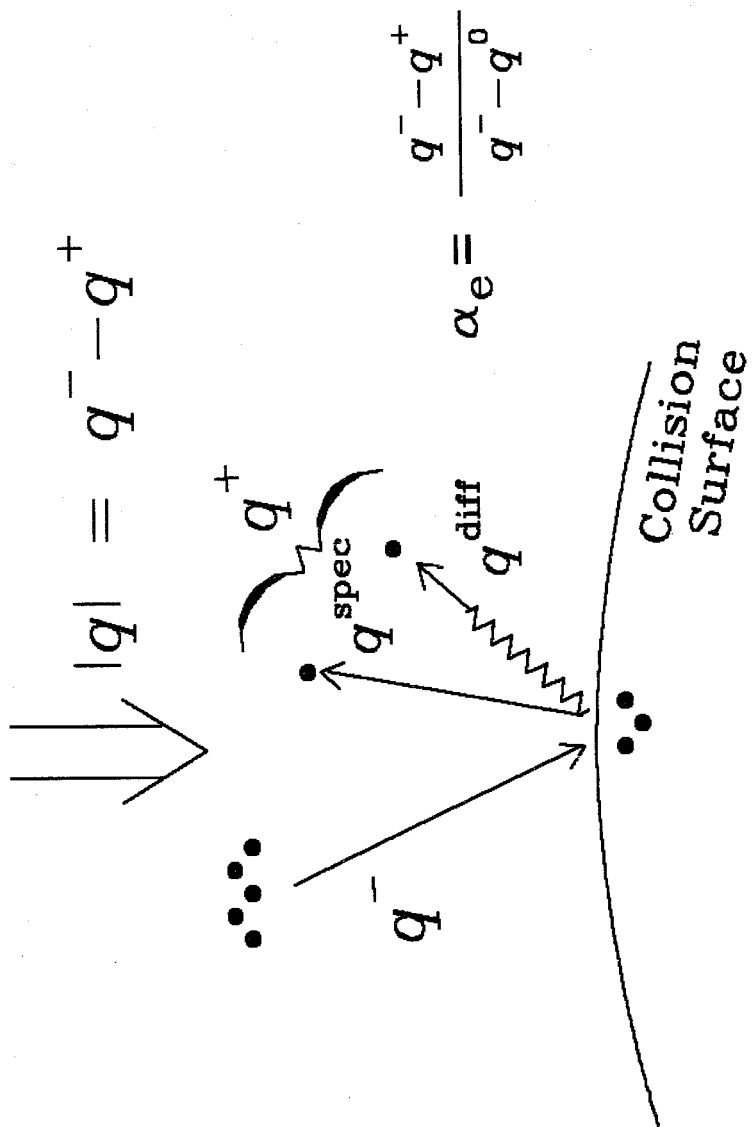


Figure 2

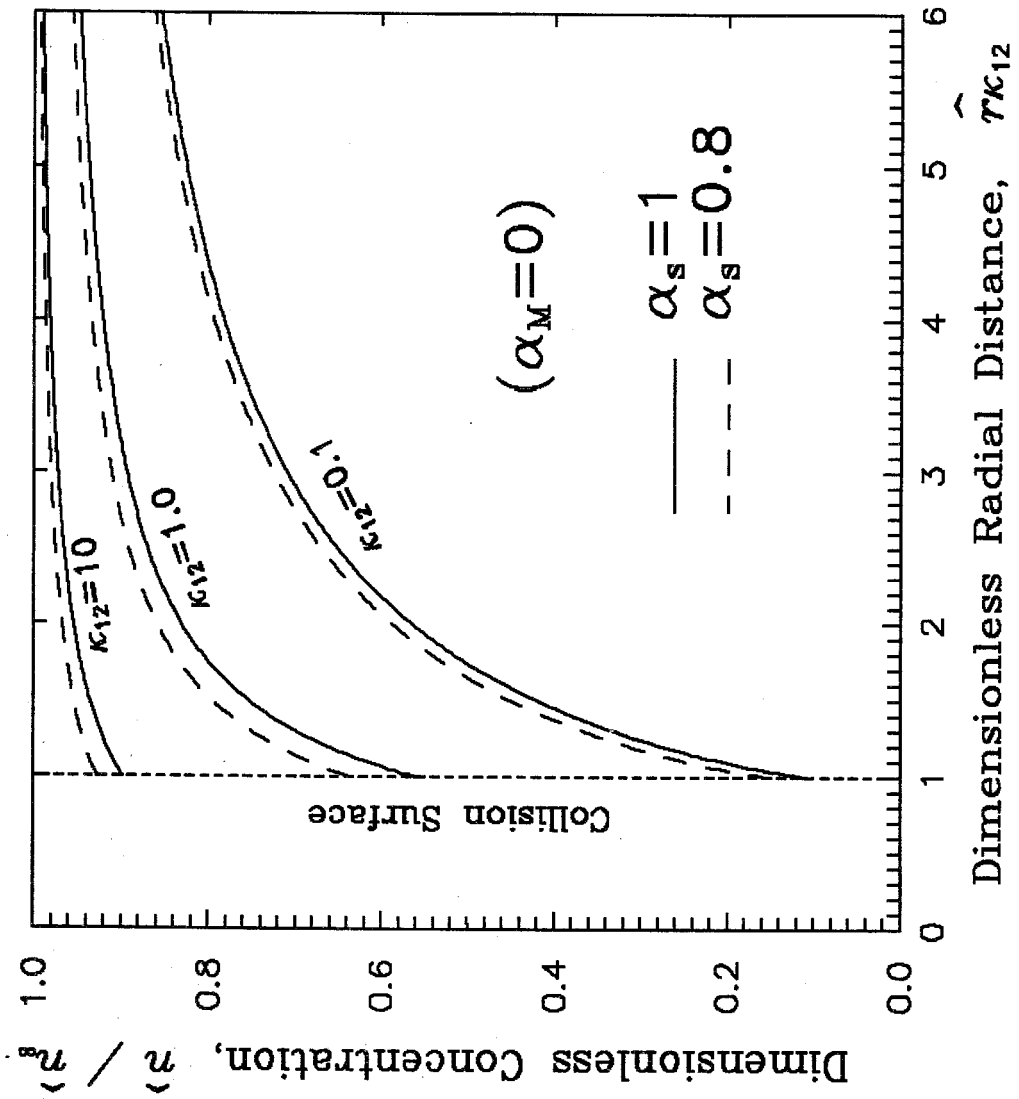


Figure 3

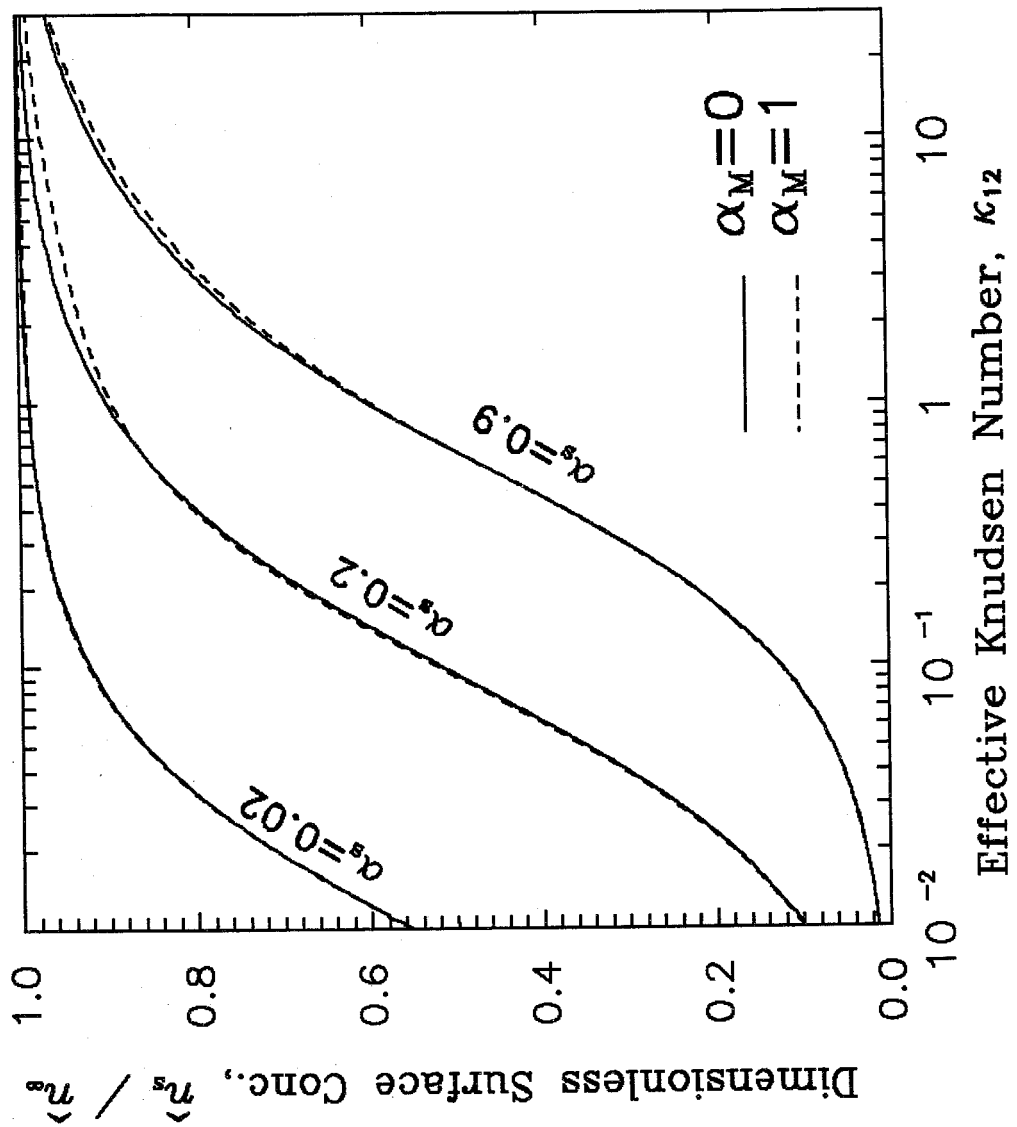


Figure 4

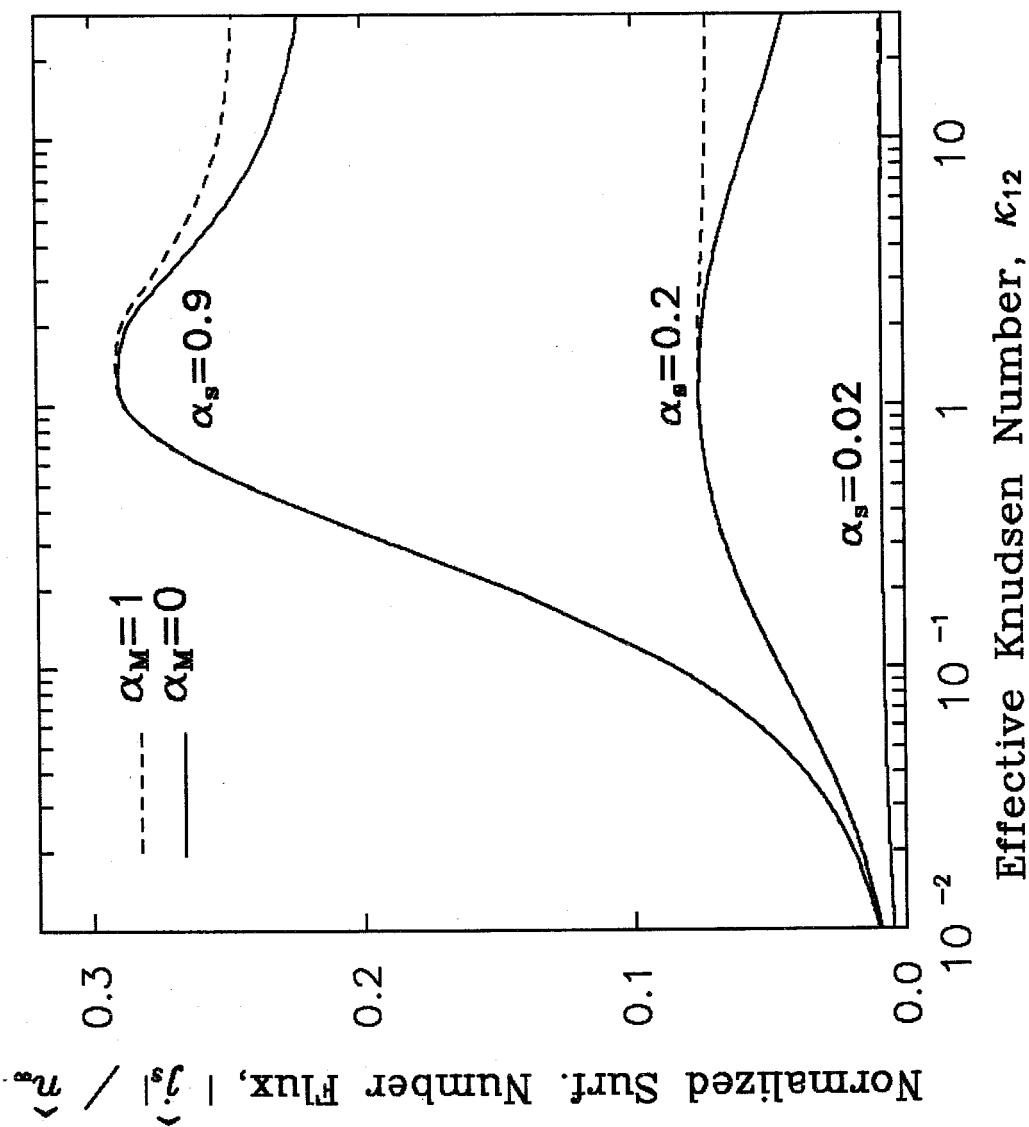


Figure 5



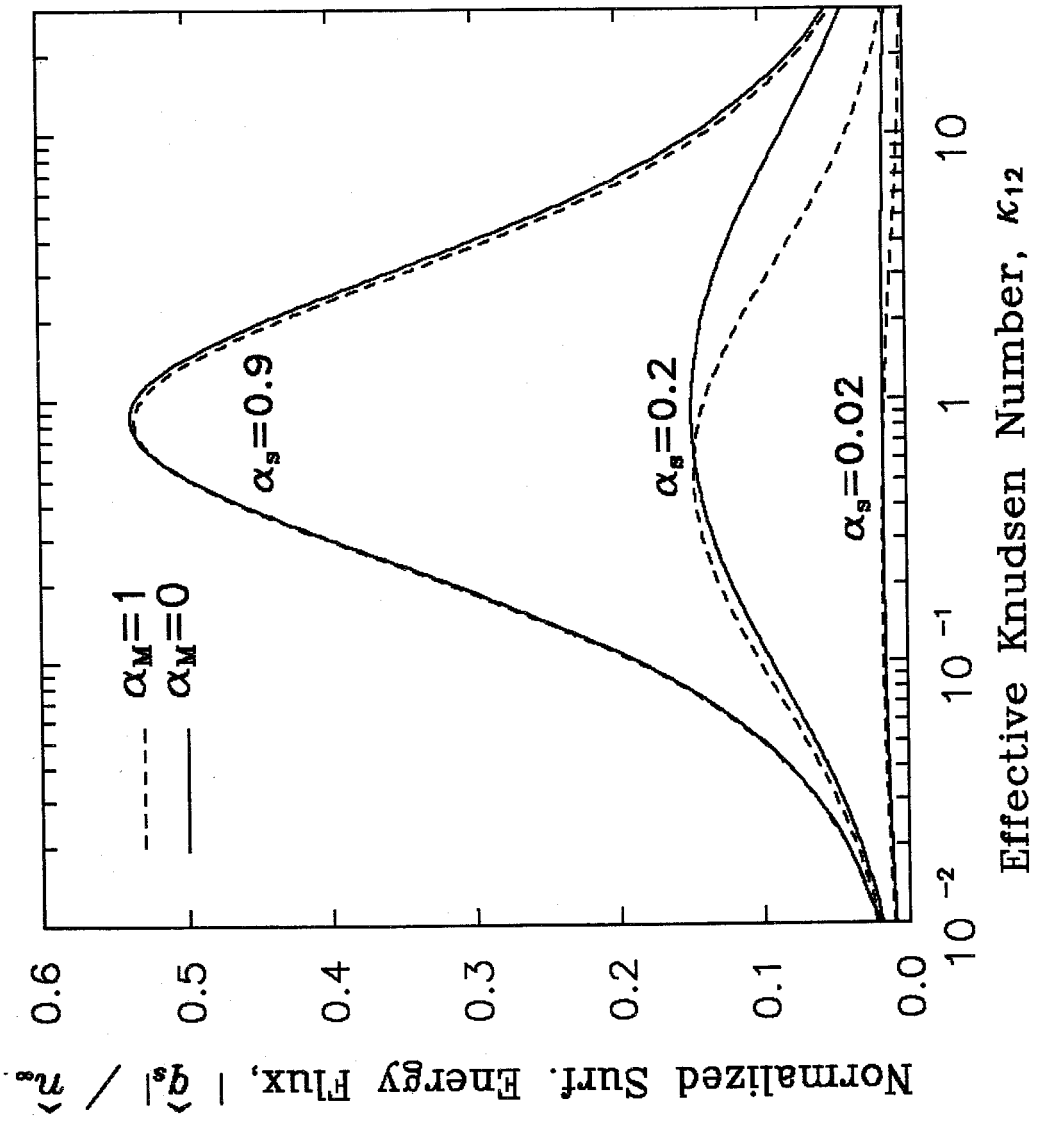


Figure 6

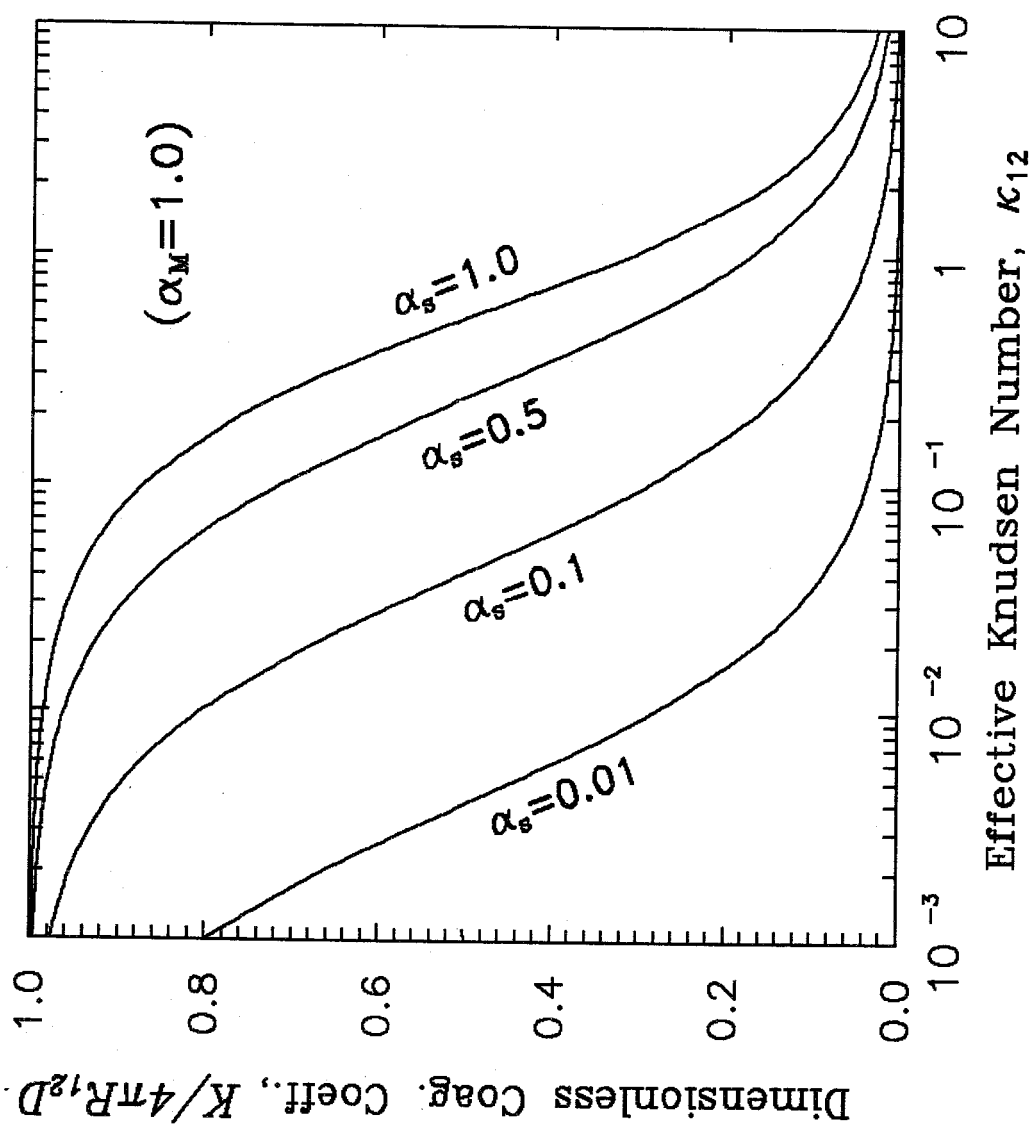


Figure 7

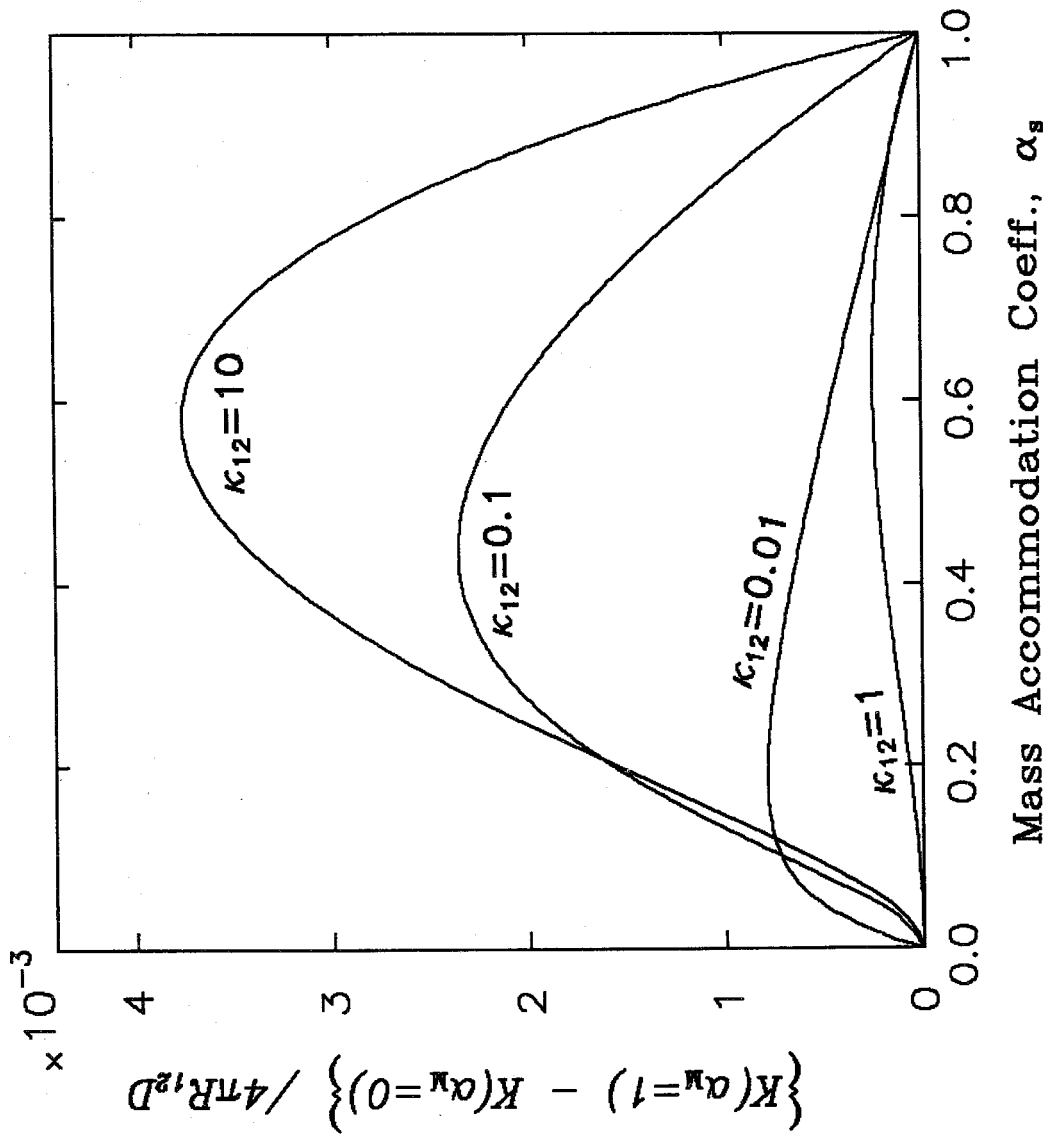


Figure 8

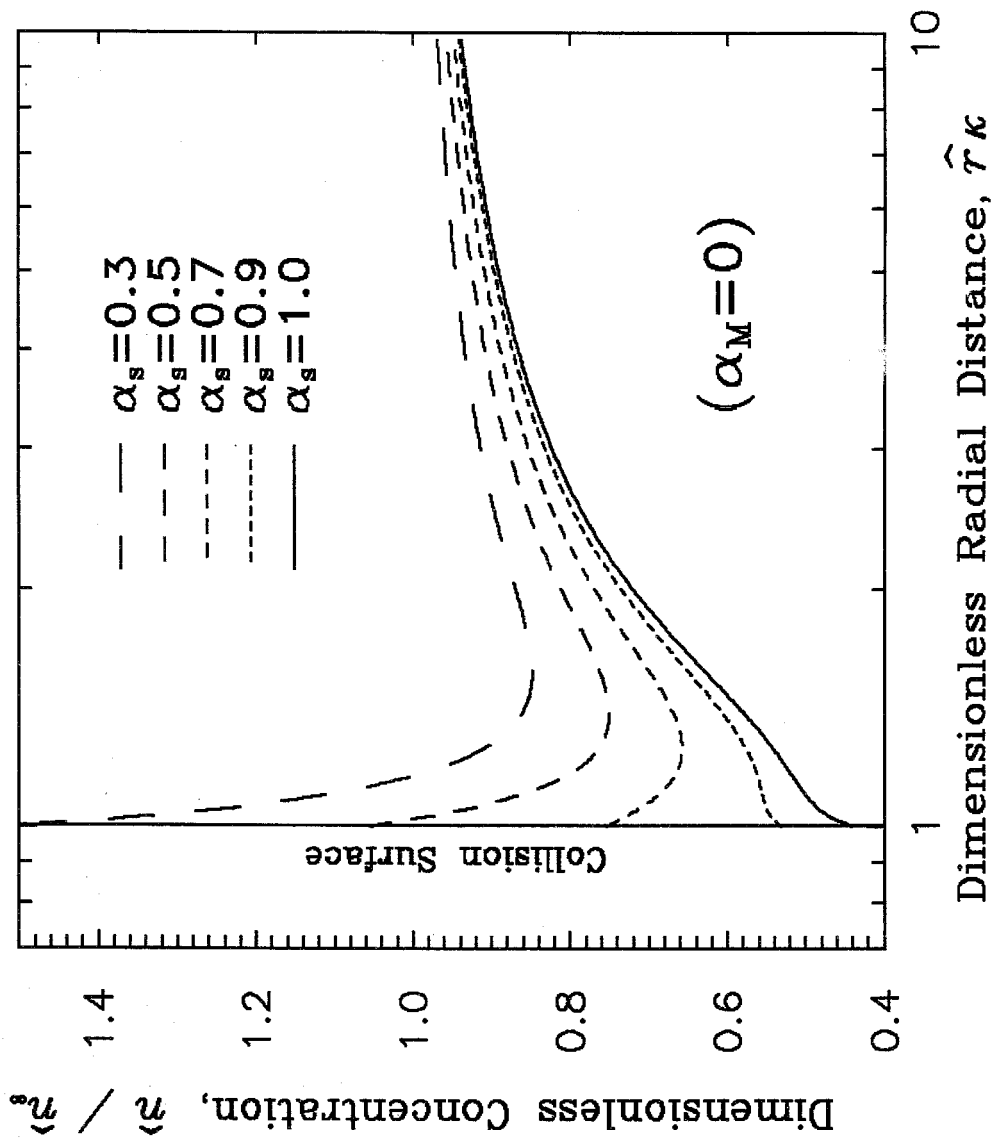


Figure 9

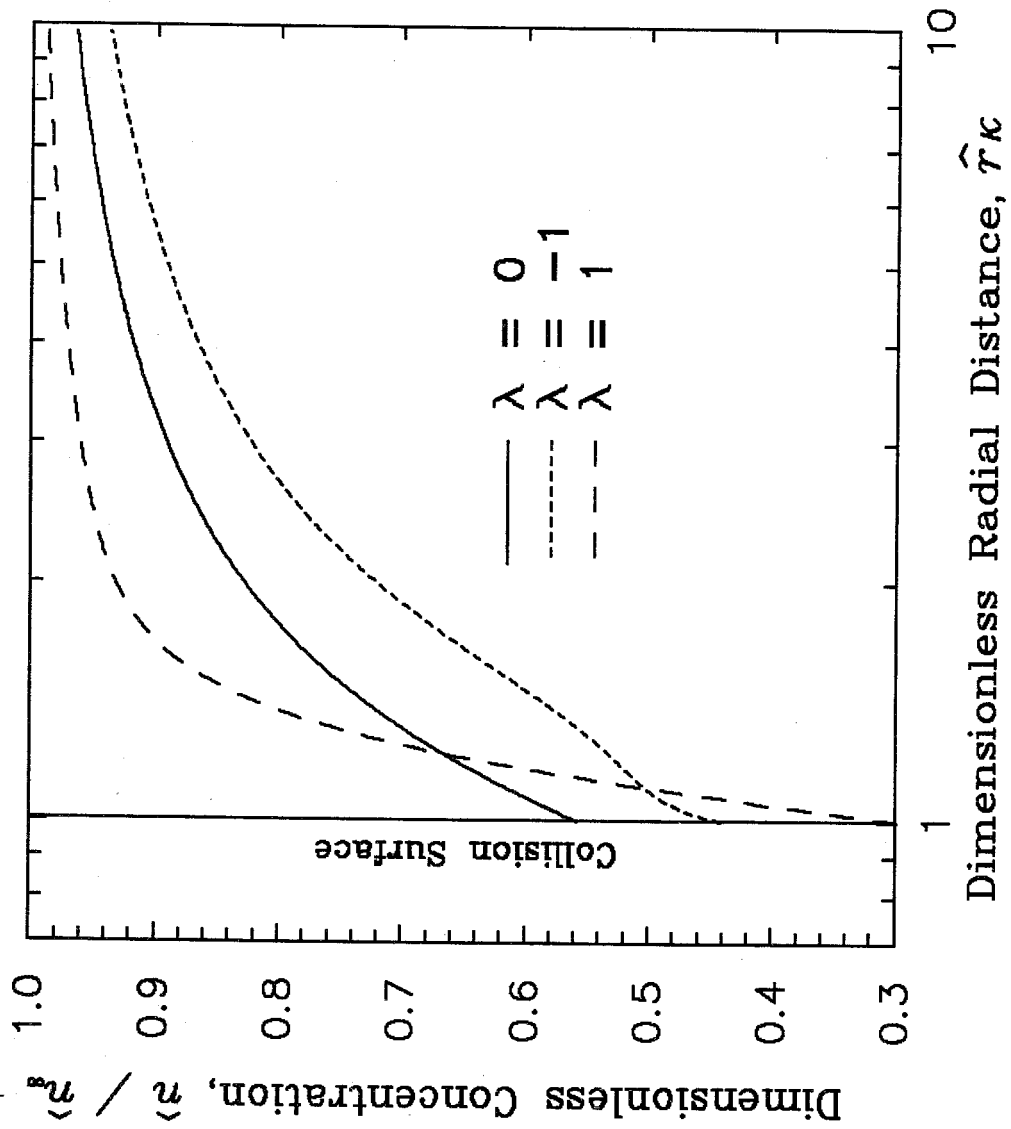


Figure 10

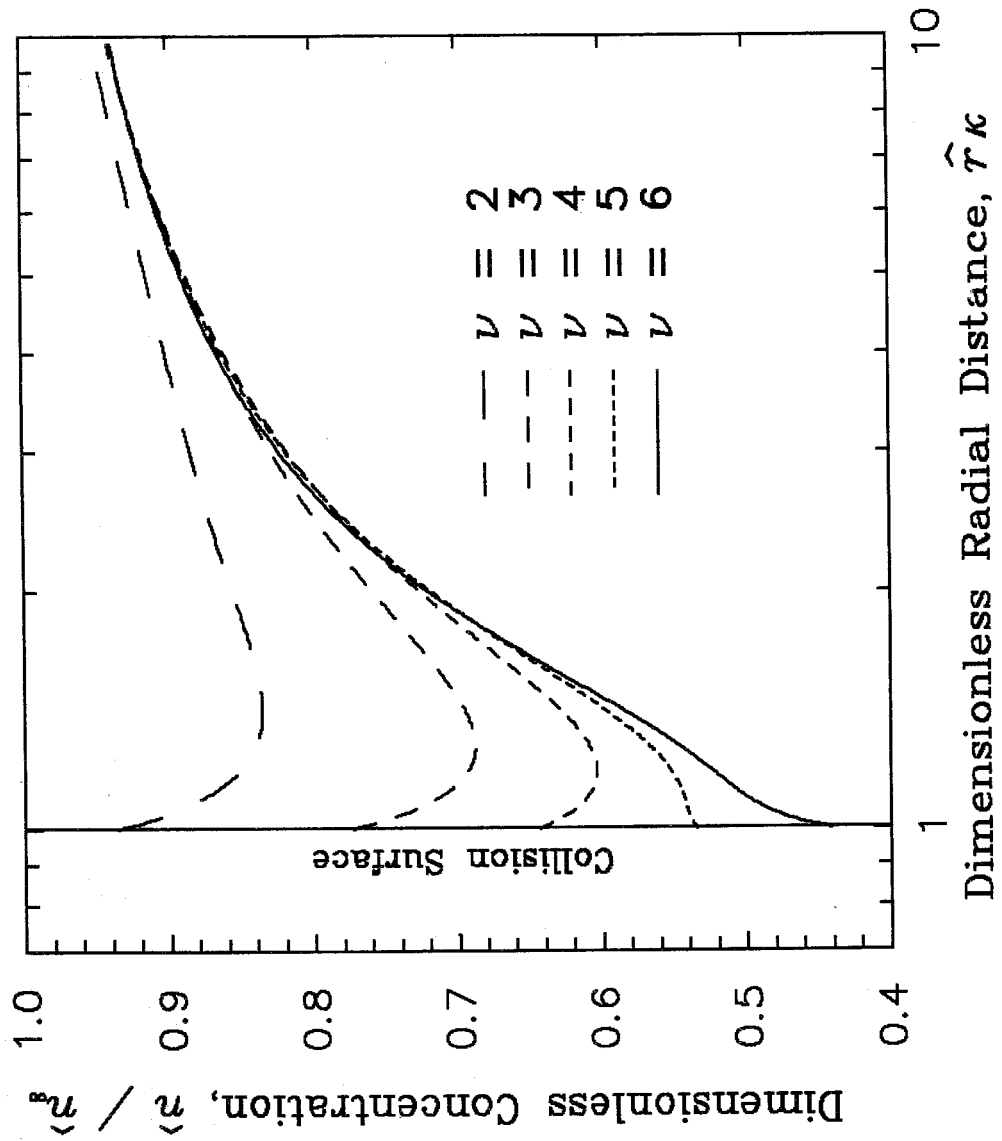


Figure 11

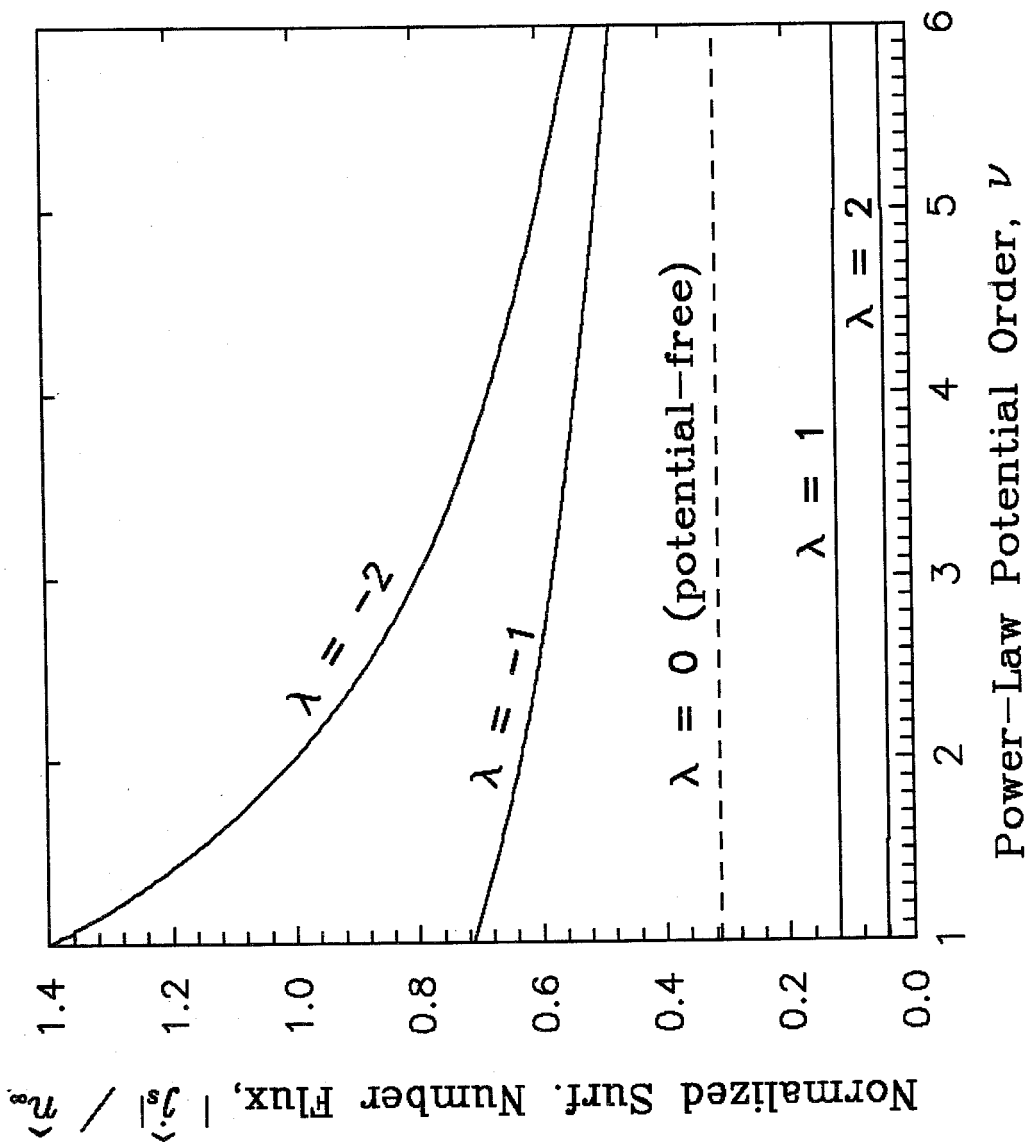


Figure 12

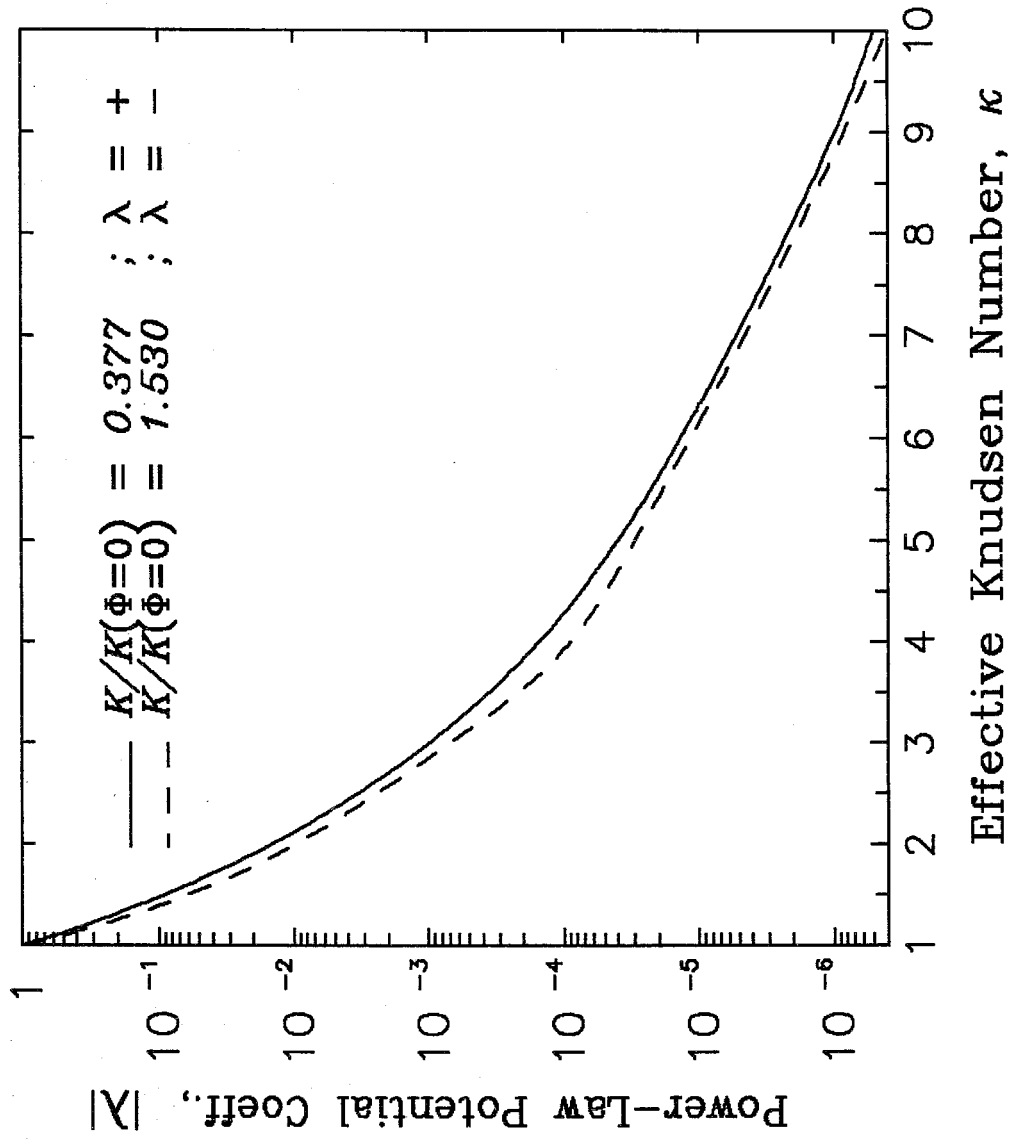


Figure 13



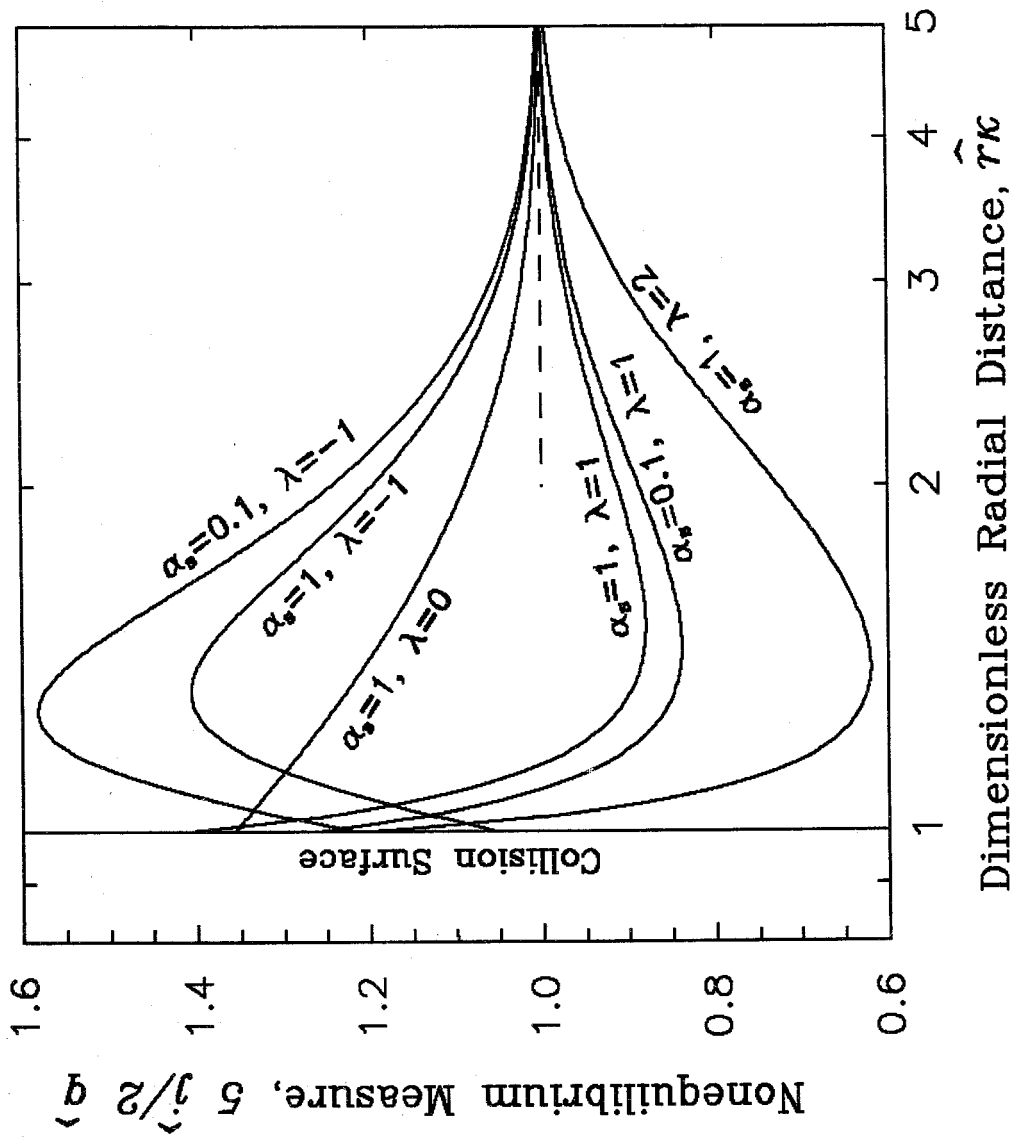


Figure 14

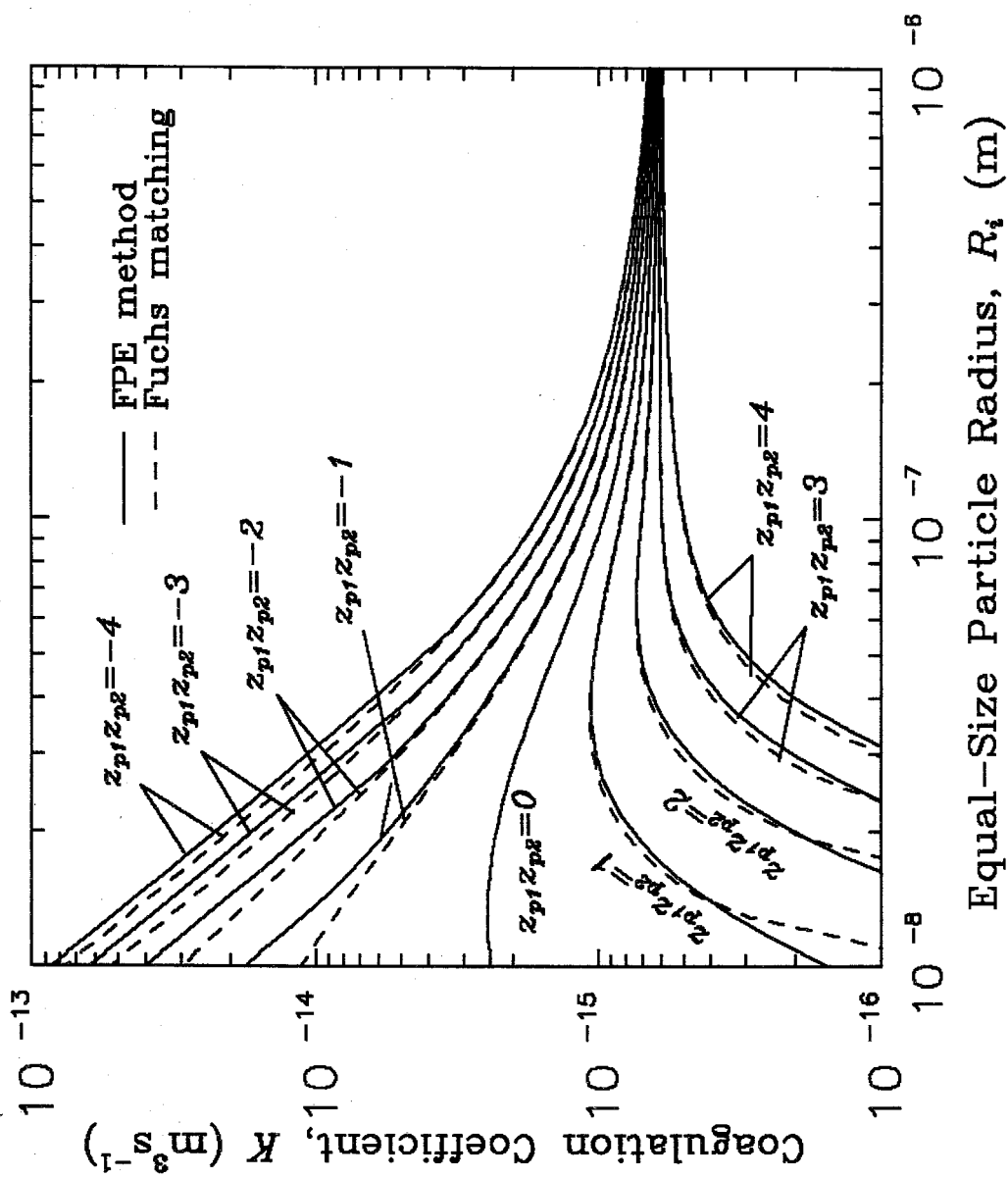


Figure 15

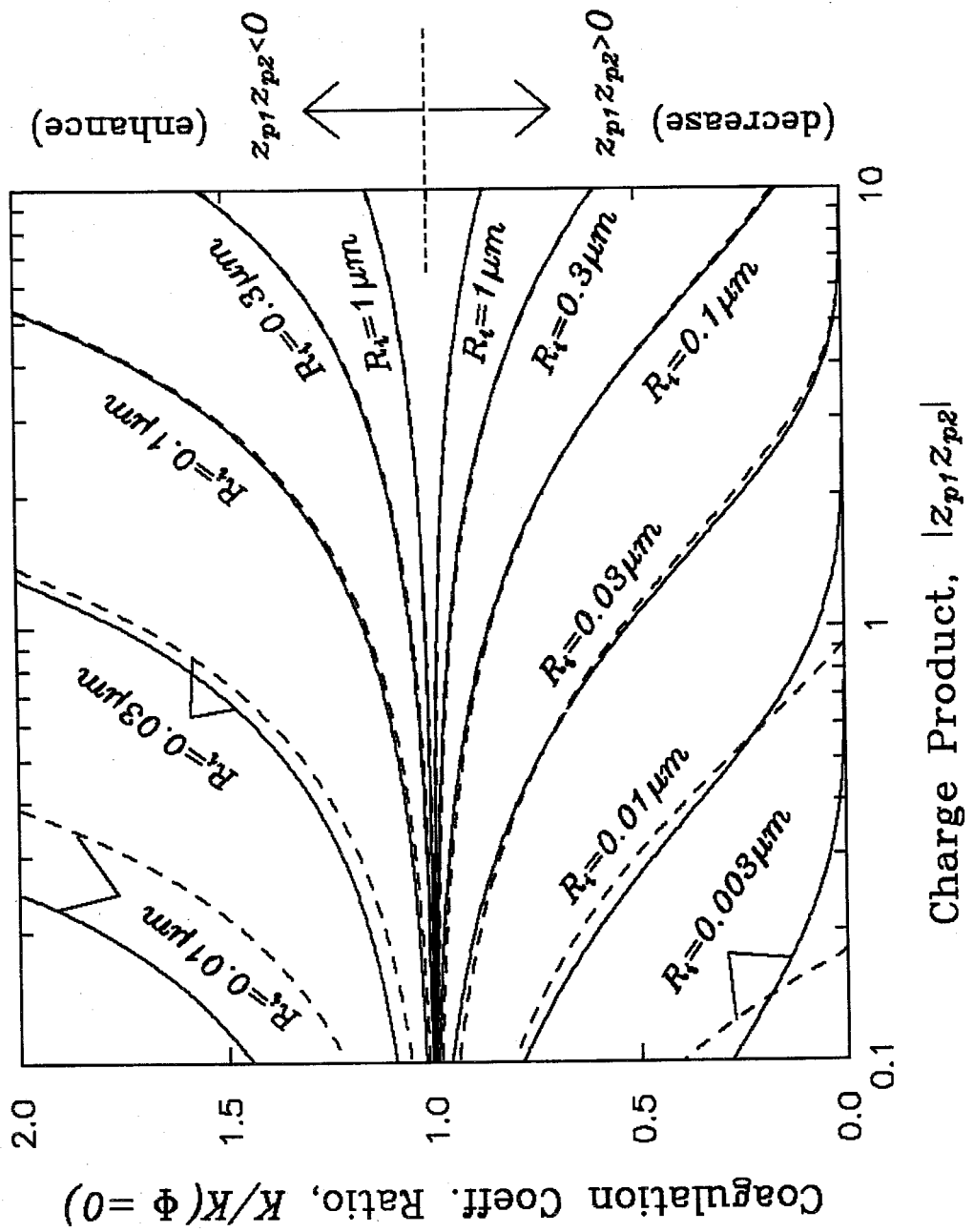


Figure 16

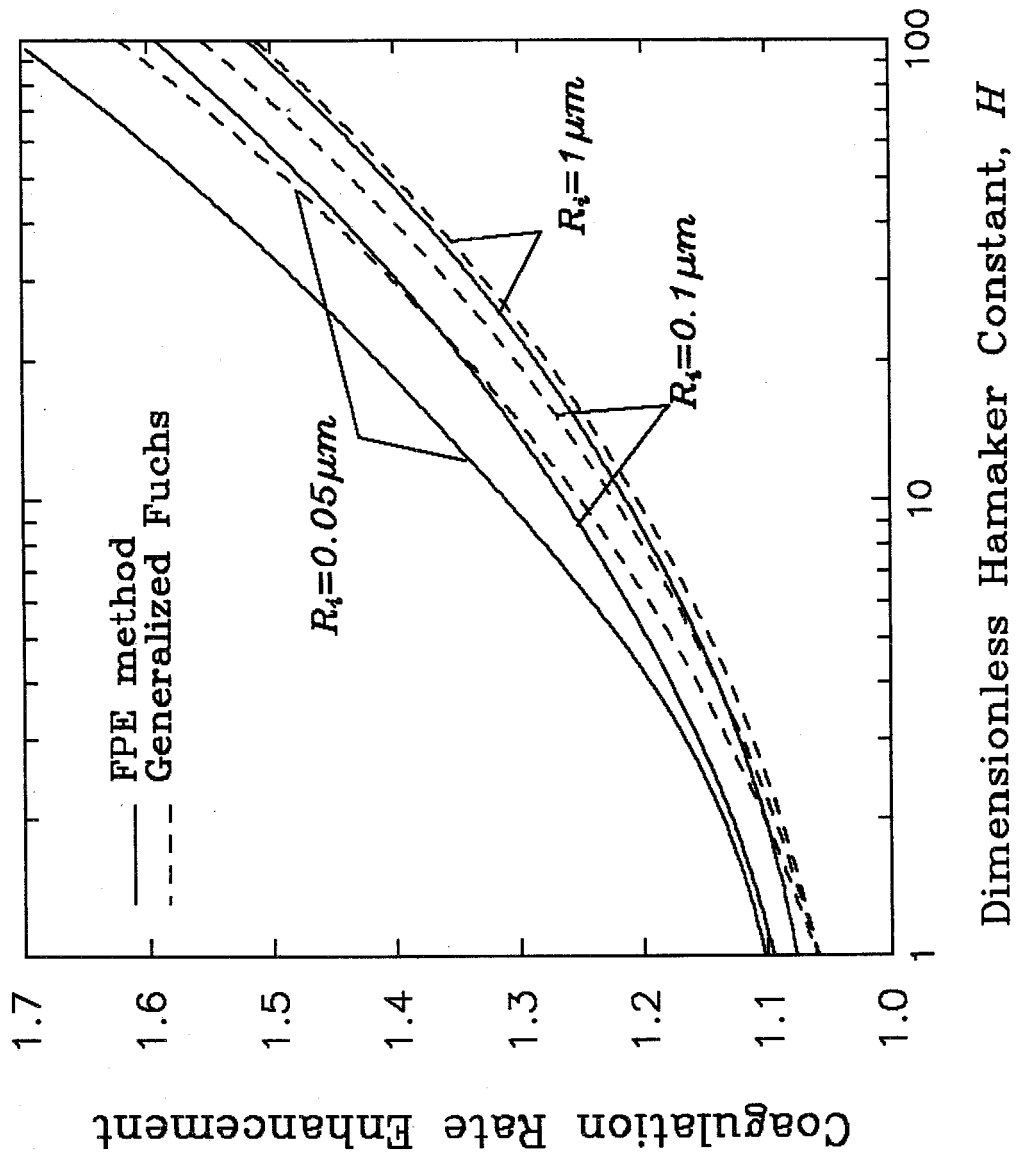


Figure 17

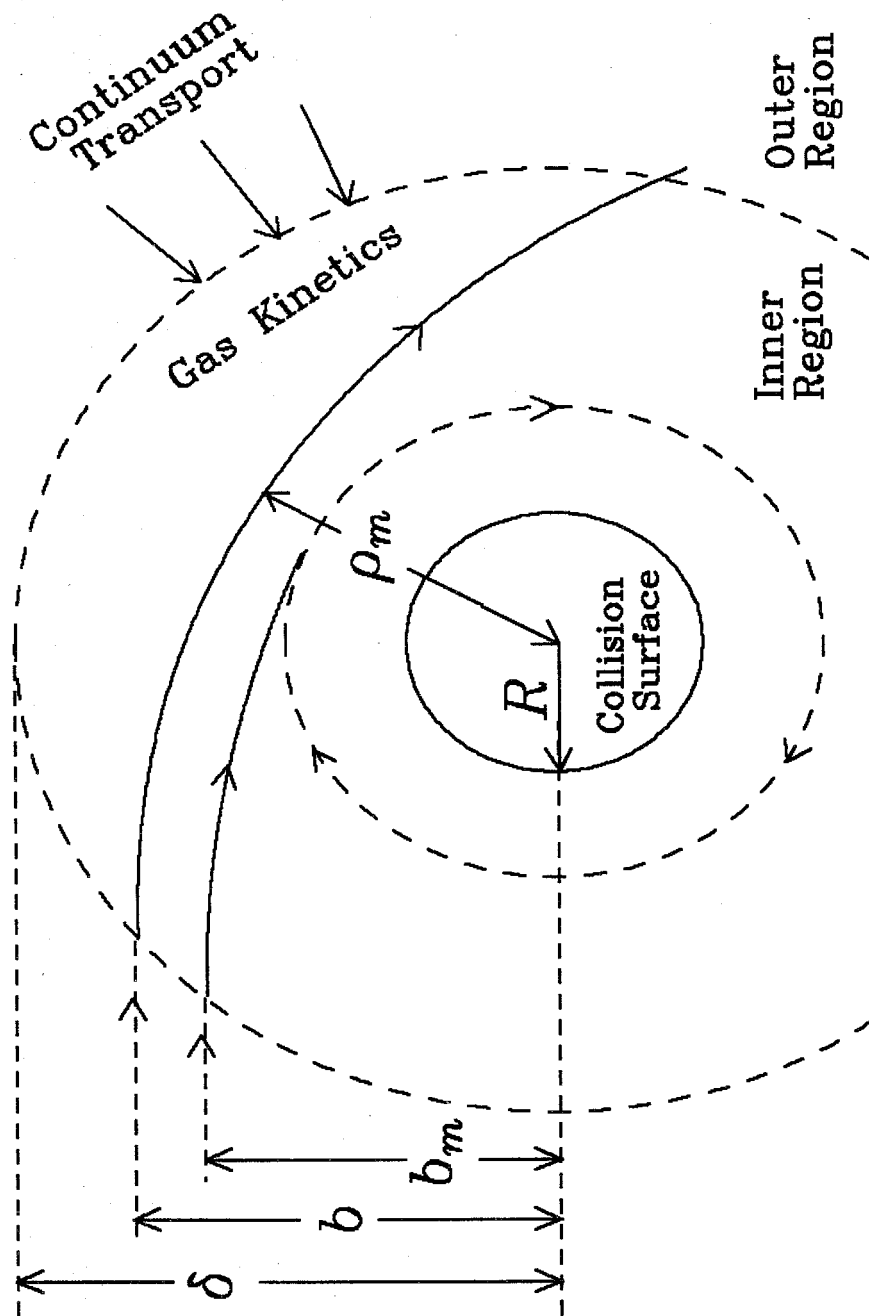


Figure 18

## **CHAPTER 4**

# **BGK EQUATION SOLUTION OF COAGULATION FOR LARGE KNUDSEN NUMBER AEROSOLS WITH A SINGULAR ATTRACTIVE CONTACT POTENTIAL**

**In cooperation with Dr. William H. Marlow,  
Texas A & M University**

**Accepted for publication in  
Journal of Colloid and Interface Science, 1990**

## ABSTRACT

Aerosol coagulation rate expressions in the presence of singular attractive contact potentials such as the van der Waals potential and the electrical image potential are obtained by integrating the characteristics of the BGK equation. The rate expression consists two parts: (A) the free-molecule regime ( $Kn \rightarrow \infty$ ) enhancement, and (B) the first-order correction for a finite but large Knudsen number. For situations involving either the van der Waals or image potential, we present closed form best-fit equations for data calculated from the theory. The experimental data of ionic charging of Pui *et al.* (9) and the data on ultrafine particle coagulation rate of Okuyama *et al.* (10, 11) are compared with the predictions from the present theory and the empirical Fuchs matching method. We have considered the situations of a combined van der Waals, Coulombic, and image potential. The conditions where either Coulombic, image, or van der Waals forces predominate are determined.

## INTRODUCTION

The coagulation rate between two free-molecule particles may be enhanced or retarded by the presence of an interparticle potential. For a monotonic repulsive potential, the coagulation rate is retarded by the factor " $\exp[-\Phi(R)/kT]$ ," which is obtained by solving the collisionless (*i.e.*, free-molecule) diffusion equation with a radial symmetry assumption.  $\Phi(R)$  is the interparticle potential at the point of contact of the two particles. For an attractive potential, computation of the enhancement or retardation of the coagulation rate is difficult because the potential can be singular, *i.e.*,  $|\Phi(R)| \gg kT$  and  $\exp[-\Phi(R)/kT]$  is ill-defined, or finite at the point of particle contact, and because the potential itself can be monotonic or nonmonotonic. Each of the attractive potential situations may lead to different values of the coagulation rate. An example of a nonmonotonic attractive potential is the long-range repulsive Coulombic force between two like-charged particles in the presence of a short-range attractive image potential; the coagulation rate between the two particles can be retarded even in presence of an attractive image potential if the Coulombic repulsion is sufficiently strong.

In many situations of aerosol coagulation, singular attractive contact potentials, either monotonic or nonmonotonic, occur; the condition that  $|\Phi(R)| \gg kT$  can be easily satisfied between ultrafine particles at room temperature in the presence of either a van der Waals force and/or an image potential, for example. The goal of this paper is to perform detailed and accurate calculations for coagulation in the presence of a singular attractive contact potential and to generalize the calculation results into a useful form.

To evaluate the enhancement or retardation of coagulation in the free-molecule regime, one can classify the situations into those of the "perfect" free-molecule case



where the Knudsen number  $Kn \rightarrow \infty$  and those of a finite but large Knudsen number correction to the  $Kn \rightarrow \infty$  case. The latter is important because free-molecule sized particles always possess a finite Knudsen number.

Evaluation of the coagulation rate in the presence of a singular attractive contact potential for the perfect free-molecule situation ( $Kn \rightarrow \infty$ ) has been a controversial issue. For example, Fuchs (1) used the impact parameter concept to obtain an expression for the enhancement factor based on an assumption that all particles possess equal kinetic energy. Sceats (2) adopted a one-dimensional Kramers reaction model (3) to obtain an effective collision surface. In both approaches, the collision rate is computed by first averaging over the incident particle initial velocities and then summing over the possible trajectories. The first rigorous derivation of the perfect free-molecule coagulation rate expression in the presence of a singular attractive contact potential was given by Marlow (4). The free-molecule coagulation rate is evaluated first by an integration over the incident trajectories, then by taking an average over the Maxwellian velocity distribution. The final expression (Eq. [21] of (4)) is, however, only good for monotonic potential situations.

The first-order finite Knudsen number correction to the free-molecule coagulation rate is not available for an interparticle singular attractive potential of arbitrary form. The only work thus far is limited to ion-particle charging situations (5, 6). In the work of Gentry (5) only a Coulombic force was considered, and in the work of Marlow and Brock (6) only Coulombic and image potentials are taken into account. In both studies, different approximations were made concerning the concentration profile for simplicity in calculation.

In this work, we shall derive a generalized rate expression for coagulation between two particles of finite large Knudsen numbers and an arbitrary size ratio in

the presence of an arbitrary interparticle potential that is singularly attractive at the two-particle contact. We use the same theoretical basis as in the work of Marlow (4) for coagulation at  $\text{Kn} \rightarrow \infty$  and, as in the work of Marlow and Brock (6), calculated the first-order correction for a finite large  $\text{Kn}$ . For  $\text{Kn} \rightarrow \infty$ , we extend the result of Marlow (4) to include both monotonic and nonmonotonic potentials. For the calculation of the first-order correction at a finite large  $\text{Kn}$ , the major technique used is the so-called Knudsen iteration (7) in solving the linearized BGK equation (8). Unlike Marlow and Brock's work, the nonequilibrium-perturbed concentrations in the regions close and far from the collision surface are distinguished.

The coagulation rate in the presence of an interparticle potential can be nondimensionalized by either the free-molecule potential-free coagulation rate at  $\text{Kn} \rightarrow \infty$ ,  $\pi R^2 \bar{c}$  (where  $\bar{c}$  is the mean thermal speed), or the potential-free coagulation rate as a function of  $\text{Kn}$ . We will refer to the two respective dimensionless coagulation rates as the *free-molecule enhancement*,  $E^{fm}$ , and the *overall enhancement*,  $E$ . The terminology "enhancement" is used for both enhancement or retardation in the coagulation rate in keeping with the conventional usage. Because the potential-free coagulation rate over the entire range of Knudsen numbers requires other approximations such as the flux-matching method, we shall generally focus on  $E^{fm}$  and evaluate its individual contributions from the  $\text{Kn} \rightarrow \infty$  case ( $E_0$ ) and the first-order large Knudsen number correction ( $E_1$ ).

Examples of singular attractive potentials that play important roles in aerosol dynamics are the van der Waals attractive potential and the electrical image potential. The coagulation rate in the following situations will be first calculated: (A) van der Waals force for arbitrary particle size ratio; (B) image force with or without the presence of either positive or negative Coulombic potential between an ion and a particle. The coagulation enhancement is a function of certain di-

mensionless groups for each of the above situations, *e.g.*, dimensionless Hamaker constant and size ratio for situation (A). The free-molecule and first-order correction,  $E_0$  and  $E_1$ , can be therefore represented in terms of the related dimensionless groups. The predictions of  $E_0$  and  $E_1$  for situations (A) and (B) will be presented both by figures and closed form best-fit equations for practical usage.

The predicted overall enhancement,  $E$ , for situations (A) and (B) will be compared with the ultrafine particle charging data of Pui *et al.* (9) and the coagulation data of Okuyama *et al.* (10, 11). Predictions from the Fuchs matching theory (1) in the presence of an interparticle potential using Marlow's enhancement expression (4) in the free-molecule regime are also compared with the data. It will be seen that without an *a priori* knowledge of the continuum solution, the transition regime coagulation rate predicted by the present method provides theoretical support for the empirical flux-matching theory in the large Knudsen number regime.

Finally, we present a calculation of a combined situation that involves simultaneous van der Waals, Coulombic and image forces for two coagulating particles of an arbitrary size ratio. Though the image force is not singular for a finite particle size ratio providing the charge is embodied in the particle, the combination with the van der Waals force always makes the overall potential singular at the particle contact. The conditions where each of the individual forces dominates are determined.

## THE BGK EQUATION

In a coagulation process, the movement of the two particles can be represented as a one-particle problem (12) in which a fictitious point incoming particle of reduced mass approaches a massless target particle with a radius equal to the sum of the two particle radii. The linearized BGK equation that can be used to describe the two-particle motion can be written as (13)

$$\mathbf{C} \cdot \nabla_{\mathbf{r}} f + \mathbf{F} \cdot \nabla_{\mathbf{C}} f = \frac{f_e - f}{\tau} \quad [1]$$

where  $f$  and  $f_e$  are the fictitious incoming particle velocity distribution function and its local Maxwellian distribution, respectively,  $\tau$  is the relaxation time (assumed a constant) of  $f$  relaxing toward  $f_e$ ,  $\mathbf{C}$  and  $\mathbf{r}$  are the incoming velocity and position of the fictitious particle, respectively, and  $\mathbf{F}$  is the force acting upon the fictitious incoming particle per unit of reduced mass.

By accounting for the angular velocity of the incoming particle that would contribute a centrifugal force between the two particles, the BGK equation becomes

$$C_r \frac{\partial f}{\partial r} + \left( \frac{J^2}{r^3} - \frac{d\Phi}{dr} \right) \frac{\partial f}{\partial C_r} = \frac{f_e - f}{\tau} \quad [2]$$

where  $J = C_t r$  is the product of the incoming particle tangential velocity and the distance from the target particle center, or, the angular momentum of the incoming particle.  $J$  is treated as a constant in the formulation of Eq. [2] because the angular momentum is conserved in each coagulation process.  $\Phi$  in Eq. [2] is the interparticle potential per unit reduced mass, *i.e.*,  $F = -d\Phi(r)/dr$ .

We can nondimensionalize Eq. [2] according to the length scale, the sum of the two-particle radii ( $R$ ), and the velocity scale, the mean thermal speed of the two

colliding particles ( $1/h$ ). That is,

$$\begin{aligned}
 hC_r &= \hat{C}_r ; & h &= \sqrt{\mu/kT} \\
 Jh/R &= \hat{J} ; & \mu &= m_1 m_2 / (m_1 + m_2) \\
 h^2 \Phi &= \hat{\Phi} ; & R &= R_1 + R_2 \\
 \tau/hR &= \hat{\tau} ; & n_\infty &= n(r \rightarrow \infty) \\
 f/n_\infty h^3 &= \hat{f} ;
 \end{aligned} \tag{3}$$

Eq. [2], after the nondimensionalization, retains exactly the same form as its dimensional counterpart. Therefore, we shall henceforth consider Eq. [2] as the dimensionless equation noting that the carat ( $\hat{\phantom{x}}$ ) is omitted.

### KNUDSEN ITERATION

The right-hand side of Eq. [2] is proportional to the inverse of the Knudsen number; we will subsequently determine a relation between the dimensionless  $\tau$  (i.e.,  $\hat{\tau}$ ) and the Knudsen number.

$1/\hat{\tau}$  represents the collision frequency between the incoming particle and the background gas molecules. From the Einstein relation, the diffusivity of a particle of reduced mass  $\mu$  is related to the dimensional collision time  $\tau$  with the background gas molecules by

$$D = \frac{\tau kT}{\mu} = \frac{\tau}{h^2} \tag{4}$$

As a result,  $\hat{\tau}$  has the following relation with the diffusivity of the fictitious particle,

$$\hat{\tau} = \frac{\tau}{hR} = \frac{Dh}{R} \tag{5}$$

In the large Knudsen number regime, particles are either molecules, molecular clusters, or of ultrafine sizes. For situations involving molecules or clusters, the evaluation of the diffusivity should take into account the interaction with individual background gas molecules. Upon assuming the interaction between a background gas molecule and the incoming particle is hard-sphere, the second-order Chapman-Enskog solution of the Boltzmann equation predicts (14)

$$D = \frac{3\pi}{64}(1 + \beta) \left( \frac{30\beta^2 + 16\beta + 13}{15\beta^2 + 8\beta + 6} \right) \lambda \sqrt{\frac{8kT}{\pi\mu}} \quad [6]$$

where  $\beta = \mu/m_B$  is the ratio of the two-particle reduced mass to the mass of a background gas molecule, and  $\lambda$  is the particle mean-free path. The effective Knudsen number  $\hat{\tau}$  is related to the particle Knudsen number  $\text{Kn} = \lambda/R$  by

$$\hat{\tau} = \left\{ \frac{3}{16} \sqrt{\frac{\pi}{2}} (1 + \beta) \left( \frac{30\beta^2 + 16\beta + 13}{15\beta^2 + 8\beta + 6} \right) \right\} \text{Kn} \quad [7]$$

Ultrafine-size particles, on the other hand, are sufficiently massive that individual background gas molecule interactions are not significant, and evaluation of the diffusivity from Brownian motion theory is more appropriate. We can focus on the Brownian motion of one of the particles while treating the other as stationary; because the motion of the two particles are assumed to be independent, the Brownian diffusivity of the two-particle relative motion is simply the sum of the two independent particle Brownian diffusivities (15). The Stokes-Einstein formula (15) with the slip correction factor expression (16) together gives

$$D = \sum_{i=1}^2 \frac{kT}{6\pi\eta R_i} \left( \frac{5 + 4\text{Kn}_i + 6\text{Kn}_i^2 + 18\text{Kn}_i^3}{5 - \text{Kn}_i + (8 + \pi)\text{Kn}_i^2} \right) \equiv \sum_{i=1}^2 D_i \quad [8]$$

where  $\text{Kn}_i = \lambda_B/R_i$  is the  $i$ th particle Knudsen number,  $D_i$  is the  $i$ th particle Brownian diffusivity,  $\lambda_B$  is the background gas mean-free path, and  $\eta$  is the vis-

cosity of the background gas. In Eq. [8], the interaction between the background gas molecules and the particles enters via the viscosity  $\eta$ .

In the large Knudsen number regime, Eq. [7] or the combination of Eqs. [5] and [8] predicts that  $\hat{\tau}$  is linearly proportional to Kn (or  $\text{Kn}_i$ ). Therefore,  $\hat{\tau}$  is termed as the “effective Knudsen number.” We now return to the dimensionless Eq. [2] where  $\tau$  being dimensionless (*i.e.*,  $\hat{\tau}$ ) is implicit.

In order to obtain the velocity distribution function in the large Knudsen number regime ( $\text{Kn} \gg 1$ ), we use a perturbation expansion of the velocity distribution function  $f$  in a series of powers of  $1/\tau$  (7),

$$f = f^{[0]} + \frac{1}{\tau} f^{[1]} + O\left(\frac{1}{\tau^2}\right) \quad [9]$$

where the numbers in the bracket superscripts are the same as the powers of  $1/\tau$  in the corresponding terms.  $f^{[0]}$  is the distribution function for an infinite Knudsen number, *i.e.*, “pure” free-molecule situation, and  $f^{[1]}$  is the first-order correction to  $f^{[0]}$  at a finite large Knudsen number. The higher order term, the third term on the right-hand side of Eq. [9], is known to involve more complicated functions of  $1/\tau$  than simple powers (17). In this work, however, no higher order corrections than the first were calculated.

Similarly, for the local Maxwellian  $f_e$ , we have

$$f_e = f_e^{[0]} + \frac{1}{\tau} f_e^{[1]} + O\left(\frac{1}{\tau^2}\right) \quad [10]$$

Substituting Eqs. [9] and [10] into Eq. [2] and equating like powers of  $1/\tau$ , the first two resulting equations are

$$C_r \frac{\partial f^{[0]}}{\partial r} + \left( \frac{J^2}{r^3} - \frac{d\Phi}{dr} \right) \frac{\partial f^{[0]}}{\partial C_r} = 0 \quad [11]$$

$$C_r \frac{\partial f^{[1]}}{\partial r} + \left( \frac{J^2}{r^3} - \frac{d\Phi}{dr} \right) \frac{\partial f^{[1]}}{\partial C_r} = f_e^{[0]} - f^{[0]} \quad [12]$$

Eq. [11] is the collisionless Boltzmann equation, which has the solution, by the method of separation of variables,

$$f^{[0]} = \frac{1}{(2\pi)^{3/2}} \exp \left\{ - \left( \frac{C_r^2}{2} + \frac{J^2}{2r^2} + \Phi(r) \right) \right\} \quad [13]$$

$f^{[0]}$  given by Eq. [8] is commonly termed the "free-molecule solution" of the distribution function  $f$ , because  $f = f^{[0]}$  when the effective Knudsen number is infinity (recall Eq. [9]).

### SOLUTION FOR $f^{[1]}$

To obtain a solution for  $f^{[1]}$  from Eq. [12], an expression for the zeroth-order local Maxwellian  $f_e^{[0]}$  is necessary. The latter can be obtained by the high-collision-frequency particle-background gas Boltzmann equation (12)

$$0 = J(f_e^{[0]}, f_B) \quad [14]$$

where  $J(\dots)$  is the Boltzmann collision operator and  $f_B$  is a Maxwellian velocity distribution for the background gas. By using Boltzmann's H-theorem, one has a solution of  $f_e^{[0]}$  of the form similar to Eq. [13],

$$f_e^{[0]} = X(r) \frac{1}{(2\pi)^{3/2}} \exp \left\{ - \left( \frac{C_r^2}{2} + \frac{J^2}{2r^2} \right) \right\} \quad [15]$$



in which  $X(r)$  is the dimensionless local particle number concentration.  $X(r)$  is obtained by integrating  $f^{[0]}$  over the velocity space of possible values,

$$\begin{aligned} X(r) &= \pi \int_{J^2/r^2=0}^{\infty} \int_{C_r=-\infty}^{C_r^*} f^{[0]} dC_r d\left(\frac{J^2}{r^2}\right) \\ &= \frac{1}{4} e^{-\Phi(r)} \int_{J^2/r^2}^{\infty} \left[1 + \operatorname{erf}\left(\frac{C_r^*}{\sqrt{2}}\right)\right] e^{-J^2/2r^2} d\left(\frac{J^2}{r^2}\right) \end{aligned} \quad [16]$$

where the normal two-fold integration over the angular and azimuthal velocities has been transformed into a single integration over the tangential velocity ( $J/r$ ). The integration over the radial velocity ( $C_r$ ), on the other hand, is truncated at an upper limit,  $C_r^* \geq 0$ , since the outgoing flux is due only to those incoming particles with an incident radial speed  $|C_r| < C_r^*$  which can escape from the attractive interparticle potential well.

The radial potential is an effective potential for the incident particle as if it has no tangential velocity. That is, the incident particle motion can be projected into a two-dimensional space where a particle with a radial velocity  $C_r$  experiences a radial (or centrifugal) energy barrier. The radial (or effective) potential is the sum of the interparticle potential and the incident particle tangential kinetic energy,

$$\Phi_{\text{eff}}(r) = \frac{J^2}{2r^2} + \Phi(r) \quad [17]$$

The maximum value of  $\Phi_{\text{eff}}$  occurs at a distance  $r = \sigma$  (i.e., the collision surface). From Eq. [17], we have the relation between  $\sigma$  and the angular (or tangential) momentum  $J$ ,

$$\frac{J^2}{\sigma^2} = \sigma \frac{d\Phi(\sigma)}{d\sigma} \quad [18]$$

With the concept of the effective potential, we now can determine the value of

$C_r^*$ . In the far field of range  $r > \sigma$ ,  $C_r^*$  can be obtained from the conservation of energy and the fact that at  $r = \sigma$  the radial kinetic energy is zero,

$$C_r^* = \left[ \frac{J^2}{\sigma^2} - \frac{J^2}{r^2} + 2(\Phi(\sigma) - \Phi(r)) \right]^{1/2} \quad (r > \sigma) \quad [19]$$

For the computation of concentration, Marlow and Brock (6) assumed that for a range within the capture distance ( $r \leq \sigma$ ) the truncation velocity  $C_r^*$  in Eq. [16] can also be obtained by Eq. [19]. However, one would rather expect that a thermalization of radial velocity in both the incoming and outgoing directions may occur in this case. Therefore, we choose  $C_r^* = \infty$  for the range  $r \leq \sigma$ , which represents the particle being captured and fully thermalized in the potential well. For situations that  $C_r^*$  is imaginary, *i.e.*, the argument in the bracket of Eq. [19] is less than zero, we also assume that  $C_r^* = \infty$  is valid because no potential barrier is present in this case and a velocity thermalization is expected. Upon combining all the situations considered, Eq. [16] can be written as

$$X(r) = \frac{1}{4} e^{-\Phi(r)} \int_{J^2/r^2=0}^{\infty} \left\{ 1 + [\theta(r > \sigma) \text{erf}(\theta(m > 0)\sqrt{m} + \theta(m \leq 0)\infty) + \theta(r \leq \sigma)] \right\} \exp\left(-\frac{J^2}{2r^2}\right) d\left(\frac{J^2}{r^2}\right) \quad [20]$$

where

$$m = \frac{J^2}{2} \left( \frac{1}{\sigma^2} - \frac{1}{r^2} \right) + \Phi(\sigma) - \Phi(r) \quad [21]$$

and  $\theta$  is the Heaviside function, being unity if its argument is true and zero otherwise. Eq. [20] can be further simplified if one writes

$$Y(r) \equiv X(r) \exp[\Phi(r)] \quad [22]$$

and

$$Y(r) - 1 = -\frac{1}{2} \int_{S=0}^{\infty} \exp(-S) \theta(r > \sigma) \operatorname{erfc}[\theta(m > 0)\sqrt{m} + \theta(m \leq 0)\infty] dS \quad [23]$$

where  $S = J^2/2r^2$  and  $m$  is given by Eq. [21]. Eq. [12] can therefore be written as

$$C_r \frac{\partial f^{[1]}}{\partial r} + \left( \frac{J^2}{r^3} - \frac{d\Phi}{dr} \right) \frac{\partial f^{[1]}}{\partial C_r} = f^{[0]} (Y(r) - 1) \quad [24]$$

The characteristics of Eq. [24] are the total Hamiltonian of the two-particle system, *i.e.*, the conservation of energy, or

$$\frac{1}{2} C_r^2 + \frac{J^2}{2r^2} + \Phi(r) = \text{constant} \quad [25]$$

Upon integrating along the characteristics, Eq. [24] has the solution

$$f^{[1]} = \frac{\exp\left\{-\left(\frac{C_r^2}{2} + \frac{J^2}{2r^2} + \Phi(r)\right)\right\}}{(2\pi)^{3/2}} \int_{r'=\infty}^r \frac{[Y(r') - 1] dr'}{\pm \sqrt{C_r^2 + \frac{J^2}{r^2} - \frac{J^2}{r'^2} + 2(\Phi(r) - \Phi(r'))}} \quad [26]$$

where the positive sign is for  $C_r > 0$  and the negative sign for  $C_r < 0$ , and we have used the boundary condition that  $f^{[1]} = 0$  at  $r \rightarrow \infty$ .

The zeroth-order and first-order solutions of the distribution function,  $f^{[0]}$  and  $f^{[1]}$ , will now be used in evaluating the coagulation rate.

## EVALUATION OF INCOMING RATE

The dimensionless coagulation rate is found by integrating the particle distribution function  $f$  over the velocity space weighted by the radial velocity  $C_r$  and

the collision surface area  $4\pi\sigma^2$ ,

$$0 \leq F = \left\{ \pi \int_{J^2/r^2=0}^{\infty} \int_{C_r=0}^{-\infty} f(4\pi\sigma^2) C_r dC_r d\left(\frac{J^2}{r^2}\right) \right\}_{r=\sigma} \quad [27]$$

or, from Eq. [9],

$$F \equiv F_0 - \frac{1}{\tau} F_1 \quad [28]$$

with

$$F_0 = 4\pi^2 \int_{J^2/\sigma^2=0}^{\infty} \int_{C_r|\sigma=0}^{-\infty} f^{[0]}|_{\sigma} \sigma^2 C_r|_{\sigma} dC_r|_{\sigma} d\left(\frac{J^2}{\sigma^2}\right) \quad [29]$$

and

$$F_1 = -4\pi^2 \int_{J^2/\sigma^2=0}^{\infty} \int_{C_r|\sigma=0}^{-\infty} f^{[1]}|_{\sigma} \sigma^2 C_r|_{\sigma} dC_r|_{\sigma} d\left(\frac{J^2}{\sigma^2}\right) \quad [30]$$

where  $F_0$  and  $F_1$  are the dimensionless free-molecule regime ( $\tau \rightarrow \infty$ ) coagulation rate and its first-order correction for the finite large Knudsen number situations, respectively.

Upon substituting Eq. [13] into Eq. [29] and using Eq. [18] to change the integration variable, the free-molecule incoming rate has the form:

$$F_0 = \sqrt{2\pi} \int_{\sigma(J=0)}^{\sigma=1} \sigma^2 \frac{d}{d\sigma} \left( \sigma \frac{d\Phi(\sigma)}{d\sigma} \right) \exp \left\{ - \left( \frac{\sigma}{2} \frac{d\Phi(\sigma)}{d\sigma} + \Phi(\sigma) \right) \right\} d\sigma \quad [31]$$

where the lower integration limit,  $\sigma(J=0)$ , is determined by setting

$$\left. \frac{d\Phi(r)}{dr} \right|_{\sigma(J=0)} = 0 \quad [32]$$

For instance, for a monotonic singular attractive contact potential such as the van der Waals potential and/or the electric image potential, Eq. [32] gives  $\sigma(J=0) = \infty$ . Eq. [31], in this special case, was first obtained by Marlow (4). For the situation in which the singular attractive contact potential is not monotonic, an

example of which is a positive Coulombic potential in the presence of a negative image potential, a short-range potential maximum occurs and the lower integration limit in Eq. [31] must be determined from the criterion Eq. [32] (also see Amadon and Marlow (18)).

The first-order correction,  $F_1$ , similarly, is found to have the following form:

$$F_1 = -\pi \int_{\sigma(J=0)}^{\sigma=1} \sigma^2 \frac{d}{d\sigma} \left( \sigma \frac{d\Phi(\sigma)}{d\sigma} \right) \int_{r=\infty}^{\sigma} [1 - Y(r)] \exp \left[ - \left( \frac{\sigma^3}{2r^2} \frac{d\Phi(\sigma)}{d\sigma} + \Phi(r) \right) \right] \times \operatorname{erfc} \left[ \theta_{>0} \left( \frac{\sigma}{2} \frac{d\Phi(\sigma)}{d\sigma} \left( 1 - \frac{\sigma^2}{r^2} \right) + \Phi(\sigma) - \Phi(r) \right)^{1/2} \right] dr d\sigma \quad [33]$$

in which  $\theta_{>0}$  is the Heaviside function which is unity if its following multiplier,  $(\dots)^{1/2}$ , is greater than zero, and zero otherwise. In deriving Eq. [33], the negative sign in Eq. [26] is used because we focus on the incoming particles for which  $C_r$  must be negative. Also a change of integration order between  $r'$  in Eq. [26] and  $C_r|_{\sigma}$  in Eq. [30] is made. Finally we have renamed  $r'$  as  $r$  in Eq. [33].

In Eq. [33],  $1 - Y(r)$  from Eq. [23], can be expressed as

$$1 - Y(r) = \frac{1}{4r^2} \int_{p(J=0)}^{p=1} \theta(r > p) \exp \left( - \frac{p^3}{2r^2} \frac{d\Phi(p)}{dp} \right) \frac{d}{dp} \left( p^3 \frac{d\Phi(p)}{dp} \right) \times \operatorname{erfc} \left\{ \theta_{>0} \left( \frac{p}{2} \frac{d\Phi(p)}{dp} \left( 1 - \frac{p^2}{r^2} \right) + \Phi(p) - \Phi(r) \right)^{1/2} + (1 - \theta_{>0}) \infty \right\} dp \quad [34]$$

where  $p$  has the same meaning as  $\sigma$ , i.e., the collision surface distance; we write  $p$  instead of  $\sigma$  because it is not to be confused with the integration over  $\sigma$  in Eq. [33].

## TRANSFORMATION AND ENHANCEMENT FACTORS

Because under many circumstances the integration limits in Eqs. [31] and [33] may have the value infinity, one seeks a transformation to facilitate numerical integration. We start by defining

$$x \equiv \frac{1}{\sigma} \quad ; \quad y \equiv \frac{1}{r} \quad ; \quad z \equiv \frac{1}{p} \quad [35]$$

Eqs. [31] and [33] become

$$F_0 = \sqrt{2\pi} \int_{x=1}^{x_0} \frac{1}{x^2} \frac{d}{dx} \left( x \frac{d\Phi(x)}{dx} \right) \exp \left[ \frac{x}{2} \frac{d\Phi(x)}{dx} - \Phi(x) \right] dx \quad [36]$$

$$F_1 = \pi \int_{x=1}^{x_0} \frac{1}{x^2} \frac{d}{dx} \left( x \frac{d\Phi(x)}{dx} \right) \int_{y=0}^x [1 - Y(y)] \frac{1}{y^2} \exp \left[ \frac{y^2}{2x} \frac{d\Phi(x)}{dx} - \Phi(y) \right] \\ \times \operatorname{erfc} \left[ \theta_{>0} \left( \frac{x}{2} \frac{d\Phi(x)}{dx} \left( \frac{y^2}{x^2} - 1 \right) + \Phi(x) - \Phi(y) \right)^{1/2} \right] dy dx \quad [37]$$

and in which

$$1 - Y(y) = \frac{y^2}{4} \int_{z=1}^{x_0} \theta(y < z) \exp \left( \frac{y^2}{2z} \frac{d\Phi(z)}{dz} \right) \frac{d}{dz} \left( \frac{1}{z} \frac{d\Phi(z)}{dz} \right) \\ \times \operatorname{erfc} \left\{ \theta_{>0} \left( \frac{z}{2} \frac{d\Phi(z)}{dz} \left( \frac{y^2}{z^2} - 1 \right) + \Phi(z) - \Phi(y) \right)^{1/2} + (1 - \theta_{>0}) \infty \right\} dz \quad [38]$$

In Eqs. [36]–[38], the integration limit  $x_0$  is determined by setting  $d\Phi(x)/dx = 0$ .

For cases of monotonic attractive singular contact potential,  $x_0 = 0$ .

The enhancement factor with respect to the pure free-molecule regime potential-free coagulation rate,  $\pi R^2 \sqrt{8kT/\pi\mu}$ , can be found by examining the nondimensionalization quantities from Eq. [3] and the definition of the dimensionless incoming particle rate, Eq. [27]. One obtains

$$E^{fm} = E_0 - \frac{1}{\tau} E_1 \equiv \frac{1}{2\sqrt{2\pi}} \left( F_0 - \frac{1}{\tau} F_1 \right) \quad [39]$$

Eq. [39] shows that  $E^{fm}$  can be broken into two parts, the enhancement at an infinite Knudsen number,  $E_0$ , and the first-order correction of enhancement for a finite large Knudsen number,  $E_1$ .

The *overall* enhancement factor,  $E$ , on the other hand, is defined as the coagulation rate divided by the potential-free coagulation rate over the *entire range* of Kn. In a later section, the overall enhancement factor  $E$  with respect to the Fuchs flux-matching potential-free situation is calculated in order to compare experimental data with the present predictions.

## THE VAN DER WAALS POTENTIAL

In this section, we shall calculate the free-molecule enhancement factor  $E_0$  and its first-order correction  $E_1$  of the coagulation rate between two particles with a nonretarded van der Waals potential (in the sum over pair interaction approximation). The retardation effect of the van der Waals interaction (see, for example, (19)) is neglected in the present calculation because it is only important in the continuum-transition regime (*i.e.*, particles of diameter greater than 20 nm at 1 atm) (19, 20). Because the van der Waals interactions occur frequently in aerosol coagulation and also because of the time-consuming computations in evaluating the integrals in Eqs. [36] and [37], we shall present least-squares best-fit equations for data calculated from the theory.

The dimensionless nonretarded van der Waals potential (with respect to  $kT$ ) between two particles of radii  $R_1$  and  $R_2$  has the form (21)

$$\Phi(r) = -\frac{H}{6} \left\{ \frac{2R_1R_2}{r^2 - (R_1 + R_2)^2} + \frac{2R_1R_2}{r^2 - (R_1 - R_2)^2} + \ln \frac{r^2 - (R_1 + R_2)^2}{r^2 - (R_1 - R_2)^2} \right\} \quad [40]$$

where  $r$ ,  $R_1$  and  $R_2$  are either all dimensional or all dimensionless.  $H$  in Eq. [40] is the dimensionless Hamaker constant (*i.e.*, the Hamaker constant divided by  $kT$ ) and is dependent on the particle material.

The coagulation enhancement factors  $E_0$  and  $E_1$  are functions only of the particle size ratio,  $R_1/R_2$ , and the dimensionless Hamaker constant,  $H$ . Figures 1 and 2 show  $E_0$  and  $E_1$  (Eq. [39]) as predicted by the present theory. For convenience,  $E_0$  and  $E_1$  can be represented by the following best-fit equations obtained by the least-squares method,

$$E_i = \mathbf{R}\mathbf{K}_i\mathbf{H}^T, \quad i = 0 \text{ or } 1 \quad [41]$$

where

$$\mathbf{R} = \left( 1, \left[ \frac{R_1}{R_1 + R_2} - 0.5 \right]^2 \right)_{1 \times 2} \quad [42]$$

$$\mathbf{H} = \left( 1, \ln H, \ln^2 H, \ln^3 H, \ln^4 H \right)_{1 \times 5} \quad [43]$$

$$\mathbf{K}_0 = \begin{pmatrix} +1.568\text{E} + 0, & +2.210\text{E} - 1, & +3.867\text{E} - 2 & +6.172\text{E} - 3, & +6.122\text{E} - 4 \\ -1.847\text{E} + 0, & -7.080\text{E} - 1, & -1.550\text{E} - 1, & -3.247\text{E} - 2, & -1.534\text{E} - 3 \end{pmatrix}_{2 \times 5} \quad [44]$$

and

$$\mathbf{K}_1 = \begin{pmatrix} +4.020\text{E} - 1, & +6.959\text{E} - 2, & +8.266\text{E} - 3 & +3.396\text{E} - 3, & +7.271\text{E} - 4 \\ -6.654\text{E} - 1, & -2.286\text{E} - 1, & -2.768\text{E} - 2, & -1.775\text{E} - 2, & -3.375\text{E} - 3 \end{pmatrix}_{2 \times 5} \quad [45]$$

The above least-squares fits are correct to 0.1% error in the range  $0.01 \leq H \leq 1000$  and  $0.1 \leq R_1/(R_1 + R_2) \leq 0.9$ .

Figures 1 and 2 indicate that the larger the value of the Hamaker constant the



greater the enhancement of coagulation when van der Waals forces are included. Also for a given Hamaker constant value, equal-sized particles exhibit a stronger van der Waals potential than unequal-sized particles as predicted by Eq. [40], and thus greatest enhancement in coagulation rate occurs for equal-sized particles.

## THE COULOMBIC AND IMAGE POTENTIAL

When two charged particles with finite dielectric constants collide, contributions to the interparticle potential exist from the Coulombic interaction between charges and the electric image potential between particles. The image potential is always attractive; for two colliding particles of comparable sizes, however, the image potential is *not* singular at the two particle contact (see, for example, Eq. [A12] of Appendix). A singular contact image potential only occurs when one particle has a size much greater than the other. An example of the latter situation is the charging of a particle by collision with ions. Therefore, in this section, we shall focus on the calculation of ion-particle charging. Particle-particle coagulation with the Coulombic-image potential, on the other hand, shall be considered in a later section together with the van der Waals force.

In the ion-particle charging problem, the particle radius  $R_p$  ( $R_2$ ) is much greater than the ion radius  $R_{ion}$  ( $R_1$ ). The Coulombic-image potential is (22, 23)

$$\Phi(y) = By - \frac{Cz_{ion}^2y^4}{1-y^2} \quad [46]$$

$$B = \frac{z_{ion}z_p e^2}{4\pi\epsilon_0 kTR_p}, \quad C = \frac{\kappa-1}{\kappa+1} \frac{e^2}{8\pi\epsilon_0 kTR_p} \quad [47]$$

where  $\kappa$  is the particle dielectric constant,  $e = 1.602 \times 10^{-19}$  C,  $r$  is the dimensional radial distance between the two particle centers,  $y = (R_1 + R_2)/r = R_p/r$  (where

$r$  is dimensional) is the same as  $y$  given in Eq. [35] (where  $r$  is dimensionless), and  $z_{\text{ion}}$  and  $z_p$  are the number and sign of charges carried by the ion and particle, respectively. In the present calculation, we assume the ions are singly-charged, *i.e.*,  $z_{\text{ion}} = \pm 1$ , and Eq. [46] becomes the classical ion-particle interaction potential (1).

Figures 3 and 4 show the values of  $E_0$  and  $E_1$ , respectively, as a function of  $B$  with  $C$  as a parameter. In both figures, we consider the ranges of  $0.1 \leq C \leq 10$  and  $-2 \leq B \leq 2$ . Situations of  $B < 0$  are characterized as *bipolar* charging, because the ion and particle carry charges of different signs. For  $B > 0$ , the ion and particle carry charges of the same sign, and the process is one of *unipolar* charging.

The Coulombic potential, the first term on the right-hand side of Eq. [46], which is inversely proportional to the radial distance  $r$ , in some cases may overwhelm the image potential contribution to the enhancement. For example, in the region where  $B < 0$  in Figure 3, the free-molecule enhancement  $E_0$  is almost independent of the image strength  $C$  because the attractive Coulombic force exceeds the attractive image force. Similarly, in the  $B > 0$  region, an increase of the repulsive Coulombic force may exponentially decrease the enhancement for a constant  $C$ . A strong image attractive potential (*e.g.*,  $C = 10$ ), however, may compensate for the repulsive Coulombic force, and the decay of  $E_0$  with increasing  $B$  is not as substantial as at a smaller value of  $C$  (*e.g.*,  $C = 0.1$ ). Figure 4 shows a similar result for the first-order enhancement correction  $E_1$ . Unlike the case of  $E_0$ ,  $E_1$  in the region  $B < 0$  is still a function of the image strength  $C$ .

Because the Coulombic-image potential situations occur in an ionic charging environment, the best-fit equations for the ranges of variables in both figures are again obtained by the least-squares method in the range of  $0.1 \leq C \leq 50$  for positive and negative  $B$ , respectively. For positive  $B$ , we find

$$E_i = \exp(\mathbf{B}\mathbf{L}_i\mathbf{C}^T) \quad i = 0 \text{ or } 1, \quad (0 \leq B \leq 2) \quad [48]$$

where

$$\mathbf{B} = \begin{pmatrix} 1, & B, & B^2 \end{pmatrix}_{1 \times 3} \quad [49]$$

$$\mathbf{C} = \begin{pmatrix} 1, & \ln C, & \ln^2 C, & \ln^3 C, & \ln^4 C \end{pmatrix}_{1 \times 5} \quad [50]$$

$\mathbf{L}_0 =$

$$\begin{pmatrix} +1.353\text{E} + 0, & +4.146\text{E} - 1, & +1.955\text{E} - 2, & -1.876\text{E} - 3, & +6.239\text{E} - 5 \\ -1.899\text{E} + 0, & +2.278\text{E} - 1, & +4.280\text{E} - 2, & -1.378\text{E} - 2, & +1.049\text{E} - 3 \\ -8.482\text{E} - 1, & +1.025\text{E} + 0, & -5.815\text{E} - 1, & +1.544\text{E} - 1, & -1.476\text{E} - 2 \end{pmatrix}_{3 \times 5} \quad [51]$$

and

$\mathbf{L}_1 =$

$$\begin{pmatrix} +2.943\text{E} - 1, & +5.518\text{E} - 1, & +2.922\text{E} - 2, & -3.913\text{E} - 4, & -1.928\text{E} - 4 \\ -3.715\text{E} + 0, & +6.814\text{E} - 1, & -2.517\text{E} - 3, & -1.260\text{E} - 2, & +1.151\text{E} - 3 \\ -1.734\text{E} + 0, & +2.015\text{E} + 0, & -1.148\text{E} + 0, & +3.058\text{E} - 1, & -2.929\text{E} - 2 \end{pmatrix}_{3 \times 5} \quad [52]$$

For negative  $B$ , on the other hand, we have the following best-fit expressions

$$\begin{aligned} E_0 = & 4.088 + 1.575 \ln C + 0.5124 \ln^2 C + 0.1013 \ln^3 C + 0.007554 \ln^4 C \\ & - 1057.4 B + 2.038 B^2 - 0.04446 B^3 + 0.003134 B^4 \quad (-2 \leq B < 0) \end{aligned} \quad [53]$$

and

$$E_1 = \exp(\mathbf{B}\mathbf{M}\mathbf{S}^T) \quad (-2 \leq B < 0) \quad [54]$$

where

$$\mathbf{S} = \begin{pmatrix} 1, & \ln C, & \ln^2 C \end{pmatrix}_{1 \times 3} \quad [55]$$

$$\mathbf{M} = \begin{pmatrix} +4.326\text{E} - 1, & +4.854\text{E} - 1, & +3.406\text{E} - 2 \\ -1.284\text{E} + 0, & +2.034\text{E} - 1, & -5.355\text{E} - 3 \\ -2.972\text{E} - 1, & +5.490\text{E} - 2, & -1.516\text{E} - 3 \end{pmatrix}_{3 \times 3} \quad [56]$$

and  $B$  is given by Eq. [49].

In the remaining part of this section, we would like to comment on a comparison of the  $E_0$  and  $E_1$  predictions of the present work and that of Marlow and Brock (6) for image forces only. The comparison is shown in Figure 5. The expression for  $E_0$ , Eqs. [36] and [39], reduces exactly to the first term of Eq. [13] of (6) when using the Coulombic and image potentials. However, in the latter work, this exact expression was mistakenly reduced to  $\sqrt{\pi C}$  for the situation of pure image force only. The comparison of the correct  $E_0$  (solid line in Figure 5) and the erroneous  $E_0$  of value  $\sqrt{\pi C}$  (dashed line in Figure 5) shows that the correct free-molecule enhancement is almost twice the previously understood value. On the other hand, a much smaller difference is found between the  $E_1$  predictions in both works. When substituting Eq. [46], Eqs. [37]–[39] reduce to a similar form of the second term of Eq. [13] in the work of Marlow and Brock. The difference between the present work and the derivation in (6) lies in the reduction of Eq. [16] to Eq. [20]. The particle concentrations in the range  $\sigma \leq r$  and  $r \leq \sigma$  were treated identically in the calculation in (6); in the present work, the Heaviside function is introduced to distinguish these two ranges. The present revised calculation as shown in Figure 5 indicates a small overshoot of the prior  $E_1$  prediction.

## COMPARISON WITH EXPERIMENTAL DATA

In this section we compare the present theory with the experimental data of Okuyama *et al.* (10, 11) for ultrafine particle coagulation in the presence of a van der Waals potential and of Pui *et al.* (9) for ion-particle charging under an image force.

In Figures 6 and 7, we show the *overall* enhancement factor  $E$  (see the dis-

cussion below Eq. [39]) as a function of the particle size. The effective Knudsen number  $\tau$  and the Knudsen number  $\text{Kn}$  are also indicated.  $E$  is calculated with respect to the Fuchs potential-free expression. The latter can be written as (15)

$$F|_{\text{Fuchs}} = \frac{\bar{c}\pi R^2}{1 + \frac{\bar{c}R^2}{4\mathcal{D}(R+g)}} \quad [57]$$

where

$$\begin{aligned} g &= (g_1^2 + g_2^2)^{1/2} ; \quad R = R_1 + R_2 \\ g_i &= \frac{1}{6R_i l_i} \left[ (2R_i + l_i)^3 - (4R_i^2 + l_i^2)^{3/2} \right] - 2R_i \\ l_i &= \frac{8\mathcal{D}_i}{\pi \bar{c}_i} ; \quad \bar{c}_i = \sqrt{\frac{8kT}{\pi m_i}} ; \quad \bar{c} = (\bar{c}_1^2 + \bar{c}_2^2)^{1/2} \end{aligned} \quad [58]$$

and  $\mathcal{D}_i$  and  $\mathcal{D}$  are given in Eq. [8].

In both Figures 6 and 7, solid lines are obtained by taking the ratio of the dimensional coagulation rate from the present theory to that given in Eq. [57]; the dashed lines, on the other hand, are obtained by taking the ratio of Fuchs's potential formula to that given in Eq. [57]. The Fuchs's potential formula is obtained by a similar idea of flux-matching as in the Fuchs potential-free situation and can be generally written as (1)

$$F|_{\text{Fuchs}(\Phi \neq 0)} = \frac{E_0 E^C R^2 \pi \bar{c}}{E^C \exp[\Phi(r = g + R)] + E_0 \frac{R^2 \bar{c}}{4\mathcal{D}(g + R)}} \quad [59]$$

where  $\bar{c}$  and  $g$  are given by Eq. [58],  $E_0$  is the enhancement at an infinite Knudsen number (recall Eq. [39]) and  $E^C$  is the continuum regime enhancement given by (15)

$$E^C = \left[ (g + R) \int_{g+R}^{\infty} \frac{\exp[\Phi(r)]}{r^2} dr \right]^{-1} \quad [60]$$

In Fuchs's original paper in deriving Eq. [59] (1), the calculation of  $E_0$  was based on averaging over all possible impact parameters and using the assumption that all the incident fictitious particles possess equal kinetic energy. Fuchs set a parameter  $\alpha = E_0 R^2 / (R + g)^2$ , better known as the Fuchs alpha and presented a table of  $\alpha$  for situations of ion-particle charging; efforts of recalculating Fuchs's  $\alpha$  under the same situations can be found elsewhere (24, 25). In our calculation in using Fuchs's potential matching formula, Eq. [59], however,  $E_0$  is given by  $F_0/2\sqrt{2}$  (Eqs. [36] and [39]) to account for the correct averaging of particle trajectories and thermal energy; this revised matching method was earlier used by Marlow (4) and Okuyama *et al.* (10, 11). Eq. [59] shall be henceforth referred to as the "generalized Fuchs matching equation." It should be pointed out that the term " $\exp[\Phi(r = g + R)]$ " in Eq. [59] is often omitted for simplicity (4, 10).

In Figure 6, the coagulation of equal-sized ultrafine particles in the presence of an interparticle van der Waals force is considered. The Hamaker constants for NaCl and  $\text{ZnCl}_2$  were both taken as  $8.93 \times 10^{-13}$  erg (which gives  $H = 21.7$  at  $25^\circ\text{C}$ ). The Hamaker constant for Ag is  $4.0 \times 10^{-12}$  erg (which gives  $H = 97.2$  at  $25^\circ\text{C}$ ). However, as suggested by Okuyama *et al.* (11), a factor of 10 higher than the bulk value is necessary to explain the experimental results of Ag. The value of the Hamaker constant for Ag was therefore taken as  $4.0 \times 10^{-11}$  erg in the calculation. Both the solid lines (present work) and the dashed lines (generalized Fuchs matching) show good agreement with each other and with the experimental data for the effective Knudsen number larger than unity (the particle diameter is less than 20 nm). Both of the solid lines fall off rapidly in the range of particle diameters larger than about 20 nm; the present theory is not applicable in this range due to the fact that the effective Knudsen number becomes less than unity.

We now consider the ion-particle charging experiments and predictions. The

data were obtained by Pui *et al.* (9) and were analyzed assuming the flow in the charger is either turbulent or laminar. Data shown in both Figures 7a and 7b are represented by open squares for the laminar flow assumption and by closed circles for the turbulent flow assumption. The values of dielectric constant for NaCl and Ag are 6.12 and  $\infty$ , respectively. The ionic mass and mobility were taken as  $m_{\text{ion}} = 109$  amu and  $Z_{\text{ion}} = 1.4$  cm<sup>2</sup>/V-s (26). The Coulombic potential is neglected since the particles in general carry zero charges. In order to evaluate the value of  $\tau$  through the use of Eq. [5], the ion-particle diffusivity is considered as the sum of the ionic diffusivity and the particle Brownian diffusivity,

$$\mathcal{D} = \frac{kT Z_{\text{ion}}}{e} + \frac{kT C_c}{6\pi\eta R_p} \quad [61]$$

where  $C_c$  is the slip correction factor,  $R_p$  is the particle radius, and the ionic diffusivity is determined by the ionic mobility through the Einstein relation.

The generalized Fuchs matching predictions for both NaCl and Ag are also shown in Figures 7a and 7b. However, a new matching distance (*i.e.*,  $g$  in Eq. [59]) was chosen that is commonly used for the charging calculation (1, 9). This new matching distance is given by

$$g = \frac{R_p^3}{\lambda_{\text{ion}}^2} \left[ \frac{1}{5} \left( 1 + \frac{\lambda_{\text{ion}}}{R_p} \right)^5 - \frac{1}{3} \left( 1 + \frac{\lambda_{\text{ion}}^2}{R_p^2} \right) \left( 1 + \frac{\lambda_{\text{ion}}}{R_p} \right)^3 + \frac{2}{15} \left( 1 + \frac{\lambda_{\text{ion}}^2}{R_p^2} \right)^{5/2} \right] - R_p \quad [62]$$

and  $\lambda_{\text{ion}}$  is calculated through the binary diffusivity theory (recall Eq. [6]),

$$\lambda_{\text{ion}} = \frac{64}{3\pi} \frac{kT Z_{\text{ion}}}{e} \frac{1}{1 + \gamma} \left( \frac{15\gamma^2 + 8\gamma + 6}{30\gamma^2 + 16\gamma + 13} \right) \sqrt{\frac{\pi m_{\text{ion}}}{8kT}} \quad [63]$$

where  $\gamma = m_{\text{ion}}/m_B$  is the mass ratio of an ion and a background gas molecule. From Figures 7a and 7b, we find that the agreement between the predictions from

the present work and the generalized Fuchs matching theory is very good for particles of diameters less than 100 nm. The laminar flow profile assumption in the charger leads to a better fit between theories and data than those calculated using the turbulent profile assumption. For particles of diameters larger than about 40 nm, in the cases of Figures 7a and 7b, the present theory is not applicable because  $\tau$  becomes less than unity. Owing to the possible change of bulk properties such as particle dielectric constant, differences between the data and the theories in both figures become significant for particles smaller than 10 nm. In this range, a decrease in  $\kappa$  seems to be necessary in matching the theoretical predictions with the data. Finally, we would like to point out that the “match” between the data and the Marlow-Brock theory in the near free-molecule regime mentioned in the work of Pui *et al.* (9) was indeed a “mismatch” because the  $E_0$  was originally mistaken as  $\sqrt{\pi C}$  in (6).

## SIMULTANEOUS VAN DER WAALS, COULOMBIC, AND IMAGE POTENTIAL

In this section, we consider an interparticle potential that is composed of simultaneous van der Waals, Coulombic, and image forces. Because the van der Waals potential has a form that is divergent (*i.e.*, singularly attractive) at the particle contact, the image potential itself does not have to be singular; as a result, the combination of the three potentials will always be singular at the particle contact. In this regard, we will not restrict ourselves only to situations of ion-particle charging; we can, in general, consider particle-particle coagulation with an arbitrary particle size ratio.

The image force between an initially-charged particle and an initially-uncharged particle can be obtained, in general, by summing the interactions between the



charge in the initially-charged particle and its infinite reflection image charges in the initially-uncharged particle (22, 23). To obtain the image force between two charged particles, one needs to sum over two initially charged-uncharged sets of image interactions (23). Image potential, subsequently, can be obtained by integrating the image force with respect to the radial distance. The exact form of an interparticle Coulombic-image potential, unlike the ion-particle situation, is not available due to its complexity. For particles that are slightly dielectric, however, a closed form of the Coulombic-image potential expression can be obtained and is given in the Appendix. The simultaneous potential together with the van der Waals potential (Eq. [40]) is

$$\begin{aligned} \Phi(y) = & -\frac{H}{6} \left\{ \frac{2q(1-q)y^2}{1-y^2} + \frac{2q(1-q)y^2}{1-(2q-1)y^2} + \ln \frac{1-y^2}{1-(2q-1)y^2} \right\} \\ & + By - Cz_1^2 \left\{ \frac{(z_2/z_1)^2 q^3 y^4}{1-q^2 y^2} + \frac{(1-q)^3 y^4}{1-(1-q)^2 y^2} \right\} \end{aligned} \quad [64]$$

where  $q = R_1/(R_1 + R_2)$ ,  $y = (R_1 + R_2)/r$ , and  $B$  and  $C$  are given by Eq. [A13].  $E_0$  and  $E_1$ , from Eq. [66], are functions of the dimensionless Hamaker constant  $H$ , particle size ratio  $q$ , particle charge ratio  $z_2/z_1$ , the product of charge and image strength  $Cz_1^2$ , and the particle dielectric constant  $\kappa$  (the dimensionless charge product  $B$  is linearly dependent on  $Cz_1^2$ ,  $z_2/z_1$ , and  $\kappa$ ). The image potential expression, the third term on the right-hand side of Eq. [64], is strictly valid for the coagulation of slightly dielectric material ( $\kappa \rightarrow 1$ ); to a first approximation, however, we shall use  $\kappa = 6.12$  (*i.e.*, the value for NaCl and  $\text{ZnCl}_2$ ) as an example to illustrate the  $E_0$  and  $E_1$  calculation in Figures 10 and 11.

Figures 8 and 9, first of all, show the predictions of  $E_0$  and  $E_1$  under  $B = 0$  (or  $z_2 = 0$ ), *i.e.*, no Coulombic force. Under such circumstances,  $E_0$  and  $E_1$  are only functions of  $q$ ,  $H$ , and  $Cz_1^2$  (*i.e.*,  $\kappa$  can be of arbitrary value in this case). In Figure 8, we again find that the higher the Hamaker constant or the higher the

image force, the larger the value of  $E_0$ ; also the closer to equal-sized coagulation, the higher the coagulation rate in the low  $Cz_1^2$  regime (where only the van der Waals force is important), and the lower the coagulation rate in the high  $Cz_1^2$  regime (where the image force predominates). The reason for this reverse effect of size ratio arises from the functional forms of the van der Waals force and image potential. For  $R_1/R_2 = 1$ , all the curves of different values of  $H$  merge at about  $Cz_1^2 = 100$ . For  $R_1/R_2 = 1/9$ , curves merge at about  $Cz_1^2 = 4$ . For extremely unequal-sized coagulation such as the ion-particle charging situation, from Figure 8, we can conclude that the van der Waals force is not important when the image force is present. For equal-sized particle collision, on the other hand, the van der Waals potential may play an important role for  $Cz_1^2 \leq 30$ . Predictions of  $E_1$  in Figure 9 are similar to that in Figure 8; the larger the coagulation enhancement in the infinite Kn situation, the stronger the first-order correction for a finite large Kn value.  $E_1$  is about half the value of  $E_0$ .

Figures 10a and 10b show the  $E_0$  predictions for the equal-sized particle coagulation ( $q = 0.5$ ) with a dielectric constant  $\kappa = 6.12$  when  $H = 20$  and  $H = 100$ , respectively. The purpose is to demonstrate influence of  $B$  for both the repulsive Coulombic force ( $z_1$  and  $z_2$  of opposite signs) and the attractive Coulombic force ( $z_1$  and  $z_2$  of same sign) situations. The parameter used in the figures is the particle charge ratio,  $z_2/z_1$ . In both figures, since

$$B = 2 (Cz_1^2) \left( \frac{z_2}{z_1} \right) \left( \frac{\kappa + 1}{\kappa - 1} \right) , \quad [65]$$

we find the higher the value of positive  $z_2/z_1$ , the stronger the Coulombic repulsion and the lower the  $E_0$ ; for negative  $z_2/z_1$ , the smaller the value of  $z_2/z_1$ , the stronger the Coulombic attraction and the higher the  $E_0$ . By comparing Figures 10a and 10b, we find that the higher the  $H$  value, the stronger the van der Waals force and

the higher the  $E_0$ .

Figures 11a and 11b are similar to Figures 10a and 10b. The former two show the predictions of the first-order finite large Knudsen number correction  $E_1$ . One notices that  $E_1$  is less sensitive to the increase of  $Cz_1^2$  for small negative  $z_2/z_1$  values than  $E_0$  in Figures 10a and 10b.

In this section, we calculate the enhancement factors in a situation of combined Coulombic, image and van der Waals forces. The calculated  $E_0$  and  $E_1$  are functions of  $H$ ,  $Cz_1^2$ ,  $\kappa$ ,  $z_2/z_1$  and the size ratio. For situations of arbitrary combination of these parameters, interpolation of Figures 8-11 is possible. Because the functional dependences are very complicated, we do not present best-fit equations for this simultaneous potential situation.

## SUMMARY AND CONCLUSION

In this work we have derived expressions for the ultrafine particle coagulation rate in the presence of a singular contact potential that is either monotonic or nonmonotonic attractive of arbitrary form.

We have, for the first time, calculated the free-molecule enhancement and its first-order correction for a large but finite Knudsen number for situations of a combined van der Waals, Coulombic, and image potential. Conditions where each component potential predominates over others are determined. The present theoretical predictions are in good agreement with experimental data of ultrafine particle coagulation and ion-particle charging. We have also shown theoretical support for the coagulation rate predicted by the empirical flux-matching method. Least-squares best-fit equations are presented for some common situations involving coagulation with van der Waals or electric Coulombic-image forces. Future application of the present results should be very useful in ion-particle, particle-particle coagulation, diffusion charging, and ion-induced nucleation.

## ACKNOWLEDGEMENT

This work was supported by National Science Foundation Grant ATM-8503103 and U.S. Department of Energy Grant DE-FG05-87ER60550.

## APPENDIX

### Image Potential Between Two Slightly Dielectric Charged Particles

Let  $q_1$ ,  $R_1$ ,  $q_2$ , and  $R_2$  be the initial charge and radius of particles 1 and 2, respectively; also denote  $\kappa$  as the particle dielectric constant and  $r$  as the distance between the two particle centers. The first image charge of  $q_2$  in particle 1 which is at a distance  $R_1^2/r$  from the center of particle 1 is (22, 23)

$$q_{1,i} = -\frac{\kappa - 1}{\kappa + 1} \frac{q_2 R_1}{r} \quad [A1]$$

The first image charge of  $q_1$  in particle 2 which is at a distance  $R_2^2/r$  from the center of particle 2 is

$$q_{2,i} = -\frac{\kappa - 1}{\kappa + 1} \frac{q_1 R_2}{r} \quad [A2]$$

The second images in both particles involve terms of order  $O[\left((\kappa - 1)/(\kappa + 1)\right)^2]$ , which, for slightly dielectric particles ( $\kappa \rightarrow 1$ ), can be neglected. The final total charge in each of the particles can therefore be approximated as

$$z_1 e = q_1 + q_{1,i} = q_1 - \frac{\kappa - 1}{\kappa + 1} \frac{R_1 q_2}{r} \quad [A3]$$

$$z_2 e = q_2 + q_{2,i} = q_2 - \frac{\kappa - 1}{\kappa + 1} \frac{R_2 q_1}{r} \quad [A4]$$

where  $z_1$  and  $z_2$  are the number and sign of the total charge carried by particles 1 and 2, respectively. Solving Eqs. [A3] and [A4] and expressing  $q_1$  and  $q_2$  in terms of  $z_1$  and  $z_2$ , one has

$$q_1 = \frac{z_1 e + z_2 e \left( \frac{\kappa - 1}{\kappa + 1} \right) \frac{R_1}{r}}{1 - \left( \frac{\kappa - 1}{\kappa + 1} \right)^2 \frac{R_1 R_2}{r^2}} \approx z_1 e + z_2 e \left( \frac{\kappa - 1}{\kappa + 1} \right) \frac{R_1}{r} \quad [A5]$$

$$q_2 = \frac{z_2 e + z_1 e \left( \frac{\kappa - 1}{\kappa + 1} \right) \frac{R_2}{r}}{1 - \left( \frac{\kappa - 1}{\kappa + 1} \right)^2 \frac{R_1 R_2}{r^2}} \approx z_1 e + z_2 e \left( \frac{\kappa - 1}{\kappa + 1} \right) \frac{R_2}{r} \quad [A6]$$

The electrical static forces are contributed by the Coulombic interactions between  $q_1$  and  $q_2$  ( $F_1$ ),  $q_1$  and  $q_{2,i}$  ( $F_2$ ),  $q_2$  and  $q_{1,i}$  ( $F_3$ ), and  $q_{1,i}$  and  $q_{2,i}$  ( $F_4$ ). Upon neglecting the  $O\left[\left((\kappa - 1)/(\kappa + 1)\right)^2\right]$  terms, we find

$$F_1 = \frac{q_1 q_2}{4\pi\epsilon_0 r^2} \approx \frac{e^2}{4\pi\epsilon_0 r^2} \left[ z_1 z_2 + z_2^2 \left( \frac{\kappa - 1}{\kappa + 1} \right) \frac{R_1}{r} + z_1^2 \left( \frac{\kappa - 1}{\kappa + 1} \right) \frac{R_2}{r} \right] \quad [A7]$$

$$F_2 = \frac{(q_1) \left( -\frac{\kappa - 1}{\kappa + 1} \frac{q_1 R_2}{r} \right)}{4\pi\epsilon_0 (r^2 - R_2^2)^2 / r^2} \approx - \frac{e^2 z_1^2 \left( \frac{\kappa - 1}{\kappa + 1} \right) R_2 r}{4\pi\epsilon_0 (r^2 - R_2^2)^2} \quad [A8]$$

$$F_3 = \frac{(q_2) \left( -\frac{\kappa - 1}{\kappa + 1} \frac{q_2 R_1}{r} \right)}{4\pi\epsilon_0 (r^2 - R_1^2)^2 / r^2} \approx - \frac{e^2 z_2^2 \left( \frac{\kappa - 1}{\kappa + 1} \right) R_1 r}{4\pi\epsilon_0 (r^2 - R_1^2)^2} \quad [A9]$$

$$F_4 = \frac{\left( \frac{\kappa - 1}{\kappa + 1} \right)^2 q_1 q_2 R_1 R_2 / r^2}{4\pi\epsilon_0 (r^2 - R_1^2 - R_2^2)^2 / r^2} \approx 0 \quad [A10]$$

The total force is thus

$$F = \frac{z_1 z_2 e^2}{4\pi\epsilon_0 r^2} - \left( \frac{\kappa - 1}{\kappa + 1} \right) \frac{e^2}{4\pi\epsilon_0 r^3} \left[ \frac{R_1^3 z_2^2 (2r^2 - R_1^2)}{(r^2 - R_1^2)^2} + \frac{R_2^3 z_1^2 (2r^2 - R_2^2)}{(r^2 - R_2^2)^2} \right] \quad [A11]$$

The dimensionless Coulombic-image potential is obtained by integrating  $F$  over  $r$  and dividing by  $kT$ :

$$\Phi(r) = -\frac{1}{kT} \int_{\infty}^r F dr = B \frac{(R_1 + R_2)}{r} - C(R_1 + R_2) \left\{ \frac{z_2^2 R_1^3}{(r^2 - R_1^2)r^2} + \frac{z_1^2 R_2^3}{(r^2 - R_2^2)r^2} \right\} \quad [A12]$$

where

$$B \equiv \frac{z_1 z_2 e^2}{4\pi\epsilon_0 kT(R_1 + R_2)} \quad , \quad C \equiv \frac{\kappa - 1}{\kappa + 1} \frac{e^2}{8\pi\epsilon_0 kT(R_1 + R_2)} \quad [A13]$$

Though Eq. [A13] is obtained by the approximation of a small dielectric constant, its limiting case for the ion-particle charging situation, Eq. [46], is an exact form of the Coulombic-image potential of an arbitrary dielectric constant because *only one* image of the ion charge exists in the particle. Also note that the  $B$  and  $C$  given in Eq. [47] are limiting cases of Eq. [A13] for the ion-particle situation.

## REFERENCES

1. Fuchs, N. A., *Geofis. Pura Appl.* **56**, 185 (1963).
2. Sceats, M. G., *J. Chem. Phys.* **84**, 5206 (1986).
3. Kramers, H. A., *Physica* **7**, 284 (1940).
4. Marlow, W. H., *J. Chem. Phys.* **73**, 6284 (1980).
5. Gentry, J. W., *Aerosol Sci.* **3**, 65 (1972).
6. Marlow, W. H., and Brock, J. R., *J. Colloid Interf. Sci.* **50**, 32 (1975).
7. Keller, J. B., *Commun. Pure Appl. Math.* **1**, 275 (1948).
8. Gross, E. P., in "Rarefied Gas Dynamics" (F. M. Devienne Ed.), p.139. Pergamon, Oxford, 1960.
9. Pui, D. Y. H., Fruin, S., and McMurtry, P. H., *Aerosol Sci. Technol.* **8**, 173 (1988).
10. Okuyama, K., Kousaka, Y., and Hayashi, K., *J. Colloid Interf. Sci.* **101**, 98 (1984).
11. Okuyama, K., Kousaka, Y., and Hayashi, K., *J. Colloid Interf. Sci.* **113**, 42 (1986).
12. Hirschfelder, J. O., Curtiss, C. F., and Bird, R. B., "Molecular Theory of Gases and Liquids." Wiley, New York, 1954.
13. Bhatnager, R. L., Gross, E. P., and Krook, M., *Phys. Rev.* **94**, 511 (1954).
14. Huang, D. D., and Seinfeld, J. H., *J. Colloid Interf. Sci.* **130**, 275 (1988).
15. Seinfeld, J. H., "Atmospheric Chemistry and Physics of Air Pollution." Wiley, New York, 1986.
16. Phillips, W. F., *Phys. Fluids* **18**, 1089 (1975).
17. Kelly, G. E., and Sengers, J. V., *J. Chem. Phys.* **57**, 1441 (1972).
18. Amadon, A. S., and Marlow, W. H., (submitted).
19. Marlow, W. H., *J. Chem. Phys.* **73**, 6288 (1980).



20. Alam, M. K., *Aerosol Sci. Technol.* **6**, 41 (1987).
21. Hamaker, H. C., *Physica* **4**, 1058 (1937).
22. Maxwell, J. C., "A Treatise on Electricity and Magnetism," Vol. I, Chapt. 11. Academic Reprints, Stanford, California, 1953.
23. Smythe, W. R., "Static and Dynamic Electricity" (3rd Ed.), Chapt. 5. McGraw-Hill, 1968.
24. Keefe, D., Nolan, P. J., M. R. I. A., and Scott, J. A., *Proc. R. Irish Acad.* **66A**, 17 (1968).
25. Hoppel, W. A., and Frick, G. M., *Aerosol Sci. Technol.* **5**, 1 (1986).
26. Adachi, M., Kousaka, Y., and Okuyama, K., *J. Aerosol Sci.* **16**, 109 (1985).

## LIST OF FIGURES

- Figure 1. Free-molecule enhancement,  $E_0$ , to the coagulation rate in the presence of a van der Waals potential as a function of the dimensionless Hamaker constant,  $H$ , and the particle size ratio.
- Figure 2. First-order large Knudsen number correction,  $E_1$ , to the coagulation rate in the presence of a van der Waals potential as a function of the dimensionless Hamaker constant,  $H$ , and the particle size ratio.
- Figure 3. Free-molecule enhancement,  $E_0$ , for ion-particle charging as a function of the dimensionless charge product,  $B$ , and the dimensionless image strength,  $C$ .
- Figure 4. First-order large Knudsen number correction,  $E_1$ , for ion-particle charging as a function of the dimensionless charge product,  $B$ , and the dimensionless image strength,  $C$ .
- Figure 5. Comparison of  $E_0$  and  $E_1$  predicted by the present work and by Marlow and Brock (6) for ion-particle charging in the presence of a pure image force.
- Figure 6. Comparison between results from the present work, the generalized Fuchs matching prediction (1, 4), and the experimental data of Okuyama *et al.* (10, 11) for ultrafine particle coagulation in the presence of a van der Waals potential.
- Figure 7. Comparison between results from the present work, the generalized Fuchs matching prediction (1, 4), and the experimental data of Pui *et al.* (9) for ion-particle charging in the presence of an image force. (a) NaCl and ZnCl<sub>2</sub>,  $\kappa = 6.12$ ; (b) Ag,  $\kappa = \infty$ .

Figure 8. Free-molecule enhancement,  $E_0$ , as a function of the product of image strength and charge,  $Cz_1^2$ , the dimensionless Hamaker constant,  $H$ , and the particle size ratio in the presence of a combined van der Waals and image potential.

Figure 9. First-order large Knudsen number correction,  $E_1$ , as a function of the product of image strength and charge,  $Cz_1^2$ , the dimensionless Hamaker constant,  $H$ , and the particle size ratio in the presence of a combined van der Waals and image potential.

Figure 10. Free-molecule enhancement,  $E_0$ , as a function of the product of image strength and charge,  $Cz_1^2$ , the dimensionless Hamaker constant,  $H$ , and the charge ratio,  $z_2/z_1$ , for equal-sized particle coagulation in the presence of a combined van der Waals, Coulombic, and image potential. Particle dielectric constant  $\kappa = 6.12$ . (a)  $H = 20$ ; (b)  $H = 100$ .

Figure 11. First-order large Knudsen number correction,  $E_1$ , as a function of the product of image strength and charge,  $Cz_1^2$ , the dimensionless Hamaker constant,  $H$ , and the charge ratio,  $z_2/z_1$ , for equal-sized particle coagulation in the presence of a combined van der Waals, Coulombic, and image potential. Particle dielectric constant  $\kappa = 6.12$ . (a)  $H = 20$ ; (b)  $H = 100$ .

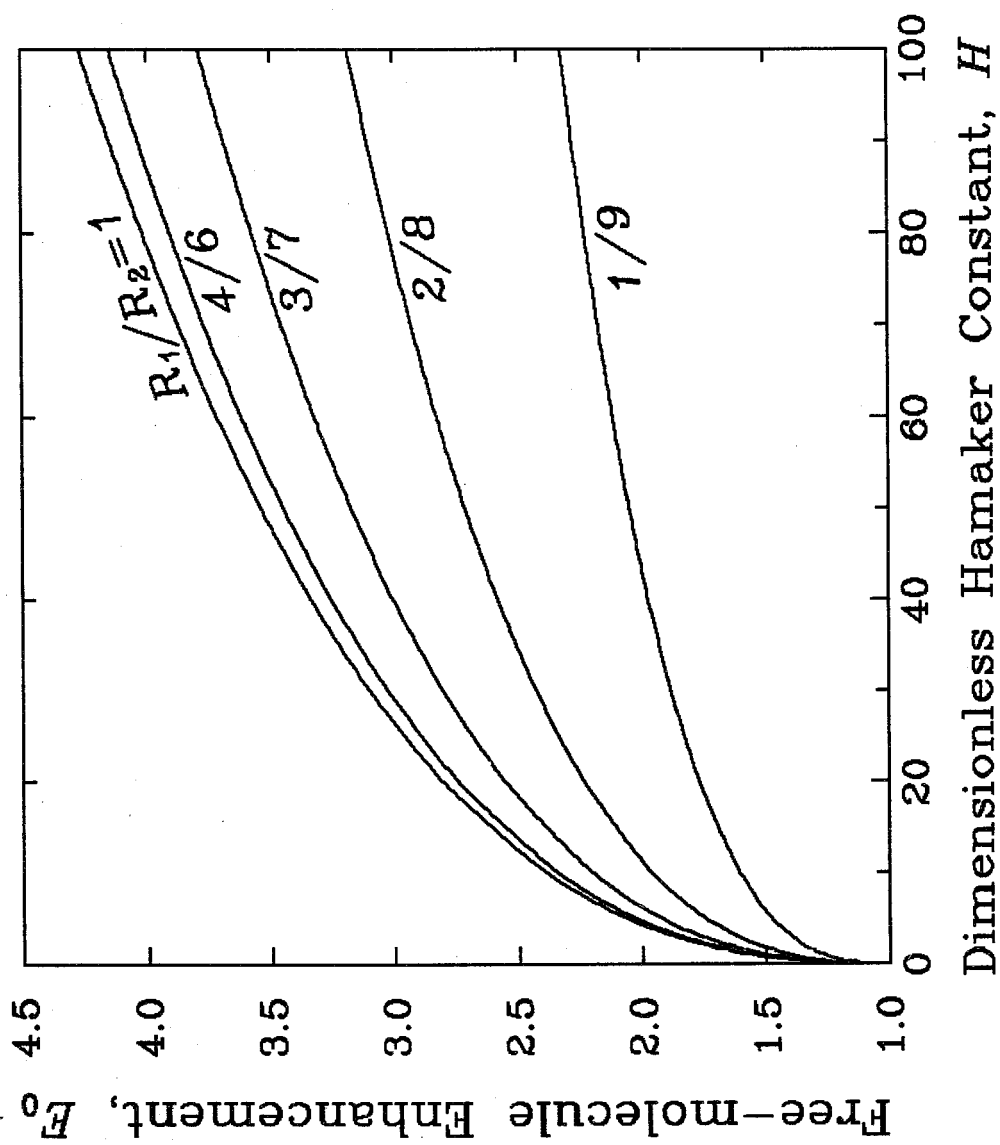


Figure 1

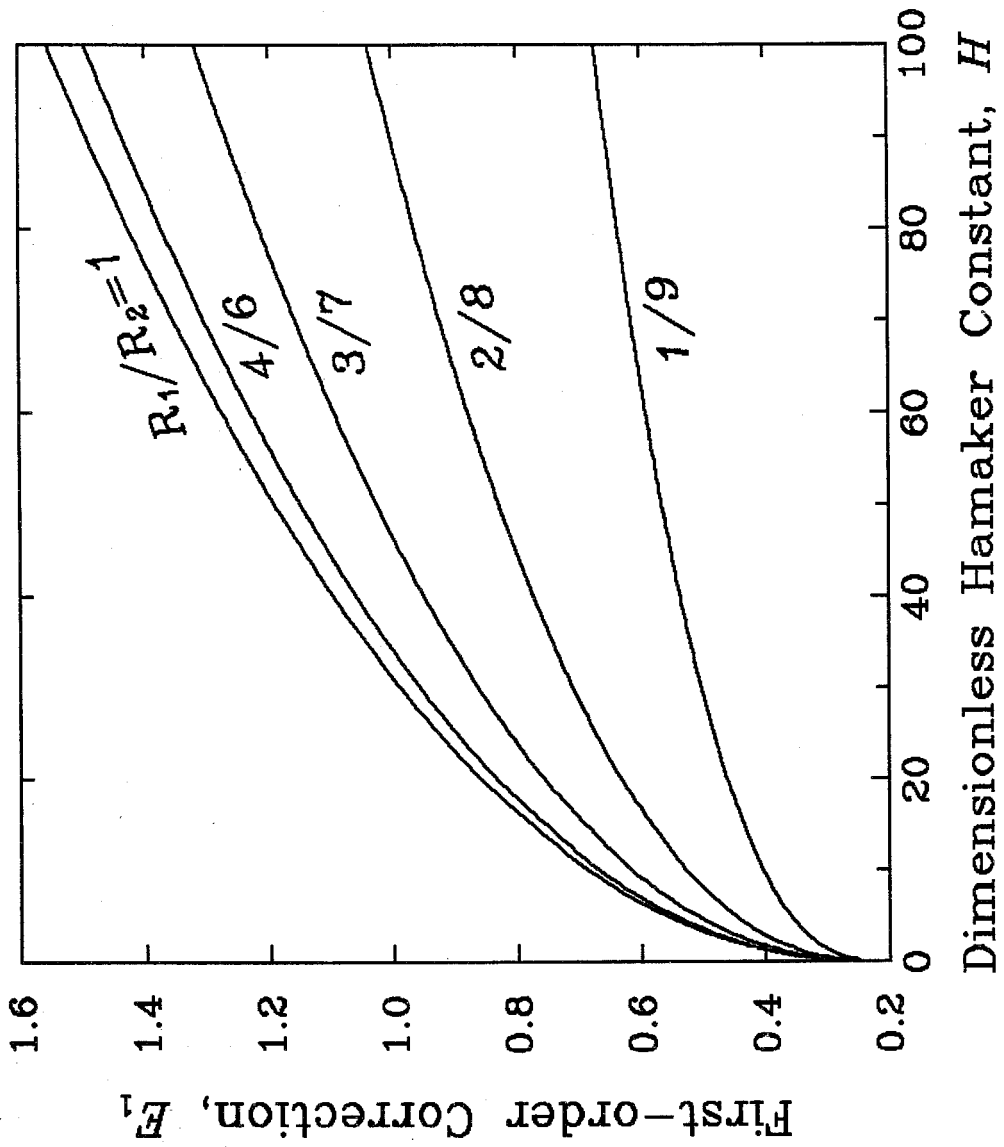


Figure 2

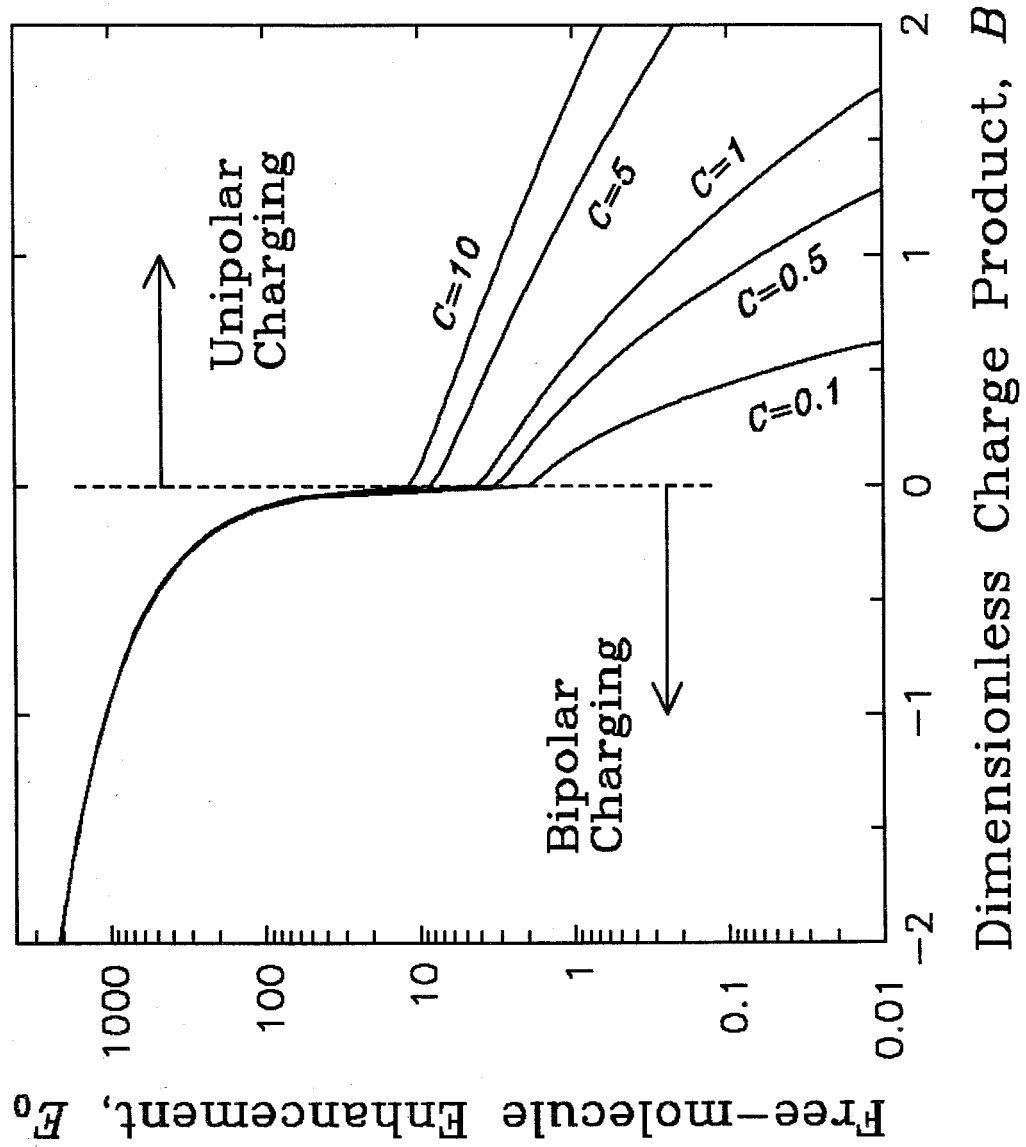


Figure 3

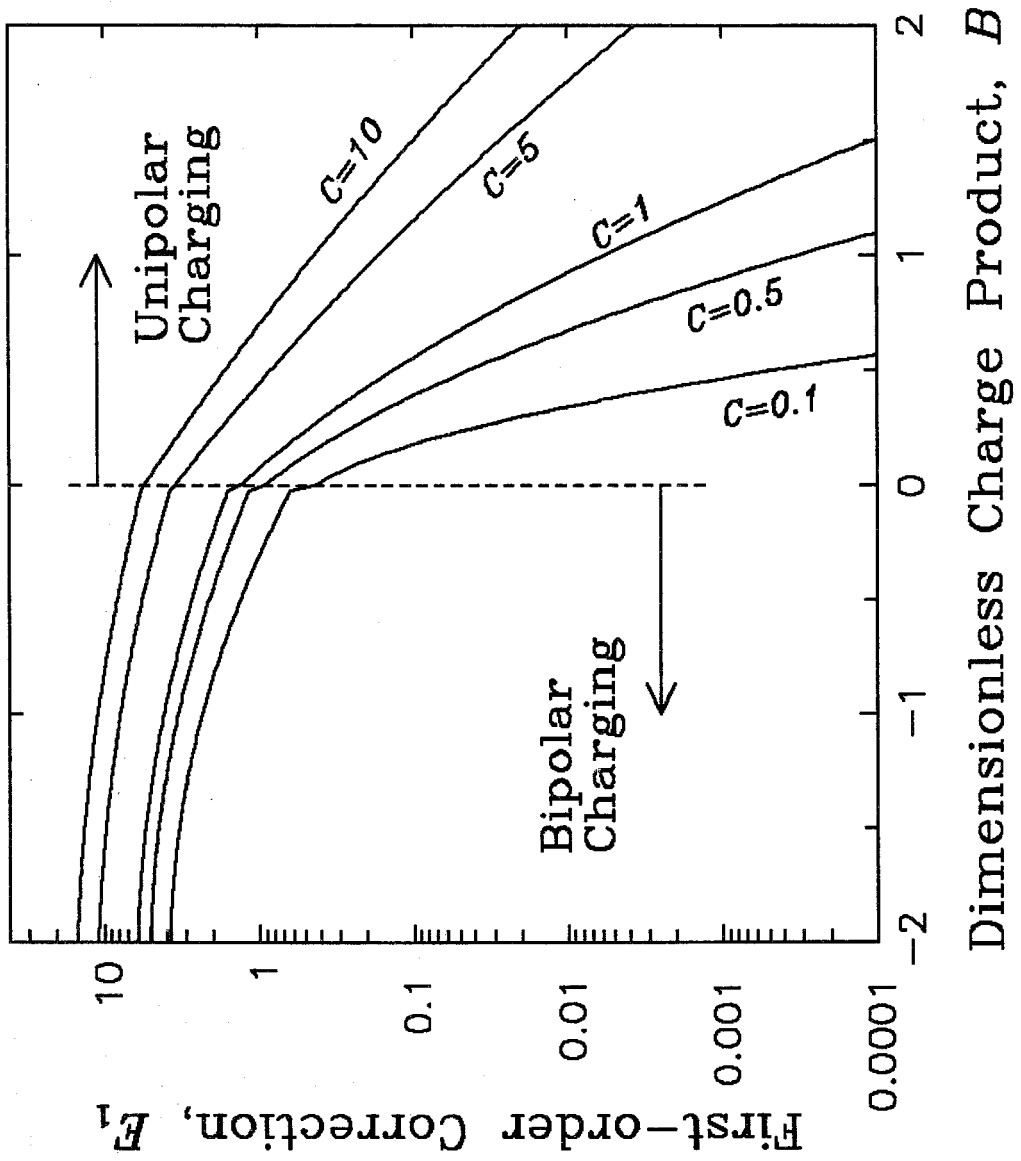


Figure 4

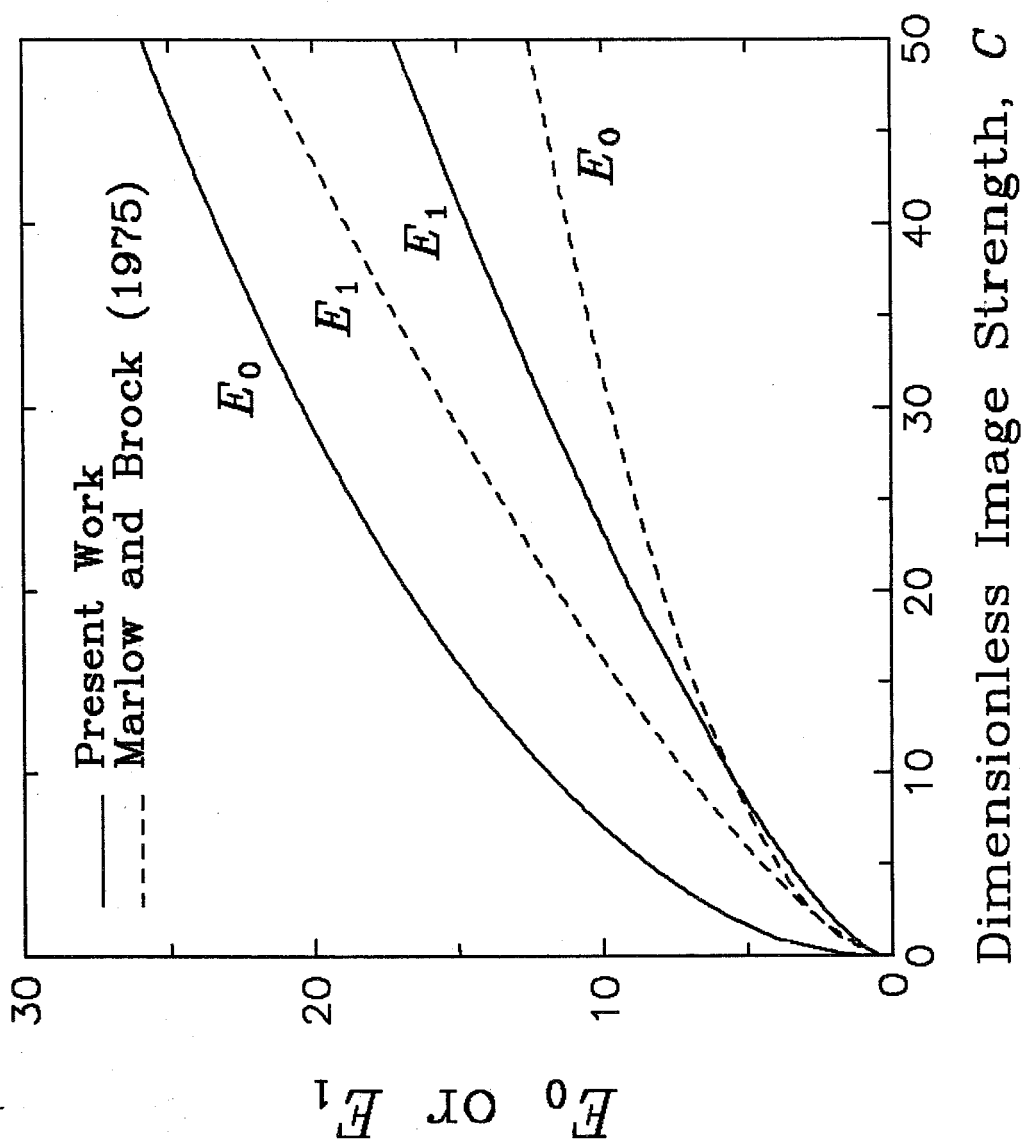


Figure 5



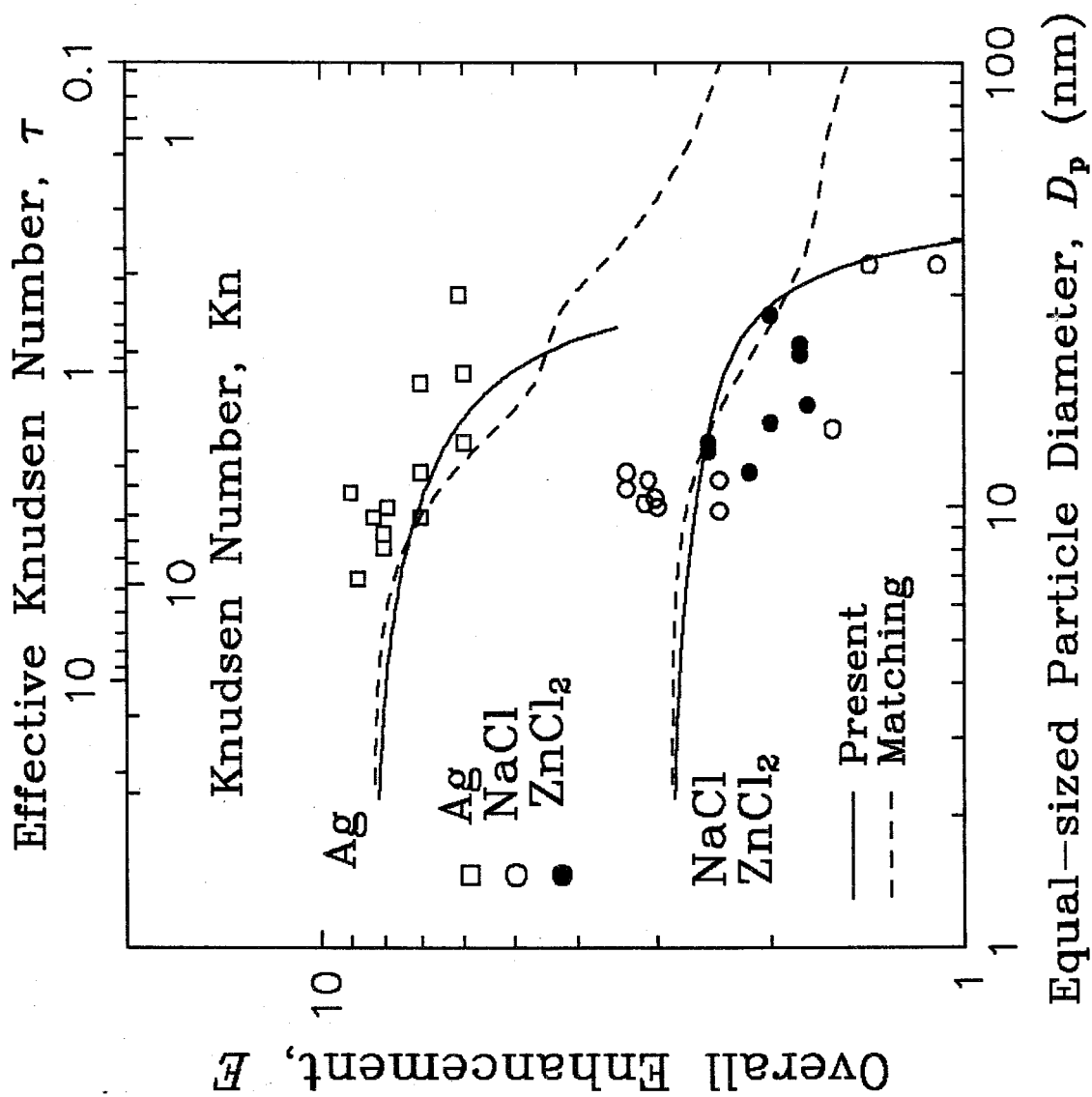


Figure 6

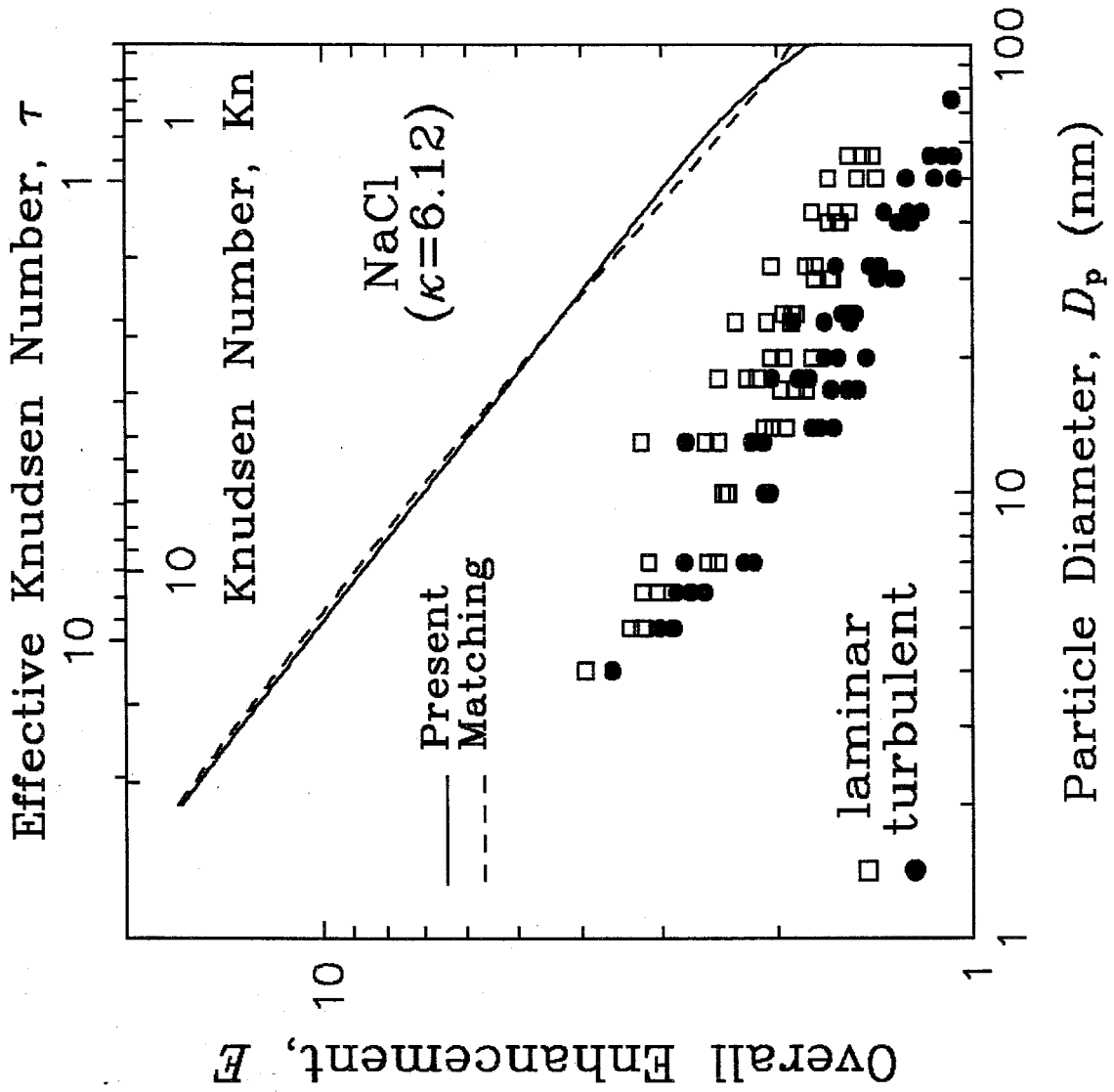


Figure 7a

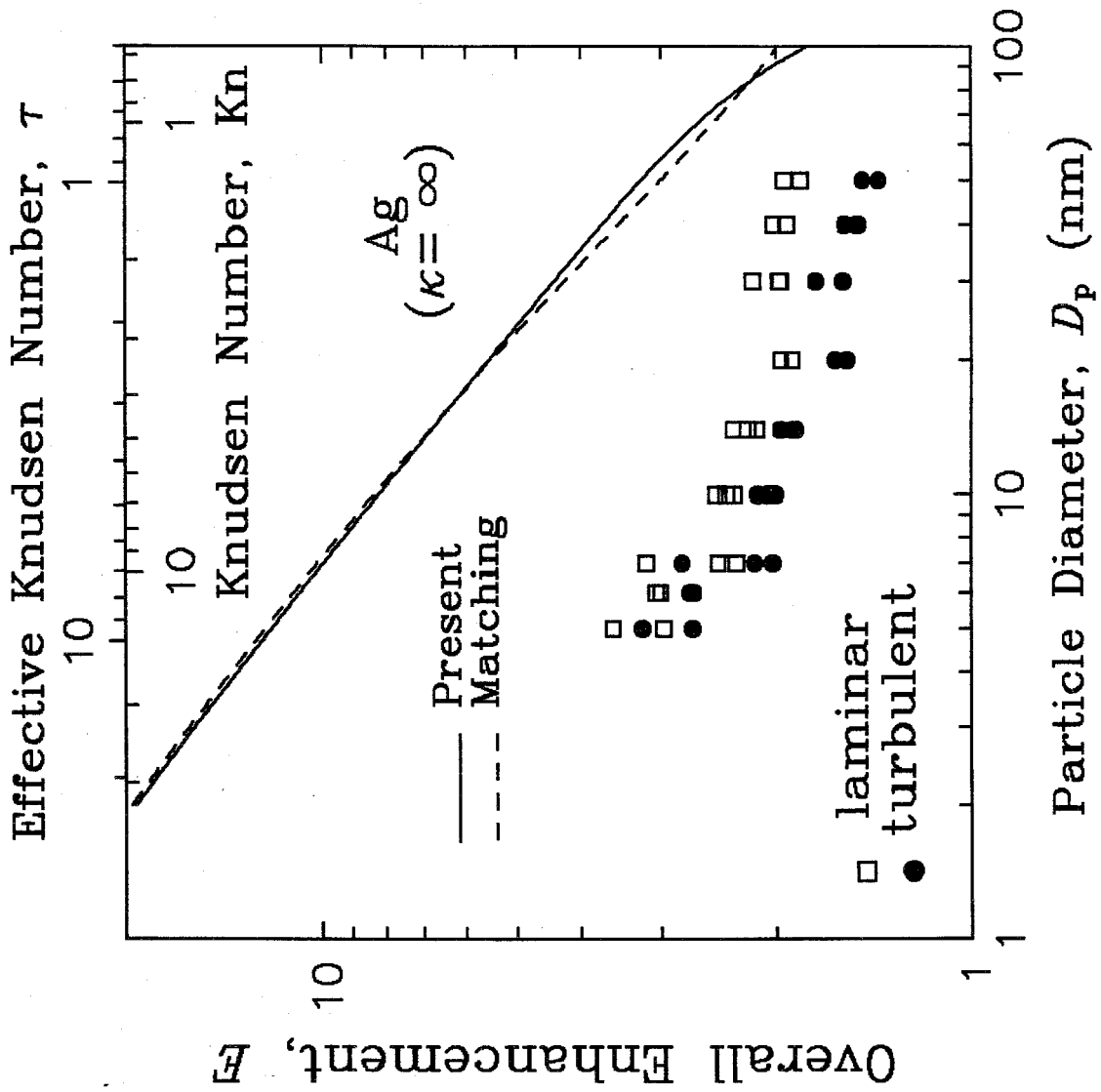


Figure 7b

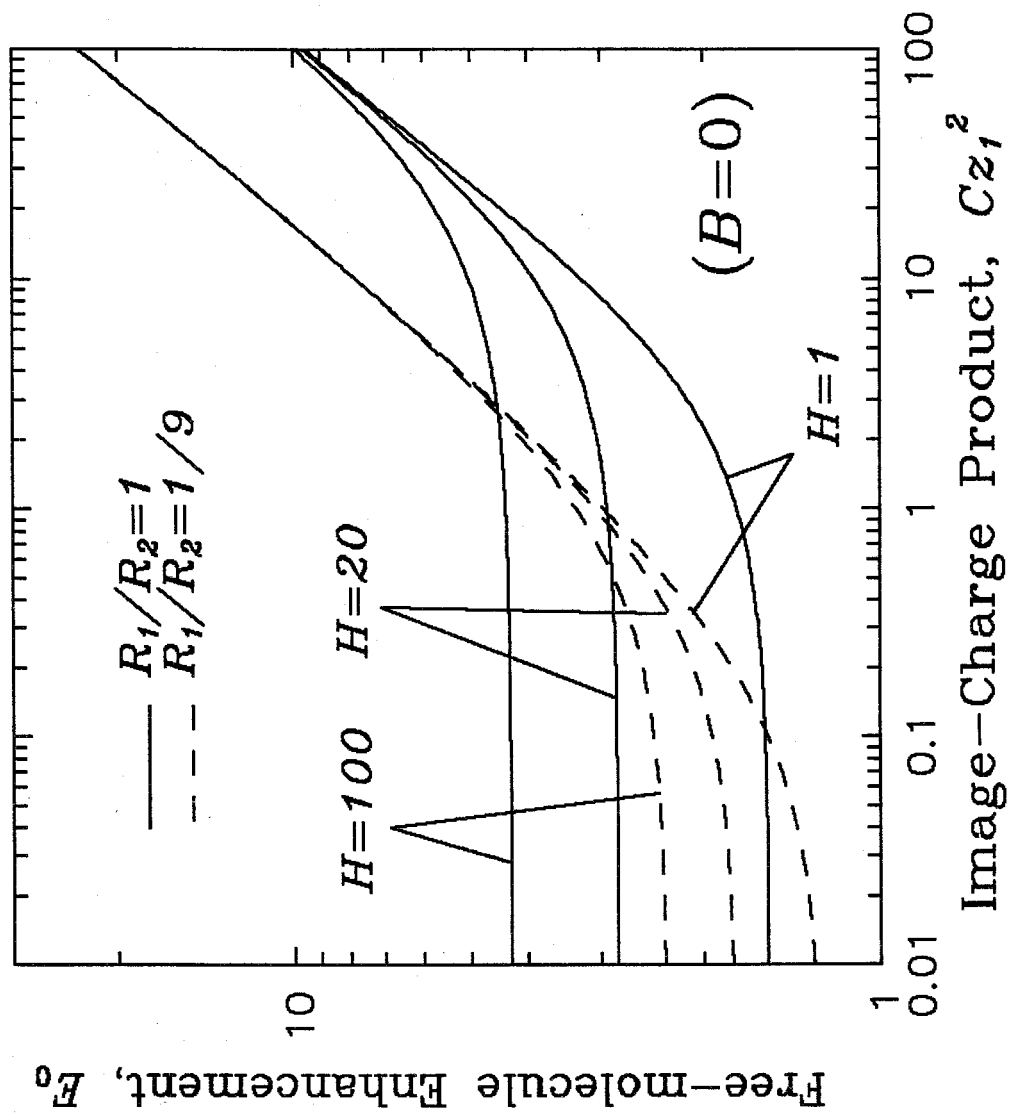


Figure 8

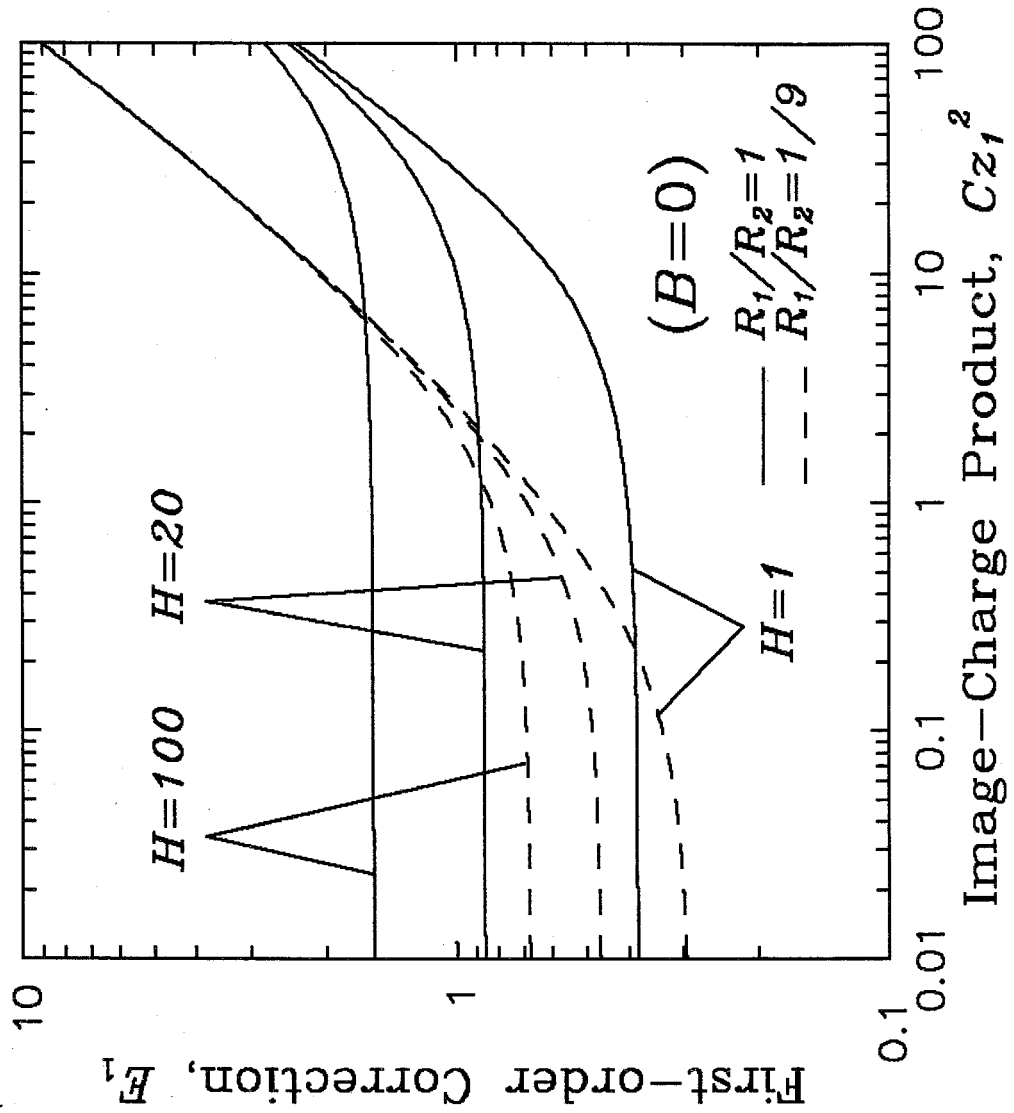


Figure 9

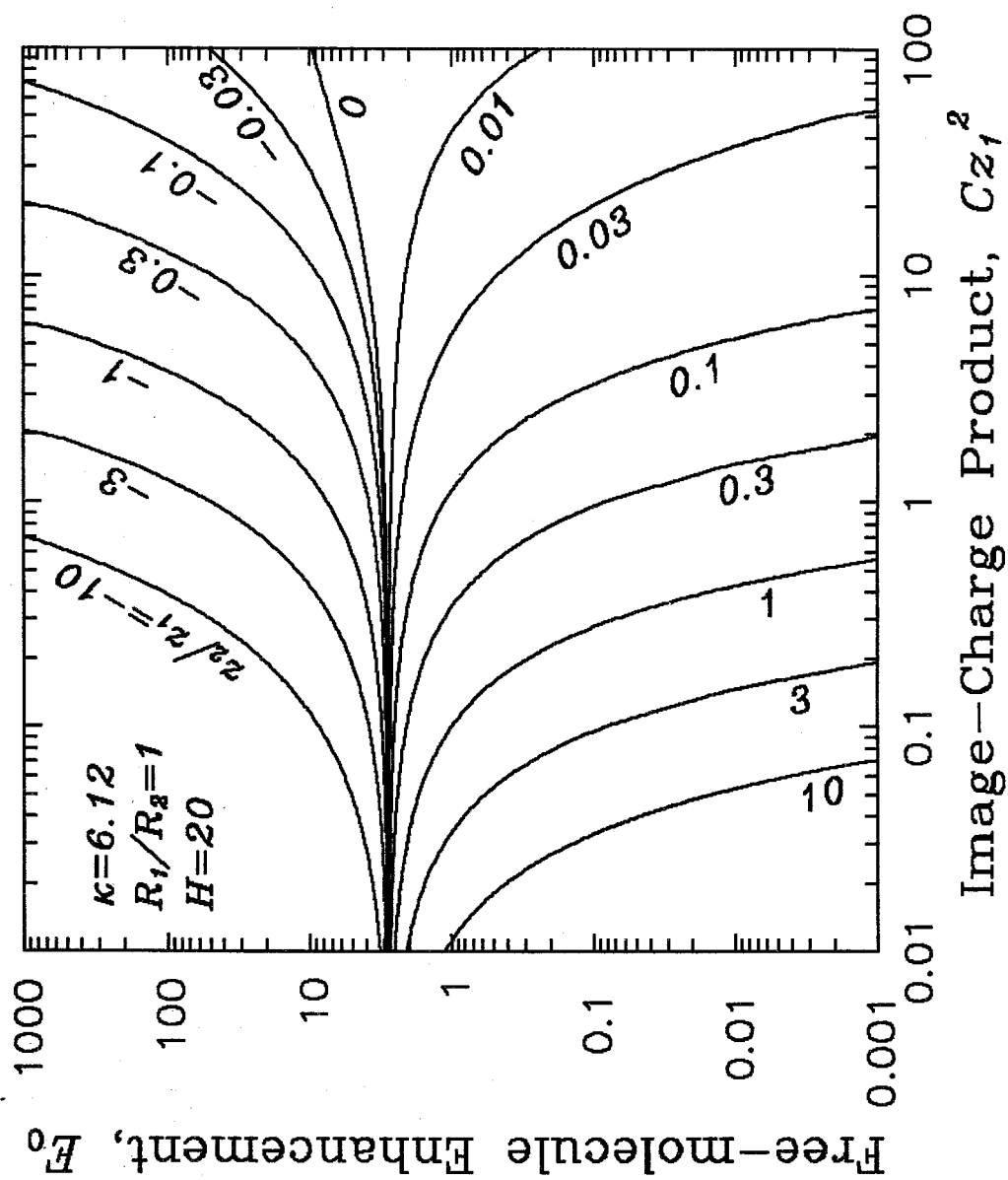


Figure 10a

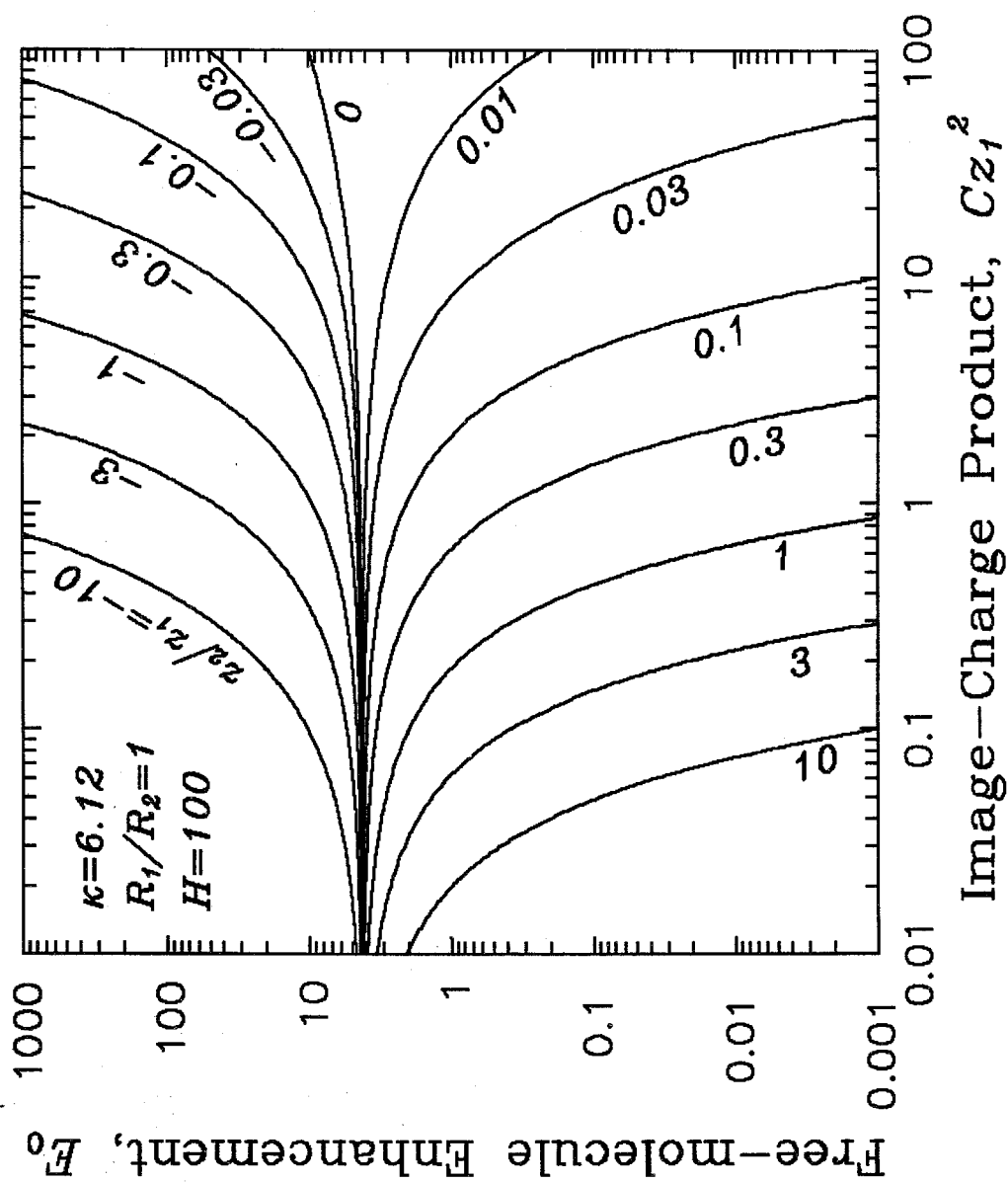


Figure 10b

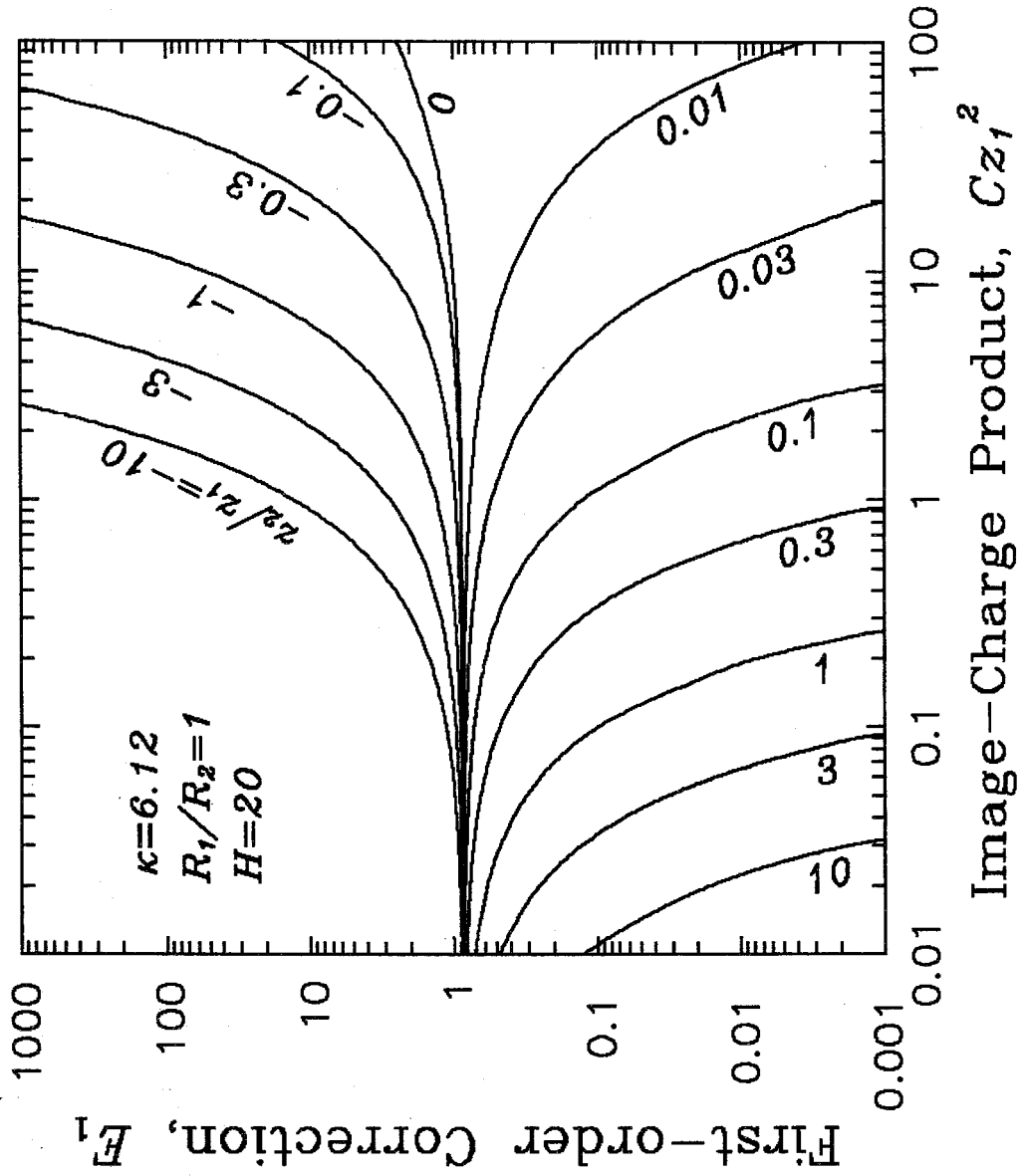


Figure 11a



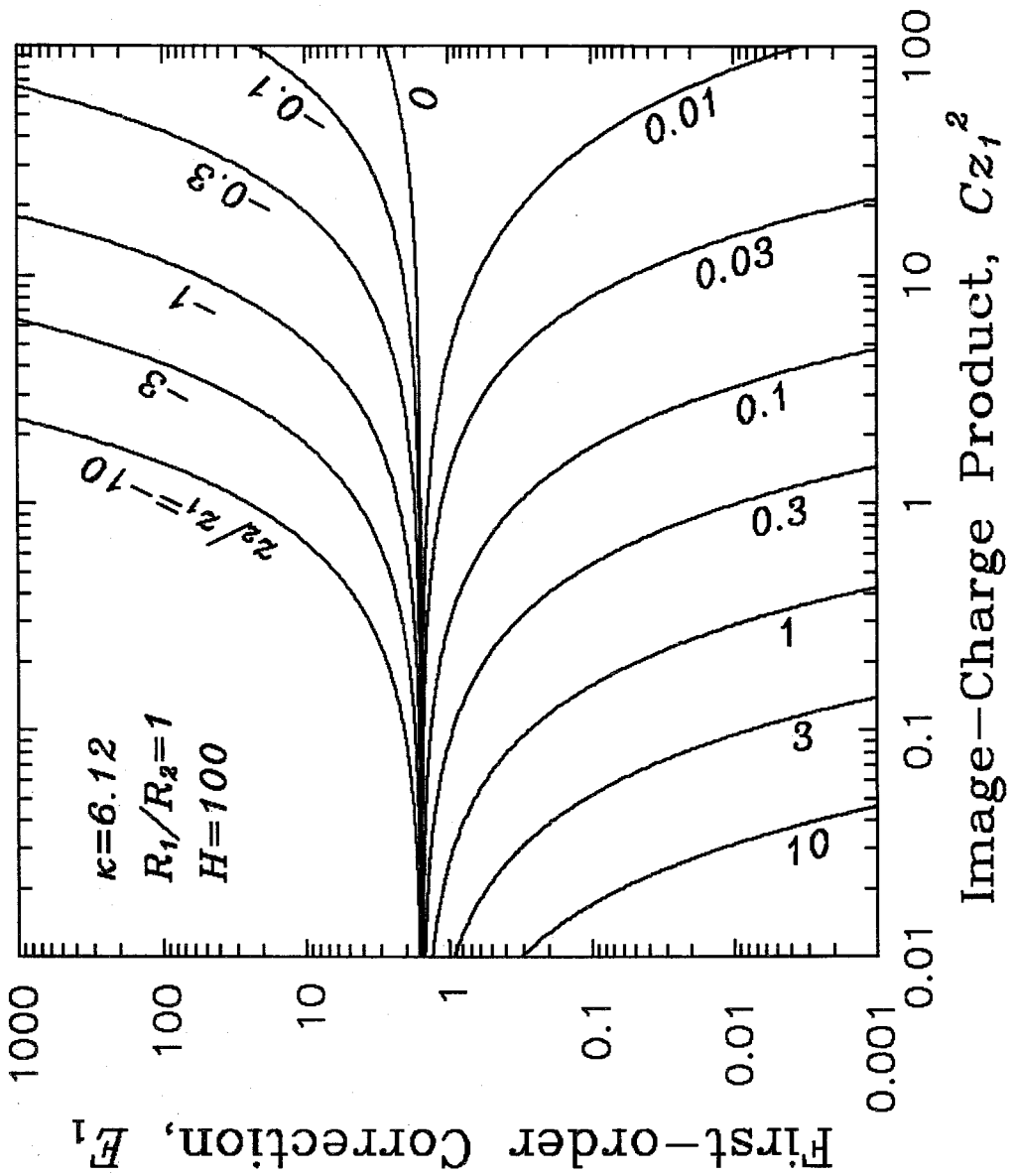


Figure 11b

## **CHAPTER 5**

# **IMAGE POTENTIAL BETWEEN A CHARGED PARTICLE AND AN UNCHARGED PARTICLE IN AEROSOL COAGULATION — ENHANCEMENT IN ALL SIZE REGIMES AND INTERPLAY WITH VAN DER WAALS FORCES**

**In cooperation with Dr. Kikuo Okuyama,  
University of Osaka Prefecture, Japan**

**Accepted for publication in  
Journal of Colloid and Interface Science, 1990**

## ABSTRACT

Coagulation between a charged particle and an uncharged particle arises in ionic aerosol clustering and in ion-induced nucleation. In this paper, we obtain an analytical expression for the image potential for situations of charged-uncharged particle coagulation. The interparticle coagulation rate enhancement in the presence of the newly-derived image potential over the entire range of Knudsen numbers is calculated. A simultaneous potential composed of the image potential and a van der Waals potential is subsequently considered. Conditions in which each of the component potentials predominates are determined.

## INTRODUCTION

Interactions between charged particles occur from Coulombic and electric image forces. If both forces exist simultaneously (*i.e.*, both particles are charged), the Coulombic force always plays a much more important role than the image force in the enhancement or retardation of the coagulation rate (1). This occurs because the Coulombic potential is linearly inversely proportional to the first power of the radial distance between two charges; the electric image potential in this case can be neglected. When only one of the colliding particles is charged, on the other hand, the Coulombic force does not exist and the electric image potential becomes a dominating factor in coagulation. Therefore, an accurate expression for the image potential in this situation is necessary; such an expression, however, has not been available in the literature.

The purpose of this paper is threefold. First, we obtain an exact expression for the electric image potential between a charged particle and an uncharged particle. Second, the interparticle coagulation rate enhancement in the presence of the electric image potential over the entire range of Knudsen numbers is calculated. The third goal is to consider simultaneous electrical image and van der Waals interactions; the latter is caused by attraction between momentary induced dipoles in both particles. We will calculate the coagulation rate enhancement in the simultaneous potential situation and determine the conditions under which each of the composite potentials predominates.

## THE CHARGED-UNCHARGED IMAGE POTENTIAL

In order to obtain the electric image potential between a charged particle and

an uncharged particle, let us first generalize the situation such that both particles may carry charges, then later we shall consider the case of the image potential between a pair of charged-uncharged particles. Let  $q_1$ ,  $R_1$ ,  $q_2$ , and  $R_2$  be the initial charge and radius of particles 1 and 2, respectively; also denote  $\kappa$  as the particle dielectric constant and  $r$  as the distance between the two particle centers. The image charge of  $q_2$  in particle 1 which is at a distance  $R_1^2/r$  from the center of particle 1 is (2, 3)

$$q_{1,i} = -\frac{\kappa - 1}{\kappa + 1} \frac{q_2 R_1}{r} \quad [1]$$

The image charge of  $q_1$  in particle 2 which is at a distance  $R_2^2/r$  from the center of particle 2 is

$$q_{2,i} = -\frac{\kappa - 1}{\kappa + 1} \frac{q_1 R_2}{r} \quad [2]$$

We assume that the higher order images (images of the image charges) are negligible in comparison to the first images, Eqs. [1] and [2]. The final total charges in each of the particles are therefore

$$z_1 e = q_1 + q_{1,i} = q_1 - \frac{\kappa - 1}{\kappa + 1} \frac{q_2 R_1}{r} \quad [3]$$

$$z_2 e = q_2 + q_{2,i} = q_2 - \frac{\kappa - 1}{\kappa + 1} \frac{q_1 R_2}{r} \quad [4]$$

where  $z_1$  and  $z_2$  are the number and sign of the total charge carried by particles 1 and 2, respectively, and  $e = 1.602 \times 10^{-19}$  C. Solving Eqs. [3] and [4] and expressing  $q_1$  and  $q_2$  in terms of  $z_1$  and  $z_2$ , one has

$$q_1 = \frac{z_1 e + z_2 e \left( \frac{\kappa - 1}{\kappa + 1} \right) \frac{R_1}{r}}{1 - \left( \frac{\kappa - 1}{\kappa + 1} \right)^2 \frac{R_1 R_2}{r^2}} \quad [5]$$

$$q_2 = \frac{z_2 e + z_1 e \left( \frac{\kappa - 1}{\kappa + 1} \right) \frac{R_2}{r}}{1 - \left( \frac{\kappa - 1}{\kappa + 1} \right)^2 \frac{R_1 R_2}{r^2}} \quad [6]$$

The electrical static forces are contributed by the Coulombic interactions between  $q_1$  and  $q_2$  ( $F_1$ ),  $q_1$  and  $q_{2,i}$  ( $F_2$ ),  $q_2$  and  $q_{1,i}$  ( $F_3$ ), and  $q_{1,i}$  and  $q_{2,i}$  ( $F_4$ ). We have

$$\begin{aligned} F_1 &= \frac{q_1 q_2}{4\pi\epsilon_0 r^2} & ; & & F_3 &= \frac{(q_2) \left( -\frac{\kappa - 1}{\kappa + 1} \frac{q_2 R_1}{r} \right)}{4\pi\epsilon_0 (r^2 - R_1^2)^2 / r^2} \\ F_2 &= \frac{(q_1) \left( -\frac{\kappa - 1}{\kappa + 1} \frac{q_1 R_2}{r} \right)}{4\pi\epsilon_0 (r^2 - R_2^2)^2 / r^2} & ; & & F_4 &= \frac{\left( \frac{\kappa - 1}{\kappa + 1} \right)^2 q_1 q_2 R_1 R_2 / r^2}{4\pi\epsilon_0 (r^2 - R_1^2 - R_2^2)^2 / r^2} \end{aligned} \quad [7]$$

where  $\epsilon_0$  is the permittivity of the background gas. We can nondimensionalize the force according to

$$\frac{(R_1 + R_2)}{kT} \sum_{i=1}^4 F_i \equiv M \sum_{i=1}^4 \mathcal{F}_i \quad [8]$$

where

$$M \equiv \frac{e^2}{4\pi\epsilon_0 kT (R_1 + R_2)} \quad [9]$$

and  $\mathcal{F}_i$  can be written as

$$\mathcal{F}_1 = k_1 k_2 x^2 \quad [10]$$

$$\mathcal{F}_2 = \frac{-p k_1^2 (1 - s) x^3}{[1 - (1 - s)^2 x^2]^2} \quad [11]$$

$$\mathcal{F}_3 = \frac{-p k_2^2 s x^3}{[1 - s^2 x^2]^2} \quad [12]$$

$$\mathcal{F}_4 = \frac{p^2 k_1 k_2 s (1 - s) x^4}{[1 - s^2 x^2 - (1 - s)^2 x^2]^2} \quad [13]$$

where

$$k_1 \equiv \frac{q_1}{e} ; \quad k_2 \equiv \frac{q_2}{e} ; \quad x \equiv \frac{R_1 + R_2}{r} ; \quad s \equiv \frac{R_1}{R_1 + R_2} ; \quad p \equiv \frac{\kappa - 1}{\kappa + 1} \quad [14]$$

The parameters in Eq. [14] stand for the number and sign of the initial charges in particles 1 and 2, the inverse of radial distance, the size ratio, and the rescaled dielectric constant, respectively.  $k_1$  and  $k_2$  in Eqs. [10]–[13], from Eqs. [5] and [6], can be expressed as follows:

$$\begin{aligned} k_1 &= \frac{z_1 + pz_2sx}{1 - p^2s(1-s)x^2} \\ k_2 &= \frac{z_2 + pz_1(1-s)x}{1 - p^2s(1-s)x^2} \end{aligned} \quad [15]$$

The dimensionless image potential  $\hat{\Phi}$  (i.e., the dimensional potential divided by  $kT$ ) is obtained by integrating the forces over the radial distance,

$$\hat{\Phi}(x) = -M \int_{x=0}^x \sum_{i=1}^4 \mathcal{F}_i d\left(\frac{1}{x}\right) \equiv \sum_{i=1}^4 \hat{\Phi}_i(x) \quad [16]$$

We now consider the situation that one of the particles (say, particle 2) is uncharged. Setting  $z_2 = 0$  in Eqs. [10]–[15] and integrating  $\mathcal{F}_i$  according to Eq. [16], the components of the dimensionless image potential are

$$\hat{\Phi}_1(x) = \frac{aMx^2}{2(1-bx^2)} \quad [17]$$

$$\hat{\Phi}_2(x) = \begin{cases} -\frac{aM}{2(b-c)^2} \left[ \frac{b^2x^2}{1-bx^2} + \frac{c^2x^2}{1-cx^2} \right] + \frac{abcM}{(b-c)^3} \ln\left(\frac{1-cx^2}{1-bx^2}\right), & (\text{if } b \neq c) \\ \frac{aM}{6b} \left[ 1 - \frac{1}{(1-bx^2)^3} \right], & (\text{if } b = c) \end{cases} \quad [18]$$

$$\hat{\Phi}_3(x) = \begin{cases} -\frac{aM}{2(b-\alpha_3)^2} \left[ \frac{b^2x^2}{1-bx^2} + \frac{bx^2\alpha_3}{1-\alpha_3x^2} \right] + M \left( \frac{ab^2 + ab\alpha_3}{2(b-\alpha_3)^3} \right) \ln\left(\frac{1-\alpha_3x^2}{1-bx^2}\right), & (\text{if } b \neq \alpha_3) \\ \frac{aM}{12b} \left[ \frac{3bx^2 - 1}{(bx^2 - 1)^3} - 1 \right], & (\text{if } b = \alpha_3) \end{cases} \quad [19]$$

$$\hat{\Phi}_4(x) = \begin{cases} \frac{aM}{2(b-\alpha_4)^2} \left[ \frac{b^2x^2}{1-bx^2} + \frac{bx^2\alpha_4}{1-\alpha_4x^2} \right] - M \left( \frac{ab^2 + ab\alpha_4}{2(b-\alpha_4)^3} \right) \ln\left(\frac{1-\alpha_4x^2}{1-bx^2}\right), & (\text{if } b \neq \alpha_4) \\ \frac{aM}{12b} \left[ 1 - \frac{3bx^2 - 1}{(bx^2 - 1)^3} \right], & (\text{if } b = \alpha_4) \end{cases} \quad [20]$$

where

$$\begin{aligned} a &\equiv pz_1^2(1-s) & ; & & \alpha_3 &\equiv s^2 \\ b &\equiv p^2s(1-s) & ; & & \alpha_4 &\equiv s^2 + (1-s)^2 = \alpha_3 + c \\ c &\equiv (1-s)^2 \end{aligned} \quad [21]$$

and  $M$  is given by Eq. [9]. The total dimensionless potential is the sum of the right hand sides of Eqs. [17]–[20].

For an ionic charging situation (*i.e.*, one of the particles is an ion with much smaller size than the other), one can set  $R_1 = R_{\text{ion}} = 0$ ,  $R_2 = R_p$ ,  $z_2 = 0$ , and  $z_1 = z_{\text{ion}} = \pm 1$ . In this case,  $b$  in Eq. [21] is zero because  $s$  (Eq. [14]) is zero, and the sum of the right-hand sides of Eqs. [17]–[20] becomes

$$\hat{\Phi}(x) = -\frac{acMx^4}{2(1-cx^2)} = -\frac{\kappa-1}{\kappa+1} \frac{e^2}{8\pi\epsilon_0 kT} \left[ \frac{R_2^2}{(r^2 - R_2^2)r^2} \right] \quad [22]$$

which is the classical ion-particle image potential (3, 4).

Figure 1 shows the total dimensionless potential (sum of the right-hand sides of Eqs. [17]–[20]) divided by  $M$  as a function of the dimensionless radial distance,  $1/x$ , when  $z_1^2 = 1$  (*i.e.*, the ionic aerosol (particle 1) is assumed to carry a unit charge). Three values of the particle dielectric constant are used in the figure. We note that the higher the dielectric constant, the larger the image charge and the stronger the image potential. For a situation that  $R_1$  is much larger than  $R_2$ , we expect that the image potential is weaker because the charge  $z_1$  in particle 1 will have a negligible image in particle 2. On the other hand, if  $R_1$  is much smaller than  $R_2$ , the image potential is stronger. This fact is shown by the comparison of dashed lines and solid lines in Figure 1; the dashed lines, which correspond to



$s = 0.1$ , *i.e.*,  $R_1/R_2 = 1/9$ , represent stronger potentials than the solid lines, which correspond to  $s = 0.3$ , or  $R_1/R_2 = 3/7$ .

For a finite value of  $s$  (colliding particles are of comparable sizes), from either of the right-hand sides of Eqs. [17]–[19] or from Figure 1, one finds the following image potential properties:  $\hat{\Phi}(1)$ =finite,  $d\hat{\Phi}/dx \leq 0$ , and  $d\hat{\Phi}/d^2x \geq 0$ . In other words, the predicted image potential is monotonically attractive but finite at the two-particle contact.

## IMAGE POTENTIAL ENHANCEMENT

The attractive image potential can enhance the interparticle coagulation rate. In this section, we will evaluate the enhancement over the entire range of Knudsen numbers. The coagulation enhancement in both the infinity and zero Knudsen number situations will be first discussed.

In the free-molecule regime ( $\text{Kn} \rightarrow \infty$ ), Marlow (5) proposed an enhancement expression for singular monotonic attractive potential. Marlow's method was pursued by Huang *et al.* (1) for situations involving nonmonotonic potential. Amadon and Marlow (6), on the other hand, considered monotonic nonsingular attractive potential situations (that is, the potential is finite at the particle contact, an example of which is the charged-uncharged image potential of the present paper). The expression of Amadon and Marlow (6) for the free-molecule regime enhancement can be written as

$$E^{\text{fm}} = \frac{1}{2} \int_1^0 \frac{1}{x^2} \frac{d}{dx} \left( x \frac{d\hat{\Phi}(x)}{dx} \right) \exp \left[ \frac{x}{2} \frac{d\hat{\Phi}(x)}{dx} - \hat{\Phi}(x) \right] dx + \exp \left[ \frac{1}{2} \frac{d\hat{\Phi}(x)}{dx} \Big|_{x=1} - \hat{\Phi}(1) \right] \quad [23]$$

In the continuum regime ( $Kn \rightarrow 0$ ) the enhancement expression can be obtained from continuum transport theory (see, for example, (7)). If one assumes that the continuum transport is valid up to a distance  $\lambda$ , which is of order of one particle mean free path from the two-particle contact, the continuum regime enhancement factor can be written as

$$E^c = \left[ (1+g) \int_0^{1/(1+g)} \exp[\hat{\Phi}(x)] dx \right]^{-1} \quad [24]$$

where  $g = \lambda / (R_1 + R_2)$ . The Fuchs flux-matching expression that predicts the coagulation rate over the entire size regime in the presence of an interparticle potential is (4)

$$\frac{K}{\pi R^2 \bar{c}} = \frac{E^{fm} E^c}{E^c \exp\left[\hat{\Phi}\left(\frac{1}{1+g}\right)\right] + E^{fm} \frac{R\bar{c}}{4D} \frac{1}{(1+g)}} \quad [25]$$

where  $K$  is the coagulation rate coefficient ( $\text{cm}^3\text{s}^{-1}$ ),  $R = R_1 + R_2$ , and  $\bar{c} = [8kT(m_1 + m_2)/\pi m_1 m_2]^{0.5}$  is the two-particle mean thermal speed.

The overall enhancement factor expression can be found by dividing the rate expression of Eq. [25] by its potential-free limit,

$$E^{\text{overall}} = \frac{K}{K(\hat{\Phi} = 0)} = \frac{[4\beta g(1+g) + 1] E^{fm} E^c}{E^{fm} + 4\beta g(1+g) \exp\left[\hat{\Phi}\left(\frac{1}{1+g}\right)\right] E^c} \quad [26]$$

where

$$\beta = \frac{D}{R\bar{c}g} = \frac{D}{\bar{c}\lambda} \quad [27]$$

We will calculate the overall coagulation enhancement due to the image attraction according to Eq. [26]. To a first approximation, we assume that the matching

distance in the Fuchs method,  $\lambda$ , is the same as the particle mean free path,  $\lambda_p$ , or

$$g \approx \text{Kn} \quad [28]$$

where  $\text{Kn} = \lambda_p / (R_1 + R_2)$  is the two-particle Knudsen number. Huang and Seinfeld (8) showed the second-order Chapman-Enskog solution of the Boltzmann equation that gives a complicated relation between the diffusivity and the particle mean free path from which the value of  $\beta$  in Eq. [27] can be evaluated. On the other hand, the so-called zeroth-order kinetic theory of gases (9) gives a much simpler result which we will use in the present calculation for illustration,

$$\beta = \frac{1}{3} \quad [29]$$

The parameter  $M$  given by Eq. [9] is a function of the Knudsen number,

$$M = \gamma \text{Kn} ; \quad \gamma \equiv \frac{e^2}{4\pi\epsilon_0 k T \lambda_p} \quad [30]$$

For situations that the particle mean free path  $\lambda_p = 0.065\mu\text{m}$ ,  $\gamma = 0.862$  when  $T = 25^\circ\text{C}$  and 0.941 when  $T = 0^\circ\text{C}$ .

Figure 2 shows the calculated overall enhancement, Eq. [26], as a function of the Knudsen number,  $\text{Kn}$ . The conditions are  $M = 0.862\text{Kn}$ , and  $z_1 = \pm 1$ . We notice that the smaller the value of particle size ratio  $s$ , the stronger the potential (see Figure 1), and the higher the enhancement of coagulation. For a constant value of  $s$ , one finds that the higher the value of  $p$ , the stronger the particle dielectric constant, the higher the image enhancement. Free-molecule regime particle coagulation, from Figure 2, always exhibits higher image enhancement than that in the continuum regime because the image strength  $M$  is linearly proportional to the Knudsen number (Eq. [30]).

Figure 3 shows the overall coagulation enhancement due to either the particle charge  $z_1$  or the temperature variation for equal-sized particle coagulation ( $s = 0.5$ ).  $p$  in Eq. [14] is taken as 0.7, which corresponds to  $\kappa = 5.67$ , a typical dielectric constant for salt particles. Because the coagulation rate at a lower temperature is smaller than that at a higher temperature, the lower temperature coagulation rate is expected to be more easily enhanced in the presence of an image potential than at higher temperatures. One finds in Figure 3 that the lower temperature dashed lines exhibit higher enhancement values than the corresponding higher temperature solid lines. For a constant temperature, we notice that the higher the particle charge  $|z_1|$ , the stronger the attractive force (see Eq. [21],  $a$  is proportional to  $z_1^2$  regardless of the sign of the charge), and the higher the overall enhancement.

## INTERPLAY WITH VAN DER WAALS POTENTIAL

In this section, we consider a simultaneous interparticle image and van der Waals potential. The nonretarded Hamaker formula for the van der Waals potential obtained by the pairwise interaction approximation (10) will be used in the calculation. Particles that fall in the continuum-transition regime (*e.g.*, particles of diameters greater than 20 nm at 1 atm) may experience viscous force or van der Waals retardation which may reduce the van der Waals attraction strength (11, 12). We do not consider these effects for simplicity. One purpose of the present calculation is to find a critical Knudsen number larger than that at which the van der Waals potential is insignificant; in this regard, one wants to use the nonretarded van der Waals expression to ensure that van der Waals force can be safely omitted for particles of sizes smaller than that of the calculated critical Knudsen number.

The nonretarded Hamaker formula for van der Waals potential can be written as (1, 10)

$$\hat{\Phi}(x)^{\text{vdw}} = -\frac{H}{6} \left\{ \frac{2s(1-s)x^2}{1-x^2} + \frac{2s(1-s)x^2}{1-(2s-1)x^2} + \ln\left(\frac{1-x^2}{1-(2s-1)x^2}\right) \right\} \quad [31]$$

where  $H$  is the dimensionless Hamaker constant, the ratio of the dimensional Hamaker constant to  $kT$ . A simultaneous potential considered is the sum of the right-hand sides of Eq. [31] and of Eqs. [17]–[20]. To calculate the overall enhancement, one again needs to evaluate  $E^c$  and  $E^{\text{fm}}$  first and then use the Fuchs flux-matching formula, Eq. [25]. The second term in Eq. [23], the Amadon-Marlow free-molecule enhancement expression, is zero for the present situation of a simultaneous potential because the van der Waals potential, Eq. [31], is always singular at the two-particle contact.

Figures 4a and 4b show the overall enhancement as a function of the Knudsen number  $\text{Kn}$ , size ratio  $s$ , and the dimensionless Hamaker constant  $H$  for situations that  $\gamma = 0.862$  (Eq. [30]) and  $z_1 = \pm 1$  for  $p = 0.7$  and  $p = 1$ , respectively. Both figures show that for small  $\text{Kn}$  the van der Waals potential is always important because the image potential diminishes. van der Waals interaction enhancement becomes insignificant for  $\text{Kn} \geq 10$  of the  $s = 0.1$  situation; for  $s = 0.5$ , on the other hand, the van der Waals force is important over the entire range of Knudsen numbers. The reason is that  $s = 0.1$  represents a stronger image potential than the  $s = 0.5$  case, and in consequence, image enhancement in the  $s = 0.1$  situation can dominate the van der Waals enhancement at large  $\text{Kn}$ . One notices that the higher the Hamaker constant  $H$ , the stronger the van der Waals attraction, and the higher the enhancement. By comparing Figures 4a and 4b, we find that a larger  $p$  value (which represents a larger dielectric constant case) causes higher enhancement in large  $\text{Kn}$  regimes because the image attraction is stronger; the

variation of enhancement due to an increase in  $p$  is less significant in the small Knudsen number regime where van der Waals force predominates over the image attraction.

In Figures 4a and 4b, for a given size ratio  $s$ , the enhancement curves for three different values of Hamaker constants tend to merge at a given Knudsen number, which we shall refer to as the “critical Knudsen number,”  $\text{Kn}^c$ . For Knudsen numbers larger than  $\text{Kn}^c$ , one can conclude that the van der Waals potential effect is not important and the image potential predominates. On the other hand, for  $\text{Kn} < \text{Kn}^c$  the van der Waals force gradually takes over the importance in coagulation enhancement. The critical Knudsen number for a given set of conditions is determined as the point where the value of the overall coagulation rate enhancement with a van der Waals Hamaker constant  $H = 100$  differs from the overall enhancement value of a pure image potential situation by 1%. In other words, the presence of a strong van der Waals potential with  $H = 100$  at  $\text{Kn}^c$  has a negligible effect in enhancing the coagulation rate, *i.e.*, 1%, in comparison to its image potential counterpart.

Figure 5 shows the critical Knudsen number as a function of particle size ratio  $s$  at  $M = 0.862\text{Kn}$ . One notices that the higher the  $|z_1|$  value, the stronger the image potential and the larger size regime that the image force can predominate. For the same reason, the dashed lines ( $p = 1$ ) representing a stronger image potential are below the corresponding solid lines ( $p = 0.5$ ). In Figure 5, if the condition falls into the upper-left region (*i.e.*, smaller  $s$  and  $\text{Kn} > \text{Kn}^c$ ) the van der Waals potential can be neglected. The correctness of the region so found is ensured because, as mentioned earlier in this section, the van der Waals retardation and the hydrodynamic viscous effects that may reduce the van der Waals strength are not considered.

## SUMMARY AND CONCLUSION

In this paper, we have derived an analytical expression for the image potential between a charged particle and an uncharged particle. The coagulation enhancement due to the charged-uncharged potential is subsequently determined for various given sets of conditions over the entire range of Knudsen numbers. We find that in the free-molecule regime, the coagulation enhancement can be exponentially increased by the image attraction as both particle sizes decrease. The particle size ratio, dielectric constant, charges, and temperature are all influential factors in the determination of coagulation enhancement.

The nonretarded van der Waals potential is also considered together with the charged-uncharged image potential in order to determine conditions where each of the component potentials predominates. We found that the image potential overwhelms the van der Waals potential for situations when the charged particle is much smaller than the uncharged particle and both particles should be significantly small (a critical Knudsen number is therefore determined). An example of the latter situation is the charging of a neutral particle by a molecular ion. In ion-induced nucleation, on the other hand, the charged particle is an ionic molecular cluster and the uncharged particle is a molecule; both particles are of similar free-molecule sizes. In this situation, the van der Waals force can be as important as the image force.

## ACKNOWLEDGEMENTS

This work is supported by National Science Foundation Grant ATM-8503103.

## REFERENCES

1. Huang, D. D., Seinfeld, J. H., and Marlow, W. H., *J. Colloid Interf. Sci.* (accepted), Manuscript #8437.
2. Smythe, W. R., "Static and Dynamic Electricity," 3rd Ed., Chapt. 5. McGraw-Hill, 1968.
3. Maxwell, J. C., "A Treatise on Electricity and Magnetism," Vol. I, Chapt. 11. Academic Reprints, Stanford, California, 1953.
4. Fuchs, N. A., *Geofis. Pura Appl.* **56**, 185 (1963).
5. Marlow, W. H., *J. Chem. Phys.* **73**, 6284 (1980).
6. Amadon, A. S., and Marlow, W. H., *J. Chem. Phys.* (submitted).
7. Seinfeld, J. H., "Atmospheric Chemistry and Physics of Air Pollution," p. 402. Wiley, New York, 1986.
8. Huang, D. D., and Seinfeld, J. H., *J. Colloid and Interf. Sci.* **125**, 733 (1988).
9. McQuarrie, D. A., "Statistical Mechanics," p. 363. Harper & Row, New York, 1976.
10. Hamaker, H. C., *Physica* **4**, 1058 (1937).
11. Marlow, W. H., *J. Chem. Phys.* **73**, 6288 (1980).
12. Alam, M. K., *Aerosol Sci. Technol.* **6**, 41 (1987).



## LIST OF FIGURES

- Figure 1. Rescaled charged-uncharged image potential,  $\hat{\Phi}(x)/M$ , as a function of the dimensionless radial distance,  $1/x$ , the particle dielectric constant, and the particle size ratio.
- Figure 2. Coagulation rate enhancement as a function of the Knudsen number,  $Kn$ , the particle dielectric constant, and the particle size ratio.
- Figure 3. Coagulation rate enhancement as a function of the Knudsen number,  $Kn$ , the particle charges, and the temperature.
- Figure 4. Coagulation rate enhancement as a function of the Knudsen number,  $Kn$ , the dimensionless Hamaker constant, and the particle size ratio in the presence of a combined charged-uncharged image and van der Waals potential. (a)  $p = 0.7$ ; (b)  $p = 1$ .
- Figure 5. Critical Knudsen Number,  $Kn^c$ , as a function of the particle size ratio, particle charges, and the particle dielectric constant.

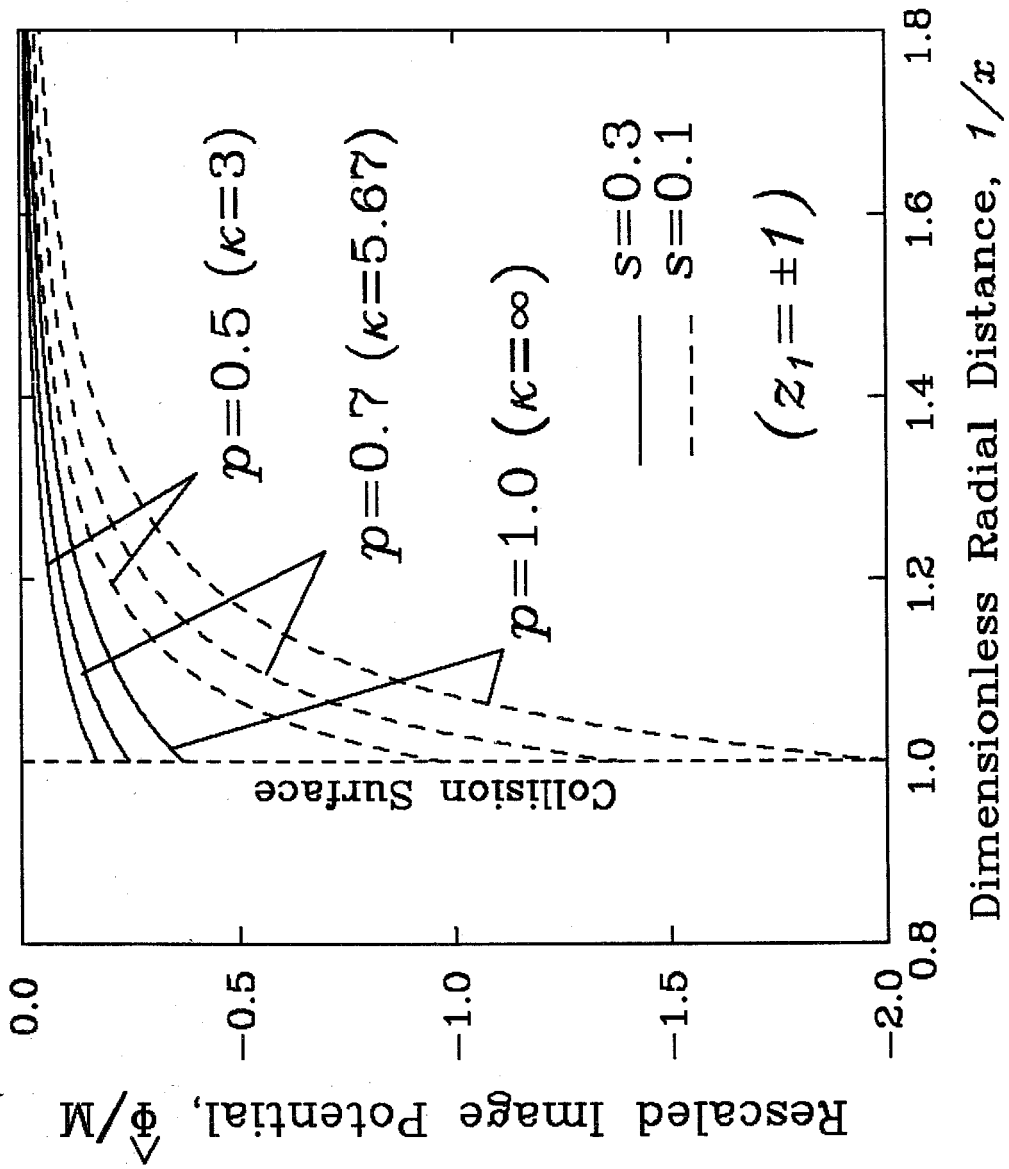


Figure 1

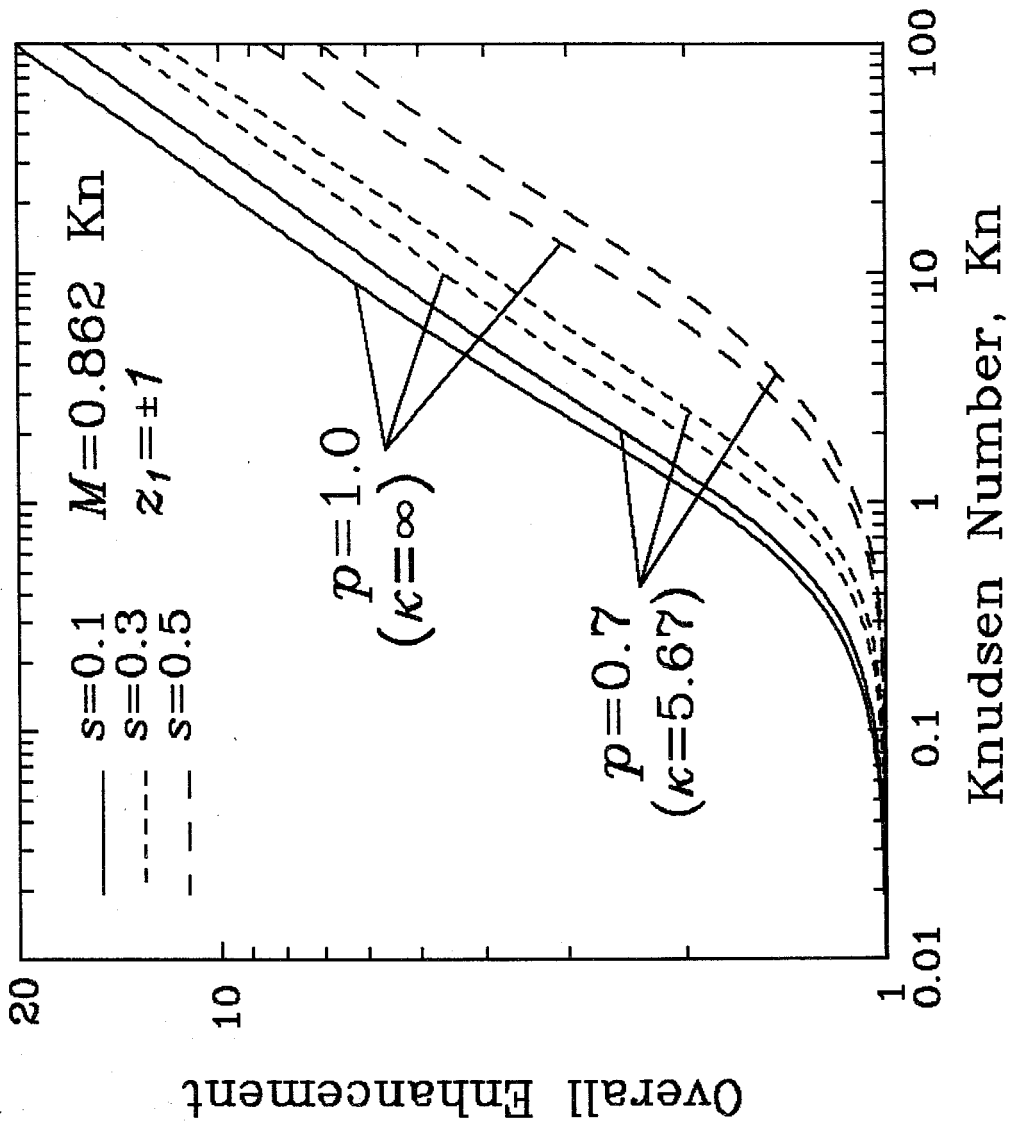


Figure 2

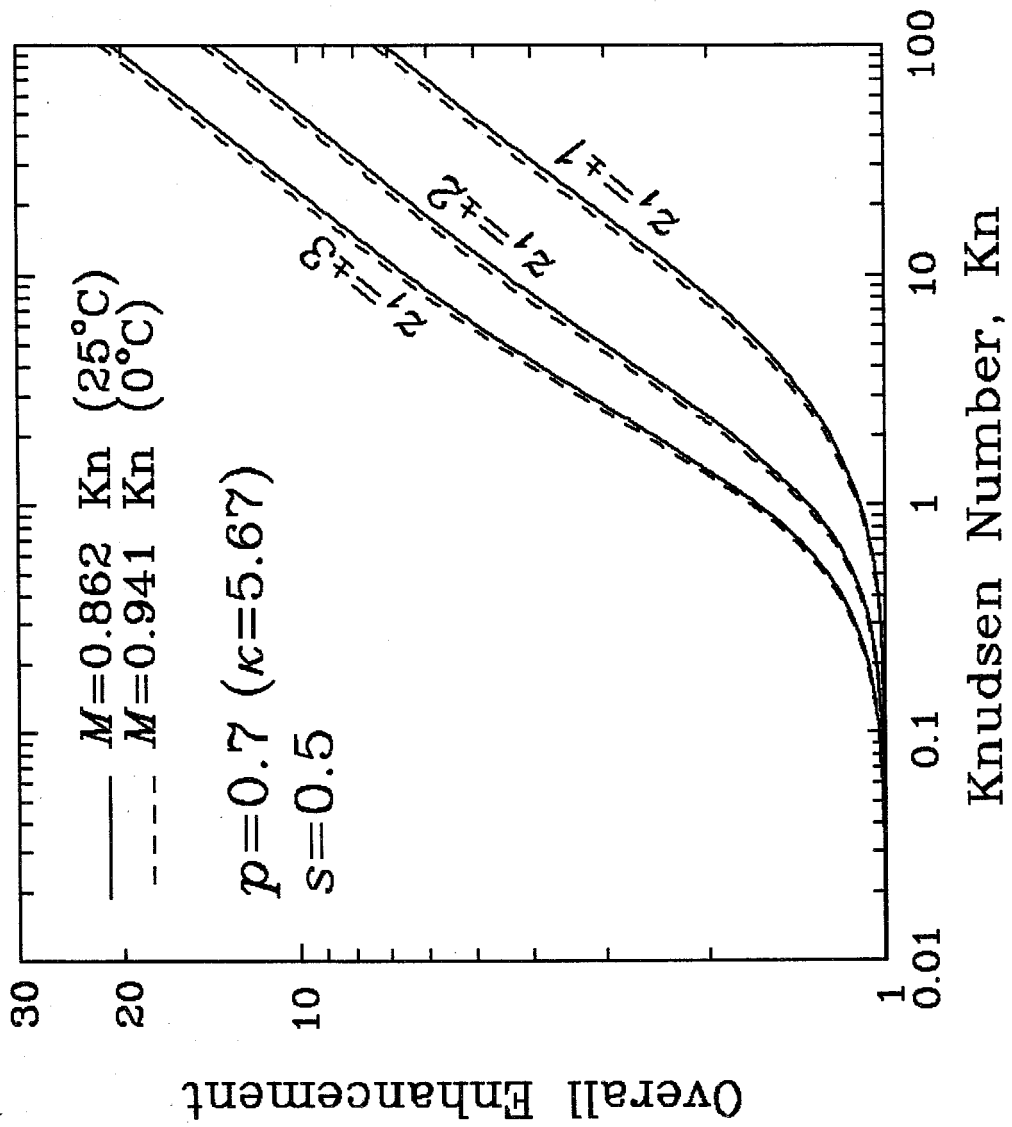


Figure 3

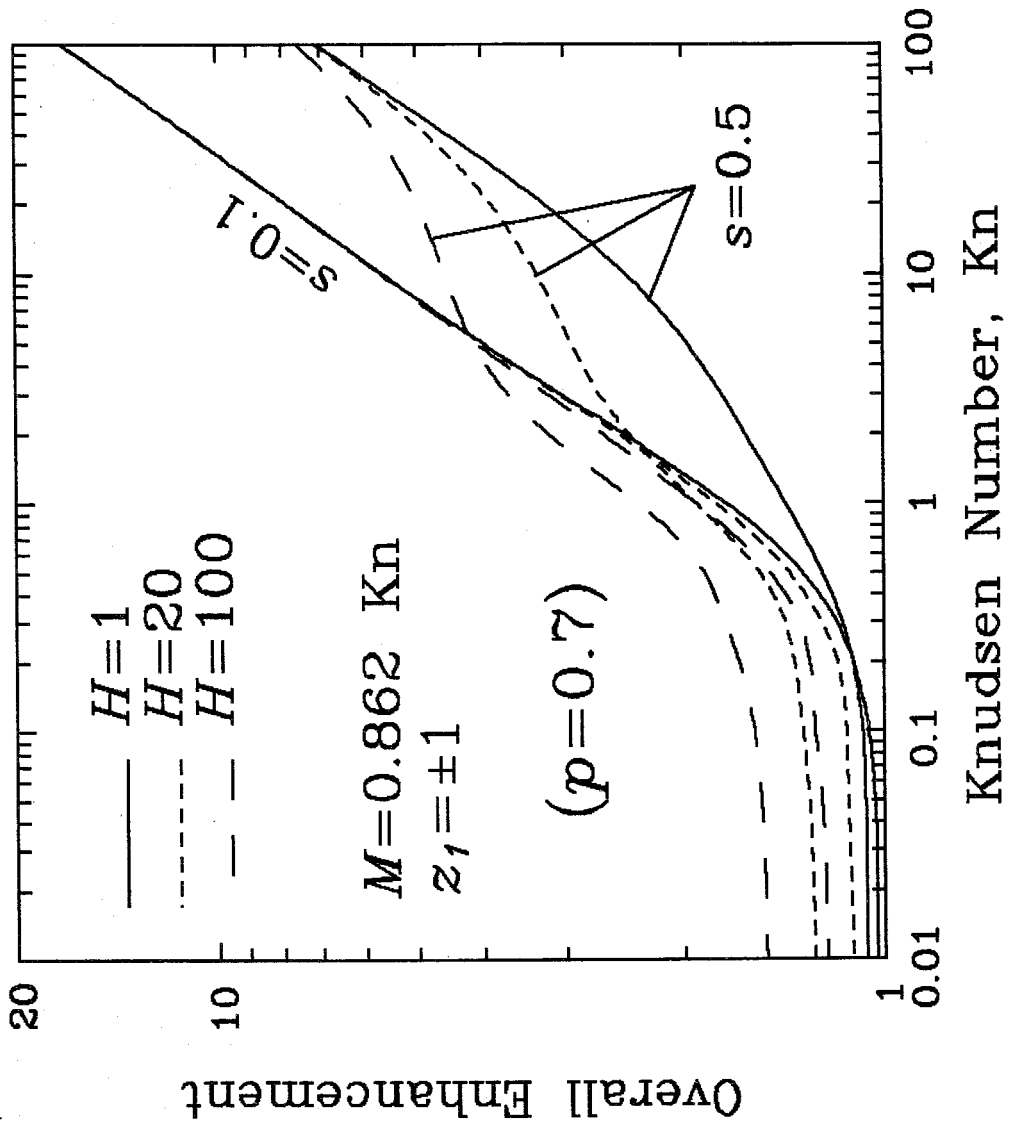


Figure 4a

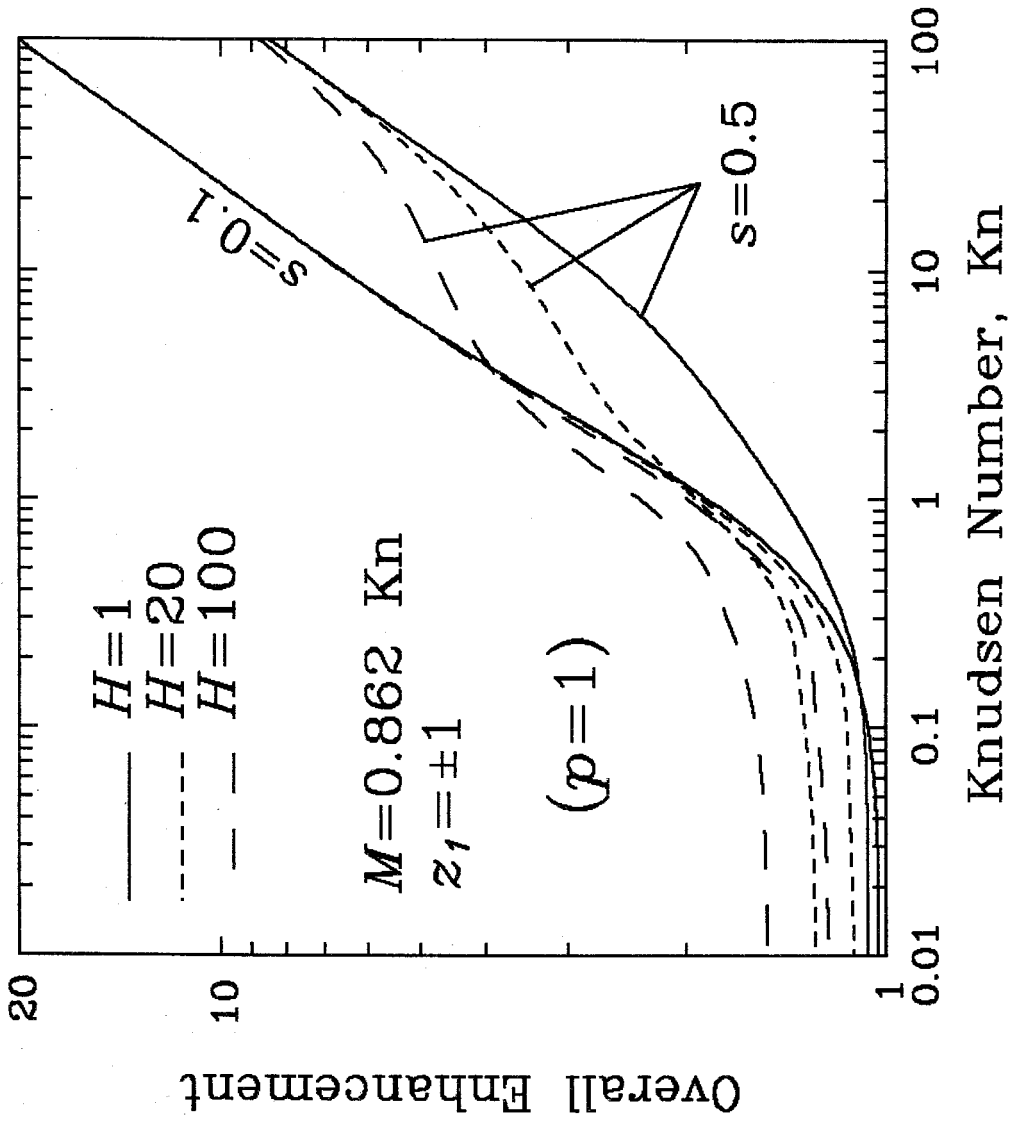


Figure 4b

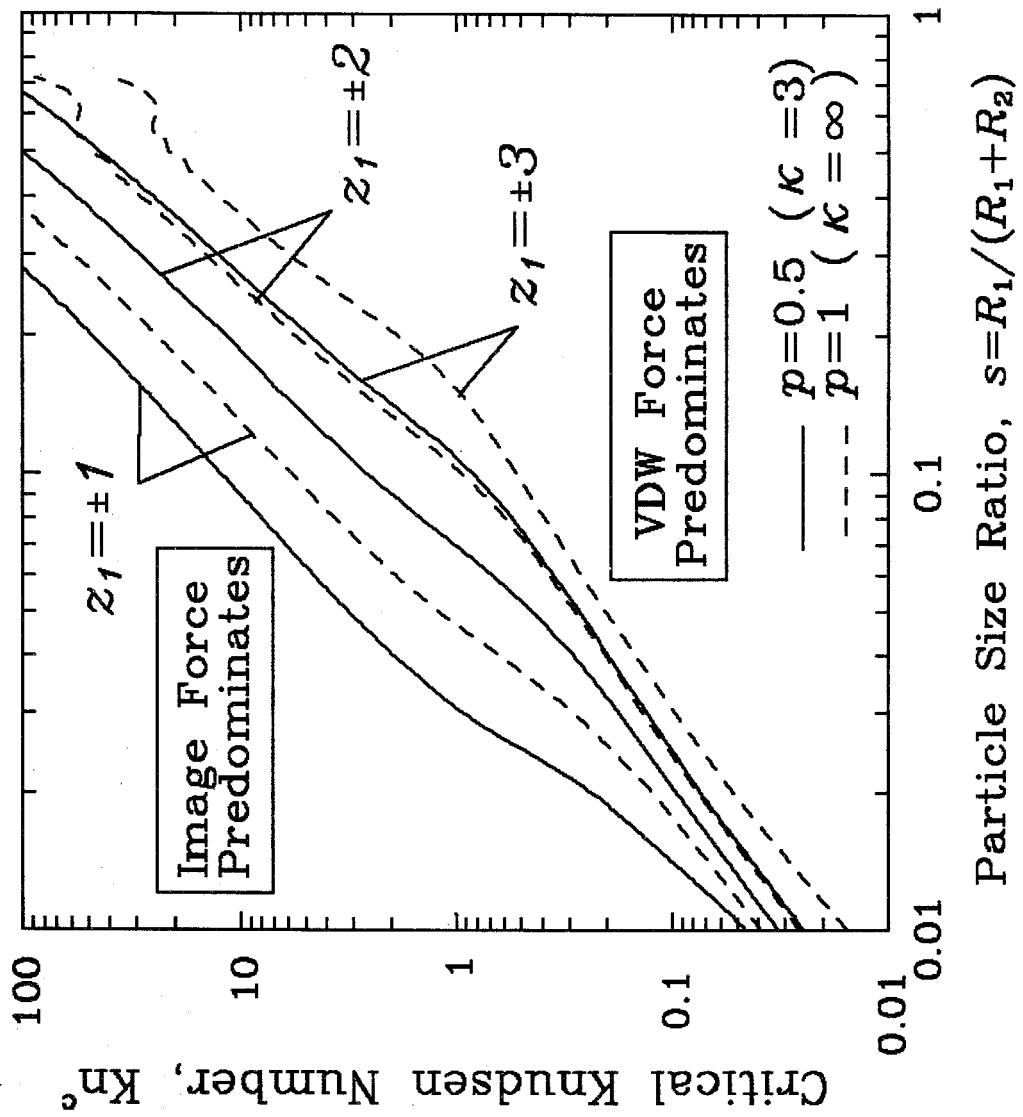


Figure 5

## **CHAPTER 6**

# **AEROSOL FORMATION BY RAPID NUCLEATION IN THE PREPARATION OF $\text{SiO}_2$ THIN FILM FROM $\text{SiCl}_4$ AND $\text{O}_2$ GASES USING THE CVD PROCESS**

**In cooperation with Dr. Kikuo Okuyama,  
University of Osaka Prefecture, Japan**

**Accepted for publication in  
Chemical Engineering Science, 1990**



## ABSTRACT

The formation of aerosol particles and molecular clusters by rapid nucleation in the semiconductor thin film preparation process by Atmospheric Pressure Chemical Vapor Deposition (APCVD) or Low Pressure Chemical Vapor Deposition (LPCVD) is evaluated by a vapor coagulation and diffusion model. Such a model is applicable for situations of a very high saturation ratio in which the evaporation of monomers from clusters is insignificant when compared with growth by coagulation. The physical processes accounted for include simultaneous generation of vapor monomer by chemical reaction, aerosol coagulation, and convective diffusion of various species to the thin film surface.  $\text{SiO}_2$  thin film preparation by thermal decomposition of  $\text{SiCl}_4$  vapor in  $\text{O}_2$  gas in a horizontal-type CVD reactor is simulated as an illustration of the model. The mass and number concentrations of various species are computed as functions of temperature, pressure, input  $\text{SiCl}_4$  concentration, and position in the reactor; and the individual contributions of monomers, clusters, and particles to the thin film growth rate are evaluated. Based on two dimensionless parameters representing the relative importance of the diffusive deposition of monomers to their generation and coagulation, the most suitable conditions where the thin film growth is dominated by monomer diffusive deposition are clarified.

## INTRODUCTION

Preparation of thin semiconductive films is accomplished by the Chemical Vapor Deposition (CVD) technique. In the CVD process, a feed source gas is first thermally decomposed by heat or plasma, and then the decomposed product diffuses onto the substrate to form a thin film. Accordingly, the growth rate and the uniformity of the thin film depend greatly on the source gas concentration, temperature and velocity profiles, operating pressure, shape of the reactor, and the carrier gas. In addition, the thin film surface morphology is quite sensitive to the operating conditions; for example, the film smoothness tends to degrade with an increase of substrate temperature or input source gas concentration. The formation of rough surfaces is often assumed to be caused by a two-dimensional surface nucleation on the thin film. An alternative cause of the surface roughness, as we will point out throughout this work, is a result of the formation of aerosol clusters and particles in the gas phase.

Vapor molecules, or monomers, which are formed by the thermal decomposition of the feed source gas, may nucleate homogeneously into clusters, which may subsequently grow to form aerosol particles. Diffusive deposition of the aerosol particles not only influences the growth rate and thickness of the film but also increases the surface roughness owing to the particles' extraordinarily large size in comparison to that of the monomers. Moreover, generated particles can be captured continuously at the reactor wall surface to form dendrites, which can be reentrained by a small vibration or the gas flow to contaminate the thin film.

Studying the effect of particle generation by gas-phase nucleation on the thin film growth is the subject of the present work. Previous simulations of CVD thin film growth have not considered gas-phase nucleation. It is generally assumed

that the decomposed vapor concentration is sufficiently low such that gas-phase nucleation and the subsequent particle formation are unimportant. As we will show later in this paper, the omission of the consideration of particle formation may cause serious errors in the evaluation of the thin film growth rate.

Okuyama *et al.* (1) evaluated the formation of Gallium Arsenide particles in the gas phase in the preparation of GaAs thin film by the Metal Organic Chemical Vapor Deposition (MOCVD) method to demonstrate the particle generation effect on the thin film growth. In that work a model was used that includes simultaneous generation of monomers by thermal decomposition of feed source gas, homogeneous nucleation (monomer-monomer and monomer-cluster coagulation and dissociation), monomer-to-particle condensation, particle-particle coagulation, and diffusive deposition to the thin film surface. Classical nucleation theory based on the liquid droplet model was used because the nucleated Ga clusters and particles are liquids and because the saturation ratio is relatively low and the number of monomers in the critical drop is relatively high.

Classical homogeneous nucleation theory is not applicable when the system saturation ratio is extraordinarily high and the number of monomers in the critical cluster is small. Clusters coagulate with monomers to form larger clusters much faster than these clusters can dissociate, so that the evaporation or dissociation processes in the classical homogeneous nucleation theory can be ignored. Such a homogeneous nucleation is called "rapid nucleation" (2). Thin films such as Si and SiO<sub>2</sub> produced by CVD are examples where the rapid nucleation concept is applicable. The vapor pressures of Si and SiO<sub>2</sub> are extremely low and their clusters are in the solid state. The evaporation of Si or SiO<sub>2</sub> monomers from clusters is negligible and monomer-cluster collisions are the dominant process in nucleation.

Particle formation in CVD reactors has been observed experimentally by Eversteijn (3), Ban and Gilbert (4), and Van der Brekel and Bollen (5) in the preparation of silicon film from  $\text{SiH}_4$  gas or  $\text{SiCl}_4$  gas. The appearance of large clusters or particles in the gas phase, which is called "snow formation," is detrimental to CVD processes where smooth solid films are desired. In the above work, a theoretical analysis was not undertaken to explain the snow formation phenomenon.

Weling (6) theoretically evaluated the growth rate of  $\text{SiO}_2$  film from  $\text{SiCl}_4$  and  $\text{O}_2$  gases in Plasma-activated Chemical Vapor Deposition (PCVD) by analytically solving the convective diffusion equation without considering cluster and particle generation in the gas phase. Weling's predictions were in good agreement with experimental observations for a pressure of 6 Torr. The amount of silica, which deposits on the reactor wall, was evaluated only by the monomer diffusive flux, not by the cluster diffusive flux. Jensen and Graves (7), Joshi (8) and Wilke *et al.* (9) studied the growth rate of Si or  $\text{SiO}_2$  films from  $\text{SiH}_4$  or  $\text{SiCl}_4$  gas in the Low Pressure CVD (LPCVD) process. These authors also did not consider the effect of gas-phase nucleation because of the low concentration of feed gas and low pressure inside the reactor. For the Atmospheric Pressure CVD (APCVD) situations, Kim and Pratsinis (10) analyzed the growth rate of silica film by solving the convective diffusion equation in the presence of aerosol particle generation. This study indicated the importance of particle formation in the thin film preparation process. The aerosol size distribution above the monomer was assumed to be log-normal, and molecular cluster dynamics were not considered.

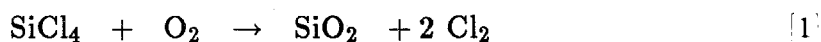
The contribution of particle formation by gas-phase rapid nucleation in the preparation of  $\text{SiO}_2$  film from  $\text{SiCl}_4$  and  $\text{O}_2$  gases by APCVD and LPCVD methods is analyzed in the present paper. We use a vapor coagulation and diffusion model, in which the size spectrum is composed of both clusters and particles.

The clusters are considered to be of sizes from monomer to  $k$ -mer ( $k$  monomers). Clusters that are larger than the  $k$ -mers are considered to be particles. The following physical processes are considered: monomer-monomer, monomer-cluster, monomer-particle, cluster-cluster, cluster-particle, and particle-particle coagulations. We shall investigate those operating conditions under which only the  $\text{SiO}_2$  monomer diffusive deposition is important in preparing  $\text{SiO}_2$  thin film.

## PREPARATION OF THIN FILM BY CVD PROCESS

Although various types of reactors are used in the formation of thin film by CVD, representative reactors are classified into horizontal, vertical and barrel types (11). We consider the simplest horizontal-type reactor, as shown in Figure 1a, in the present simulation. In the reactor, there exist two typical types of temperature profiles: a uniform temperature achieved by heating both reactor walls, and a linear temperature profile achieved by heating one reactor wall. When both top and bottom walls are heated, the temperature becomes uniform inside the reactor, and thin films can be formed on both walls as shown in Figure 1b. The situation treated in the present study is also attained in the plasma CVD process. If either top or bottom wall is heated, vapor is thermally decomposed within the linear temperature profile and the thin film is mainly produced on the heated substrate. This situation is also attained in the laser-assisted CVD process.

For our analysis of thin film production by CVD, we consider the preparation of  $\text{SiO}_2$  thin film by the thermal decomposition of  $\text{SiCl}_4$  gas in  $\text{O}_2$  based on the reaction



Kinetics of the  $\text{SiCl}_4$  oxidation were studied by Powers (12). If  $N_v$ ,  $N_1$ , and  $N_{\text{O}_2}$  are the number concentrations of the  $\text{SiCl}_4$  vapor,  $\text{SiO}_2$  monomer, and  $\text{O}_2$  gas, respectively, the local rate of consumption of  $\text{SiCl}_4$  and the generation rate of  $\text{SiO}_2$  vapor was presented by Powers (12) as

$$-\frac{dN_v}{dt} = \frac{dN_1}{dt} = k_{1v}N_v + k_{2v}N_vN_{\text{O}_2}/N_{\text{AV}} \quad [2]$$

where  $k_{1v}$  and  $k_{2v}$  were reported by Powers (12) to have the forms ( $T$  in K):

$$k_{1v} = 1.7 \times 10^{14} \exp(-48400/T) \quad [\text{s}^{-1}] \quad [3]$$

$$k_{2v} = 3.1 \times 10^{19} \exp(-48400/T) \quad [\text{cm}^3\text{mol}^{-1}\text{s}^{-1}] \quad [4]$$

In the present work we will assume the kinetics are described by Eq. [2].

Figure 2 schematically indicates the physical situation of simultaneous generation of monomer  $\text{SiO}_2$ , rapid nucleation, monomer clustering, and the diffusion of all the species toward the thin film surface. We will focus on the simulation of these physical processes in the next section.

## SIMULATION OF AEROSOL EVOLUTION IN CVD REACTOR

In the chemical reaction of the  $\text{SiCl}_4$  and  $\text{O}_2$  gases, the  $\text{SiO}_2$  vapor produced can easily become highly saturated in the CVD reactor because of its extremely low saturation vapor pressure. Homogeneous nucleation of  $\text{SiO}_2$  vapor may therefore occur and form  $\text{SiO}_2$  clusters and particles. The melting point of bulk  $\text{SiO}_2$  is 1678 K, so  $\text{SiO}_2$  clusters and particles are solid-like. The monomer-monomer and monomer-cluster coagulation processes will overwhelm the reverse evaporation processes.

The kinetic behavior of monomers, clusters, and particles is often described by the General Dynamic Equation (GDE) (13, 14). Of various models based on the GDE reported in previous studies, the so-called "discrete-sectional" GDE (15) is the most appropriate approach to evaluate aerosol formation and growth under a high monomer generation rate condition (16). In the discrete-sectional GDE, the particle size spectrum is separated into two parts: (I) the smaller clusters represented by discrete sizes (*i.e.*, monomer, dimer, etc.) and (II) the larger particles represented in a continuous size regime. Whereas this discrete-sectional model provides a detailed representation for the evolution of the size spectrum, the computational demands may become severe in the cases of nonuniform temperature, concentration and gas velocity in the CVD reactor.

A model that considerably simplifies the discrete-sectional GDE was termed the Simplified Reaction and Coagulation model (SRC) (16), in which clusters in the discrete size spectrum are lumped into a single mode and particles in the continuous size spectrum are lumped into another single mode. The evolution of the total cluster or particle concentration can be evaluated by considering the inter-mode and intra-mode coagulations. As expected, this two-mode SRC model oversimplifies the evolution of clusters. Here the  $\text{SiO}_2$  monomer is of a high saturation ratio, and small clusters (*e.g.*, dimer, trimer, etc.) that result from the monomer clustering become significant. It is necessary, therefore, to extend the concept of the SRC model to include more discrete cluster sizes. The current size spectrum representation, shown by Figure 3, is similar to that of the discrete-sectional GDE, except that we only use one section to describe the particles (*i.e.*, particles are approximated as monodisperse). As we will show later, in the cases studied, particle sizes could only be as large as 10 nm in diameter, therefore, the simplification of a monodisperse particle size is reasonable in the thin film growth rate evaluation.

The size representation of Figure 3 is composed of three modes (monomer mode, cluster mode, and particle mode). All modes are described by the evolution of their number concentrations ( $N_1$ ,  $N_l$ , and  $N_p$ ). The monomers are continually reinforced by the chemical reaction (i.e., Eq. [1]), so an equation that governs the feed source  $\text{SiCl}_4$  vapor concentration ( $N_v$ ) must be solved simultaneously with those governing  $N_1$ ,  $N_l$ , and  $N_p$ . The particle mass concentration ( $M_p$ ) evolution is also monitored, since  $(M_p/N_p)^{1/3}$  represents the particle average diameter (see Eq. [15]). Our current model which includes simultaneous monomer generation, rapid nucleation, coagulation, and diffusive deposition shall be referred to as the Vapor Nucleation and Diffusion (VND) model.

#### *Basic conservation equations based on the VND model*

In order to accurately evaluate the thin film growth rate by the deposition of monomer, cluster, and particles in cases of nonuniform temperature and flow field, one has to simultaneously solve the energy, momentum, and mass conservation equations. In previous studies, such a simulation has not been carried out. We will invoke the following assumptions:

- I. At the entry of the reactor, the velocity profile of gas  $U$  is a fully developed laminar flow having the average flow velocity of  $U_{av}$ , and the temperature of gas is uniform at  $T_0$ .
- II. Natural convection flow can be ignored.
- III. Particles produced are spherical and electrically neutral.
- IV. When monomers and particles collide with the substrate surface, they are captured irreversibly.
- V. Brownian diffusion of  $\text{SiO}_2$  monomers and particles in the axial direction can be neglected relative to convection.



The temperature profile inside the CVD reactor is governed by the energy equation,

$$\rho_g c_{pg} \left( U \frac{\partial T}{\partial x} + V \frac{\partial T}{\partial z} \right) = \frac{\partial}{\partial z} \left( \lambda_{Tg} \frac{\partial T}{\partial z} \right) \quad [5]$$

where  $\rho_g$  is the density,  $c_{pg}$  the specific heat, and  $\lambda_{Tg}$  the thermal conductivity of the gas.

The velocity distribution of the gas is governed by the Navier-Stokes and continuity equations:

$$\rho_g c_{pg} \left( U \frac{\partial U}{\partial x} + V \frac{\partial U}{\partial z} \right) = \frac{\partial}{\partial z} \left( \mu_g \frac{\partial T}{\partial z} \right) - \frac{\partial p_T}{\partial x} \quad [6]$$

$$\frac{1}{\rho_g} \frac{\partial p_T}{\partial z} = 0 \quad [7]$$

$$\frac{\partial(\rho_g U)}{\partial x} + \frac{\partial(\rho_g V)}{\partial z} = 0 \quad [8]$$

where  $\mu_g$  is the gas viscosity,  $p_T$  is the total gas pressure, and

$$\rho_g = \frac{p_T M_g}{RT} \quad [9]$$

The basic equations of convective diffusion for the various species are formulated as follows. The number concentration of the  $\text{SiO}_2$  monomer,  $N_1$ , is governed by

$$\begin{aligned} \frac{\partial(UN_1)}{\partial x} + \frac{\partial(VN_1)}{\partial z} &= \frac{\partial}{\partial z} \left( D_1 \frac{\partial N_1}{\partial z} \right) - \frac{\partial(V_{th}N_1)}{\partial z} \\ &- N_1 \sum_{j=1}^k \beta_{1,j} N_j - \beta_{1,p} N_1 N_p + k_{1v} N_v + k_{2v} N_v N_{\text{O}_2} / N_{\text{AV}} \end{aligned} \quad [10]$$

in which  $D_1$  is the  $\text{SiO}_2$  monomer diffusivity.  $\beta_{1,j}$  and  $\beta_{1,p}$  are the coagulation coefficients of monomer- $j$ -mer and the monomer-particle, respectively.  $U$  and  $V$

are the flow velocity in the CVD reactor at any length  $x$  and height  $z$ .  $V_{th}$  is the thermophoretic velocity. The terms on the RHS of Eq. [10] represent, in order, the monomer diffusion, monomer migration by thermophoresis, monomer consumption due to coagulation with clusters, monomer consumption due to coagulation with particles, and monomer generation due to the chemical reaction.

The change in the number concentration of  $\text{SiO}_2$  clusters which contain  $l$  monomers ( $2 \leq l \leq k$ ), in general, is governed by

$$\begin{aligned} \frac{\partial(UN_l)}{\partial x} + \frac{\partial(UN_l)}{\partial z} = \frac{\partial}{\partial z} \left( D_l \frac{\partial N_l}{\partial z} \right) - \frac{\partial(V_{th}N_l)}{\partial z} \\ + \frac{1}{2} \sum_{j=1}^{l-1} \beta_{l-j,j} N_{l-j} N_j - N_l \sum_{j=1}^k \beta_{l,j} N_j - \beta_{l,p} N_l N_p ; \quad (2 \leq l \leq k) \end{aligned} \quad [11]$$

where  $D_l$  is the diffusivity of the  $l$ -mer cluster.  $\beta_{l,j}$  and  $\beta_{l,p}$  are the coagulation coefficients of the  $l$ -mer- $j$ -mer collision and the  $l$ -mer-particle collision, respectively. The terms on the RHS of Eq. [11] represent the diffusive deposition of the  $l$ -mer,  $l$ -mer migration by thermophoretic force, generation of the  $l$ -mers from the sub-cluster range, loss of the  $l$ -mers by coagulation with all the clusters, and loss of the  $l$ -mers by coagulation with particles. Similarly, the change in number concentration of  $\text{SiO}_2$  particles (above  $(k+1)$ -mer) is governed by

$$\begin{aligned} \frac{\partial(UN_p)}{\partial x} + \frac{\partial(VN_p)}{\partial z} = \frac{\partial}{\partial z} \left( D_p \frac{\partial N_p}{\partial z} \right) - \frac{\partial(V_{th}N_p)}{\partial z} \\ + \frac{1}{2} \sum_{i=1}^k \sum_{j=i}^k \beta_{k+i-j,j} N_{k+i-j} N_j - \frac{1}{2} \beta_{p,p} N_p^2 \end{aligned} \quad [12]$$

where  $D_p$  is the diffusivity of  $\text{SiO}_2$  particles.  $\beta_{p,p}$  is the coagulation coefficient between two particles both with an average diameter  $d_p$ . The physical significance of the fourth term on the RHS is the depletion of particle number concentration by self-coagulation between particles.

The mass concentration of  $\text{SiO}_2$  particles,  $M_p$ , is governed by

$$\begin{aligned} \frac{\partial(UM_p)}{\partial x} + \frac{\partial(VM_p)}{\partial z} = \frac{\partial}{\partial z} \left( D_p \frac{\partial M_p}{\partial z} \right) - \frac{\partial(V_{th}M_p)}{\partial z} \\ + \frac{1}{2} m_{k+i} \sum_{i=1}^k \sum_{j=i}^k \beta_{k+i-j,j} N_{k+i-j} N_j + N_p \sum_{j=1}^k m_j \beta_{j,p} N_j \end{aligned} \quad [13]$$

where the third and fourth terms on the RHS account for the mass accumulation due to cluster-cluster coagulation and cluster-particle coagulation, respectively.

Finally, the convective diffusion equation for the number concentration of  $\text{SiCl}_4$  gas molecules,  $N_v$ , is

$$\begin{aligned} \frac{\partial(UN_v)}{\partial x} + \frac{\partial(VN_v)}{\partial z} = \frac{\partial}{\partial z} \left[ D_v \left( \frac{\partial N_v}{\partial z} + k_T N_v \frac{\partial \ln T}{\partial z} \right) \right] \\ - k_{1v} N_v - k_{2v} N_v N_{\text{O}_2} / N_{\text{AV}} \end{aligned} \quad [14]$$

in which  $D_v$  is the  $\text{SiCl}_4$  gas molecule diffusivity. The average diameters of the monomer,  $j$ -mer cluster, and particle are given by

$$d_1 = \left( \frac{6m_1}{\pi \rho_{\text{SiO}_2}} \right)^{1/3} ; \quad d_j = \left( \frac{6jm_1}{\pi \rho_{\text{SiO}_2}} \right)^{1/3}, \quad (j \leq k) ; \quad d_p = \left( \frac{6M_p}{\pi \rho_{\text{SiO}_2} N_p} \right)^{1/3} \quad [15]$$

where  $\rho_{\text{SiO}_2}$  is the density of  $\text{SiO}_2$ , and  $m_1$  is the mass of a  $\text{SiO}_2$  monomer.

A general expression for the coagulation coefficients in Eqs. [10]–[13] is the Fuchs interpolation formula (14). The Fuchs formula matches the solution by kinetic theory of gases in the free-molecule regime and the solution by continuum transport theory in the continuum regime. For a collision between two spheres (denoted as  $A$  and  $B$ ) of diameters  $d_A$  and  $d_B$ , the coagulation coefficient is

$$\begin{aligned}
 \beta_{A,B} &= 2\pi(D_A + D_B)d_{A,B} \left[ \frac{d_{A,B}}{d_{A,B} + 2g_{A,B}} + \frac{8(D_A + D_B)}{\bar{c}_{A,B} d_{A,B}} \right]^{-1} \\
 d_{A,B} &= d_A + d_B \quad ; \quad g_{A,B} = (g_A^2 + g_B^2)^{0.5} \quad ; \quad \bar{c}_{A,B} = (\bar{c}_A^2 + \bar{c}_B^2)^{0.5} \\
 g_A &= \frac{1}{3d_A l_A} \left[ (d_A + l_A)^3 - (d_A^2 + l_A^2)^{3/2} \right] - d_A \\
 \text{Kn}_A &= 2\lambda_g/d_A \quad ; \quad l_A = 8D_A/\pi\bar{c}_A \quad ; \quad \bar{c}_A = (8k_B T/\pi m_A)^{0.5}
 \end{aligned} \tag{16}$$

in which  $\lambda_g$  is the carrier gas mean free path.  $D_A$ ,  $m_A$ ,  $\bar{c}_A$ , and  $\text{Kn}_A$  are the diffusivity (discussed below), mass, mean thermal speed and Knudsen number of sphere  $A$ , respectively. The diameters  $d_A$  and  $d_B$  in Eq. [16] can be obtained by Eq. [15] depending on whether the sphere is a monomer, cluster, or particle.

The binary diffusivities of  $\text{SiO}_2$  monomers and clusters and the  $\text{SiCl}_4$  vapor molecules can be obtained from the second-order Chapman-Enskog binary diffusion solution (17)

$$\begin{aligned}
 D_A &= \frac{3\pi}{64}(1 + z_A) \left( \frac{30z_A^2 + 16z_A + 13}{15z_A^2 + 8z_A + 6} \right) \lambda_A \bar{c}_A \\
 \lambda_A &= \frac{4k_B T}{\pi(1 + z_A)^{1/2} p_{\text{gas}}(d_A + d_{\text{gas}})^2} \quad ; \\
 &\quad (A = 1 \leq j \leq k, \text{ or } A = v)
 \end{aligned} \tag{17}$$

in which  $z_A = m_A/m_{\text{gas}}$  is the ratio of the mass of species  $A$  to that of a carrier gas molecule,  $\lambda_A$  is the mean free path of sphere  $A$  in the carrier gas, and  $d_{\text{gas}}$  is the diameter of a carrier gas molecule. In Eq. [17], we have assumed that the carrier gas is in sufficient quantity that the total pressure is essentially as the carrier gas partial pressure. The diffusivity of a particle,  $D_p$ , is given by the Stokes-Einstein relation (14)

$$D_p = \frac{k_B T}{3\pi\mu_{\text{gas}} d_p} C_{c_p} \tag{18}$$

in which  $\mu_{\text{gas}}$  is the viscosity of the carrier gas.  $C_{c_p}$  is the slip correction factor given by (18)

$$C_{c_p} = 1 + \text{Kn}_p \left\{ 1.252 + 0.399 \exp(-1.1/\text{Kn}_p) \right\} ; \quad \text{Kn}_p = \frac{\lambda_{\text{gas}}}{d_p} \quad [19]$$

and  $\text{Kn}_p$  is the particle Knudsen number.

$V_{th}$  in Eqs. [10]–[12] is the thermophoretic velocity which results from the temperature nonuniformity (13)

$$V_{th} = -0.55 \frac{\mu_g}{\rho_g} \frac{\partial \ln T}{\partial z} . \quad [20]$$

This equation is valid for particles whose diameters are smaller mean free path,  $\text{Kn}_p (= 2\lambda_g/d_p) \gg 1$ .

On the RHS of Eq. [14],  $k_T$  indicates the thermal diffusion ratio of  $\text{SiCl}_4$  gas which is represented by thermal diffusion factor  $\alpha_T$  and mole fractions  $x_v$ ,  $x_g$  in the binary system as discussed by Holstein (19)

$$k_T = \alpha_T x_v x_g . \quad [21]$$

Provided that the mole fraction of carrier gas component,  $x_g$ , is nearly 1 and  $N$  is the total number concentration of molecules, the thermal diffusion term is represented as follows

$$k_T N = \alpha_T x_v x_g N = \alpha_T N_v x_g \approx \alpha_T N_v . \quad [22]$$

Now  $\alpha_T$  can be evaluated by

$$\alpha_T = \frac{5\sqrt{2}}{8} \left( \frac{\sigma_{vg}}{\sigma_g} \right)^2 \left( \frac{6\Omega_v^{(1,2)*} - 5\Omega_{vg}^{(1,1)*}}{\Omega_g^{(2,2)*}} \right) \left( 1 - \frac{3M_g}{2M_v} \right) \quad [23]$$

where  $\sigma$  and  $\epsilon/k$  are Lennard-Jones parameters, and  $\Omega$  is the collision integral.  $\Omega$  is a function of  $kT/\epsilon$ ,  $\sigma_{vg} = (\sigma_g + \sigma_v)/2$ , and  $\Omega_{vg}$  is a function of  $kT/\epsilon_{vg}$  with  $\epsilon_{vg} = (\epsilon_v \epsilon_g)^{1/2}$ .

For a nonuniform temperature profile, the initial and boundary conditions governing Eqs. [5]–[14] are given as follows:

*Initial conditions:*

$$\begin{aligned} x = 0, \quad 0 \leq z \leq H; \quad N_l = 0, \quad \text{for } l = 1 \sim k \\ N_p = 0, \quad M_p = 0, \quad N_v = N_{v0} \end{aligned} \quad [24]$$

*Boundary conditions:*

$$\begin{aligned} x > 0, \quad z = 0; \quad N_l = 0, \quad \text{for } l = 1 \sim k \\ N_p = 0, \quad M_p = 0, \quad \partial N_v / \partial z = 0 \end{aligned} \quad [25]$$

$$\begin{aligned} x > 0, \quad z = H; \quad N_l = 0, \quad \text{for } l = 1 \sim k \\ N_p = 0, \quad M_p = 0, \quad \partial N_v / \partial z = 0 \end{aligned} \quad [26]$$

As seen from Eqs. [25] and [26], the surface reaction of  $\text{SiCl}_4$  at the substrate is assumed to be ignored. Kim and Pratsinis (10) showed that optical waveguide fabrication the surface reaction can be ignored. This assumption will also be made here.

Eqs. [5]–[14] are approximated by finite difference formulas and integrated by the Crank-Nicolson method. In order to ensure the accuracy of the numerical results, comparisons were made between numerical solutions with different step sizes; most of the calculations were made with 50 lateral points and 5000 axial points. As an additional check of the accuracy of the numerical solutions, the total volume of the  $\text{SiO}_2$  vapor, plus that deposited onto the substrate in form of

monomers, clusters, and particles, were found to be within 3% of the total volume of the SiO<sub>2</sub> produced by thermal decomposition.

The thin film growth rates due to monomers, clusters, and particles, are evaluated by their corresponding mass fluxes at the substrate surface ( $z = 0$ ),

$$\begin{aligned} G_1 &= D_1 v_1 \left( \frac{\partial N_1}{\partial z} \right) \Big|_{z=0} ; \quad G_l = D_l v_l \left( \frac{\partial N_l}{\partial z} \right) \Big|_{z=0} \quad (l = 2 \sim k) \\ G_p &= D_p v_p \left( \frac{\partial N_p}{\partial z} \right) \Big|_{z=0} \end{aligned} \quad [27]$$

in which  $v_1$ ,  $v_l$ , and  $v_p$  are the volumes of a SiO<sub>2</sub> monomer,  $l$ -mer, and particle, respectively.

In the simulation, the average gas velocity,  $U_{av}$ , is taken to be 6.1 cm s<sup>-1</sup>, and the reactor height  $H$  is 1.8 cm. These are typical values for CVD reactors (20–22). The temperature of the gas at the inlet of the reaction,  $T_0$ , is assumed to be 300 K.

#### *Determination of the appropriate value of $k$*

To determine an appropriate value of the cluster number  $k$ , numerical results obtained for different  $k$  are compared. We first examine the situation where there is no diffusive deposition and flow, namely, in Eqs. [5]–[14], we drop the diffusion and migration terms on the RHS and substitute the convective flow terms on the LHS with the corresponding time derivatives of concentration,  $\partial N / \partial t$ . Figure 4 shows the calculated concentration evolution of SiO<sub>2</sub> monomer ( $l = 1$ ), trimer ( $l = 3$ ), and pentamer ( $l = 5$ ) at four different values of  $k$  ( $k = 1, 5, 10$ , and 20). In this calculation, the total pressure  $p_T$  was 1 atm, initial SiCl<sub>4</sub> vapor number concentration was  $4.0 \times 10^{-10}$  mol cm<sup>-3</sup>, and  $T_s = 1500$  K. It is seen that  $k$  should

be at least 5 to reasonably approximate the more exact result.

Our second comparison to determine the most appropriate minimum value of  $k$  was made by solving Eqs. [5]–[14] without abbreviation. To simplify the comparison, it is assumed that the temperature profile inside the reactor is uniform and the gas velocity is in plug flow. The operating conditions are:  $p_T = 1$  atm;  $T_s = 1400$  K; and  $c_{v0} = 4.0 \times 10^{-10} \text{ mol cm}^{-3}$ . Figure 5 shows the sum of  $\text{SiO}_2$  thin film growth rates due to clusters and particles ( $\sum_{l=2}^k G_l + G_p$ ) as a function of axial position  $x$ . Four different values of  $k$  ( $k=1, 4, 5$ , and  $7$ ) were used in the comparison. The thin film growth rate due to  $\text{SiO}_2$  monomers ( $G_1$ ) is not included because the predicted  $G_1$  values at different  $k$  are more or less the same. In Figure 5, growth rates evaluated from values  $k \geq 5$  are found to be the same. Therefore, we shall use  $k = 5$  in our subsequent simulation.

#### *Temperature and velocity profiles in the reactor*

Figure 6 shows the calculated temperature and velocity profiles in the reactor at  $p_T = 1.0$  atm and  $p_T = 0.01$  atm. In this calculation, the temperature of the substrate,  $T_s$ , is 1700 K, and the temperature of inlet gas,  $T_0$ , is 300 K.  $z/H = 0$  indicates the substrate surface and  $z/H = 0.5$  the center of the reactor. The broken lines indicate the values at the inlet of the reactor. Under atmospheric conditions, temperature gradually approaches a uniform distribution, which will affect the change in the velocity distribution due to the thermal expansion of gas. For the conditions chosen the uniform temperature is attained in about 20 cm. On the other hand, under the low pressure conditions, the temperature becomes uniform almost at the entrance of the reactor.



### *Number and mass concentrations profiles in the reactor*

Figures 7a and 7b show the number and dimensionless mass concentration profiles at  $p_T = 1.0$  atm and  $p_T = 0.01$  atm, respectively. The mass concentrations are normalized by the mass concentration of the  $\text{SiO}_2$  vapor,  $M_{\text{SiO}_2}^0$ , that would result from a total thermal decomposition of the input  $\text{SiCl}_4$  vapor. The input partial concentration of  $\text{SiCl}_4$  and the reactor temperature are  $5 \times 10^{-10} \text{ mol cm}^{-3}$  and 1500 K, respectively. At atmospheric pressure conditions, the number and mass concentrations near the reactor wall are found to be higher than those in the center due to the temperature profile as shown in Figure 6. It is also seen that the concentration profiles in Figure 7b are closer to parabolic than those in Figure 7a because a decrease in total pressure may increase the mean free paths of all species, and as a result, increase the diffusivities (recall Eqs. [17] and [18]). In either the atmospheric or low pressure conditions, a considerable number of  $\text{SiO}_2$  cluster and particles are predicted to be formed in the reactor. Comparing Figures 7a and 7b, we find that particle number concentrations decrease when pressure decreases. The reason for this behavior is that at low pressure conditions, particle formation is suppressed by the enhancement of monomer and cluster deposition due to the diffusivity increase.

Particle formation is more pronounced as evidenced by the dimensionless mass concentration profiles shown in Figure 7a because the particles are much heavier than the monomers and clusters, and particle mass concentrations at both  $x = 4$  and 10 cm overwhelm the monomer and cluster mass concentrations. This indicates that most of the newly decomposed  $\text{SiO}_2$  monomers aggregate to form particles before they can reach the film surface.

The average number concentrations across the reactor are determined from

$$\begin{aligned}
 (N_j)_{av} &= W \int_0^H U(z) N_j dz / Q = \frac{1}{H} \int_0^H N_j(z) dz, \quad (1 \leq j \leq k) \\
 (N_p)_{av} &= W \int_0^H U(z) N_p dz / Q = \frac{1}{H} \int_0^H N_p(z) dz \\
 Q &= W \int_0^H U(z) dz = W H U_{av}
 \end{aligned} \tag{28}$$

where  $W$  is the width of the reactor, and  $Q$  is the volumetric flow rate in the reactor. Figures 8a and 8b show the average number concentrations of different species (monomer, cluster, and particle) as a functions of the axial position  $x$  at three different temperatures at (a)  $p_T = 1$  atm and  $p_T = 0.01$  atm, respectively. Under atmospheric conditions, concentrations of all species tend first to increase in the axial direction due to the progress of the thermal decomposition, then they start to decrease as a result of deposition. Under low pressure conditions, concentrations of all species decrease down the length  $x$ , again, due to diffusive deposition. In both conditions, with an increase in temperature, it is seen that the monomer and cluster concentrations decrease and the particle concentration significantly increases. In the case of  $T_s = 1700$  K and  $p_T = 1$  atm, most of species at the exit of the reactor are particles. This phenomenon is due to the fact that the temperature increase enhances the thermal speed of monomers and clusters, and as a result, increases the coagulation process.

Figures 9a and 9b show the dimensionless average mass concentration profiles under the same operating conditions as in Figure 8. The average mass concentrations are defined by

$$\begin{aligned}
 (M_j)_{av} &= j m_1 W \int_0^H U(z) N_j(z) dz / Q = \frac{j m_1}{H} \int_0^H N_j(z) dz, \quad (j = 1 \sim k) \\
 (M_p)_{av} &= W \int_0^H U(z) M_p(z) dz / Q = \frac{1}{H} \int_0^H M_p(z) dz \\
 (M_v)_{av} &= m_v W \int_0^H U(z) N_v(z) dz / Q = \frac{m_v}{H} \int_0^H N_v(z) dz
 \end{aligned} \tag{29}$$

where  $m_v$  is the molecular mass of  $\text{SiCl}_4$ .

In Figure 9, the average mass concentrations of  $\text{SiO}_2$  monomer, cluster, and particle are normalized with respect to  $M_{\text{SiO}_2}^0$  (from a total dissociation of  $\text{SiCl}_4$  vapor), whereas the mass concentration of  $\text{SiCl}_4$  gas is normalized with respect to the input  $\text{SiCl}_4$  mass concentration,  $M_{\text{SiCl}_4}^0$ . As shown in Figure 8c,  $\text{SiCl}_4$  gas is consumed more quickly at  $T_s = 1700$  K along the length  $x$  than at the lower temperatures, because the thermal decomposition rate increases as temperature increases. Also, the mass concentration of  $\text{SiO}_2$  particles overwhelms the concentrations of other species as the axial position increases.

Particles that are formed through the subcluster coagulation process may differ in size at different temperatures and axial positions. Figure 10 shows the predicted average diameter of the  $\text{SiO}_2$  particles as a function of axial position  $x$  at four temperatures for the same operating conditions as in Figures 8 and 9. The size of the largest cluster ( $k = 5$ ) is shown by the dashed line. Because a temperature increase may result in the increase of monomer-particle, cluster-particle, and particle-particle coagulation, the average particle size shown in Figure 10 increases with temperature. As discussed in Figure 7, particle formation is significantly suppressed at low pressure conditions. However, at  $p_T = 0.01$  atm and  $T_s = 1800$  K, Figure 10 indicates that large particles of diameter 3 nm (*i.e.*,  $10^{-6}$  cm) can be easily formed in the reactor.

### *Growth rate of $\text{SiO}_2$ film*

Figures 11a and 11b show the dependence of  $\text{SiO}_2$  thin film growth rate on temperature and axial position  $x$  at (a)  $p_T = 1$  atm and (b)  $p_T = 0.01$  atm, respectively. The growth rates due to monomer ( $l = 1$ ), cluster ( $l = 2 \sim 5$ ), and particle

diffusive deposition at  $z = 0$  are calculated by Eq. [18] and expressed in  $\mu\text{m}/\text{min}$ . As seen from Figure 11a, at atmospheric pressure and  $T_s = 1500$  K, the thin film growth rate is predicted to be equally dominated by the deposition of monomers and particles. At higher temperatures, however, deposition of particles that are produced by rapid nucleation becomes important in the thin film growth. At the low pressure condition as in Figure 11b, the contribution of monomers and clusters to the thin film growth rate is enhanced in comparison with the atmospheric pressure situation due to the increase of the diffusivities. The particle contribution to the thin film growth rate at the low pressure condition, on the other hand, is reduced at  $T_s = 1600$  K owing to the enhancement of monomer and cluster deposition; the particle contribution increases at  $T_s = 1700$  K because of the increase of thermal coagulation. At higher  $T_s$ , it is seen that there exist significant distributions in the formed thin film with the axial length.

Figures 12a and 12b show the effect of the reactor temperature on the growth rate of film at axial distances  $x = 4, 10$ , and  $18$  cm for an input  $\text{SiCl}_4$  vapor concentration of  $5 \times 10^{-10} \text{ mol cm}^{-3}$ . When the reactor temperature is lower than about  $1600$  K at both  $p_T = 1$  atm and  $p_T = 0.01$  atm, the growth rate due to monomers and clusters possess maxima in the range of  $T_s = 1500$  to  $1600$  K. Monomer and cluster contributions decrease at higher temperature because of the occurrence of particle formation by rapid nucleation. In Figure 12b, we note that low pressure conditions can lead to an increase in the monomer and cluster contributions to the thin film growth rate for temperatures lower than  $1600$  K. In Figure 12a, the growth rate due to particles (shown by dashed lines) has a maximum because the larger particles that are formed at higher temperatures have lower diffusivities.

The effect of the input  $\text{SiCl}_4$  gas concentration,  $c_{v0}$ , on the thin film growth

at 1500 K is shown in Figure 13. As expected, the thin film growth rate increases with input  $\text{SiCl}_4$  gas concentration. When  $c_{v0}$  is lower than about  $10^{-9} \text{ mol cm}^{-3}$  under the low pressure condition (Figure 13b), the generation of  $\text{SiO}_2$  particles can be neglected. Particle contribution to the growth rate is also enhanced for an increase in  $c_{v0}$ .

Figure 14 shows the effect of the total pressure ( $p_T$ ) on the  $\text{SiO}_2$  film growth rate. With a decrease in  $p_T$ , the monomer, cluster, and particle diffusivities increase, and therefore, the thin film growth rate increases. At very low pressures ( $p_T \leq 0.02 \text{ atm}$ ), monomer deposition overwhelms the generation of clusters and particles and, in consequence, suppresses the cluster and particle contribution to the film growth rate. We conclude, from this simulation, that if thin film preparation is not operated at  $p_T$  less than about 0.02 atm at 1500 K, particle diffusive deposition cannot be ignored.

### GROWTH FRACTION BY MONOMERS, $R_M$

Because thin films that are made purely from monomer deposition are considered to be of the highest quality, we begin by considering the relative importances of monomer diffusive deposition, monomer generation by thermal decomposition, and monomer-monomer coagulation that would form clusters and particles. The following dimensionless quantities are defined in this regard:

$$DC = \frac{D_1}{\beta_{1,1} H^2 |N_1|} = \frac{\text{Diffusion Rate}}{\text{Coagulation Rate}} \quad [30]$$

$$DG = \frac{D_1 |N_1|}{(k_{1v} N_{v0} + k_{2v} N_{v0} N_{\text{O}_{2,0}} / N_{\text{AV}}) H^2} = \frac{\text{Diffusion Rate}}{\text{Generation Rate}} \quad [31]$$

In Eqs. [30] and [31], the monomer concentration at the exit of the reactor

$x = L$ ,  $|N_1|$ , can be related to the input  $\text{SiCl}_4$  gas concentration,  $N_{v0}$ . This  $|N_1|$  was calculated by solving the basic equation, Eq. [14]. The ratio of the thin film growth rate by monomer deposition to the total thin film growth rate can be written as

$$R_M = \frac{\int_0^L G_1 dx}{\int_0^L \left( \sum_{j=1}^k G_j + G_p \right) dx} \quad [32]$$

Figure 15, which shows  $R_M$  as a function of both  $DC$  and  $DG$ , was obtained under the conditions of different temperatures in an APCVD or LPCVD reactor of the present study as shown in Table I. Filled points are for atmospheric conditions. Because a larger  $DC$  value means that either the monomer deposition is dominant or the monomer-monomer coagulation is weak, it is seen that the value of  $R_M$  (i.e., monomer contribution to the film growth rate) differs between the APCVD and LPCVD reactors. In LPCVD reactor,  $R_M$  would increase if  $DC$  increases at a constant  $DG$  value. In the range  $10^{-6} < DC < 10^{-4}$ , however, sizes of the generated particles are small, and the decrease of particle diffusivity relatively increases as  $DC$  decreases. On the other hand, for situations of constant generation rate and  $DC$  value, the stronger the monomer deposition the higher the value of  $R_M$ . In the case of APCVD, the values of  $R_M$  become independent of the dimensionless value of  $DG$  because the  $\text{SiO}_2$  monomer generation is sufficiently large compared with the deposition rate of the  $\text{SiO}_2$  monomer.

To produce good quality thin films, operating conditions such as temperature, feed vapor concentration, reactor dimension and pressure, should be chosen such that  $R_M$  can be as close to unity as possible. This monomer deposition predominant regime can be reached if one chooses, for example,  $DC > 0.01$  and  $DG > 0.002$  in APCVD and  $DC > 0.01$  and  $DG > 1.5$  in LPCVD.

## CONCLUSION

In this work we have evaluated the importance of particle formation by rapid nucleation and coagulation in the preparation of thin film in a CVD reactor. The thin film growth rate by monomers, clusters, and particles is found to depend greatly upon the reactor temperature, velocity, initial gas concentration, reactor total pressure, and the axial distance from the reactor entrance.

For low pressure situations, the diffusivities of monomers, clusters, and particles are enhanced due to the increase of the species mean free paths, and, in consequence, the total film growth rate can be enhanced. The thin film growth rate by monomers and clusters may, however, decrease at high temperatures due to the formation of particles.

The best operating conditions for producing high quality thin films (those made mostly by monomer deposition) are clearly defined by the values of two dimensionless parameters,  $DC$  and  $DG$ , which govern the relative importance of monomer deposition to coagulation and monomer deposition to monomer generation, respectively. Because the thin film growth rate attainable under the predicted best operating conditions, however, is not as large as when temperatures and inlet vapor concentrations are higher, the optimum operating conditions should be carefully determined.

# LIST OF SYMBOLS

- $\bar{c}$  mean thermal speed ( $\text{cm s}^{-1}$ )
- $C_{c,p}$  particle slip correction factor (-)
- $c_{pg}$  specific heat of carrier gas ( $\text{erg g}^{-1}\text{K}^{-1}$ )
- $c_{v0}$  input mol concentration of  $\text{SiCl}_4$  vapor ( $\text{mol cm}^{-3}$ )
- $d$  diameter (cm)
- $D$  Brownian or binary diffusivity ( $\text{cm}^2 \text{s}^{-1}$ )
- $DC$  ratio of monomer deposition to monomer-monomer coagulation (-)
- $DG$  ratio of monomer deposition to monomer generation (-)
- $G$  thin film growth rate by monomers, clusters, or particles ( $\text{cm s}^{-1}$ )
- $H$  reactor height (cm)
- $k$  number of cluster cutoff in discrete size spectrum (-)
- $k_B$  Boltzmann constant,  $1.3806 \times 10^{-23}$  ( $\text{J K}^{-1}$ )
- $k_{1v}$   $\text{SiCl}_4$  vapor thermal decomposition rate constant ( $\text{s}^{-1}$ )
- $k_{2v}$   $\text{SiCl}_4$  vapor thermal decomposition rate constant ( $\text{cm}^3 \text{s}^{-1}$ )
- $\text{Kn}$  Knudsen number (-)
- $k_T$  thermal diffusion ratio (-)
- $L$  reactor width (cm)
- $m$  mass of a monomer, cluster, or particle (g)
- $M$  gas-phase mass concentration ( $\text{g cm}^{-3}$ )
- $M_{\text{SiO}_2}^0$  monomer mass concentration at a total dissociation of  $\text{SiCl}_4$  vapor ( $\text{g cm}^{-3}$ )
- $M_{\text{SiCl}_4}^0$  input mass concentration of  $\text{SiCl}_4$  vapor ( $\text{g cm}^{-3}$ )
- $M_g$   $\text{O}_2$  carrier gas molecular weight ( $\text{g mol}^{-1}$ )
- $M_v$   $\text{SiCl}_4$  vapor molecular weight ( $\text{g mol}^{-1}$ )
- $N$  gas-phase number concentration ( $\text{cm}^{-3}$ )



- $N_{v0}$  input  $\text{SiCl}_4$  vapor concentration ( $\text{cm}^{-3}$ )
- $|N_1|$  total monomer concentration at exit ( $\text{cm}^{-3}$ )
- $p_{\text{SiCl}_4}^0$  input partial pressure of  $\text{SiCl}_4$  vapor (Pa)
- $p_T$  total pressure in CVD reactor ( $\text{dyn cm}^{-2}$ )
- $Q$  volumetric gas flow rate ( $\text{cm}^3 \text{ s}^{-1}$ )
- $R_M$  fraction of film growth rate by monomer contribution (–)
- $T$  temperature (K)
- $T_s$  temperature of reactor wall or heated substrate (K)
- $U, V$  reactor flow velocity ( $\text{cm s}^{-1}$ )
- $v$  volume of a  $\text{SiO}_2$  monomer, cluster or particle ( $\text{cm}^3$ )
- $v_{th}$  thermal velocity ( $\text{cm s}^{-1}$ )
- $W$  reactor width (cm)
- $x$  downstream distance from reactor entrance (cm)
- $z$  vertical height from thin film surface (cm)
- $z_A$  mass ratio of sphere  $A$  to a carrier gas molecule (–)

## Greek Letters

- $\alpha$  thermal diffusion factor (–)
- $\beta$  coagulation coefficient between two spheres ( $\text{cm}^3 \text{ s}^{-1}$ )
- $\epsilon/k$  Lennard-Jones parameter (K)
- $\lambda$  mean free path (cm)
- $\lambda_{Tg}$  thermal conductivity ( $\text{erg cm}^{-1} \text{ s}^{-1} \text{ K}$ )
- $\mu_{\text{gas}}$  carrier gas viscosity ( $\text{g cm}^{-1} \text{ s}^{-1}$ )
- $\rho_g$  carrier gas mass density ( $\text{g cm}^{-3}$ )
- $\rho_{\text{SiO}_2}$  mass density of  $\text{SiO}_2$  ( $\text{g cm}^{-3}$ )
- $\sigma$  Lennard-Jones parameter (cm)
- $\Omega$  collision integral (–)

## Subscripts

*av* average value

*A, B* arbitrary sphere *A* or *B*

*g* O<sub>2</sub> carrier gas

*i, j, l* SiO<sub>2</sub> monomer or cluster that contains *i, j*, or *l* monomers

*p* SiO<sub>2</sub> particle

*v* SiCl<sub>4</sub> vapor

## REFERENCES

1. Okuyama, K., Huang, D. D., Seinfeld, J. H., and Tani, Y., *J. Electrochem. Soc.*, submitted (1990).
2. Okuyama, K., and Yoshizawa, A., *J. Aerosol Res. Japan* **3**, 6 (1988).
3. Eversteijn, F. C., *Philips Res. Repts.* **26**, 134 (1971).
4. Ban, V. S., and Gilbert, S. L., *J. Crystal Growth* **31**, 284 (1975).
5. Van de Brekel, C. H. J., and Bollen, L. J. M., *J. Crystal Growth* **54**, 310 (1981).
6. Weling, F., *J. Appl. Phys.* **57**, 4441 (1985).
7. Jensen, K. F., and Graves, D. B., *J. Electrochem. Soc.* **130**, 1950 (1983).
8. Joshi, M. G., *J. Electrochem. Soc.* **134**, 3118 (1987).
9. Wilke, T. E., Turner, K. A., and Takoudis, C. G., *Chem. Eng. Sci.* **41**, 643 (1986).
10. Kim, K-S., and Pratsinis, S. E. Pratsinis, *AIChE J.* **34**, 912 (1988).
11. Jensen, K. F., *Adv. Chemistry* **221**, ACS (1989).
12. Power, D. R., *J. Am. Ceram. Soc.* **61**, 295 (1978).
13. Friedlander, S. K., "Smoke, Dust and Haze." Wiley, New York, 1977.
14. Seinfeld, J. H., "Atmospheric Chemistry and Physics of Air Pollution." Wiley, New York, 1986.
15. Wu, J. J., and Flagan, R. C., *J. Colloid Interface Sci.* **123**, 338 (1988).
16. Wu, J. J., Nguyen, H. V., Flagan, R. C., Okuyama, K., and Kousaka, Y., *AIChE J.* **34**, 1249 (1988).

17. Huang, D. D., and Seinfeld, J. H., *J. Colloid Interface Sci.* **125**, 733 (1988).
18. Jennings, S. G., *J. Aerosol Sci.* **19**, 159 (1988).
19. Holstein, W. L., *J. Electrochem. Soc.* **135**, 1788 (1988).
20. Reep, D. H., and Ghandhi, S. K., *J. Electrochem. Soc.* **130**, 675 (1983).
21. Suzuki M., and Sato, M., *J. Electrochem. Soc.* **132**, 1684 (1985).
22. Van de Ven, J., Rutten, G. M. J., Raaijmakers, M. J., and Giling, L. J., *J. Crystal Growth* **76**, 352 (1986).

Table I. Simulated Conditions and Values of  $DG$ ,  $DC$ , and  $R_M$

$T_s$ [K]	$p_r$ [atm]	$c_{v,0}$ [mol·cm <sup>-1</sup> ]	$DG$ [-]	$DC$ [-]	$R_M$ [-]	Key in Fig.15
1500	0.01	$1.0 \times 10^{-11}$	$3.22 \times 10^1$	$3.53 \times 10^{-2}$	$9.99 \times 10^{-1}$	○
		$1.0 \times 10^{-10}$	$3.22 \times 10^1$	$3.53 \times 10^{-3}$	$9.91 \times 10^{-1}$	
		$5.0 \times 10^{-10}$	$3.23 \times 10^1$	$7.07 \times 10^{-4}$	$9.57 \times 10^{-1}$	
		$3.0 \times 10^{-9}$	$3.23 \times 10^1$	$1.18 \times 10^{-4}$	$8.05 \times 10^{-1}$	
		$1.0 \times 10^{-8}$	$3.23 \times 10^1$	$3.53 \times 10^{-5}$	$5.97 \times 10^{-1}$	
		$5.0 \times 10^{-8}$	$3.33 \times 10^1$	$7.07 \times 10^{-6}$	$6.19 \times 10^{-1}$	
		$3.0 \times 10^{-7}$	$3.34 \times 10^1$	$1.19 \times 10^{-6}$	$6.61 \times 10^{-1}$	
1600	0.01	$1.0 \times 10^{-11}$	7.13	$2.50 \times 10^{-2}$	$9.96 \times 10^{-1}$	△
		$1.0 \times 10^{-10}$	7.13	$2.50 \times 10^{-3}$	$9.63 \times 10^{-1}$	
		$5.0 \times 10^{-10}$	7.13	$5.00 \times 10^{-4}$	$8.53 \times 10^{-1}$	
		$3.0 \times 10^{-9}$	7.13	$8.33 \times 10^{-5}$	$5.84 \times 10^{-1}$	
		$3.0 \times 10^{-8}$	7.17	$8.33 \times 10^{-6}$	$5.96 \times 10^{-1}$	
1700	0.01	$1.0 \times 10^{-12}$	1.32	$2.66 \times 10^{-1}$	$9.98 \times 10^{-1}$	□
		$3.0 \times 10^{-11}$	1.32	$8.85 \times 10^{-2}$	$9.55 \times 10^{-1}$	
		$1.0 \times 10^{-10}$	1.32	$2.66 \times 10^{-2}$	$8.74 \times 10^{-1}$	
		$5.0 \times 10^{-10}$	1.32	$5.31 \times 10^{-3}$	$6.57 \times 10^{-1}$	
		$3.0 \times 10^{-9}$	1.32	$8.85 \times 10^{-4}$	$4.96 \times 10^{-1}$	
		$1.0 \times 10^{-8}$	1.32	$2.66 \times 10^{-5}$	$5.23 \times 10^{-1}$	
1500	1.0	$1.0 \times 10^{-12}$	$2.65 \times 10^{-2}$	$5.40 \times 10^{-3}$	$9.52 \times 10^{-1}$	●
		$5.0 \times 10^{-12}$	$2.65 \times 10^{-2}$	$1.10 \times 10^{-3}$	$8.72 \times 10^{-1}$	
		$3.0 \times 10^{-11}$	$2.64 \times 10^{-2}$	$1.81 \times 10^{-4}$	$7.90 \times 10^{-1}$	
		$1.0 \times 10^{-10}$	$2.64 \times 10^{-2}$	$5.50 \times 10^{-5}$	$7.49 \times 10^{-1}$	
		$5.0 \times 10^{-10}$	$2.64 \times 10^{-2}$	$1.10 \times 10^{-5}$	$7.05 \times 10^{-1}$	
		$3.0 \times 10^{-9}$	$2.64 \times 10^{-2}$	$1.84 \times 10^{-6}$	$6.50 \times 10^{-1}$	
1600	1.0	$1.0 \times 10^{-12}$	$8.78 \times 10^{-3}$	$2.60 \times 10^{-2}$	$9.85 \times 10^{-1}$	▲
		$1.0 \times 10^{-12}$	$8.78 \times 10^{-3}$	$2.60 \times 10^{-3}$	$9.12 \times 10^{-1}$	
		$1.0 \times 10^{-11}$	$8.78 \times 10^{-3}$	$2.60 \times 10^{-4}$	$8.18 \times 10^{-1}$	
		$5.0 \times 10^{-11}$	$8.77 \times 10^{-3}$	$5.19 \times 10^{-5}$	$7.77 \times 10^{-1}$	
		$5.0 \times 10^{-10}$	$8.77 \times 10^{-3}$	$5.19 \times 10^{-6}$	$7.13 \times 10^{-1}$	
1700	1.0	$1.0 \times 10^{-12}$	$1.69 \times 10^{-3}$	$2.66 \times 10^{-2}$	$9.84 \times 10^{-1}$	■
		$1.0 \times 10^{-12}$	$1.69 \times 10^{-3}$	$2.66 \times 10^{-3}$	$9.11 \times 10^{-1}$	
		$5.0 \times 10^{-11}$	$1.69 \times 10^{-3}$	$5.31 \times 10^{-5}$	$7.97 \times 10^{-1}$	
		$5.0 \times 10^{-10}$	$1.69 \times 10^{-3}$	$5.31 \times 10^{-6}$	$7.13 \times 10^{-1}$	

## LIST OF FIGURES

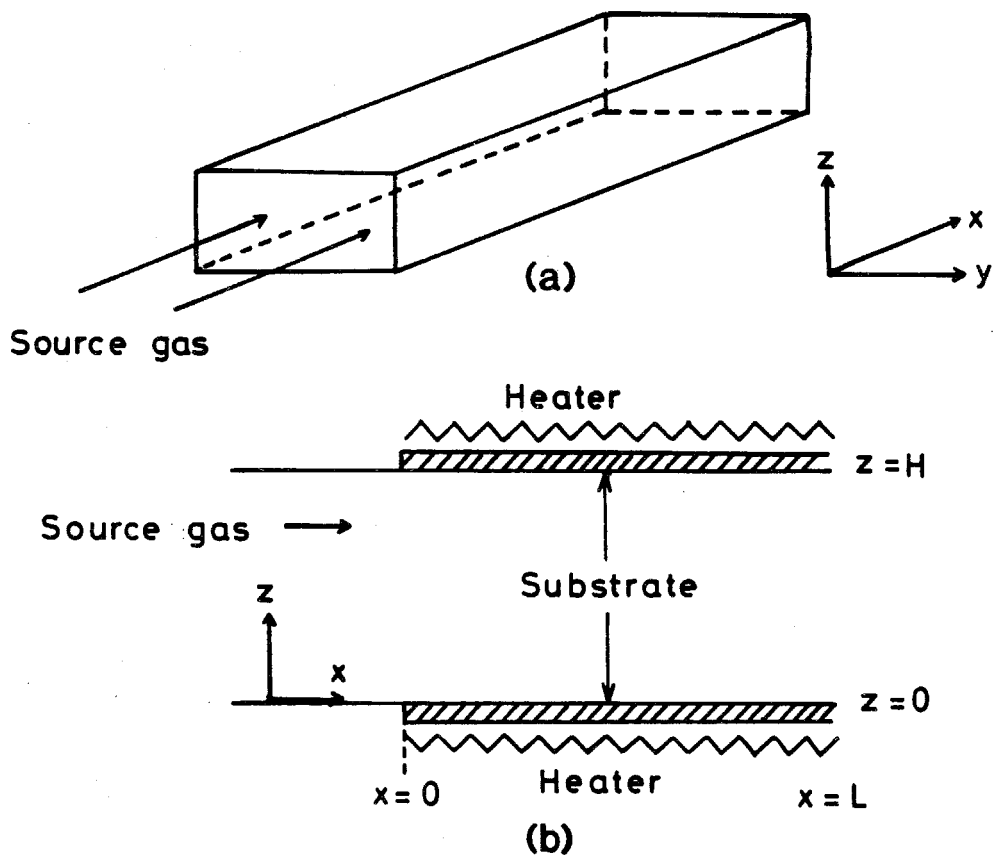
- Figure 1. Horizontal CVD reactor.
- Figure 2. Processes contributing to thin film preparation in the CVD method.
- Figure 3. Representation of particle size spectrum.
- Figure 4. Time-dependent change of  $\text{SiO}_2$  monomer, trimer, and pentamer number concentrations by chemical reaction and coagulation for a reactor temperature of 1500 K and the input  $\text{SiCl}_4$  vapor of 1 Pa.
- Figure 5. Effect of value  $k$  on the film growth rate by clusters and particles.
- Figure 6. Temperature and velocity profiles in the CVD reactor at  $T_s = 1700$  K and  $p_{\text{SiCl}_4}^o = 1$  Pa. (a) temperature profile; (b) velocity profile.
- Figure 7. Number concentration and dimensionless mass profiles for  $\text{SiO}_2$  monomers, clusters, and particles in the CVD reactor at  $T_s = 1500$  K and  $p_{\text{SiCl}_4}^o = 1$  Pa. (a)  $p_T = 1$  atm; (b)  $p_T = 0.01$  atm.
- Figure 8. Average number concentrations of  $\text{SiO}_2$  monomers, clusters, and particles at different temperatures under  $p_{\text{SiCl}_4}^o = 1$  Pa. (a)  $p_T = 1$  atm; (b)  $p_T = 0.01$  atm.
- Figure 9. Normalized average mass concentrations of  $\text{SiO}_2$  monomers, clusters, and particles and  $\text{SiCl}_4$  vapor at different temperatures. (a)  $p_T = 1$  atm; (b)  $p_T = 0.01$  atm.
- Figure 10. Average diameter of particles as a function of the axial distance  $x$  at different temperatures.
- Figure 11.  $\text{SiO}_2$  film growth rate as a function of axial position at different temperatures for the input  $\text{SiCl}_4$  vapor of  $5 \times 10^{-10} \text{ mol cm}^{-3}$ . (a)  $p_T = 1$  atm; (b)  $p_T = 0.01$  atm.

Figure 12.  $\text{SiO}_2$  film growth rate as a function of reactor temperature for the input  $\text{SiCl}_4$  vapor of  $5 \times 10^{-10} \text{ mol cm}^{-3}$ . (a)  $p_T = 1 \text{ atm}$ ; (b)  $p_T = 0.01 \text{ atm}$ .

Figure 13.  $\text{SiO}_2$  film growth rate as a function of initial number concentration of  $\text{SiCl}_4$  vapor for a reactor temperature of 1500 K. (a)  $p_T = 1 \text{ atm}$ ; (b)  $p_T = 0.01 \text{ atm}$ .

Figure 14. Effect of the reactor total pressure on the  $\text{SiO}_2$  thin film growth rate at  $T_s = 1500 \text{ K}$  and  $c_{v0}^o = 5 \times 10^{-10} \text{ mol cm}^{-3}$ .

Figure 15. Fraction of  $\text{SiO}_2$  thin film growth rate by monomers as a function of parameters  $DC$  and  $DG$ .



**Figure 1**



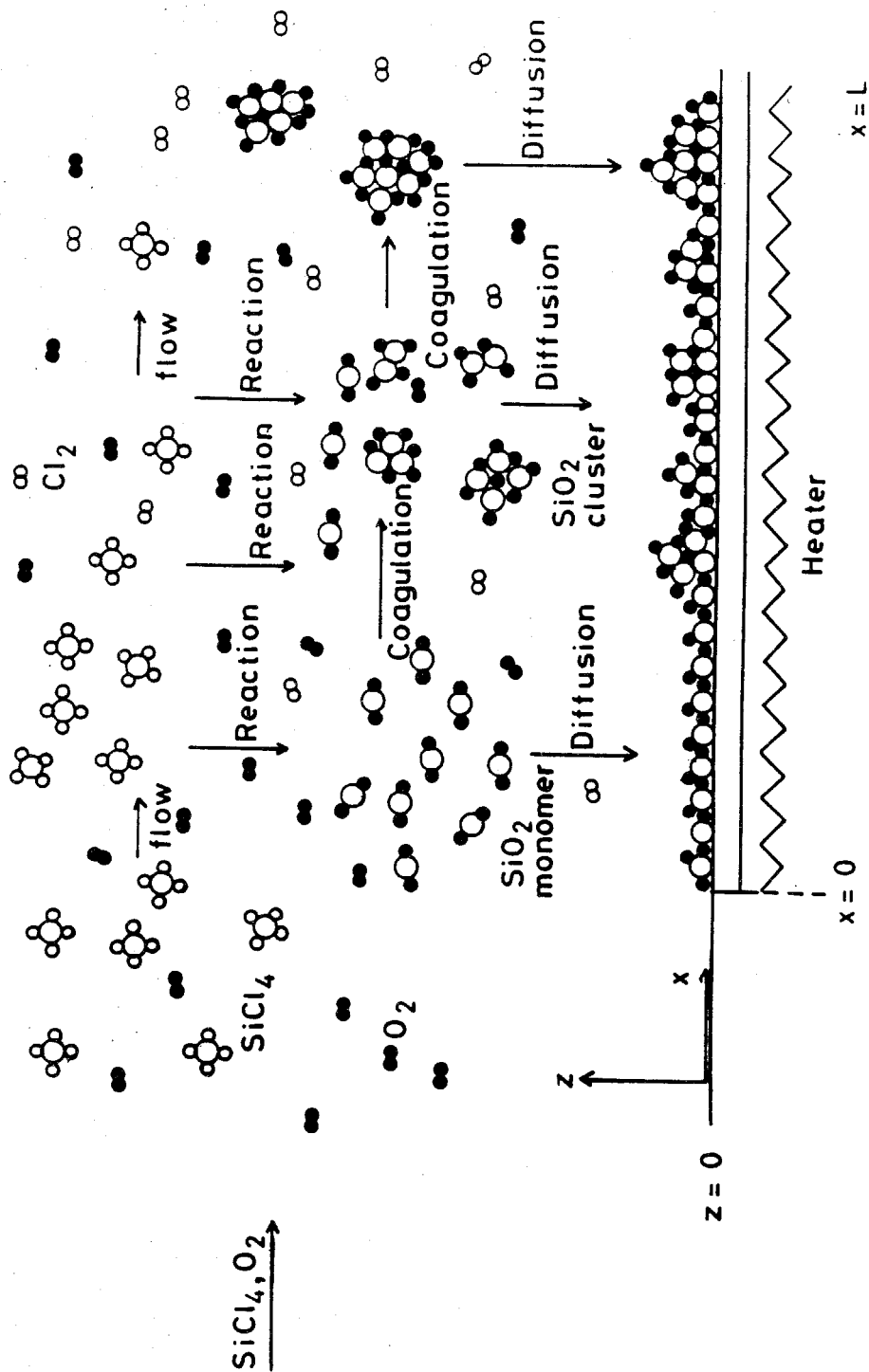


Figure 2

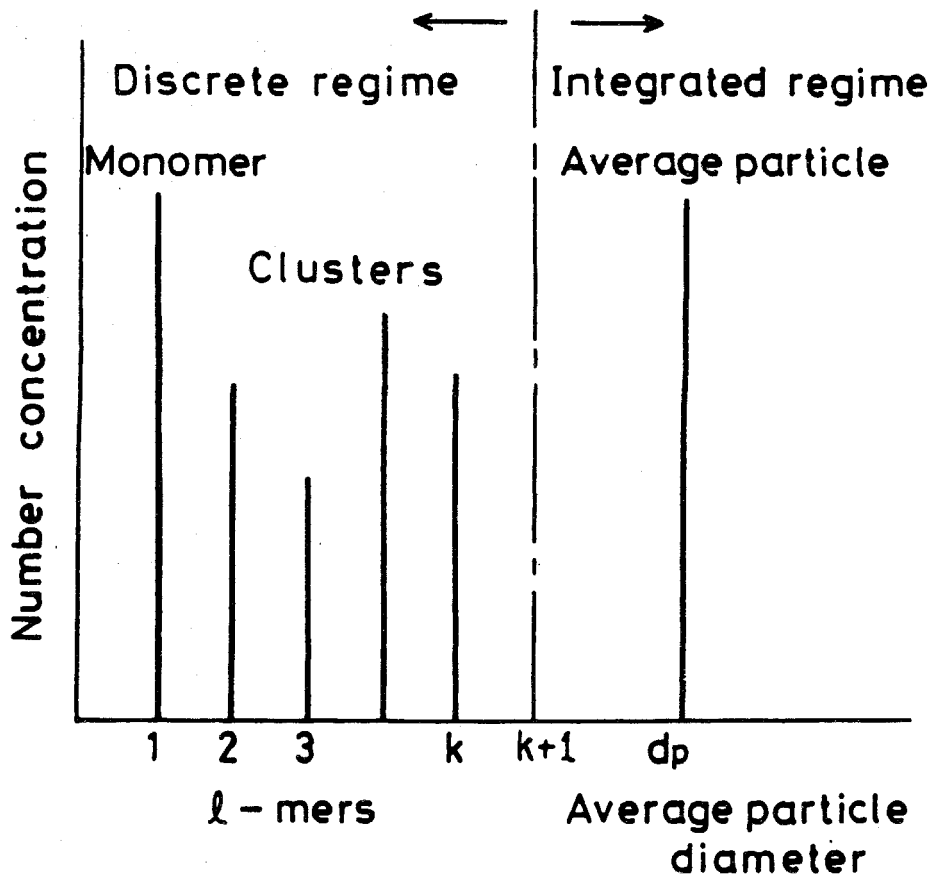


Figure 3

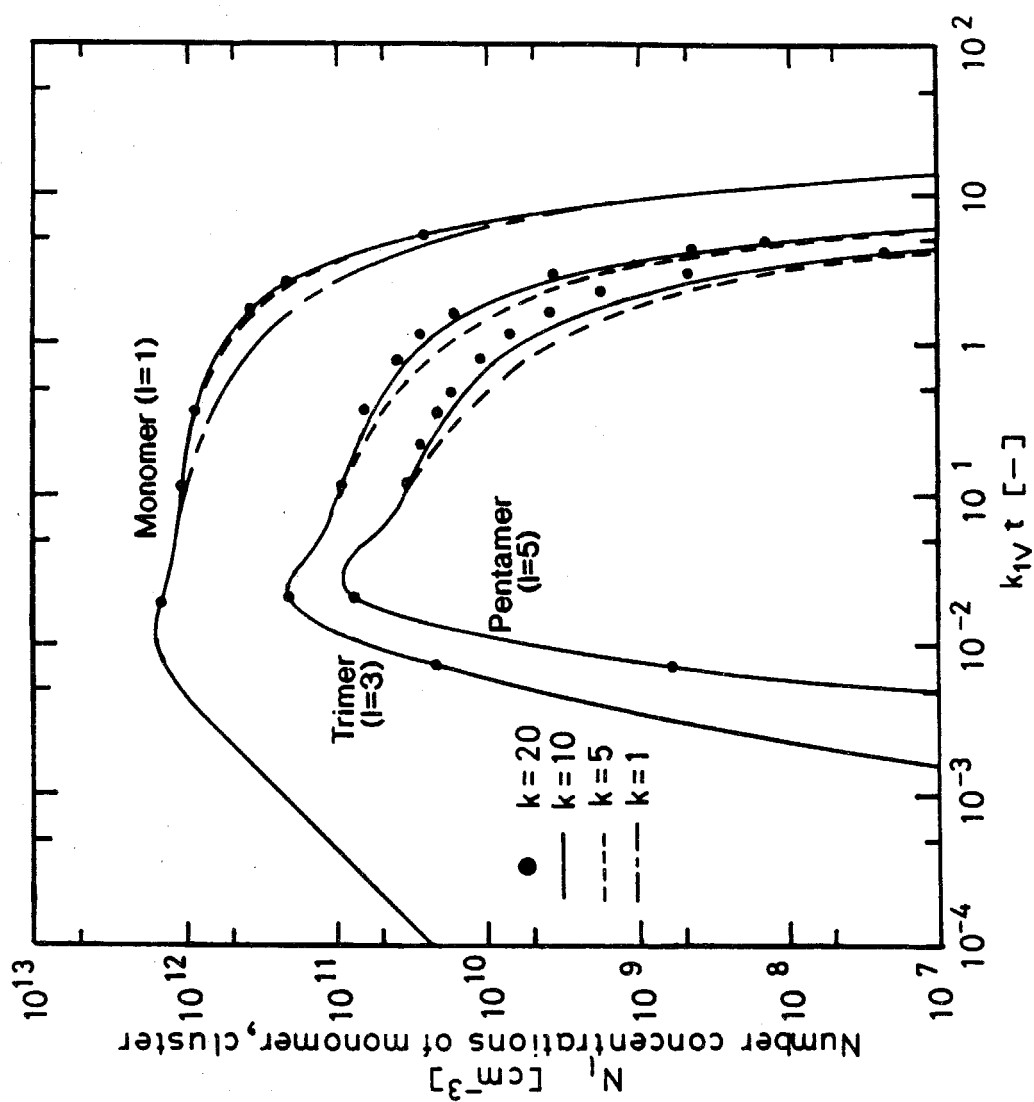


Figure 4

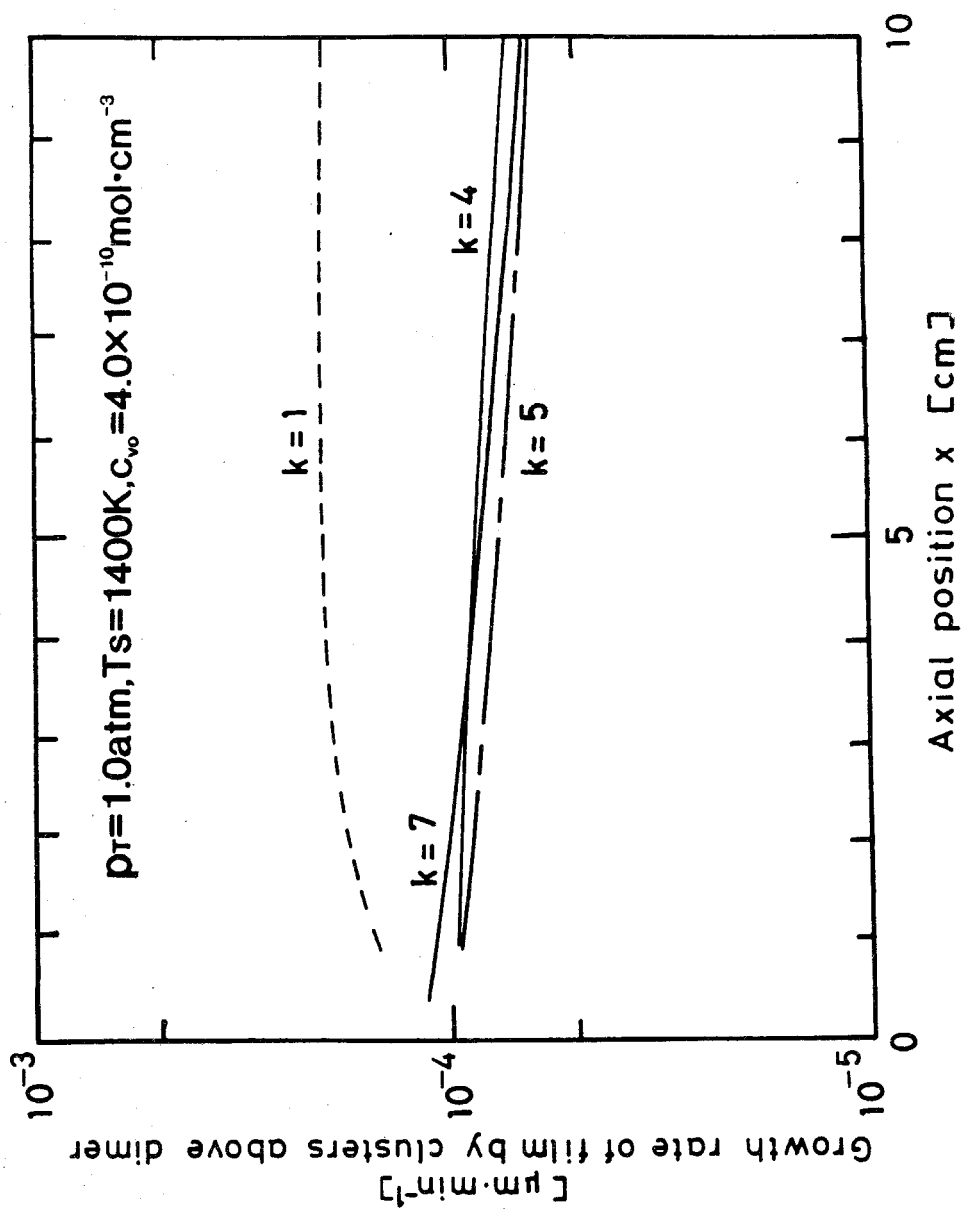


Figure 5

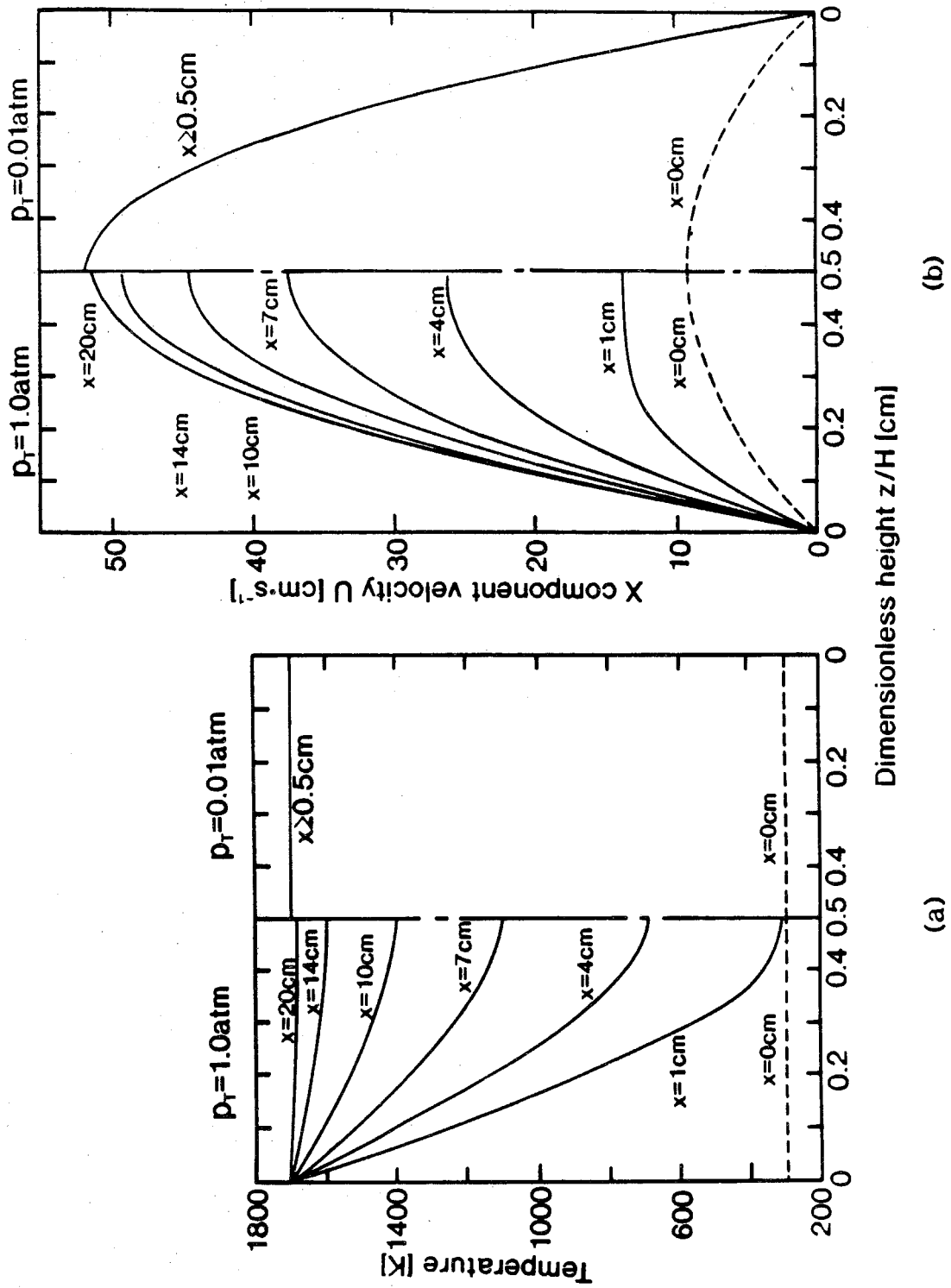


Figure 6

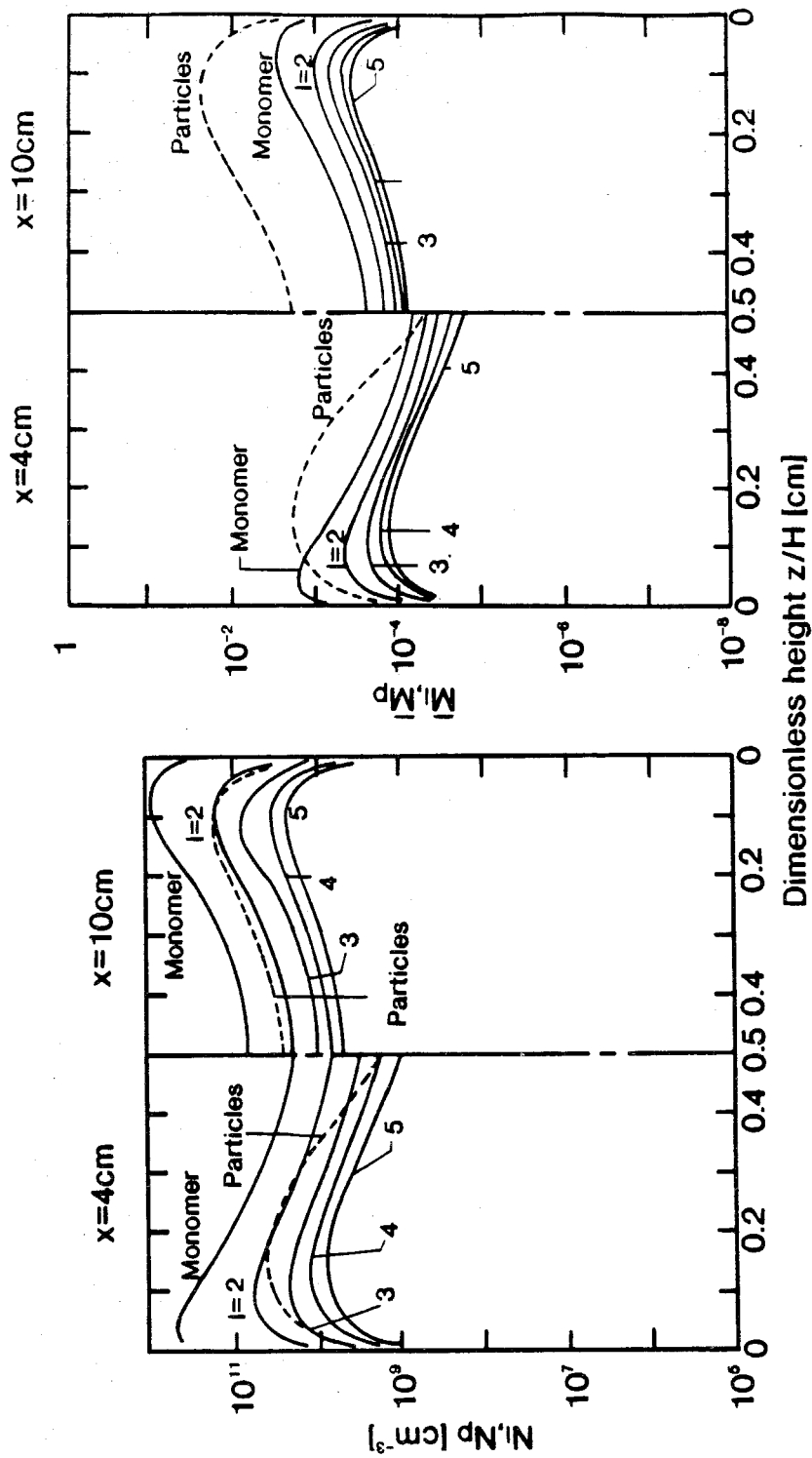


Figure 7a

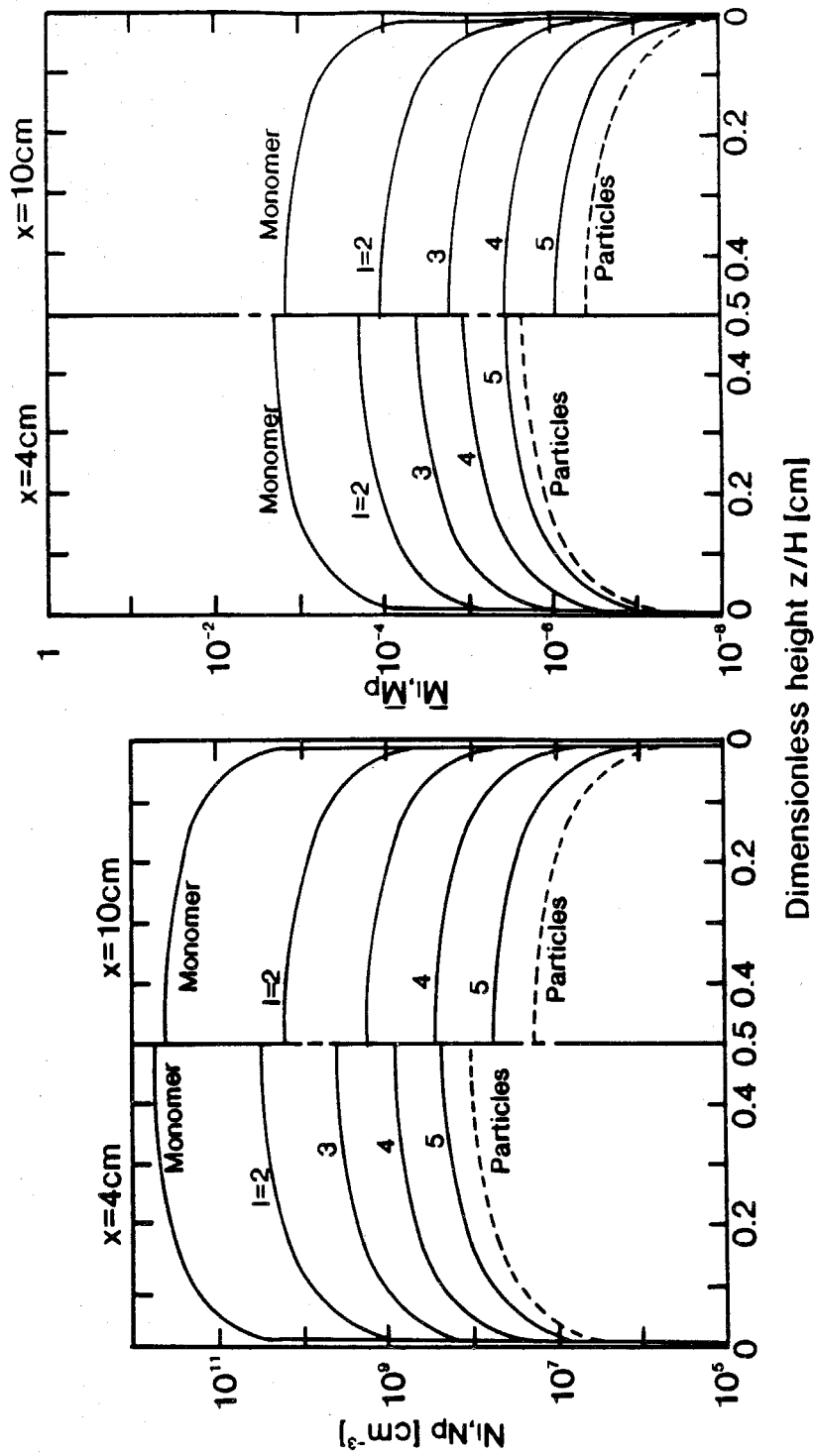


Figure 7b

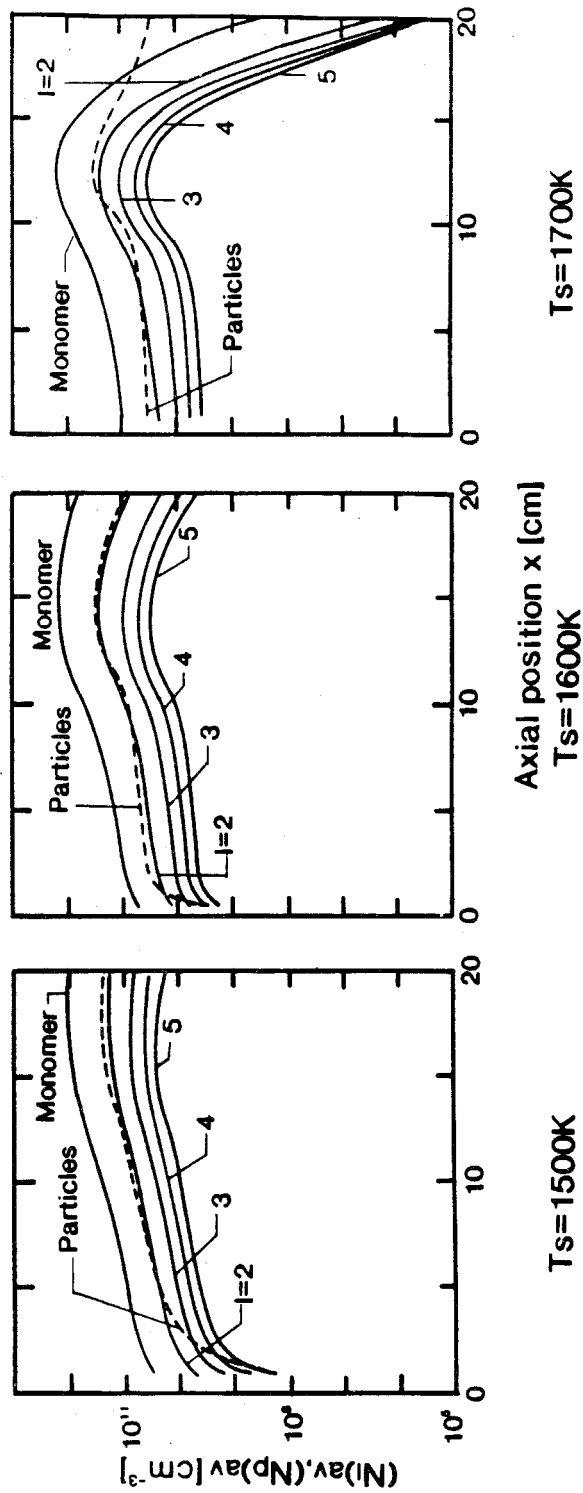


Figure 8a



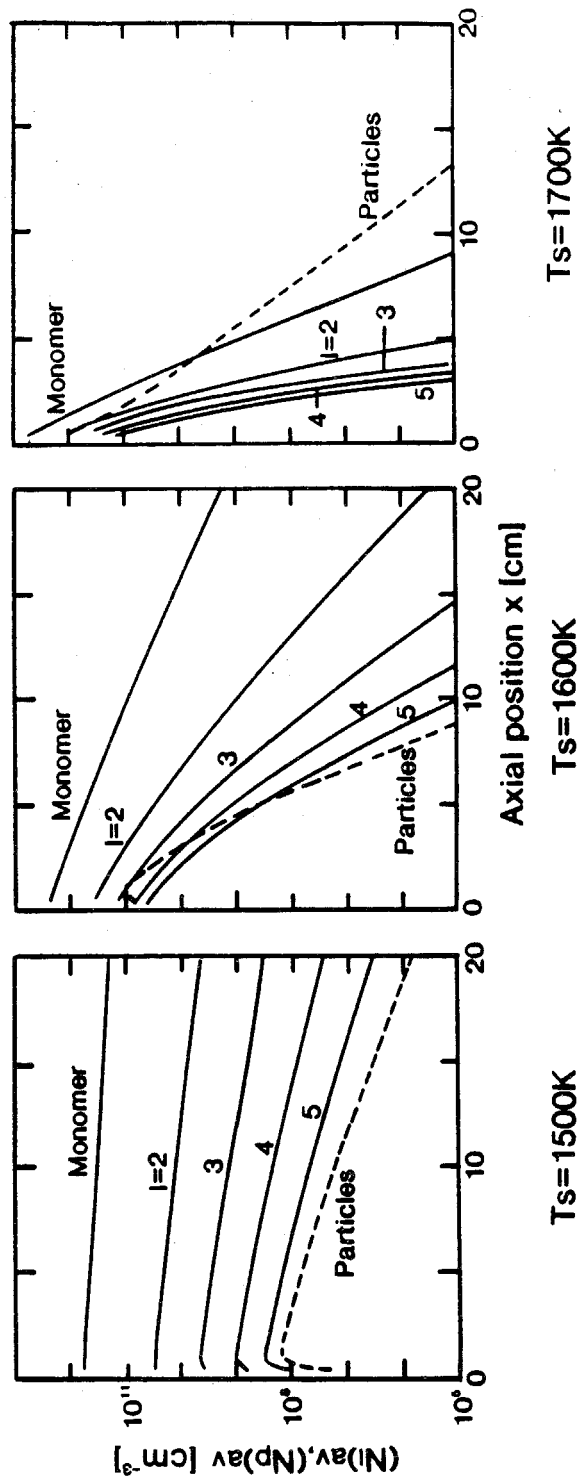


Figure 8b

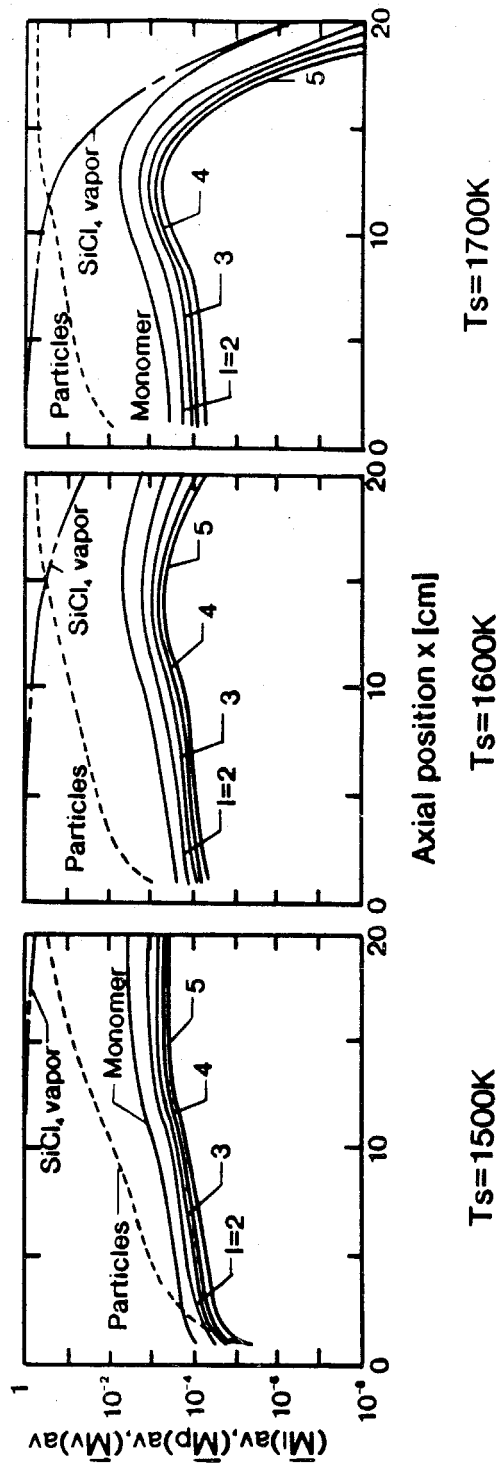


Figure 9a

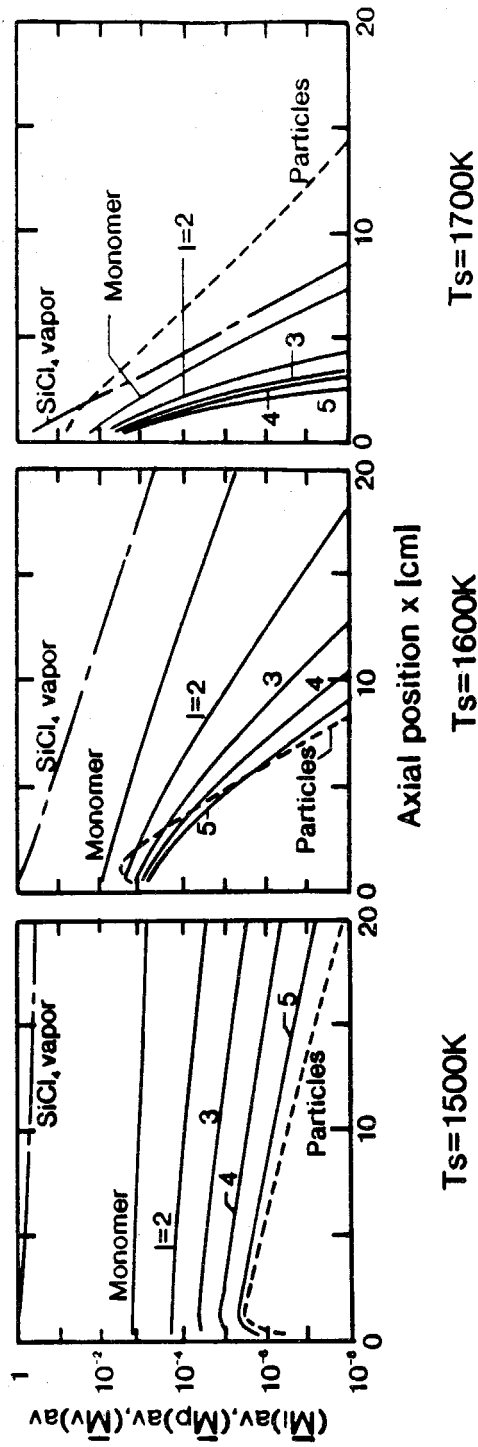


Figure 9b

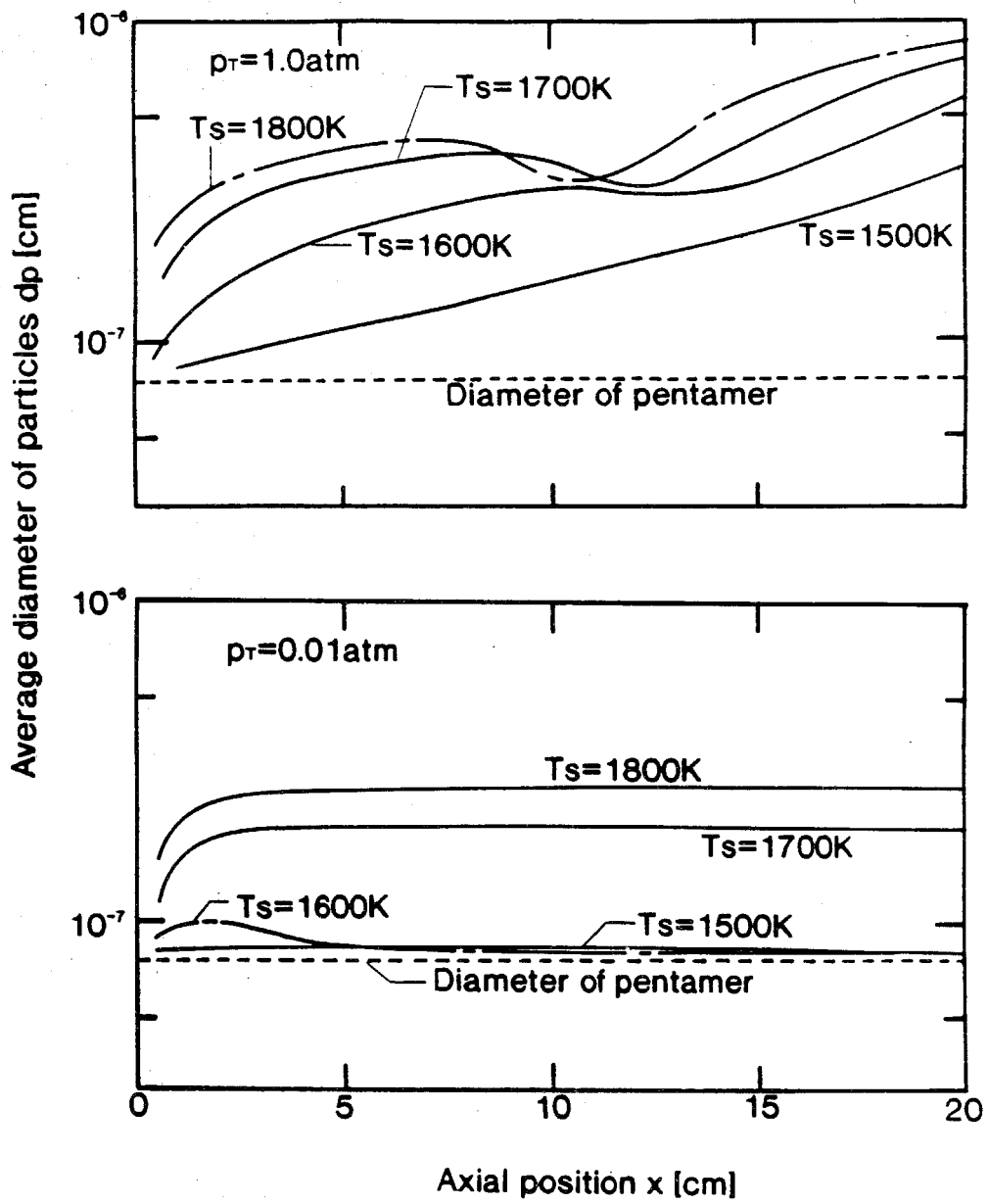


Figure 10

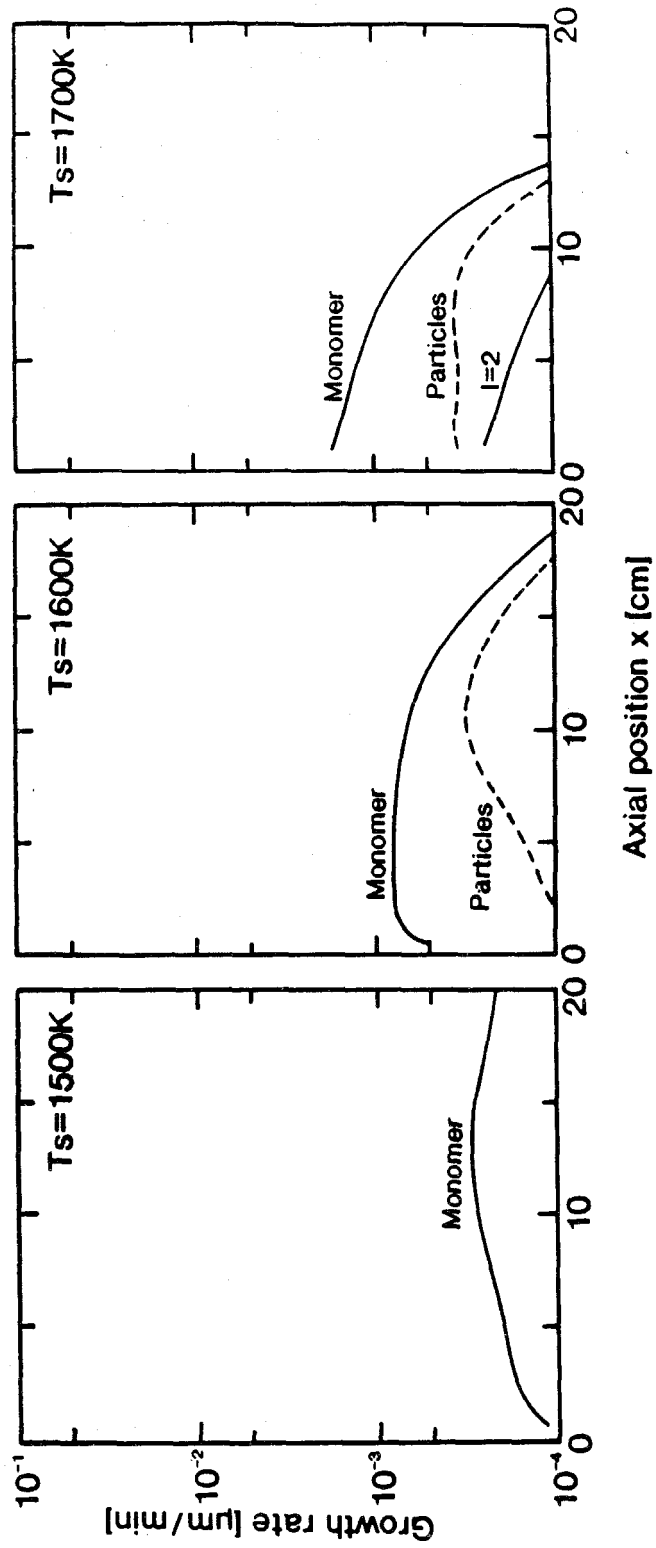


Figure 11a

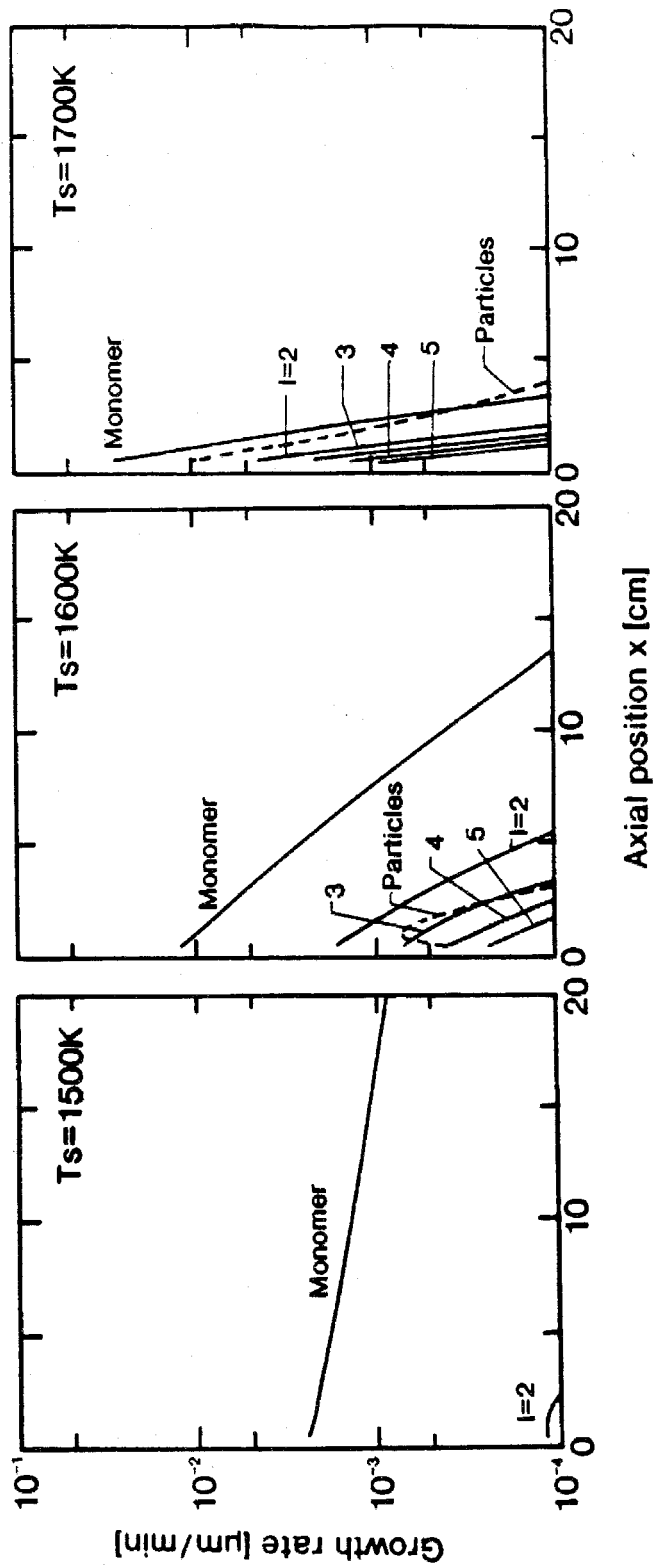


Figure 11b

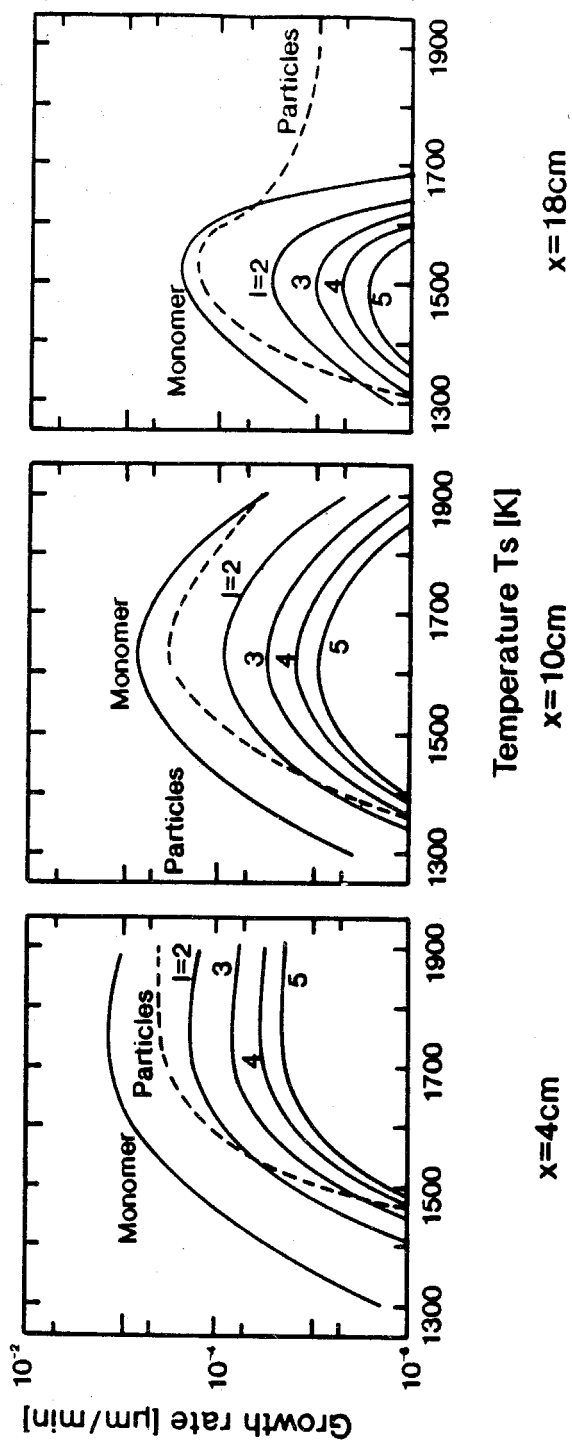


Figure 12a

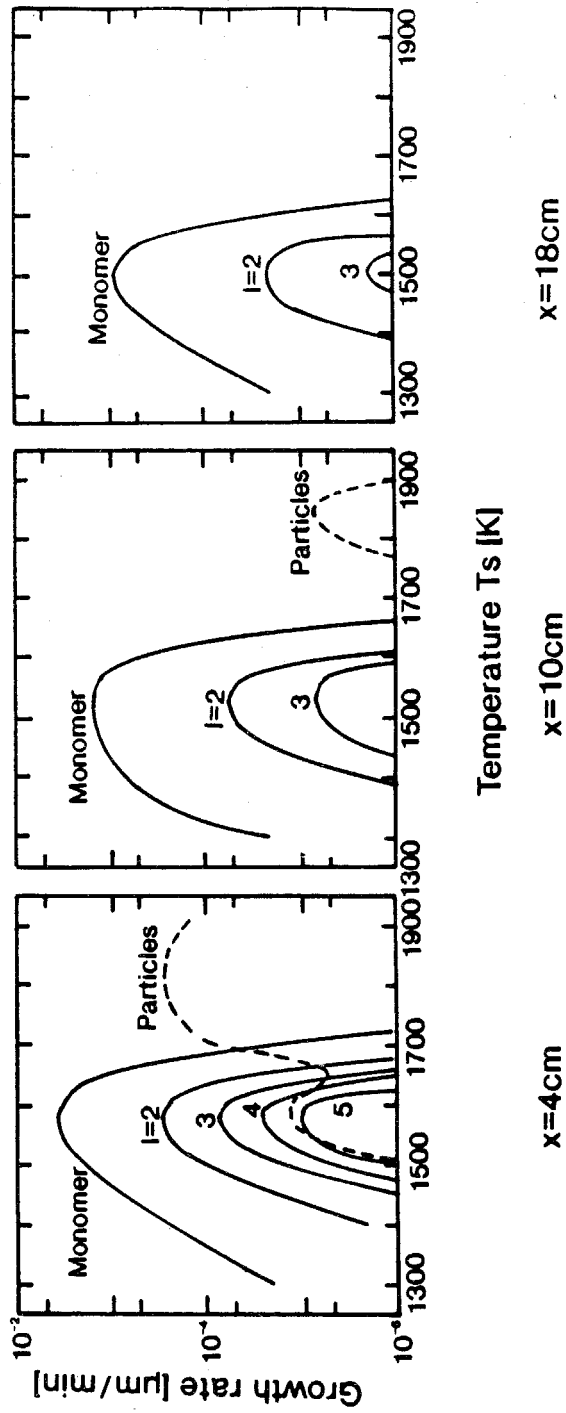


Figure 12b



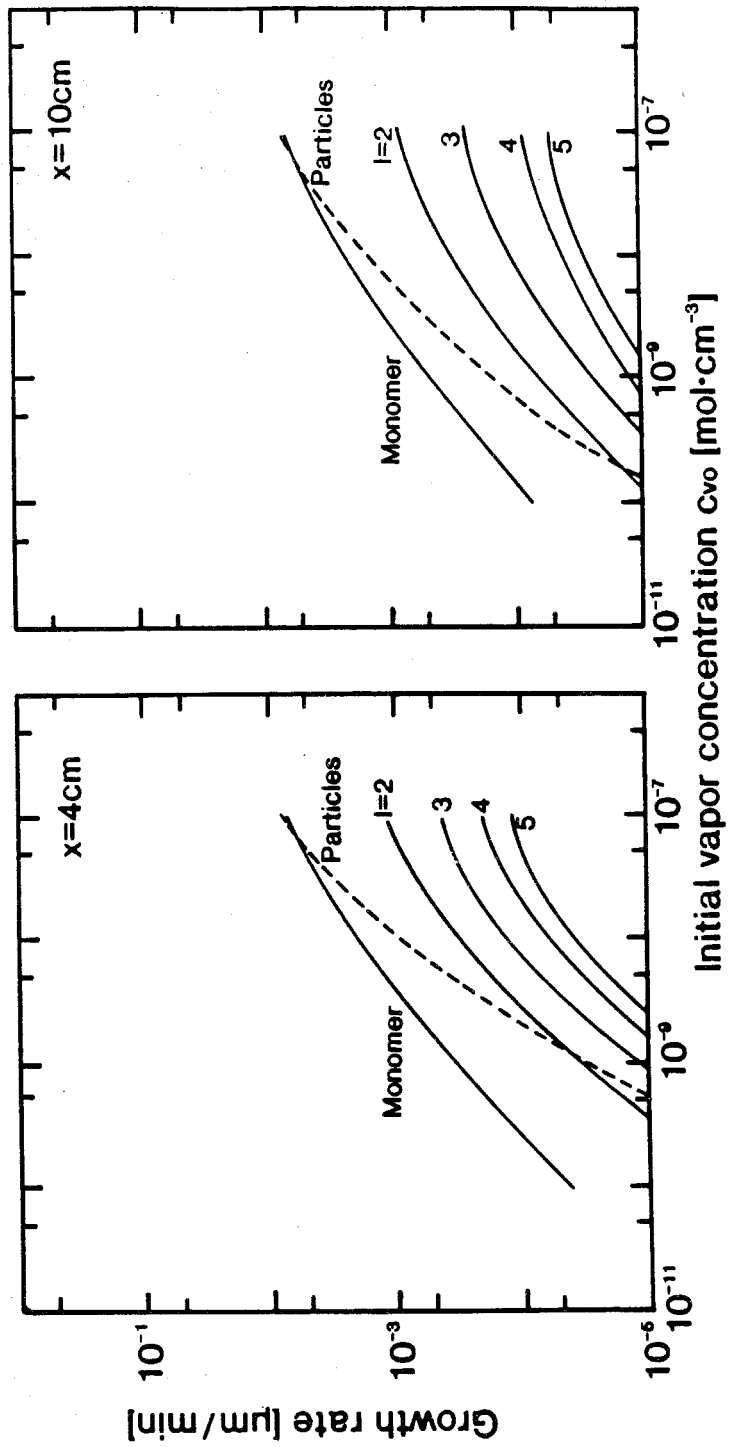


Figure 13a

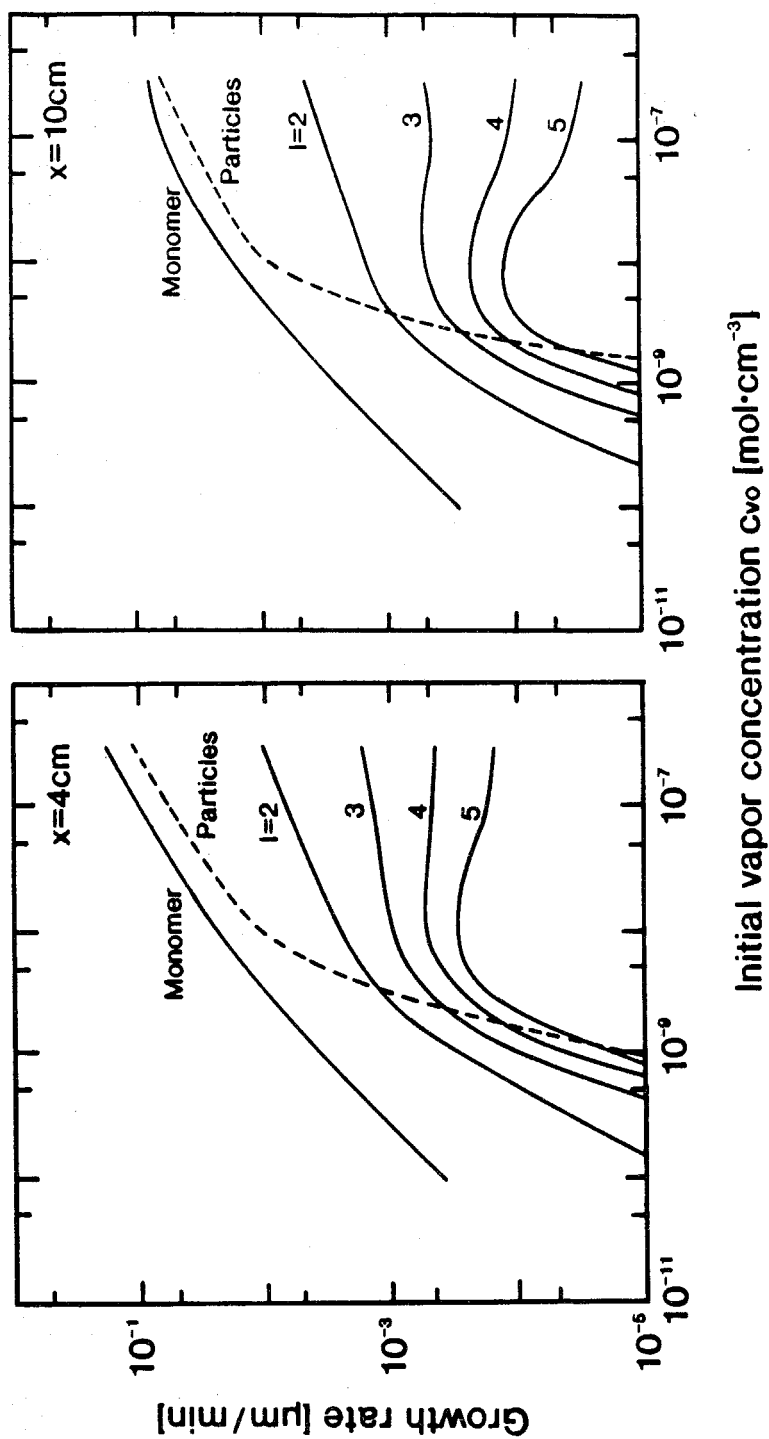


Figure 13b

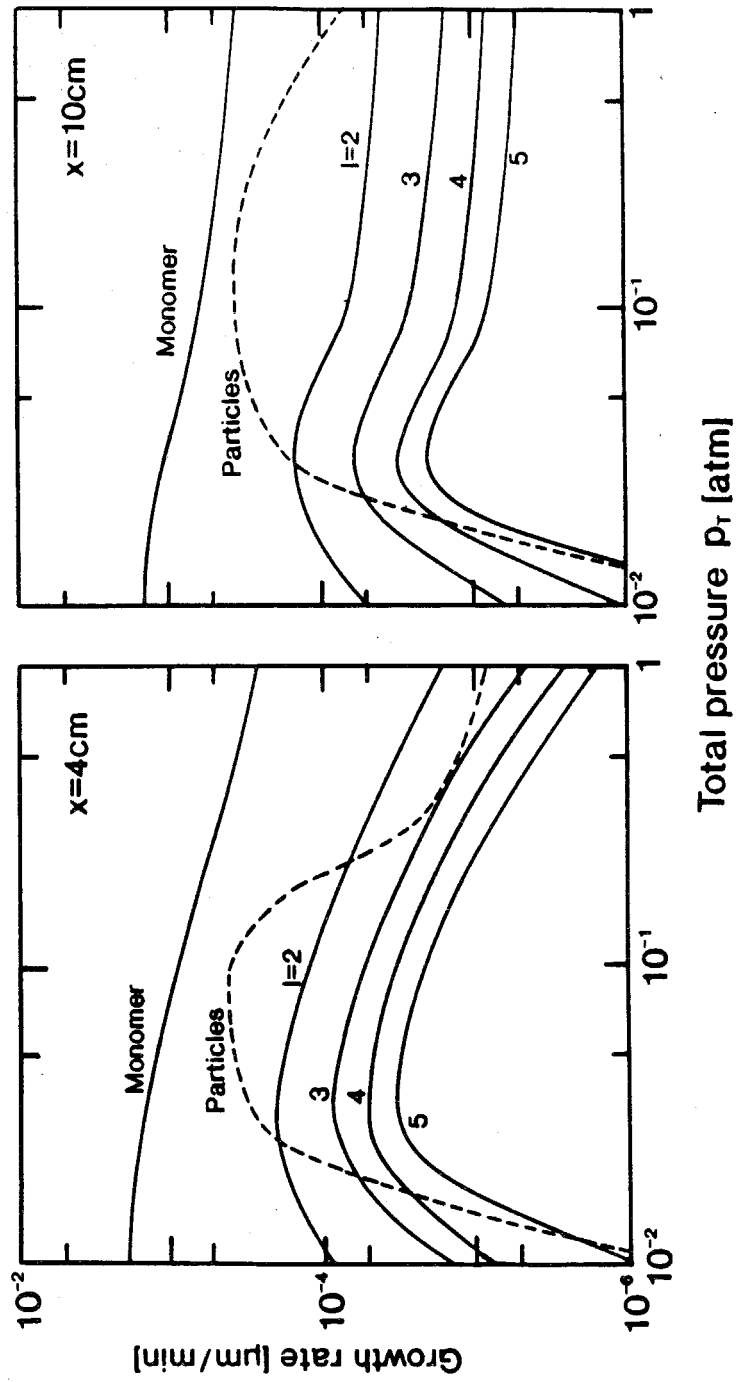


Figure 14

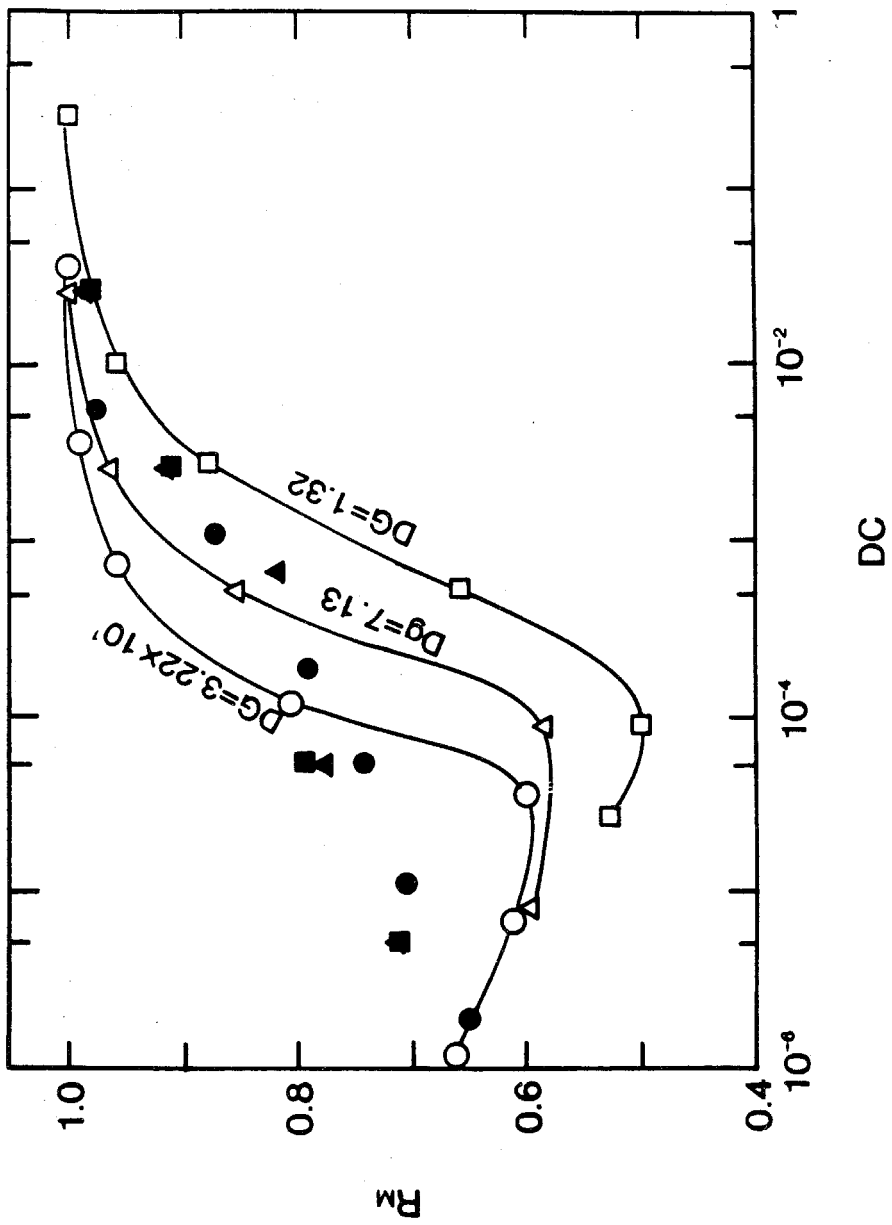


Figure 15

## **CHAPTER 7**

# **REEXAMINATION OF HOMOGENEOUS NUCLEATION FREE ENERGY CHANGE**

**Submitted for publication in  
Journal of Statistical Physics, 1990**

## ABSTRACT

The free energy change of cluster formation in homogeneous nucleation is re-examined by statistical mechanics. We show that the law of mass action can be obtained regardless the choice of ensemble used. The Maxwell Demon assumption in the classical nucleation formulation is discussed. The inclusion of the cluster translational and rotational motion in the cluster formation free energy change is shown to be appropriate. The cluster free energy change expressions from classical and statistical thermodynamics are shown to be consistent. Earlier work of Blander and Katz and of Fukuta is commented upon.

### Key Words:

Nucleation, cluster, free energy change, partition function, supersaturation, nonequilibrium, law of mass action, Maxwell Demon.

## INTRODUCTION

The first complete theory of homogeneous nucleation, now called the classical theory, was developed by Volmer and Weber (1), Farkas (2), Becker and Doering (3), and Zeldovich (4). It is apparent in the classical theory that a dominant factor in predicting the rate of homogeneous nucleation of a vapor is the free energy change of the formation of a cluster. The classical theory uses bulk properties of liquids, such as the bulk surface tension and bulk liquid density, to predict the cluster formation free energy change. The latter is thus the sum of the free energy of the same number of monomers in the bulk liquid and the cluster surface free energy.

Frenkel (5), Kuhrt (6), Lothe and Pound (7-9), Dunning (10), and Reiss and coworkers (11-14) have argued that the free energy of a cluster should include translational, rotational, and vibrational contributions. The theory of Lothe and Pound (7-9) indicates that for a common vapor at room temperature, the predicted nucleation rate is higher than the classical theory prediction by a factor of about  $10^{17}$ . Reiss *et al.* (13, 14) disagreed with the Lothe-Pound viewpoint and raised the "translational-rotational paradox;" they argued that the cluster center of mass may only fluctuate with high probability over a volume comparable to that of the cluster, not in the entire gas-cluster system. The final nucleation rate predicted by Reiss *et al.* (14) remains a value within a factor between  $10^4$  and  $10^5$  of that predicted by the classical theory. However, Lothe and Pound (9,15) and Abraham and Pound (16) pointed out that the internal distortions associated with the center-of-mass movements considered by Reiss and Katz (13) must also be regarded as phases of the internal oscillations of droplets in the vapor and are present with the same probability either in the cluster or in the bulk phase.

The Lothe-Pound theory is still controversial; Blander and Katz (17) argued that the basis for the Lothe-Pound theory is inconsistent with classical thermodynamics, however, Nishioka and Russell (18) suggested that Blander and Katz misinterpreted the Gibbs' definition of surface energy. Nishioka and Russell asserted that disproof or confirmation of the Lothe-Pound treatment must be based on a statistical mechanical model. Blander and Katz (19) later pointed out that Nishioka and Russell's work is in error because the latter authors incorrectly handled the standard states. More recently, Fukuta (20) argued that Lothe-Pound theory is erroneous because the traditional canonical ensemble formulation in the Lothe-Pound theory should be replaced by one based on the grand canonical ensemble.

Despite the above interpretations, the Lothe-Pound considerations for cluster translational, rotational, and vibrational motions, indeed have led to a mixing of classical thermodynamics and statistical mechanics; that is, the surface and volume contributions to the cluster formation free energy change are obtained from a macroscopic viewpoint, and the translational and rotational contributions are obtained in a microscopic sense. Because the problem of finding free energy change expressions in the limit of very small clusters must be faced, there naturally arises another theory that is more securely grounded at the molecular level, now known as the *atomistic theory* (21-26) since it was first used for situations involving monatomic species. This theory is based purely on statistical mechanics which provides formulas for the cluster translational, rotational, and vibrational partition functions. One can then relate the total partition function of the cluster and the absolute cluster free energy through thermodynamics, and the free energy change of the gas-cluster system can be subsequently evaluated.

Questions naturally arise: Would different statistical ensemble formulations



lead to different results as suggested by Fukuta (20)? In the atomistic theory, the cluster translational and rotational motions are accounted for, so would any disproof of the Lothe-Pound inclusion of cluster translational and rotational motions be contradictory to the atomistic theory? Since classical thermodynamics must be consistent with the statistical mechanical results, can a formulation of free energy change based on statistical mechanics reach the same conclusion as in Blander and Katz's paper (17)? If not, then where is the discrepancy? We intend to address these questions in this paper.

In the next section, we will use statistical mechanics based on a canonical ensemble to determine the most probable cluster concentration distribution and to obtain a relation between cluster concentrations and the monomer concentration, the law of mass action. The purpose is to demonstrate that the law of mass action can be obtained equally from a canonical ensemble formulation as well as from a grand canonical ensemble formulation (27). It will be shown that a crucial factor in the determination of the free energy change is the cluster canonical ensemble partition function. We will discuss how the free energy change interfaces with the evaluation of the nucleation rate. The Maxwell Demon assumption in traditional nucleation kinetics will also be commented upon.

In the remainder sections of the paper, we start from the law of mass action and cluster partition function to confirm the necessity of the inclusion of cluster translational and rotational motion in the free energy change. The omission of intramolecular motion in the formulation is also discussed. A general discussion of the papers by Blander and Katz (17) and Fukuta (20) will be given.

## STATISTICAL MECHANICS OF THE GAS-CLUSTER SYSTEM

Assuming the gas contains a mixture of noninteracting clusters, clusters of each size are individually an ideal gas, and the canonical ensemble partition function of the entire system, over the distribution of particle sizes, can be written as

$$Q(N, V, T) = \sum_{\{n_i\}} \prod_{i=1}^l \frac{q_i^{n_i}}{n_i!} \quad [1]$$

where  $q_i$  is the  $i$ -mer partition function,  $l$ -mer is the largest cluster size considered,  $n_i$  is the number of  $i$ -mers, and  $\sum_{\{n_i\}}$  denotes summing over all possible sets of the distribution of  $n_i$ .  $V$  is the free volume of the entire gas-cluster system. For a particular set of  $\{n_i\}$ , the sum of all monomers in clusters must equal  $N$ , the total number of molecules in the system,

$$\sum_{i=1}^l i n_i = N. \quad [2]$$

In evaluating  $Q(N, V, T)$ , the sum of all possible sets of  $\{n_i\}$  in Eq. [1] can be approximated by a largest term in which the set of the distribution  $n_i$  is the most probable distribution,  $\{n_i\} = \{n_i\}^*$ . To determine  $n_i$  ( $i = 1, \dots, l$ ) in the most probable set  $\{n_i\}^*$ , one uses the method of undetermined Lagrange multipliers subject to the constraint of Eq. [2] with an understanding that  $Q$  is a constant for a small variation of  $n_i$ ,

$$\frac{\partial}{\partial n_i} \left[ \ln Q - \alpha \sum_{i=1}^l i n_i \right] = 0 \quad [3]$$

where  $\alpha$  is the undetermined Lagrange multiplier. Using Stirling's formula for approximating  $\ln n!$ , Eq. [1] gives

$$\ln Q(N, V, T) = \sum_{i=1}^l n_i \left[ \ln \left( \frac{q_i e}{n_i} \right) \right] . \quad [4]$$

Therefore, Eq. [3] yields

$$n_i = \frac{q_i}{e^{i\alpha}} . \quad [5]$$

Applying  $i = 1$  and  $i = i$  in Eq. [5], one gets the "law of mass action,"

$$n_i = n_1^i \frac{q_i}{q_1^i} . \quad [6]$$

Equation [5] can be alternatively derived from the formulation involving the grand canonical ensemble partition function (27). Equation [6] gives the number of  $i$ -mers ( $i = 1, \dots, l$ ) in the most probable set  $\{n_i\}^*$ . Now with  $n_i$  so determined, a relation between the chemical potential of an  $i$ -mer and that of a monomer can be subsequently found by

$$\mu_i = -k_B T \left( \frac{\partial \ln Q}{\partial n_i} \right)_{T, V, n_{k \neq i}} = -k_B T \ln \left( \frac{q_i}{n_i} \right) = i k_B T \ln \left( \frac{n_1}{q_1} \right) = i \mu_1 \quad [7]$$

where  $k_B$  is the Boltzmann constant. In other words, for arbitrary reaction at equilibrium,



the Gibbs free energy change is zero ( $\mu_j - \mu_{i-j} - \mu_i = 0$ ). True equilibrium only occurs when the system is at saturation or under saturation. The saturation ratio is defined by

$$S = \frac{p_1}{p_{\{\text{sat}\}}} \quad [9]$$

where  $p_1$  is the monomer partial pressure, and  $p^{\{\text{sat}\}}$  is the saturation pressure. Because the monomers are in a much higher concentration than the clusters,  $p_1$  is related to the total free volume  $V$  by the ideal gas law,

$$V = \frac{n_1 k_B T}{p_1} = \frac{n_1 k_B T}{p^{\{\text{sat}\}} S} . \quad [10]$$

For supersaturation conditions ( $S > 1$ ), an artificial equilibrium may be imposed if one invokes the concept of a "Maxwell Demon" that can disintegrate the  $l$ -mers (*i.e.*, the largest clusters in the system) back into monomers. There has been discussion about whether invoking the Maxwell Demon is necessary in formulating nucleation kinetics (28). It is useful to digress briefly to consider this issue. If one writes the  $i$ -mer concentration from the law of mass action, Eq. [6], for both  $S = 1$  (no Maxwell Demon) and  $S > 1$  (with Maxwell Demon), one obtains

$$n_i^{\{\text{sat}\}} = n_1^{\{\text{sat}\}} \exp \left[ -\frac{1}{k_B T} (F_i - iF_1 + (1-i)k_B T \ln n_1^{\{\text{sat}\}}) \right] \quad [11a]$$

$$n_i = n_1 \exp \left[ -\frac{1}{k_B T} (F_i - iF_1 + (1-i)k_B T \ln n_1) \right] \quad [11b]$$

in which

$$F_i = -k_B T \ln q_i \quad [12]$$

is the absolute Helmholtz energy for an  $i$ -mer;  $n_i^{\{\text{sat}\}}$  and  $n_i$  are the numbers of  $i$ -mers in the system at  $S = 1$  and  $S > 1$ , respectively. Our purpose in determining the  $i$ -mer concentration from either Eq. [11a] or Eq. [11b] is to express the rate of loss of monomers from a cluster, the evaporation coefficient, in terms of the rate of collision of monomers with clusters through a detailed balance in either a saturation equilibrium condition or a supersaturation constrained equilibrium condition,

$$e_i^{\{S=1\}} = \frac{\beta_{1,i-1}(n_1^{\{\text{sat}\}}/V)(n_{i-1}^{\{\text{sat}\}}/V)}{(n_i^{\{\text{sat}\}}/V)} \quad [13a]$$

$$e_i^{\{S>1\}} = \frac{\beta_{1,i-1}(n_1/V)(n_{i-1}/V)}{(n_i/V)} \quad [13b]$$

such that the net rate passing from the  $(i-1)$ -mers to the  $i$ -mers (or the so-called “forward flux”) in a nonequilibrium supersaturated system can be evaluated. In Eqs. [13a] and [13b],  $\beta_{1,i-1}$  is the coagulation coefficient between a monomer and an  $(i-1)$ -mer; the expression for the coagulation coefficient can be obtained from the gas kinetics. By denoting the nonequilibrium  $i$ -mer concentration as  $f_i$ , this forward flux can be written as

$$J_i(t) = \beta_{1,i-1} \frac{n_1(t)}{V} f_{i-1}(t) - e_i f_i(t) . \quad [14]$$

The relevant question is which expression, Eq. [13a] or Eq. [13b], should be used for the realistic *supersaturated nonequilibrium evaporation coefficient*,  $e_i$ , to evaluate the forward flux. There is no rigorous way to exactly evaluate  $e_i$  because nucleation is indeed a nonequilibrium process. If Eq. [13a] is used, no Maxwell Demon is invoked; one first has to approximate that the evaporation coefficient  $e_i^{\{S=1\}}$  can be used in a supersaturated state ( $S > 1$ ), and then assume that  $e_i^{\{S=1\}}$ , though obtained from an equilibrium condition, can be used in a nonequilibrium situation. If, on the other hand, Eq. [13b] is used, a Maxwell Demon is invoked, and one only has to approximate the supersaturated *nonequilibrium* evaporation coefficient,  $e_i$ , as the supersaturated *constrained equilibrium* evaporation coefficient,  $e_i^{\{S>1\}}$ . It is our opinion that, of the two possible approximations, the second one seems more defensible because conditions at the actual  $S$  are being used. While some authors have criticized the Maxwell Demon assumption because a constrained equilibrium does not occur realistically, we would like to point out

that in a nucleation process, one deals with realistic concentrations  $f_i(t)$  under a supersaturated state, not  $n_i^{\{\text{sat}\}}/V$  under a saturation state. This issue is relevant to the present work because we will use Eq. [11b] rather than Eq. [11a] to interpret the energy change of formation of an  $i$ -mer in the next section.

## THE CLUSTER FREE ENERGY CHANGE

Upon assuming that for a cluster the Hamiltonian of translational energy is separable from that of the vibrational, rotational and binding energies, and electronic and quantum effects are not considered, the canonical ensemble partition function of an  $i$ -mer can be written as

$$q_i = q_{i,\text{trans}} q_i^* \quad [15]$$

where  $q_i^*$  represents the partition function of an  $i$ -mer due to rotation, vibration and cluster binding. To a first approximation, one can assume ideal gas for evaluation of  $q_{i,\text{trans}}$ ,

$$q_{i,\text{trans}}(T, V) = V \left( \frac{2\pi m_1 i k_B T}{h^2} \right)^{3/2} = \frac{V i^{3/2}}{\Lambda^3} \quad [16]$$

where  $m_1$  is the mass of a monomer,  $\Lambda = h/\sqrt{2\pi m_1 k_B T}$  is the de Broglie wavelength, and  $h$  is Planck's constant.

The absolute Helmholtz energy of an  $i$ -mer is related to the  $i$ -mer partition function and can be written as

$$F_i = -k_B T \ln q_i = -k_B T \ln(q_{i,\text{trans}} q_i^*) . \quad [17]$$

The monomer Helmholtz energy is given by

$$F_1 = -k_B T \ln\left(\frac{V}{\Lambda^3}\right) = -k_B T \ln\left(\frac{n_1 k_B T}{\Lambda^3 p_{\{\text{sat}\}} S}\right). \quad [18]$$

If we write Eq. [11b] in the form

$$n_i = n_1 \exp(-\Delta F_i^\dagger / k_B T) \quad [19]$$

where  $\Delta F_i^\dagger$ , upon using Eqs. [17] and [18], is given by

$$\Delta F_i^\dagger = -k_B T \left[ \ln\left(\frac{i^{3/2} V}{\Lambda^3 n_1}\right) + \ln q_i^* \right] - i k_B T \ln\left(\frac{1}{\Lambda^3} \frac{V}{n_1}\right). \quad [20]$$

The RHS of Eq. [20] is the difference of the absolute Helmholtz energies of an  $i$ -mer and that of a system composed of  $i$  gaseous monomers at the same temperature  $T$  in a gaseous molecular volume  $V/n_1$ . We will refer to  $\Delta F_i^\dagger$  as the "free energy change" in the remainder of the text. Equation [20] can be further rewritten in the form

$$\Delta F_i^\dagger = -k_B T \ln\left(\frac{i^{3/2} k_B T}{\Lambda^3 p_{\{\text{sat}\}} S}\right) - i k_B T \ln S - k_B T \ln q_i^* + i k_B T \ln\left(\frac{k_B T}{\Lambda^3 p_{\{\text{sat}\}}}\right). \quad [21]$$

The first two terms on the RHS of Eq. [21] are the contributions due to the  $i$ -mer translational motion and volume creation. In particular, the first term indicates that the  $i$ -mer translational energy is due to the  $i$ -mer translation in a molecular volume in the gaseous state at  $p_1$  and  $T$ ,  $k_B T/p_1$ , not the entire free volume  $V = n_1 k_B T/p_1$ . This is in agreement with the Lothe-Pound free energy expression (7). The cluster rotational motion is implicitly accounted for in the third term on the RHS of Eq. [21]. The work needed to create the  $i$ -mer surface, the so-called surface contribution, should be also evaluated from the third and the fourth terms on the RHS of Eq. [21].

The puzzle regarding the inclusion of the cluster translational motion, the first term on the RHS of Eq. [21], in the formulation of cluster free energy change can be revealed if we find an expression for the saturation vapor pressure  $p^{\{\text{sat}\}}$ . We do this by equating the chemical potential of a molecule at its saturated gaseous and liquid states. The chemical potential of a gaseous monomer at saturation is given by

$$\mu_{\text{gas}}^{\{\text{sat}\}} = -k_B T \ln \left( \frac{k_B T}{p^{\{\text{sat}\}} \Lambda^3} \right). \quad [22]$$

The chemical potential of a liquid molecule at saturation is

$$\mu_{\text{liq}}^{\{\text{sat}\}} = \left. \frac{\partial F_i}{\partial i} \right|_{i \rightarrow \infty} \bigg|_{T,V} = -k_B T \left. \frac{\partial (\ln q_i)}{\partial i} \right|_{T,V,i \rightarrow \infty}. \quad [23]$$

Equating, one finds

$$p^{\{\text{sat}\}} = \frac{k_B T}{\Lambda^3} \exp \left( \frac{\mu_{\text{liq}}^{\{\text{sat}\}}}{k_B T} \right) = \frac{k_B T}{\Lambda^3} \exp \left( - \left. \frac{\partial (\ln q_i)}{\partial i} \right|_{i \rightarrow \infty} \right). \quad [24]$$

Therefore,  $\Delta F_i^\dagger$  becomes

$$\Delta F_i^\dagger = -k_B T \ln \left( \frac{q_{i,\text{trans}}}{n_1} \right) - i k_B T \ln S - k_B T \ln q_i^* + i \left[ \left. \frac{\partial (\ln q_i)}{\partial i} \right|_{i \rightarrow \infty} \right]. \quad [25]$$

The bracketed part of the last term on the RHS of Eq. [25] is not a function of  $i$  because the saturation vapor pressure in Eq. [24] is evaluated through a chemical potential balance over a bulk liquid surface ( $i \rightarrow \infty$ ). The translational term, the first term on the RHS of Eq. [25], is associated with  $\ln i^{3/2}$  (see Eq. [16]), and it cannot be cancelled by any means with the fourth term. A similar conclusion can be made for the cluster rotational contribution, because the  $i$ -mer rotational motion is implicitly accounted for in the third term on the RHS of Eq. [25],



$-k_B T \ln q_i^*$ , and it cannot be cancelled with the fourth term. We thus conclude that the inclusion of the cluster translational and rotational motion is appropriate in the cluster free energy change in nucleation.

Before ending this section, we digress to comment upon the above partition function formulation. In Eq. [18], we ignored the *intramolecular* vibrational and rotational motion; the latter should indeed be taken into account since a monomer is in general a polyatomic molecule. However, the intramolecular motion can be assumed to remain the same in a cluster though the molecule is a part of it. In other words, if one adds an additional term  $-k_B T \ln q_{1,\text{intra}}$  to the RHS side of Eq. [18] to include intramolecular motion, the RHS of Eq. [15] must also be multiplied by a factor of  $q_{1,\text{intra}}^i$  for the same purpose. As a net result, in Eq. [21] the intramolecular contributions cancel exactly. The assumption that the intramolecular motions are the same in an isolated molecule and in a molecule of a large cluster is reasonable especially for larger clusters because molecules in a large cluster presumably can vibrate and rotate more freely than molecules in a smaller cluster. The same assumption, however, if introduced in the atomistic theory (21-26), may cause some errors in the estimation of free energy change.

## COMMENTS ON PRIOR PAPERS

The free energy change,  $\Delta F_i^\dagger$ , obtained by statistical thermodynamics must be in agreement with those obtained by classical thermodynamics. In the previous section, we have seen that statistical thermodynamics *does* support the inclusion of the cluster translational and rotational motion in the free energy change. This must be reconciled with the disproof of the Lothe-Pound theory by Blander and Katz (17) via a classical thermodynamic route. We will point out the discrepancies in Blander and Katz's paper. Another disproof of the Lothe-Pound theory by Fukuta

(20) will also be commented on.

Blander and Katz (17) were the first to attempt to use only classical thermodynamics to disprove the Lothe-Pound inclusion of cluster translational and rotational motion in the cluster free energy change. They started by equating the equilibrium constants at constrained supersaturation and saturation conditions,

$$K_p \equiv \frac{p_i/p^0}{p_1/p^0} = \frac{p_i^{\{\text{sat}\}}/p^0}{p_1^{\{\text{sat}\}}/p^0} \quad [26]$$

and obtained

$$\Delta F_i^\dagger = -(i-1)k_B T \ln S + [\mu_i^0 - \mu_1^0 - (i-1)\mu_{\text{liq}}^{\{\text{sat}\}}] . \quad [27]$$

In Eq. [26],  $p_i$  is the partial pressure of the  $i$ -mers at a constrained supersaturation,  $p^0$  is an arbitrary standard state,  $p_i^{\{\text{sat}\}}$  is the partial pressure of the  $i$ -mers at a saturation condition ( $S = 1$ ). In Eq. [27],  $\mu_i^0$  and  $\mu_{\text{liq}}^{\{\text{sat}\}}$  are the chemical potentials of a gaseous  $i$ -mer at the chosen standard state and of a molecule in the liquid phase at  $S = 1$ , respectively. Blander and Katz then argued that, from Eq. [27], the coefficient of  $\ln S$  is  $(i-1)$ , not  $i$ , and the second bracketed term on the RHS of Eq. [27],  $\mu_i^0 - \mu_1^0 - \dots$ , simply states that to form a gaseous  $i$ -mer the overall translational contribution can only enter as the difference between the translational contributions of *an  $i$ -mer* and *a monomer*, not the translational contribution of an  $i$ -mer only as in the statistical expression (see the first term on the RHS of Eq. [25]). Nishioka and Russell (18) disagreed with Blander and Katz's paper by commenting that the interpretation of the second term on the RHS of Eq. [27] is erroneous while they agreed with Blander and Katz's thermodynamic formulation. Blander and Katz (19) responded to Nishioka and Russell's comments by pointing out that the latter authors chose a standard state  $p^0 = p_1$  to reach an incorrect criticism.

As we will now demonstrate, Blander and Katz's starting equation, Eq. [26] (*i.e.*, Eq. [2] in Ref. (18)), may lead to some thermodynamic discrepancies and influence the following discussions by Nishioka and Russell (18) and by Blander and Katz (19). Equation [26] presents a paradox; it simply states that "the equilibrium constants for an arbitrary reaction at a constrained equilibrium ( $S > 1$ ) and a saturation condition ( $S = 1$ ) are equal." We will now show this to be equivalent to saying that we do not need a Maxwell Demon problem.

Considering a monomer-addition reaction,  $A_{i-1} + A_1 \rightleftharpoons A_i$ , the equilibrium constant can be written as

$$K_i = \frac{n_i/V}{(n_{i-1}/V)(n_1/V)} = \frac{\beta_{1,i-1}}{e_i}; \quad [28]$$

If the equilibrium constant at  $S = 1$  and  $S > 1$  are equal,  $K_i^{\{S>1\}} = K_i^{\{S=1\}}$ , from Eq. [28] one must have

$$\beta_{1,i-1}/e_i^{\{S>1\}} = \beta_{1,i-1}/e_i^{\{S=1\}}. \quad [29]$$

In other words, a consequence of equating the equilibrium constant at  $S = 1$  and  $S > 1$  is that evaporation coefficients of an  $i$ -mer at these conditions are equal.

The overall equilibrium constant  $K$  of the reaction  $i A_1 \rightleftharpoons A_i$ , can be written as

$$K^{\{S>1\}} = \prod_{j=1}^{i-1} \beta_{1,j}/e_{j+1}^{\{S>1\}} = \prod_{j=1}^{i-1} \beta_{1,j}/e_{j+1}^{\{S=1\}} = K^{\{S=1\}} \quad [30]$$

which is just Eq. [26] (here we used the equilibrium constant  $K$  based on concentrations). Therefore we see that an implication of Eq. [26] is assuming that  $e_i^{\{S=1\}} = e_i^{\{S>1\}}$ ; that is, one need not invoke the Maxwell Demon assumption to

obtain the final value of the evaporation coefficient. On the other hand, if one takes the ratio of Eq. [13a] and [13b], one has, for sufficiently large  $i$ ,

$$\frac{e_i^{\{S=1\}}}{e_i^{\{S>1\}}} = \frac{n_i}{n_{i-1}} \frac{n_{i-1}^{\{\text{sat}\}}}{n_i^{\{\text{sat}\}}} \frac{1}{S} \approx \frac{1}{S} . \quad [31]$$

That is, from only detailed balance formulations,  $e_i^{\{S=1\}}$  and  $e_i^{\{S>1\}}$  are found to differ by about a factor of  $S$ . Thus the assumption that  $e_i^{\{S=1\}} = e_i^{\{S>1\}}$ , as well as Eq. [26], contradict the results from thermodynamic detailed balancing. An explanation of the incorrectness of Eq. [26] is that at a constrained equilibrium situation ( $S > 1$ ), additional work must be added to the system to decompose a large cluster into monomers, and thus the equilibrium constant would be different from that at a saturation condition ( $S = 1$ ).

We now show what one can do from classical thermodynamics. The chemical potential of an  $i$ -mer at a constrained equilibrium condition  $S > 1$  is

$$\mu_i = \mu_i^0 + k_B T \ln \frac{p_i}{p^0} . \quad [32]$$

For the reaction  $iA_1 \rightleftharpoons A_i$ , from Eq. [7], the chemical potential difference of this equilibrium reaction is zero,

$$0 = \mu_i - i\mu_1 = \mu_i^0 - i\mu_1^0 + k_B T \ln \frac{p_i/p^0}{(p_1/p^0)^i} . \quad [33]$$

Equation [33] can be written in the form

$$p_i = p_1 \exp \left[ -\frac{1}{k_B T} \left( \mu_i^0 - i\mu_1^0 - \{i-1\} k_B T \ln \frac{p_1}{p^0} \right) \right] . \quad [34]$$

Equation [34] represents the full extent that classical thermodynamics can reach in the evaluation of the  $i$ -mer concentration. Using Eqs. [32], [7], and [12], and

the ideal gas law,  $p_i V = n_i k_B T$ , one can transform Eq. [34] into Eq. [11b], the result obtained by statistical mechanics. Therefore, as expected, classical and statistical thermodynamics do agree. However, unlike the statistical results, classical thermodynamics does not provide an explanation of the free energy change term, the parenthesized term in Eq. [34]. Therefore, one must postulate its physical significance if only classical thermodynamics is used. The classical nucleation theory corresponds to postulating that since the  $i$ -mers are in thermal equilibrium, the probability that they have a certain energy  $\Delta F_i^\dagger$  is just the probability for their existence, if we interpret  $\Delta F_i^\dagger$  as the energy of formation of an  $i$ -mer. The question then becomes: what is the appropriate energy of formation of an  $i$ -mer; should it include the cluster translational and rotational motion? This is the often debated classical issue. The statistical mechanical expression for  $\Delta F_i^\dagger$ , Eq. [21], does not have this problem; each of the terms is clearly defined and the cluster translational and rotational motions were shown earlier to be accounted for.

In the paper by Blander and Katz (17), classical thermodynamics is applied differently than in the above formulation; they wrote the chemical potential of an  $i$ -mer at  $S = 1$ ,  $\mu_i^{\{\text{sat}\}}$ , as

$$i \mu_{\text{liq}}^{\{\text{sat}\}} = \mu_i^{\{\text{sat}\}} = \mu_i^0 \{\text{sat}\} + k_B T \ln \frac{p_i^{\{\text{sat}\}}}{p^0} . \quad [35]$$

The standard chemical potentials of an  $i$ -mer at  $S > 1$  and  $S = 1$ ,  $\mu_i^0$  and  $\mu_i^0 \{\text{sat}\}$ , must be equal, because the standard states in Eqs. [32] and [35] must be the same,

$$\mu_i^0 = \mu_i^0 \{\text{sat}\} ; \quad [36]$$

so combining Eqs. [32] and [35], one obtains

$$p_i = p_1 \exp \left[ -\frac{1}{k_B T} \left( \mu_i - \mu_{\text{liq}}^{\{\text{sat}\}} + k_B T \ln \frac{p_i^{\{\text{sat}\}}}{p_1} \right) \right] . \quad [37]$$

Blander and Katz used Eq. [26] to express the  $i$ -mer partial pressure at  $S = 1$ ,  $p_i^{\{\text{sat}\}}$ , in terms of the saturation ratio  $S$ . However, classical thermodynamics itself does not provide any explanation of  $p_i^{\{\text{sat}\}}$  (or  $n_i$ ), and therefore Eq. [37] is again a dead end.

In the remainder of this section, we comment on Fukuta's criticism (20) of the inclusion of cluster translational and rotational motion. Fukuta argued that the ensemble used in the formulation of statistical mechanics should be the *grand canonical ensemble* instead of the canonical ensemble because we are dealing with an open system, and as a consequence, the translational and rotational motions are "screened" on purpose and should not be taken into account. Fukuta's viewpoint is nevertheless erroneous, because the thermodynamic results are independent of the ensembles chosen; as pointed out by Hill (29) "... one can choose an ensemble from which to calculate thermodynamic functions on the basis of convenience, and irrespective of the actual environment of a system (heat bath, constant pressure, etc.)." A direct support of Hill's statement is that we have shown earlier that the mass action law, Eq. [6], is obtainable by a canonical ensemble formulation, and the same result can be obtained from a grand canonical ensemble formulation (27).

Fukuta (20) wrote, "... the grand canonical ensemble thus describes the status or the probability of a system whose internal energy level and the number of molecules are *simultaneously* but *independently*  $U$  (an energy state) and  $N$  (total number of clusters)." and "... the  $U$  term drops out from the probability of our interest, and it may be considered as screened." The energy state  $U$  in the grand canonical ensemble is indeed a function of  $N$  (29) and therefore  $U$  cannot be "screened on purpose."

## SUMMARY AND CONCLUDING REMARKS

In this paper, we have reexamined the homogeneous nucleation free energy change. We summarize our findings as follows. First, from a statistical mechanical point of view, the inclusion of cluster translational and rotational motion in the nucleation free energy change is shown to be appropriate. As an aside, it is our opinion that the Maxwell Demon assumption in the evaluation of the evaporation coefficient is more defensible than if it is not invoked. The omission of intramolecular motion in the nucleation thermodynamic formulation is a reasonable assumption especially for large clusters. We have shown the extent of classical thermodynamics in the evaluation of cluster free energy change, and we have demonstrated the agreements between classical and statistical thermodynamic formulations in the cluster free energy change.

## ACKNOWLEDGEMENTS

This work is supported by National Science Foundation Grant ATM-9003186.

## REFERENCES

1. Volmer, M., and Weber, A., *Z. Phys. Chem. (Leipzig)* **119**, 277 (1926).
2. Farkas, L., *Z. Phys. Chem.* **125**, 236 (1927).
3. Becker, R., and Doering, W., *Ann Phys.* **24**, 719 (1935).
4. Zeldovich, Y. B., *Zh. Eksp. Teor. Fiz.* **12**, 525 (1942).
5. Frenkel, J., "Kinetic Theory of Liquids," Chapt. 7. Oxford University Press, New York, 1946.
6. Kuhrt, F., *Z. Phys.* **131**, 185, 205 (1952).
7. Lothe, J., and Pound, G. M., *J. Chem. Phys.* **36**, 2080 (1962).
8. Lothe, J., and Pound, G. M., *J. Chem. Phys.* **45**, 630 (1966).
9. Lothe, J., and Pound, G. M., *J. Chem. Phys.* **48**, 1849 (1968).
10. Dunning, W. J., "Colloques Internationaux du Centre National de la Recherche Scientifique," No. 152, p. 369. CNRS, Paris, 1965.
11. Reiss, H., *J. Stat. Phys.* **2**, 83 (1970).
12. Reiss, H., in "Nucleation Phenomena," (A. C. Zettlemoyer Ed.), Vol. 7, pp. 1-66. Elsevier, New York, 1977.
13. Reiss, H., and Katz, J. L., *J. Chem. Phys.* **46**, 2496 (1967).
14. Reiss, H., Katz, J. L., and Cohen, E. R., *J. Chem. Phys.* **48**, 5553 (1968).
15. Lothe, J., and Pound, G. M., in "Nucleation," (A. C. Zettlemoyer Ed.), Chapt. 3. Marcel Dekker, New York, 1969,
16. Abraham, F. F., and Pound, G. M., *J. Chem. Phys.* **48**, 732 (1968).
17. Blander, M., and Katz, J. L., *J. Statist. Phys.* **4**, 55 (1972).
18. Nishioka, K., and Russell, K. C., *Surf. Sci.* **104**, L213 (1981).
19. Blander, M., and Katz, J. L., *Surf. Sci.* **104**, L217 (1981).
20. Fukuta, N., in "Atmospheric Aerosols and Nucleation," (P. E. Wagner and G. Vali Ed.), pp. 462-465. Springer-Verlag, Berlin, 1988.



21. Reed, S. G., *J. Chem. Phys.* **20**, 208 (1952).
22. McGinty, D. J., *J. Chem. Phys.* **55**, 580 (1971).
23. McGinty, D. J., *Chem. Phys. Lett.* **13**, 525 (1972).
24. McGinty, D. J., *J. Chem. Phys.* **58**, 4733 (1973).
25. Burton, J. J., *J. Chem. Phys.* **52**, 345 (1970).
26. Hoare, M. R., and Pal, P., *Adv. Phys.* **20**, 161 (1971).
27. Pruppacher, H. R., and Klett, J. D., "Microphysics of Clouds and Precipitation," pp. 163-164. Reidel Publishing, 1980.
28. Katz, J. L., and Wiedersich, H., *J. Colloid Interf. Sci.* **61**, 351 (1977).
29. Hill, T. L., "An Introduction to Statistical Thermodynamics," Chapt. 1. Dover Publications, New York, 1986.

## **CHAPTER 8**

# **PREDICTION OF HOMOGENEOUS NUCLEATION FREE ENERGY CHANGE FROM THE CELL MODEL OF LIQUIDS**

**Submitted for publication in  
Journal of Chemical Physics, 1990**

## ABSTRACT

The free energy change of cluster formation in gas-phase homogeneous nucleation and the cluster partition functions are studied based on the cell model of liquids. We provide a new molecular level theory that is applicable in the larger cluster size range where liquid-like properties begin to emerge and a cluster surface is present. The microcluster surface tension can be appropriately defined. A microscopic expression for the surface tension variation with cluster size is obtained and the calculated result is compared with that predicted from the Tolman approach. The cluster rotational contribution to the free energy change is shown to become insignificant for liquid-like clusters. The energy change of cluster formation from the classical capillary approximation, Lothe-Pound theory and the atomistic theory are compared with that of the present theory.

## INTRODUCTION

The foundation of the prediction of the rate of nucleation of a vapor is the determination of the free energy change from the vapor to a molecular cluster. Classical homogeneous nucleation theory (1-4) employs bulk surface tension and bulk liquid density in evaluating the cluster formation free energy change. The Lothe-Pound theory (5-7) accounts for, in addition to the classical free energy terms, the contributions from cluster translational and rotational motion. Neither the classical nor Lothe-Pound theories provides a microscopic explanation of the nature of the cluster surface as the surface tension is ill-defined in the microcluster size range by classical thermodynamics. Unlike these two theories, the atomistic theory of nucleation (8-19) is grounded purely on a molecular level. Kulmala and coworkers (18, 19) were the first to attempt to obtain a closed form expression for the free energy change as a function of cluster size by the atomistic theory. One expects that the atomistic theory is most applicable for small clusters; for large clusters detailed information on cluster vibrational frequencies will be lacking as liquid-like properties begin to emerge. The atomistic theory, although based on a molecular level description, also does not reveal the nature of a surface, that is, there are no terms in the free energy change expression that are proportional to the number of cluster surface molecules.

In sum, a molecular level theory that provides a closed form expression for the free energy change associated with relatively large cluster formation is lacking. A natural result of such a theory should be a definition of the microcluster surface tension. The goal of this work is to employ a fundamental approach based on statistical mechanics, the cell model of liquids (20-23), to predict the free energy change in homogeneous nucleation. By this approach we will be able to appropriately define the microcluster surface tension; a closed form expression for the

surface contribution to the free energy change will be obtained with the surface energy contribution proportional to the number of cluster surface molecules.

## PARTITION FUNCTIONS AND FREE ENERGY CHANGE

The "law of mass action," obtained from either a grand canonical ensemble approach (24) or a canonical ensemble formulation (25), provides a relation between the number of  $i$ -mers and monomers through their partition functions,

$$n_i = n_1 \frac{q_i}{q_1} \quad [1]$$

where  $n_1$  and  $n_i$  are the number of monomers and  $i$ -mers in the system, respectively.  $q_1$  and  $q_i$  are the monomer and  $i$ -mer canonical ensemble partition functions. Equation [1] can be rewritten in the form

$$n_i = n_1 \exp \left[ - \frac{1}{k_B T} (F_i - i F_1 + (1 - i) k_B T \ln n_1) \right] \quad [2]$$

in which

$$F_i = - k_B T \ln q_i \quad [3]$$

is the absolute Helmholtz energy for an  $i$ -mer. The free energy change of cluster formation in nucleation can be obtained if one compares Eq. [2] with the classical expression

$$n_i = n_1 \exp(-\Delta F_i^\dagger / k_B T) , \quad [4]$$

one has

$$\Delta F_i^\dagger / k_B T \equiv (F_i - i F_1) / k_B T + (1 - i) \ln n_1 . \quad [5]$$

We see that, from Eqs. [3] and [5], the crucial factor in determining the free energy change of cluster formation is the cluster partition function. Upon assuming that for a cluster, the Hamiltonian of translational energy is separable from that of the vibrational, rotational and binding energies, and electronic and quantum effects are not considered, the partition function of an  $i$ -mer can be written as

$$q_i = q_{i,\text{trans}} q_i^* , \quad [6]$$

where  $q_i^*$  represents the partition function of an  $i$ -mer due to rotation, vibration and cluster binding. To a first approximation, one can assume ideal gas for evaluation of  $q_{i,\text{trans}}$ ,

$$q_{i,\text{trans}}(T, V) = V \left( \frac{2\pi m_1 i k_B T}{h^2} \right)^{3/2} = \frac{V i^{3/2}}{\Lambda^3} , \quad [7]$$

where  $m_1$  is the mass of a monomer,  $\Lambda = h/\sqrt{2\pi m_1 k_B T}$  is the de Broglie wavelength,  $h$  is Planck's constant, and  $V$  is the total free-volume of the monomer-cluster system. Because the monomers are in a much higher concentration than the clusters,  $V$  can be related to the monomer partial pressure by the ideal gas law,

$$V = \frac{n_1 k_B T}{p_1} = \frac{n_1 k_B T}{p^{\{\text{sat}\}} S} , \quad [8]$$

where  $S = p_1/p^{\{\text{sat}\}}$  is the saturation ratio, and  $p^{\{\text{sat}\}}$  is the saturation pressure.

The monomer Helmholtz energy is given by

$$F_1 = -k_B T \ln \left( \frac{V}{\Lambda^3} \right) = -k_B T \ln \left( \frac{n_1 k_B T}{\Lambda^3 p^{\{\text{sat}\}} S} \right) . \quad [9]$$

Upon substituting Eqs. [3], and [6]–[9] into Eq. [5], the free energy change  $\Delta F_1^\dagger$  becomes

$$\Delta F_i^\dagger = -k_B T \ln \left( \frac{i^{3/2}}{\Lambda^3} \frac{k_B T}{p^{\{\text{sat}\}} S} \right) - i k_B T \ln S - k_B T \ln q_i^* + i k_B T \ln \left( \frac{k_B T}{\Lambda^3 p^{\{\text{sat}\}}} \right). \quad [10]$$

One can further find an expression for the saturation vapor pressure  $p^{\{\text{sat}\}}$  through equating the chemical potential of a molecule at its saturated gaseous and liquid states. The chemical potential of a gaseous monomer at saturation is given by

$$\mu_{\text{gas}}^{\{\text{sat}\}} = -k_B T \ln \left( \frac{k_B T}{p^{\{\text{sat}\}} \Lambda^3} \right). \quad [11]$$

The chemical potential of a liquid molecule at saturation is

$$\mu_{\text{liq}}^{\{\text{sat}\}} = \left. \frac{\partial F_i}{\partial i} \right|_{T,V} \Big|_{i \rightarrow \infty} = -k_B T \left. \frac{\partial (\ln q_i)}{\partial i} \right|_{T,V,i \rightarrow \infty}. \quad [12]$$

Equating, one finds

$$p^{\{\text{sat}\}} = \frac{k_B T}{\Lambda^3} \exp \left( \frac{\mu_{\text{liq}}^{\{\text{sat}\}}}{k_B T} \right) = \frac{k_B T}{\Lambda^3} \exp \left( - \left. \frac{\partial (\ln q_i)}{\partial i} \right|_{i \rightarrow \infty} \right). \quad [13]$$

Therefore,  $\Delta F_i^\dagger$  becomes

$$\Delta F_i^\dagger = -k_B T \ln \left( \frac{q_{i,\text{trans}}}{n_1} \right) - i k_B T \ln S - k_B T \ln q_i^* + i \left[ \left. \frac{\partial (\ln q_i)}{\partial i} \right|_{i \rightarrow \infty} \right]. \quad [14]$$

The first two terms on the RHS of Eq. [14] are the contributions due to the  $i$ -mer translational motion and volume creation. The  $i$ -mer rotational, vibrational, and binding energies are implicitly accounted for in the last two terms on the RHS of Eq. [14]. In the next few sections, we shall provide models for the  $i$ -mer partition function  $q_i$  such that  $\Delta F_i^\dagger$  can be evaluated.

## CLUSTER PARTITION FUNCTION BY ATOMISTIC THEORY

In this section, we will briefly review the only theoretical evaluation of the cluster partition function that exists so far, the so-called “atomistic theory” of nucleation (8–19), and we will point out its limitations in the prediction of free energy change associated with relatively large cluster formation. In the following section, we will present a new method to evaluate the cluster partition function in the larger cluster size range in which the shortcomings of the atomistic approach are overcome.

In the atomistic theory, the Hamiltonians of translational, vibrational, rotational, and binding energies of a cluster are assumed to be separable from each other, the  $i$ -mer partition function can be written as

$$q_i = q_{i,\text{trans}} q_i^* ; \quad q_i^* = q_{i,\text{rot}} q_{i,\text{vib}} q_{i,\text{bind}} \quad [15]$$

where  $q_{i,\text{rot}}$ ,  $q_{i,\text{vib}}$ , and  $q_{i,\text{bind}}$  are contributions to the  $i$ -mer partition function due to rotation, vibration and cluster binding, respectively. The following approximations are customarily used in the atomistic theory: ideal gas for evaluation of  $q_{i,\text{trans}}$  (i.e., Eq. [7]), rigid body rotator for evaluation of  $q_{i,\text{rot}}$ , harmonic oscillator for evaluation of  $q_{i,\text{vib}}$ , and pairwise potential additivity for evaluation of  $q_{i,\text{bind}}$ . The latter three are formulated as follows:

$$q_{i,\text{rot}}(T) = \frac{\sqrt{\pi}}{\eta_i} \left( \frac{8\pi^2 k_B T}{h^2} \right)^{3/2} (I_{i,1} I_{i,2} I_{i,3})^{1/2} , \quad (i \geq 3) \quad [16a]$$

$$q_{i,\text{rot}}(T) = \frac{8\pi^2 I_2 k_B T}{\eta_2 h^2} , \quad (i = 2) \quad [16b]$$

where  $\eta_i$  is the rotational symmetry number of an  $i$ -mer; for a dimer,  $\eta_2 = 2$  in Eq. [16b].  $I_{i,j}$  is the  $j$ -th principal moment of inertia of an  $i$ -mer;



$$q_{i,\text{vib}}(T) = \prod_{j=1}^{3i-6} \frac{\exp(-h\nu_{i,j}/2k_B T)}{1 - \exp(-h\nu_{i,j}/k_B T)} , \quad (i \geq 3) \quad [17a]$$

$$q_{i,\text{vib}}(T) = \frac{\exp(-h\nu_2/2k_B T)}{1 - \exp(-h\nu_2/k_B T)} , \quad (i = 2) \quad [17b]$$

where  $\nu_{i,j}$  is the  $j$ -th normal vibrational frequency of an  $i$ -mer.  $\nu_2$  is the vibrational frequency of an dimer;

$$q_{i,\text{bind}}(T) = \exp\left(-\frac{V_0(i)}{k_B T}\right) \quad [18]$$

where  $V_0(i)$ , the binding energy of an  $i$ -mer, is calculated by summing over all intermolecular potentials that exist between any two molecules in a cluster.

We make the following four general comments concerning the atomistic theory: (A) The rotational symmetry factor,  $\eta_i$ , is difficult to determine as a function of  $i$  once the cluster becomes large. For any icosahedral clusters (26),  $\eta_i = 60$ ; also for small clusters, Reed (8) shows that  $\eta_3 = 6$  (equilateral triangle),  $\eta_4 = 12$  (tetrahedron),  $\eta_5 = 6$  (trigonal bipyramid),  $\eta_6 = 24$  (octahedron), and  $\eta_8 = 12$  (double tetrahedron). Many authors (19, 27-29) simply take  $\eta_i = 1$  by assuming that there exist no identical positions in the rotation of a spherical-shaped cluster. However, we expect that a crystalline cluster may exhibit a symmetrical configuration, and the rotational symmetry number can be quite large and, from Eq. [16a], reduces the value of the rotational partition function. (B) For small clusters (*e.g.*,  $i < 10$ ), the position of each of the molecules is fixed in the physical space with respect to one another except for small vibrations of normal modes in the intermolecular potential wells around the molecules. For larger microclusters, however, one expects that liquid-like properties will appear. For a liquid in which the density is slightly less than that in a solid, the amplitude of the motion of the

molecules is larger. The concept of small vibrations is not valid in a liquid; the molecules, therefore, are not confined to the vicinity of a particular position but can wander over the entire volume of the liquid-like cluster. (C) The calculation of normal modes of vibrational frequency  $\nu_{i,j}$  needs information on intermolecular bond lengths and bond angles (30, 31) as well as solving a  $3i \times 3i$  force constant matrix (26, 32-34). These approaches are difficult and many approximations are implicit, for example, decoupling between the vibrational and rotational degrees of freedom is necessary even when possible anharmonicity is significant and more degrees of freedom are activated for larger clusters. (D) The binding energy can only be evaluated accurately by searching for a minimum configuration of a polyhedron in the many-dimensional neighborhood of some appropriately chosen starting configuration, followed by summing over potentials between any two molecules at their equilibrium positions, *i.e.*, summing over all bond energies (15, 35, 36).

Many authors use various approximations in the determination of vibrational and binding energy contributions to the partition function in the atomistic theory. For example, Andres (37) adopted a model of Herschbach *et al.* (38) of expressing a polyatomic system partition function in terms of the local properties of its atoms that neglect off-diagonal terms in the force constant matrix. The final expression of Andres corresponds to assuming that all normal modes of vibration are the same and only interaction with nearest-neighbor molecules is considered. Kulmala (18, 19) considered an effective second nearest-neighbor interaction and assumed equal normal modes of vibration. For the purpose of later comparison with results of the present paper, we briefly formulate Kulmala's approach in the remainder of this section.

For larger clusters, one can assume the three principal moments of inertia can be approximated as that of a sphere

$$I_{i,1} = I_{i,2} = I_{i,3} = \frac{2}{5} i^{5/3} m_1 r_1^2 . \quad [19]$$

We now consider the intermolecular potential is a Lennard-Jones 6-12 potential:

$$u(r) = 4\epsilon \left[ \left( \frac{\delta}{r} \right)^{12} - \left( \frac{\delta}{r} \right)^6 \right] , \quad [20]$$

where  $\epsilon$  and  $\delta$  are the Lennard-Jones potential parameters. The moment of inertia of a dimer ( $i=2$ ) is therefore given by

$$I_2 = \frac{1}{2} m_1 (2^{1/6} \delta)^2 = \left( \frac{1}{2} \right)^{2/3} m_1 \delta^2 . \quad [21]$$

The normal modes of vibration are assumed equal and can be estimated from the intermolecular potential vibrational frequency:

$$\nu_{i,j} = \nu_2 = \text{constant} \equiv \nu = \frac{1}{2\pi} \left( \frac{d^2 u(r)/dr^2}{m_1/2} \right)^{1/2} \bigg|_{r=2^{1/6}\delta} \quad [22]$$

or

$$\nu = 1.7015 \left( \frac{\epsilon}{m_1 \delta^2} \right)^{1/2} . \quad [23]$$

With  $\nu$  given by Eq. [23], for  $i \geq 3$  situations, the  $(3i - 6)$  vibrational degrees of freedom now correspond to vibrations between a center molecule and its  $(3i - 6)$  neighbors (*i.e.*, the first layer). However, vibration between the center molecule and the other non-nearest neighbors should also be taken into account; this is accomplished by considering additional vibrational degrees of freedom. The effective second-layer vibrational degrees of freedom are found to be

$$\left[ \frac{i(i-1)}{2} - (3i-6) \right] / 11.5694 ,$$

where the bracket is the difference of numbers between all interaction pairs,  $i(i-1)/2$ , and nearest interaction pairs,  $3i-6$ . The value 11.5694 is obtained by assuming an "effective" second-layer with a mean distance  $\sqrt{2\sqrt{2}}(2^{1/6}\delta)$ , which gives the effective potential energy per second-layer interaction of  $u(r) = -\epsilon/11.5694$  from the Lennard-Jones formula, Eq. [20]. The vibrational partition function now becomes, under these approximations,

$$q_{i,\text{vib}}(T) = \left[ \frac{\exp(-h\nu/2k_B T)}{1 - \exp(-h\nu/k_B T)} \right]^{\{3i-6+(i(i-1)/2-3i+6)/11.5694\}}, \quad (i \geq 3) \quad [24a]$$

$$q_{i,\text{vib}}(T) = \frac{\exp(-h\nu/2k_B T)}{1 - \exp(-h\nu/k_B T)}, \quad (i = 2) \quad [24b]$$

Because  $\epsilon$  is the magnitude of the intermolecular potential  $u(r)$  at its maximum depth, the binding energy can be deduced by a similar argument as in the vibrational case; it was found that

$$V_0(i) = -\epsilon \left[ 3i - 6 + \left( \frac{i^2 - i}{2} - 3i + 6 \right) / 11.5694 \right], \quad (i \geq 3) \quad [25a]$$

$$V_0(i) = -\epsilon, \quad (i = 2). \quad [25b]$$

Altogether, the Helmholtz energy of an  $i$ -mer is related to the  $i$ -mer partition function (Eq. [15]) and can be written as

$$\begin{aligned} F_i(V, T) &= -k_B T \left[ \ln q_{\text{trans}} + \ln q_{\text{rot}} + \ln q_{\text{vib}} + \ln q_{\text{bind}} \right]_{i\text{-mer}} \\ &= -k_B T \ln \left[ V \left( \frac{2\pi m_1 i k_B T}{h^2} \right)^{3/2} \right] \\ &\quad - k_B T \begin{cases} \ln \left[ \frac{64\pi^2}{\eta_i} \left( \frac{\pi}{5} \right)^{3/2} \left( \frac{k_B T}{h^2} \right)^{3/2} i^{5/2} m_1^{3/2} r_1^3 \right], & (i \geq 3) \\ \ln \left[ 2^{4/3} \pi^2 \left( \frac{k_B T}{h^2} \right) m_1 \delta^2 \right], & (i = 2) \end{cases} \\ &\quad + \begin{cases} (E_{\text{vib}} - \epsilon) (4.3217 \times 10^{-2} i^2 + 2.6975 i - 5.4814), & (i \geq 3) \\ E_{\text{vib}} - \epsilon, & (i = 2) \end{cases} \end{aligned} \quad [26]$$

where

$$\begin{aligned} E_{\text{vib}} &= k_B T \left[ \frac{h\nu}{2k_B T} + \ln \left( 1 - \exp\left(-\frac{h\nu}{k_B T}\right) \right) \right] \\ &= 0.8508 h \left( \frac{\epsilon}{m_1 \delta^2} \right)^{1/2} + k_B T \ln \left[ 1 - \exp\left(-\frac{1.7015 h}{k_B T} \sqrt{\frac{\epsilon}{m_1 \delta^2}}\right) \right] \end{aligned} \quad [27]$$

is the average vibrational energy. Substituting Eqs. [9] and [26] into Eq. [5], the free energy change predicted by Kulmala's atomistic theory is

$$\begin{aligned} \Delta F_i^\dagger / k_B T &= (i-1) \ln \left( \frac{k_B T}{p_{\{\text{sat}\}} \Lambda^3} \right) - (i-1) \ln S - \frac{3}{2} \ln i \\ &\quad - \ln \left[ \frac{64\pi^2}{\eta_i} \left( \frac{\pi}{5} \right)^{3/2} \left( \frac{k_B T}{h^2} \right)^{3/2} i^{5/2} m_1^{3/2} r_1^3 \right] \\ &\quad + \frac{E_{\text{vib}} - \epsilon}{k_B T} \left( 4.3217 \times 10^{-2} i^2 + 2.6975 i - 5.4814 \right) , \end{aligned} \quad [28]$$

(atomistic theory;  $i \geq 3$ )

and for the dimers,

$$\frac{\Delta F_2^\dagger}{k_B T} = \ln \left( \frac{k_B T}{p_{\{\text{sat}\}} \Lambda^3} \right) - \ln \left[ 2^{17/6} \pi^2 \left( \frac{k_B T}{h^2} \right) m_1 \delta^2 S \right] + \frac{E_{\text{vib}} - \epsilon}{k_B T} . \quad [29]$$

Equations [28] and [29] shall be used for later comparison.

It is considerably easier to accurately calculate by atomistic theory the vibrational frequencies, rotational symmetry factor, and the binding energy of clusters composed of relatively few molecules as opposed to the calculations for larger clusters. Thus, in a nucleation situation atomistic theory should apply if the supersaturation is sufficiently high that the critical clusters are sufficiently small.

In the next section, we present a new statistical mechanical approach to nucleation. We intend to calculate the partition function for clusters of larger sizes ( $i \geq 20$ ) where liquid-like properties start to appear and the atomistic theory becomes less appropriate and less accurate.

## A NEW THEORY FOR THE CLUSTER PARTITION FUNCTION

In this section, we will present a new approach to calculating the free energy of formation of clusters sufficiently large that they start to possess liquid-like properties. Table 1 summarizes the basic ideas of the atomistic approach and the present work. For external motion of the clusters, we will again consider cluster translation as in the atomistic theory. We will, instead, use a cell model of liquids to describe the motion of molecules within a cluster. In the cell model of liquids (20-23), each of the molecules is assumed to possess a cell; each cell does not allow double occupancy of molecules. Interchanging positions between cells is permitted by the addition of what is termed the *communal entropy* to the cluster internal entropy. Because of this interchanging motion, *the cluster rotation is therefore accounted for*. The ambiguity of the determination of the rotational symmetry factor in the atomistic theory is avoided. For vibrational motion, molecules in a cluster are now allowed to vibrate in all directions and any at magnitude within their own cells, and we do not need to obtain detailed information about vibrational frequencies as is needed in the atomistic theory. Binding energy calculations, on the other hand, are the same as in the atomistic approach; that is, the minimum potential a molecule experiences is calculated. In addition, the molecules in the outermost shell (the surface molecules) will be treated as a different group from those of the interior molecules because the surface molecules experience different potentials from the interior ones (39-41). As will be shown later (see Eq. [37] and the discussion following), this consideration leads to a microscopic description of the surface tension of a cluster.

The canonical ensemble partition function of a cluster composed of  $i$  molecules is now written as

$$q_i(V, T) = q_{i,\text{trans}} q_i^* \quad ; \quad q_i^* = q_{i,\text{int}} q_{i,\text{surf}} \quad [30]$$

where  $q_{i,\text{trans}}$  is given by Eq. [7], and

$$q_{i,\text{int}} = \left[ \frac{v_{f,\text{int}} e}{\Lambda^3} \exp\left(-\frac{\varphi_{\text{int}}^*}{2k_B T}\right) \right]^{i-i_{\text{surf}}} \quad [31]$$

and

$$q_{i,\text{surf}} = \left[ \frac{v_{f,\text{surf}} e}{\Lambda^3} \exp\left(-\frac{\varphi_{\text{surf}}^*}{2k_B T}\right) \right]^{i_{\text{surf}}} \quad [32]$$

are the partition functions of the total *interior* molecules and the *surface* molecules, respectively. In Eqs. [31] and [32],  $v_f$ 's denote *effective* volume available to a molecule;  $\varphi^*$ 's denote the minimum potential energy within a cell; and  $i_{\text{surf}}$  is the number of surface molecules. The factor  $e$ , so introduced in Eqs. [31] and [32], accounts for the addition of a full communal entropy (20–23). The dividing factors  $(i - i_{\text{surf}})!$  and  $i_{\text{surf}}!$  do not appear in Eqs. [29] and [30] because the cells are distinguishable (the cells can be labeled). Also in these two equations,  $\varphi^*$  is divided by a factor of 2 because each intermolecular interaction is shared by two molecules. (Note that in the atomistic theory, the factor 2 is not included because the number of interaction *pairs* are calculated.) As will be evaluated later (see Eqs. [43], [61], [66], and [67]),  $\varphi_{\text{surf}}^*$  and  $v_{f,\text{surf}}$  are weak functions of  $i$ , though not expressed explicitly, because the surface curvature may influence the potential experienced by the surface molecules.

The  $i$ -mer Helmholtz energy  $F_i$  therefore becomes

$$\begin{aligned} F_i &= -k_B T \ln q_i \\ &= -k_B T \left\{ \frac{3}{2} \ln i + \ln \left( \frac{V}{\Lambda^3} \right) + (i - i_{\text{surf}}) \left[ \ln \left( \frac{v_{f,\text{int}}}{\Lambda^3} \right) + 1 - \frac{\varphi_{\text{int}}^*}{2k_B T} \right] \right. \\ &\quad \left. + i_{\text{surf}} \left[ \ln \left( \frac{v_{f,\text{surf}}}{\Lambda^3} \right) + 1 - \frac{\varphi_{\text{surf}}^*}{2k_B T} \right] \right\}. \end{aligned} \quad [33]$$

For a bulk phase,  $i$  approaches infinity, so one sets  $i \gg i_{\text{surf}} \gg \ln i$  in Eq. [33], and the bracketed part in the last term on the right-hand side of Eq. [14] becomes,

$$\left. \frac{\partial \ln q_i}{\partial i} \right|_{i \rightarrow \infty} = - \frac{1}{k_B T} \left( \frac{\partial F_i|_{i \rightarrow \infty}}{\partial i} \right) \Big|_{T,V} = \ln \left[ \frac{v_{f,\text{int}} e}{\Lambda^3} \exp \left( - \frac{\varphi_{\text{int}}^*}{2k_B T} \right) \right]. \quad [34]$$

Substituting Eqs. [31], [32], and [34] into Eq. [14], one obtains

$$\begin{aligned} \frac{\Delta F_i^\dagger}{k_B T} = & - \ln \left[ \left( \frac{\sqrt{2\pi m_1 i k_B T}}{h} \right)^3 \frac{k_B T}{p_1} \right] - i \ln S \\ & + i_{\text{surf}} \left[ \frac{\varphi_{\text{surf}}^* - \varphi_{\text{int}}^*}{2k_B T} + \ln \left( \frac{v_{f,\text{int}}}{v_{f,\text{surf}}} \right) \right]. \end{aligned} \quad [35]$$

The terms of Eq. [35] are, respectively, the cluster translation energy, the energy released by condensing  $i$  molecules (or the volume contribution), and the energy needed in creating a surface composed of  $i_{\text{surf}}$  molecules (or the “surface contribution”). The second and third terms are the same as in the classical nucleation theory except we now have a theoretical expression for the *microcluster surface energy* in terms of the intermolecular potential. The bracketed last term on the right-hand side of Eq. [35] was first obtained by Lennard-Jones and Corner (40) as an expression of surface tension for *bulk* liquids by using the cell model from a different approach; they directly took the difference of Helmholtz energies of a bulk liquid system with and without the presence of a surface and reached this result. In Eq. [35], on the other hand, we have shown that the same expression can be used for a microscopic definition of *microcluster* surface energy. Furthermore, the free volume available to a microcluster surface molecule,  $v_{f,\text{surf}}$ , is different from that available to a bulk liquid surface molecule,  $v_{f,\text{surf}}|_{\text{planar}}$ , due to the curvature of the cluster. We will return to this point in a later section.



We will now explain from a physical viewpoint why the last term in Eq. [35] corresponds to a surface energy contribution. Owing to the intermolecular repulsions, the probability of observing the central molecule in a given element of volume must be obtained from a Boltzmann factor (20, 21). As a result, the effective volume  $v_f$  (for either an interior cell or a surface cell) is reduced to a value less than  $v$  (the molecular volume of the liquid) and can be obtained by the cell configuration integral,

$$v_{f,\text{int}} = \int \exp\left\{-\frac{1}{k_B T} [\varphi_{\text{int}}(\mathbf{r}) - \varphi_{\text{int}}^*]\right\} d\mathbf{r} \equiv \exp\left\{-\frac{1}{k_B T} [\bar{\varphi}_{\text{int}} - \varphi_{\text{int}}^*]\right\} v \quad [36a]$$

$$v_{f,\text{surf}} = \int \exp\left\{-\frac{1}{k_B T} [\varphi_{\text{surf}}(\mathbf{r}) - \varphi_{\text{surf}}^*]\right\} d\mathbf{r} \equiv \exp\left\{-\frac{1}{k_B T} [\bar{\varphi}_{\text{surf}} - \varphi_{\text{surf}}^*]\right\} v \quad [36b]$$

where the integrations are carried over the entire cell volume, and  $\bar{\varphi}_{\text{int}}$  and  $\bar{\varphi}_{\text{surf}}$  are the mean potentials (defined by Eqs. [36a] and [36b]) of an interior cell and a surface cell, respectively. The last term of Eq. [35] can therefore be written as

$$i_{\text{surf}} \left[ \frac{\varphi_{\text{surf}}^* - \varphi_{\text{int}}^*}{2k_B T} + \ln \left( \frac{v_{f,\text{int}}}{v_{f,\text{surf}}} \right) \right] = \frac{i_{\text{surf}}}{k_B T} \left\{ [\bar{\varphi}_{\text{surf}} - \bar{\varphi}_{\text{int}}] - \left[ \frac{\varphi_{\text{surf}}^* - \varphi_{\text{int}}^*}{2} \right] \right\}. \quad [37]$$

In Eq. [37], the first bracketed term on the right-hand side is the difference between the mean potentials of an interior cell and a surface cell; on the other hand, the second bracketed term on the right-hand side is the difference of the binding energy per interior cell molecule and the binding energy per surface cell molecule. The sum of the two bracketed terms is simply the energy needed to elevate a molecule from an interior cell to a surface cell. In other words, to expose an interior cell molecule to a surface cell, not only the net potential energy difference between the two cells should be provided, but an additional energy,  $\frac{1}{2}\varphi_{\text{int}}^* - \frac{1}{2}\varphi_{\text{surf}}^*$ , which corresponds to the destruction of the binding energy of the interior cell molecule

and the reconstruction of the binding energy of the same molecule in a surface cell, should be provided. Therefore, the right-hand side of Eq. [37] represents the total energy needed (normalized by  $k_B T$ ) to create a surface composed of  $i_{\text{surf}}$  molecules and corresponds to the classical  $4\pi R^2 \sigma / k_B T$  expression, where  $\sigma$  is the surface tension.

The present evaluation for the microcluster surface energy term only takes into account a single layer of surface molecules, and the remainder of the molecules in the cluster are treated the same, that is, the interior molecules are, to a first approximation, assumed to experience the same potential regardless their location. However, if we consider non-nearest neighbor (long-range) interaction around a interior cell, the interior molecules adjacent to the surface molecules, for example, must experience a different potential from those interior molecules far from the surface. A question therefore arises: Will the present model that is based on a single layer of surface molecules predict the correct bulk surface tension? In a later section of this paper, it will be shown that the bulk surface tensions predicted by our model are within 35% for six different test materials. This shows promise for the present first approximation model. We will combine the present model with the use of the measured bulk surface tension value to obtain a final expression for  $\Delta F_i^\dagger$  that is to be compared with other theories. In other words, Eq. [35] is not regarded as a final form for the free energy change prediction; with the detailed calculation of the cell potentials and effective molecular volumes in the next few sections, the final  $\Delta F_i^\dagger$  expression of the present model will be given later.

In the remainder of this section, we will present a general discussion of the appearance and disappearance of the cluster rotational degree of freedom. In Eq. [35], one notices that no terms corresponding to the cluster rotational motion appear because we have assumed that the surface molecules and the interior molecules

are fully communal or interchangeable. This is particularly applicable for larger clusters with liquid-like properties.

As a more general formulation, we now consider a situation in which the cells within a cluster are not fully communal, *i.e.*, the cells cannot freely interchange their positions. Realistically, this case arises for clusters composed of relatively few aggregated molecules (*e.g.*,  $i \leq 30$ ). The natural logarithmic constant “ $e$ ” in Eqs. [31] and [32] should now be replaced by a factor “ $\bar{\sigma}$ ” having value between 1 and  $e$  (here we use the same notation as in Ref. (21);  $\bar{\sigma}$  should not be confused with the surface tension notation). Situations of  $\bar{\sigma} = 1$  and  $\bar{\sigma} = e$  correspond to non-communal and full-communal intercellular motions, respectively. We have already considered the latter case; for the former situation ( $\bar{\sigma} = 1$ ), the cells are rigidly connected lattices in which molecules can vibrate, and the rotational degree of freedom of the entire cluster should then be considered as in the atomistic theory. In other words, as clusters become smaller, we expect that the liquid-like property of a cluster should gradually disappear, and the rotational degree of freedom should gradually emerge. As an illustration, if we assume this emergence of cluster rotational degree of freedom is linear in  $(e - 1)$ , the  $i$ -mer absolute Helmholtz free energy can be written as

$$F_i = -k_B T \left[ \ln(q_{i,\text{trans}} q_{i,\text{int}} q_{i,\text{surf}}) + \left( \frac{e - \bar{\sigma}}{e - 1} \right) \ln q_{i,\text{rot}} \right], \quad [38]$$

where  $q_{i,\text{trans}}$  is given by Eq. [7];  $q_{i,\text{int}}$  and  $q_{i,\text{surf}}$  are given by Eqs. [31] and [32] except the factor  $e$  is replaced by  $\bar{\sigma}$ ; and  $q_{i,\text{rot}}$  is given by Eq. [16a]. It is reasonable to assume that a bulk liquid phase must possess a full communal property and Eq. [34] still holds. Upon combining Eqs. [7], [34], and [38], Eq. [14] now becomes

$$\begin{aligned} \Delta F_i^\dagger / k_B T = & \\ & - \ln \left[ \left( \frac{\sqrt{2\pi m_1 i k_B T}}{h} \right)^3 \frac{k_B T}{p_1} \right] - \left( \frac{e - \bar{\sigma}}{e - 1} \right) \ln \left\{ \frac{\sqrt{\pi}}{\eta_i} \left( \frac{8\pi^2 k_B T}{h^2} \right)^{3/2} (I_{i,1} I_{i,2} I_{i,3})^{1/2} \right\} \\ & + i \ln \left( \frac{e}{\bar{\sigma}} \right) - i \ln S + i_{\text{surf}} \left[ \frac{\varphi_{\text{surf}}^* - \varphi_{\text{int}}^*}{2k_B T} + \ln \left( \frac{v_{f,\text{int}}}{v_{f,\text{surf}}} \right) \right], \end{aligned} \quad [39]$$

where the last two terms correspond to the usual volume and surface contributions; the former three terms correspond to the contributions due to cluster translation and rotation and non-liquidification (i.e., loss of communal property), respectively. Equation [39] is quite similar to the energy change expression of the Lothe-Pound theory of nucleation (5-7, 27, 28). Lothe and Pound in their theory, considered an imaginary experiment in which a cluster is reversibly cut from a bulk liquid phase; six degrees of freedom of the cluster must be deactivated before they can be replaced by the free translational and rotational motions in vapor. The six degrees of freedom deactivated are the small translational and torsional motions of the cluster as a whole in bulk liquid with the relative positions of the molecules in the cluster remaining fixed. Accordingly, the increase in free energy resulting from the deactivation can be described by a replacement term,  $k_B T \ln q_{i,\text{rep}} \geq 0$ , better known as the "replacement factor." The third term in Eq. [39],  $i \ln(e/\bar{\sigma})$ , arises from the fact that the cluster loses its communal property, which corresponds to fixing the relative position of molecules during the deactivation process in the Lothe-Pound imaginary experiment, and has exactly the same physical meaning as the replacement factor of the Lothe-Pound theory. The expression of Eq. [39] itself, however, is not totally equivalent to the Lothe-Pound free energy expression; for example, we pointed out that the cluster rotational degree of freedom should disappear when the cluster size becomes sufficiently large that the molecules in the cluster have communal properties; the Lothe-Pound theory does not include

this consideration. Also the replacement factor in the Lothe-Pound theory is not a function of cluster size, while in our expression,  $\bar{\sigma}$  is a function of cluster size (recall that  $\bar{\sigma}$  has the value of  $\epsilon$  for very large clusters, and has the value of unity for clusters containing only a few molecules).

Another major difference between the current theory and the Lothe-Pound theory is that the present work includes an expression for the microcluster surface energy. Our point in this discussion on the partially communal intercellular motion in a cluster is to show that the free energy change expression of the present theory can reduce to a form similar to that of the Lothe-Pound theory; however, because the functional dependence on cluster size of  $\bar{\sigma}$  is still unknown, and also because the assumption of linear appearance of the rotational degree of freedom in Eq. [38] is a qualitative approximation, we shall return to Eq. [35] for the cases of clusters with full communal properties, which is presumably a good approximation for larger liquid-like clusters.

## CELL POTENTIALS

In this section, we give a detailed description of the methods to calculate the potentials in either an interior cell or a surface cell. The effective volumes of these two kinds of cells will also be calculated.

In the traditional cell theory of Lennard-Jones and Devonshire (LJD theory) (20–23), each molecule moves within its own cell in the potential field of its nearest neighbors which are assumed fixed at the centers of their cells. The problem is simplified by assuming that the  $c$  nearest neighbors are uniformly “smeared” over a spherical surface of radius  $a$ , and the potential at any position within the sphere can be calculated by an integration over spherical coordinates; the vari-

able  $a$  stands for the mean nearest-neighbor distance. In our current model for liquid-like clusters, the interior cells are surrounded by  $c$  nearest neighbors and correspond to the cells of the LJD theory. On the other hand, the surface cells are surrounded by only  $c'$  molecules ( $c' \leq c$ ), which can be assumed uniformly smeared over a broken spherical surface of radius  $a$  with an open angle  $2\chi$  (see Figure 1). Note that an interior cell (*i.e.*, that of the LJD theory) corresponds to a limiting case of a surface cell with an open angle  $2\chi = 0$ . We will first calculate the potential field and the effective volume of a surface cell in a general sense and, later on, the calculated results can be reduced to either the surface cell situation by appropriately specifying  $\chi$ , or the interior cell situation by setting  $\chi = 0$ .

Figure 1 shows the coordinates of a surface cell; the nearest neighbor molecules are assumed uniformly smeared over a broken spherical surface which is defined as the radial distance  $r = a$  with a range of position angles from  $\theta_2 = \chi$  to  $\pi$  and with a range of azimuthal angles  $\phi$  from 0 to  $2\pi$ ;  $\theta_2$  is measured from the center of the hole. The present goal is to calculate the potential at any point within the surface cell. In Figure 1, point  $P$  is at a distance  $r$  from the cell center with a position angle  $\theta_1$  measured from the center of the hole and an azimuthal angle  $\phi = 0$ . Point  $Q$ , on the other hand, is at a distance  $a$  from the cell center (*i.e.*,  $Q$  is on the smeared surface) with a position angle  $\theta_2$  and an azimuthal angle  $\phi$ . The distance between point  $P$  and point  $Q$  is denoted as  $\mathcal{R}$ . One finds

$$\mathcal{R}^2 = a^2 + r^2 - 2ar \left[ \sin \theta_1 \sin \theta_2 \cos \phi + \cos \theta_2 \cos \theta_1 \right]. \quad [40]$$

The unit surface area at point  $Q$  is  $a^2 \sin \theta_2 d\phi d\theta_2$ . Assume  $c'$  nearest neighbors are uniformly distributed on the smearing surface, the total number of smeared molecules at point  $Q$  is therefore

$$a^2 \sin \theta_2 d\phi d\theta_2 \times \frac{c'}{(1 - \frac{\chi}{\pi}) 4\pi a^2} = \left[ \frac{c'}{4(\pi - \chi)} \right] \sin \theta_2 d\phi d\theta_2 . \quad [41]$$

The intermolecular potential  $u(r)$ , in the subsequent calculation, will be approximated by the Lennard-Jones 6-12 potential given in Eq. [20]. One can obtain the total potential at point  $P$  by carrying out the following integral

$$\begin{aligned} \varphi_{\text{surf}}(r, \theta_1, \chi) &= \left[ \frac{c'}{4(\pi - \chi)} \right] \int_{\theta_2=\chi}^{\pi} \int_{\phi=0}^{2\pi} u(r = \mathcal{R}) \sin \theta_2 d\phi d\theta_2 \\ &= \left[ \frac{c'}{4(\pi - \chi)} \right] \int_{\theta_2=\chi}^{\pi} \int_{\phi=0}^{2\pi} \left[ 4\epsilon \left\{ \left( \frac{\delta}{\mathcal{R}(r, \theta_1, \theta_2)} \right)^{12} - \left( \frac{\delta}{\mathcal{R}(r, \theta_1, \theta_2)} \right)^6 \right\} \right] \sin \theta_2 d\phi d\theta_2 , \end{aligned} \quad [42]$$

where the subscript "surf" denotes that the cell is a surface cell. Upon substituting Eq. [40] into Eq. [42] and integrating over  $\phi$ , Eq. [42] becomes

$$\begin{aligned} \frac{\varphi_{\text{surf}}(x, z, \theta_1, \chi)}{k_B T} &= \left( \frac{c' \pi}{c(\pi - \chi)} \right) \left( \frac{c\epsilon}{k_B T} \right) \\ &\times \int_{\theta_2=\chi}^{\pi} \left[ z^6 \frac{A(8A^4 + 40A^2 B^2 + 15B^4)}{4(A^2 - B^2)^{11/2}} - z^3 \frac{2A^2 + B^2}{(A^2 - B^2)^{5/2}} \right] \sin \theta_2 d\theta_2 \end{aligned} \quad [43]$$

where

$$\begin{aligned} A &= 1 + x - 2\sqrt{x} \cos \theta_1 \cos \theta_2 \\ B &= - 2\sqrt{x} \sin \theta_1 \sin \theta_2 \\ x &= \left( \frac{r}{a} \right)^2 , \quad z = \left( \frac{\delta}{a} \right)^2 . \end{aligned} \quad [44]$$

In Eqs. [43] and [44],  $x^{1/2}$  stands for the dimensionless radial distance;  $z^{1/2}$  stands for the ratio of the Lennard-Jones interaction length  $\delta$  to the intermolecular distance  $a$ .

For an interior cell, the open angle is zero, and the number of surrounding nearest neighbors is  $c$ . Therefore, by setting  $\chi = 0$  and  $c' = c$  in Eq. [43] and integrating, the LJD cell potential (20-23) is recovered:

$$\varphi_{\text{int}}(x, z) = 4c\epsilon \left\{ z^6 [l(x) + 1] - z^3 [m(x) + 1] \right\} \quad [45]$$

with

$$\begin{aligned} l(x) &= (1 + 12x + 25.2x^2 + 12x^3 + x^4)(1 - x)^{-10} - 1 \\ m(x) &= (1 + x)(1 - x)^{-4} - 1. \end{aligned} \quad [46]$$

As expected, a difference between the potentials of a surface cell and an interior cell is that the former depends not only on the radial distance  $x$  but also on the position angle  $\theta_1$ , and on the (half) open angle  $\chi$ .

A final note of calculating the cell potential presented in this section (see Eq. [42]) is that only the nearest-neighbor interactions are accounted for. Potentials so calculated comprise about 83% (22) of the actual cell potential where long-range non-nearest neighbor interactions are also considered. However, the final goal for calculating the cell potential is to calculate the microcluster surface energy, and it was shown earlier in Eq. [37] that the cell potential enters the microcluster surface energy calculation only in the form of *differences*. That is, much of the errors that are caused by the approximation of nearest-neighbor interaction will cancel in the microcluster surface energy calculation. Also, the present evaluation of cell potential by only considering the nearest-neighbor interaction is in agreement with the earlier statistical formulation where only a single layer of surface molecules is treated as a group different from the interior ones (see Eqs. [31] and [32]). Moreover, we will later use the measured bulk surface tension as a final correction of our theory. Therefore, in the next few sections we will continue to calculate minimum potentials and effective molecular volumes based on the approximation of nearest-neighbor interaction.



## MINIMUM POTENTIALS AND $z$

As we pointed out earlier in Eqs. [36] and [37], the minimum potentials of both interior cells and surface cells are important factors in the determination of either effective volume or surface energy per molecule. In this section, we continue our analysis of cell theory to determine the minimum potentials of interior cells and surface cells.

The minimum potentials of a surface cell and an interior cell,  $\varphi_{\text{surf}}^*$  and  $\varphi_{\text{int}}^*$ , are not necessarily located at the center of the cells. The position of the interior cell minimum potential, for example, is approximately at a dimensionless distance  $x^{1/2} = 1 - z^{1/2}$  from the cell center if the ratio  $\delta/a$  (or  $z^{1/2}$ ) is low, because under such a situation the smeared neighbor molecules are too far from the cell center to have an effective attraction to make the center potential minimum. Figure 2 shows  $\varphi_{\text{int}}/c\epsilon$  from Eq. [45] as a function of the radial distance  $x^{1/2}$  with  $z$  as a parameter. It is seen that the minimum potential position is offset from the cell center for small  $z$  values. We also note that as  $z$  increases the minimum potential position approaches the cell center and the potential well width narrows, because the smeared neighbor molecules interact at a closer distance (the larger the  $z$  the larger the Lennard-Jones parameter  $\delta$ ). The situation that  $a = 2^{1/6}\delta$  (or  $z = 0.8$ ) corresponds to all molecules at their equilibrium positions. At a  $z$  value larger than 0.8, the minimum potential is smaller than the  $z = 0.8$  case because the intermolecular distance is shorter than the equilibrium distance,  $2^{1/6}\delta$ , and the repulsive forces of the surrounding neighbors become predominant. As a result, short-range repulsive forces from the neighbor molecules overlap with each other thus elevating the minimum potential at the cell center.

Figure 3 shows the interior cell minimum potential as a function of  $z^3$ . For

$z^3 \leq 0.5$ , the larger the value of  $z$ , the stronger the overlapping of the nearest-neighbor long-range attraction, and the deeper the minimum potential. Also shown in Figure 3 is the location of the minimum potential  $x^* = (r^*/a)^2$  as a function of  $z^3$ . For  $z^3 \geq 0.23$  (or  $z^{1/2} = \delta/a \geq 0.783$ ), the minimum potential is at the cell center. The interior cell minimum potential in Figure 3 can be represented by the following equations; for the off-centered minimum potential situations,

$$\frac{\varphi_{\text{int}}^*}{c\epsilon} = -0.104244 - 3.3504z^3 + 3.06078z^6 \quad (0.464 \leq z^{1/2} \leq 0.783) \quad [47a]$$

and for the centered minimum potential situations,

$$\frac{\varphi_{\text{int}}^*}{c\epsilon} = 4(z^6 - z^3) \quad (z^{1/2} \geq 0.783) . \quad [47b]$$

Equation [47a] is obtained by a least-squares fit, and Eq. [47b] is the exact representation of  $\varphi_{\text{int}}^*$  obtained from setting  $x = 0$  in Eq. [45]. We see that  $z^{1/2}$  is an important factor to determine. In the remainder of this section, we will use both Eqs. [47a] and [47b] to show that  $z^{1/2}$  is a function of  $c\epsilon/k_B T$  only. The determined  $z^{1/2}$  will then be used in the calculation of the potential field in a surface cell, Eq. [43], from which one can find the surface cell minimum potential. We first seek an appropriate relation between  $z^{1/2}$  and  $c\epsilon/k_B T$ .

The  $i$ -mer Helmholtz energy  $F_i$  is given by Eq. [33]. For a bulk phase,  $i \gg \ln i \gg i_{\text{surf}}$ , all molecules are present in interior cells, and we have

$$F_i|_{i \rightarrow \infty} = -i k_B T \left[ \ln \left( \frac{v_{f,\text{int}}}{\Lambda^3} \right) + 1 - \frac{\varphi_{\text{int}}^*}{2k_B T} \right] . \quad [48]$$

The pressure within the bulk phase can be found through the thermodynamic relation

$$\begin{aligned}
 p &= - \left( \frac{\partial F_i}{\partial (iv)} \right) \Big|_{T, i \rightarrow \infty} = - \frac{1}{i} \left( \frac{\partial F_i}{\partial v} \Big|_{i \rightarrow \infty} \right) \Big|_{T, i} \\
 &= k_B T \left[ \frac{1}{v_{f, \text{int}}} \frac{\partial v_{f, \text{int}}}{\partial v} - \frac{1}{2} \frac{\partial (\varphi_{\text{int}}^* / k_B T)}{\partial v} \right] .
 \end{aligned} \tag{49}$$

in which  $v$  is the volume of a cell (*i.e.*, the molecular volume of the liquid, or the reciprocal of the liquid density). The smeared sphere radius  $a$  can be related to  $v$  by

$$a^3 = \gamma v . \tag{50}$$

where  $\gamma$  is a constant depending on the type of packing of the cells. For example,  $\gamma$  has the value of  $\sqrt{2}$  for a face-centered cubic (f.c.c.) packing (20). The radius of a cell (or the effective radius of a molecule) is, therefore,

$$r_1 = \left( \frac{3}{4\pi} v \right)^{1/3} = \left( \frac{a^3}{\gamma} \frac{3}{4\pi} \right)^{1/3} . \tag{51}$$

With the cell radius given by Eq. [51], the effective volume of an interior cell molecule, Eq. [36a], can be written as

$$\begin{aligned}
 v_{f, \text{int}} &= \int_{r=0}^{r_1} \exp \left\{ - \frac{1}{k_B T} [\varphi_{\text{int}} - \varphi_{\text{int}}^*] \right\} 4\pi r^2 dr \\
 &= 2\pi\gamma v \int_{x=0}^{\left( \frac{3}{4\pi\gamma} \right)^{2/3}} \exp \left\{ - \frac{1}{k_B T} [\varphi_{\text{int}} - \varphi_{\text{int}}^*] \right\} \sqrt{x} dx .
 \end{aligned} \tag{52}$$

Substituting Eq. [52] into Eq. [49] and differentiating with respect to  $z$ , Eq. [49] becomes

$$\begin{aligned}
 \frac{pv}{k_B T} &= 1 - \frac{2}{3g} \left( \frac{c\epsilon}{k_B T} \right) \left[ \left( \frac{z}{c\epsilon} \frac{\partial \varphi_{\text{int}}^*}{\partial z} - 24z^6 \right. \right. \\
 &\quad \left. \left. + 12z^3 \right) g - 24z^6 g_l + 12z^3 g_m \right] + \frac{1}{3} \left( \frac{c\epsilon}{k_B T} \right) \left( \frac{z}{c\epsilon} \frac{\partial \varphi_{\text{int}}^*}{\partial z} \right)
 \end{aligned} \tag{53}$$

where

$$\begin{aligned}
 g &\equiv \int_{x=0}^{\left(\frac{3}{4\pi\gamma}\right)^{2/3}} \exp\left\{-\frac{1}{k_B T} [\varphi_{\text{int}} - \varphi_{\text{int}}^*]\right\} \sqrt{x} dx \\
 g_l &\equiv \int_{x=0}^{\left(\frac{3}{4\pi\gamma}\right)^{2/3}} \exp\left\{-\frac{1}{k_B T} [\varphi_{\text{int}} - \varphi_{\text{int}}^*]\right\} l(x) \sqrt{x} dx \\
 g_m &\equiv \int_{x=0}^{\left(\frac{3}{4\pi\gamma}\right)^{2/3}} \exp\left\{-\frac{1}{k_B T} [\varphi_{\text{int}} - \varphi_{\text{int}}^*]\right\} m(x) \sqrt{x} dx .
 \end{aligned} \tag{54}$$

Equation [53] is the *equation of state* of the present theory with the expressions for  $\varphi_{\text{int}}^*$  given by Eqs. [47a] and [47b].

At an equilibrium saturation condition, combining Eqs. [12] and [34], we have

$$\frac{pv}{k_B T} = \frac{v}{v_{f,\text{int}}} \exp\left[\frac{\varphi_{\text{int}}^*}{2k_B T} - 1\right] = \frac{1}{2\pi\gamma g} \exp\left[\frac{\varphi_{\text{int}}^*}{2k_B T} - 1\right] . \tag{55}$$

Equating Eqs. [53] and [55], one obtains

$$\begin{aligned}
 1 - \frac{2}{3g} \left(\frac{c\epsilon}{k_B T}\right) \left[ \left( z \frac{\partial(\varphi_{\text{int}}^*/c\epsilon)}{\partial z} - 24z^6 + 12z^3 \right) g - 24z^6 g_l + 12z^3 g_m \right] \\
 + \frac{1}{3} \left(\frac{c\epsilon}{k_B T}\right) z \frac{\partial(\varphi_{\text{int}}^*/c\epsilon)}{\partial z} = \frac{1}{2\pi\gamma g} \exp\left[ \frac{1}{2} \left(\frac{c\epsilon}{k_B T}\right) \frac{\varphi_{\text{int}}^*}{c\epsilon} - 1 \right] .
 \end{aligned} \tag{56}$$

Equation [56] is a highly nonlinear integral equation which relates  $z^{1/2}$  uniquely with  $c\epsilon/k_B T$ . We solve this by Newton-Raphson's method with the use of Eqs. [47a] and [47b], and the result is shown in Figure 4. The value of  $\gamma = \sqrt{2}$  has been used, which corresponds to the f.c.c. packing situation. As expected, the lower the temperature, the closer the nearest-neighbor molecules, and the higher the value  $z^{1/2}$ . The curve in Figure 4 can be represented by the following least-squares best-fit polynomial:

$$\begin{aligned} \frac{\delta}{a} = z^{1/2} = & -2.43779 + 5.97756 \times 10^{-1} \left( \frac{c\epsilon}{k_B T} \right) - 4.50665 \times 10^{-2} \left( \frac{c\epsilon}{k_B T} \right)^2 \\ & + 1.79339 \times 10^{-3} \left( \frac{c\epsilon}{k_B T} \right)^3 - 3.95503 \times 10^{-5} \left( \frac{c\epsilon}{k_B T} \right)^4 \\ & + 4.57711 \times 10^{-7} \left( \frac{c\epsilon}{k_B T} \right)^5 - 2.17152 \times 10^{-9} \left( \frac{c\epsilon}{k_B T} \right)^6. \end{aligned} \quad [57]$$

For most of the situations in which we are interested in a nucleation process (that is, at low temperature conditions)  $c\epsilon/k_B T$  lies between 20 and 40; for example, for an f.c.c. packing  $c = 12$ ,  $c\epsilon/k_B T = 34.31$  for water at  $10^\circ\text{C}$ . We see that, from Figure 4,  $z^{1/2}$  in this range of  $c\epsilon/k_B T$  has a value between 0.83 and 0.875. This range of values of  $z^{1/2}$  is expected since  $z^{1/2}$  should not be greater than  $2^{-1/6} (= 0.891)$  at which molecules are repulsive in nature, nor should  $z^{1/2}$  be too small which may correspond to a situation in which molecules are dissociated.

Although the present relation between  $z^{1/2}$  and  $c\epsilon/k_B T$  is found from an analysis of interior cells, it will be applied for surface cells. The reason is that both the interior cells and the surface cells of a cluster must have the same intermolecular distance  $a$  and Lennard-Jones parameter  $\delta$  such that the value of  $z^{1/2}$  is the same throughout the entire cluster. Also Eq. [57] is obtained from thermodynamic equilibrium relations at saturation conditions, however, one can approximate that Eq. [57] is applicable for non-equilibrium supersaturation situations, because microscopic intermolecular interactions in a cluster are not affected by the macroscopic supersaturation.

## MORE ON SURFACE CELLS AND SURFACE ENERGY

With the relation determined between  $z$  and  $c\epsilon/k_B T$ , Eq. [57] in the previous section, the potential field in a surface cell (Eq. [43]) as well as the effective volume of a surface molecule can be now evaluated. There are four goals, therefore, in this

section concerning surface cells: (A) To find a relation between the surface cell (half) open angle,  $\chi$ , and the number of molecules in a cluster; (B) With  $\chi$  so determined and with  $z^{1/2}$  given by Eq. [57], to calculate the potential numerically based on an integration of Eq. [43] for both the planar surface and the nonplanar cluster situations. The minimum potentials of surface cells will be compared with that of the interior cells; (C) To calculate the molecular effective volume in a surface cell and compare it with those of the interior cells; and (D) With  $\varphi_{\text{surf}}^*$ ,  $\varphi_{\text{int}}^*$ ,  $v_{f,\text{int}}$ , and  $v_{f,\text{surf}}$ , to calculate the surface energy per molecule based on Eq. [37].

*The relations between  $\chi$ ,  $i_{\text{surf}}$ , and  $i$*  — We recall that a surface molecule is surrounded by  $c'$  nearest molecules; these molecules were assumed to be smeared over a broken spherical surface in order to calculate the potential within the cell. For a molecule on a planar liquid surface, in particular, the “surface density” (*i.e.*, the number of molecules per unit area of the smeared surface) can be approximated to be the same as for an interior cell, in which case,  $c$  nearest neighbors were assumed uniformly smeared over the entire  $4\pi a^2$  area. In other words,  $\chi$  can be determined by

$$\chi_{\text{planar}} = \pi \left( 1 - \frac{c'}{c} \right). \quad [58]$$

The situation is shown schematically in the upper part of Figure 5. For a surface molecule of a cluster, the number of nearest neighbors is still  $c'$ , however, these molecules are closer to one another than in the planar surface case, and the surface density is presumably higher. We show this situation in the lower part of Figure 5, where the angle between the original planar surface and the tangent line along the cluster surface is denoted as  $\xi$ . The angle  $\xi$  can be estimated through a relation with the total number of surface molecules. Consider an  $i$ -mer of radius  $R_i$  whose

number of surface molecules is  $i_{\text{surf}}$ ; one can approximate the relation

$$i_{\text{surf}} \approx \frac{4\pi R_i^2}{\pi a^2} . \quad [59]$$

From geometry (see Figure 5) together with the use of Eq. [59],  $\xi$  can be estimated as

$$\xi \approx \frac{a}{R_i} \approx \frac{2}{\sqrt{i_{\text{surf}}}} . \quad [60]$$

The open angle  $\chi$ , in the present case, is the sum of  $\xi$  and that of a planar surface situation,

$$\chi = \chi_{\text{planar}} + \xi = \pi \left(1 - \frac{c'}{c}\right) + \frac{2}{\sqrt{i_{\text{surf}}}} . \quad [61]$$

The effect of the nonplanar correction of  $\chi$ , the last term of Eq. [67], is expected to be larger as cluster size decreases.

There naturally arises a problem of finding a closed form relation between the number of molecules contained in an  $i$ -mer ( $i$ ) and the number of surface molecules of an  $i$ -mer ( $i_{\text{surf}}$ ). For smaller clusters, the exact relation between  $i_{\text{surf}}$  and  $i$  is difficult to find because the shape of the clusters is not necessarily spherical. In this regard, we will use the idea of a series of icosahedral packing clusters derived from Mackay (35, 42), for which a closed form relation between  $i$  and  $i_{\text{surf}}$  is available. In Mackay's icosahedron, the intermolecular geometry is basically an f.c.c. packing, however, a small distortion is required to preserve overall icosahedral symmetry. Geometrical considerations give (35)

$$i(X) = \frac{1}{3}(10X^3 + 15X^2 + 11X + 3) \quad [62]$$

and

$$i_{\text{surf}}(X) = \frac{i(X) - i(X-1)}{i(X)} = 10X^2 + 2 \quad [63]$$

where  $X$  is the number of molecule layers ( $X \geq 1$ ) around a central molecule. For example, for  $X = 1$ , the icosahedron corresponds to a 13-mer (Eq. [62]), and there exists only one layer composed of 12 surface molecules (Eq. [63]). For a very large cluster, as expected, the number of surface molecules is proportional to the two-thirds power of the total number of molecules,

$$i_{\text{surf}} = (3\sqrt{10}i)^{2/3} = 4.4814i^{2/3} \quad (\text{for large } i) . \quad [64]$$

Equation [64] will later be used to evaluate a relation between the microcluster surface tension and the bulk surface tension.

From Eqs. [62] and [63], we obtain, by directly cancelling  $X$ ,

$$i = \frac{i_{\text{surf}}}{2} + \frac{1}{3\sqrt{10}} (i_{\text{surf}} + 9)\sqrt{i_{\text{surf}} - 2} . \quad [65]$$

Equation [65] expresses  $i$  as a function of  $i_{\text{surf}}$ . However, we want to obtain an explicit relation that expresses  $i_{\text{surf}}$  as a function of  $i$  that can be used in the calculation for the surface energy term of Eq. [35] (or Eq. [37]), and for a direct relation between  $\chi$  and  $i$  in Eq. [61]. Note that the relation between  $i$  and  $i_{\text{surf}}$  in Eq. [65] is strictly valid only when both  $i$  and  $i_{\text{surf}}$  are integers (for example, when  $i = 55$ ,  $i_{\text{surf}} = 42$ ). To obtain an expression for  $i_{\text{surf}}$  as a function of  $i$ , to a first approximation, we solve Eq. [65] by assuming that the result is valid even for situations where the outermost shell in the icosahedron is not fully covered, and the calculated  $i_{\text{surf}}$ , if fractional, will be truncated to integers. Using a least-squares fit for inverting Eq. [65], we obtain the following formula,

$$i_{\text{surf}} = \text{Integer} \left\{ \exp \left[ 5.752 \times 10^{-2} + 1.026 \ln i - 3.160 \times 10^{-2} \ln^2 i + 9.547 \times 10^{-4} \ln^3 i \right] \right\} . \quad [66]$$



*The Numerical Calculation of Surface Potentials* — We will now show the calculation of the integral of Eq. [43] for evaluating the surface cell potential field. We assume that the cluster obeys an f.c.c. packing lattice; the number of nearest neighbors of an interior cell molecule is 12 ( $c = 12$ ), and the value of  $\gamma$  in Eq. [50] is  $\sqrt{2}$ . We choose f.c.c. packing as an illustration not only because Mackay's icosahedron (35, 42) has an f.c.c. packing which results in a closed form relation between  $i_{\text{surf}}$  and  $i$ , but also because it is the most natural packing arrangement of spheres if their interactions are sufficiently weak that the molecules lose any directional orientation preference. This appears to be a good approximation especially for liquid-like microclusters. It is, however, first necessary to decide which face of the f.c.c. lattice is exposed. Corner (41) showed that the (111)-plane is preferred; this corresponds to the number of nearest neighbors of a surface molecule as 9 ( $c' = 9$ , 6 of them are surface molecules themselves, and 3 of them are interior molecules; see the upper-left part of Figure 5). The planar surface half open angle,  $\chi_{\text{planar}}$  in Eq. [58], is therefore equal to  $\pi/4$  in our subsequent calculations.

Figure 6a schematically shows a side view of a surface cell, *i.e.*, a view of a cross section at an arbitrary constant azimuthal angle  $\phi$ . The surface cell can be divided into two portions along the  $\theta_1 = \pi/2$  surface; a molecule in the "sealed side" ( $\pi/2 \leq \theta_1 \leq \pi$ ) experiences stronger intermolecular interactions than if it is in the "open side" ( $0 \leq \theta_1 \leq \pi/2$ ). Three cross sections at  $\theta_1 = 0$ ,  $\pi/5$ , and  $\pi/2$  (see Figure 6a) are chosen to see the variation of the potential as a function of position angles.

Figures 6b–6d show the potential profiles of a cell that belongs to a planar surface ( $i_{\text{surf}} = \infty$ ), a 55-mer surface ( $i_{\text{surf}} = 42$ ), and a 13-mer surface ( $i_{\text{surf}} = 12$ ), respectively. The reason for choosing the 55-mer and 13-mer situations is that these

are the smallest perfect icosahedra. For the 13-mer case, for example, it is the most curved surface from which the present analysis based on cell theory is valid; 12 molecules are exposed at the surface, and  $\chi = \pi/4 + 2/\sqrt{12}$ . Three solid lines which correspond to the aforementioned three cross sections are shown in Figures 6b-6d. The internal cell potential is also shown in these figures by a dashed line for comparison. We have used  $c\epsilon/k_B T = 25$  in the computation as an illustration. On the sealed side of a surface molecule, as expected, the potential fields shown in Figures 6b-6d are very close to that of an interior cell. Along the  $\theta_1 = \pi/2$  cross section, the potential profiles in Figures 6b-6d are exactly symmetrical to the cell center. The  $\theta_1 = \pi/2$  profiles are also the most narrow ones in comparison to the profiles of  $\theta_1 = 0$  and  $\theta_1 = \pi/5$ . The potential profiles along the  $\theta_1 = 0$  cross section, on the other hand, are the most unsymmetrical profiles, because the intermolecular interactions substantially decrease close to the edge of the smeared surface at the open side of the cell. Also one notices that a potential barrier may occur along the  $\theta_1 = 0$  cross section at the open side as shown in Figure 6b, even though no molecules are smeared in the open angle region; a molecule can be moved out of the cell cage only when enough energy is provided to the molecule to overcome the potential barrier. Comparing Figures 6b-6d, we find that the potential humps of the  $\theta_1 = 0$  curve at the open side of the cell disappear as the surface cell changes from a planar case to a cluster case. The open side potential along  $\theta_1 = \pi/5$  also substantially decreases as a cluster becomes smaller due to a wider open angle  $\chi$ .

The minimum potential in a surface cell always occurs at the sealed side along the  $\theta_1 = 0$  cross section, as shown in Figures 6b-6d. Figure 7 shows the calculated minimum potential of a surface cell. A line for the interior cell minimum potential is also shown for comparison. In Figure 7, the surface cell minimum potentials of

a planar surface, a 55-mer, and a 13-mer, are all higher than that of the interior cell since the latter has more nearest interacting neighbors. For smaller clusters, the open angle  $\chi$  is larger, and, therefore, the minimum potential is more shallow. One also notices in Figure 7 that the higher the value of  $c\epsilon/k_B T$  (or the lower the temperature), the closer the intermolecular distance, and the deeper the minimum potential for all cells.

*Surface Cell Effective Volume Calculations* — The effective volume was discussed earlier above Eq. [36a]. The expression for an interior cell effective volume,  $v_{f,\text{int}}$ , was first given by Eq. [36a] and reformulated in Eq. [52]. Similarly, the expression for a surface cell effective volume,  $v_{f,\text{surf}}$ , was given by Eq. [36b], which can be rewritten as the following cell configuration integral

$$\begin{aligned} v_{f,\text{surf}} &= \int_{r=0}^{r_1} \int_{\theta_1=0}^{\pi} \exp\left\{-\frac{1}{k_B T} [\varphi_{\text{surf}} - \varphi_{\text{surf}}^*]\right\} 2\pi r^2 \sin \theta_1 d\theta_1 dr \\ &= \pi \gamma v \int_{x=0}^{\left(\frac{3}{4\pi\gamma}\right)^{2/3}} \int_{\theta_1=0}^{\pi} \exp\left\{-\frac{1}{k_B T} [\varphi_{\text{surf}} - \varphi_{\text{surf}}^*]\right\} \sqrt{x} \sin \theta_1 d\theta_1 dx . \end{aligned} \quad [67]$$

Figure 8 shows the calculated  $v_{f,\text{surf}}/v$  as a function of  $c\epsilon/k_B T$  for the planar surface, 55-mer surface, and 13-mer surface situations. The dashed line is  $v_{f,\text{int}}/v$  for the interior cell case. We find the following: (A) The interior molecule effective volume is always smaller than that of a *planar* surface molecule because a planar surface molecule is not as tightly bound as in the interior cells; (B) For a given number of nearest neighbors,  $c' = 9$ , *the smaller the cluster, the smaller the effective volume*. At first glance, this seems contradictory to intuition because a smaller cluster should have a wider open angle  $\chi$ , and in consequence, the surface molecule should move more freely. On the other hand, if the open angle does not vary dramatically (in our calculations,  $\chi$  varies from  $0.25\pi$  for a planar surface to  $0.43\pi$

for a 13-mer), the number density of molecules on the smeared surface for a smaller cluster is higher than that of a larger cluster because  $c'$  is constant, and thus the surface cell molecule of a smaller cluster would be more confined than that of a larger cluster. Figure 8 shows that under the conditions considered, the effect of increasing surface density that lowers the effective volume predominates over the effect of the wider open angle that would increase the effective volume. (C) For a molecule present in any cell, the lower the temperature, the lower the kinetic energy, and the lower the effective volume.

*Calculation of the Surface Energy Per Molecule* — Based on knowledge of the effective volume and cell potential discussed in this section, we now present the calculations of the surface energy per molecule, the bracketed term on the left-hand side of Eq. [37]. Figure 9 shows the latter as a function of  $\chi$  and  $c\epsilon/k_B T$ . We find that the higher the temperature the lower the surface energy per molecule. Though this phenomenon is commonly observed experimentally for bulk surface tension of many liquids, the *microscopic* explanation from the present theory is that an increase in temperature will decrease the difference of the average potentials between an interior cell and a surface cell, and the energy needed to elevate a molecule from interior to surface will be lowered. Also we notice that for smaller clusters, the surface energy per molecule is higher because, from Figure 7, the difference between  $\varphi_{\text{surf}}^*$  and  $\varphi_{\text{int}}^*$  for a smaller cluster is greater than that of a larger cluster.

## MICROCLUSTER SURFACE TENSION AND COMPARISON

In this section, microcluster surface tension will be appropriately related to the surface energy per molecule. The surface tension variation as a function of cluster size can be subsequently calculated by the present cell model and will be compared

with that predicted by the Tolman approach. With a self-consistent bulk surface tension expression, we will provide the final form of free energy change that is to be compared with expressions from other theories in the next section.

The surface energy contribution to the cluster formation free energy change, the last term in Eq. [35], is a simple product of two parts: the number of surface molecules,  $i_{\text{surf}}$ , and the surface energy per molecule. The expression for  $i_{\text{surf}}$  was given by Eq. [66]; and the calculations for the surface energy per molecule were shown in Figure 9. To relate the surface energy contribution to the *surface tension* of a liquid-like microcluster, the work needed to form a microcluster from a macroscopic thermodynamic viewpoint is necessary. In this regard, we will first make a distinction between the *equimolar dividing surface* and the *surface of tension* due to Tolman (43).

According to Tolman (43), the location of “equimolar dividing surface” is where the surface excess concentration is zero; the location of “surface of tension,” on the other hand, is where the surface tension is defined thermodynamically by the Laplace equation. The difference between the distances of these two surfaces from the cluster center is denoted as  $\delta_T$ , better known as the Tolman delta. We denote the radii of these two surfaces, from the center of the spherical droplet, as  $R_e$  and  $R_s$ , respectively, and

$$\delta_T = R_e - R_s . \quad [68]$$

In the recent work of Bartell (44), it was shown that in terms of these two radii the work needed to create a surface is

$$\text{surface work} = \frac{4}{3}\pi\sigma\left(\frac{2R_e^3}{R_s} + R_s^2\right) . \quad [69]$$

That is, the surface work is not simply  $4\pi R^2\sigma$ . The surface work for creating a droplet with large surface area, however, approaches  $4\pi R_e^2\sigma_\infty$ , since  $R_e$  and  $R_s$  will be identical in this case, and the surface tension approaches its bulk value  $\sigma_\infty$ . The ratio of the surface work given by Eq. [69] to  $4\pi R_e^2\sigma_\infty$  will be termed "effective surface tension ratio" since it represents the ratio of actual surface work needed for creating a liquid-like cluster surface to that of a fictitious situation where the cluster radius is  $R_e$  and surface tension remains its bulk value  $\sigma_\infty$ .

By equating the surface energy contribution expression of the present work, the last term of Eq. [35], with the macroscopic thermodynamic surface work expression, Eq. [69], one has

$$i_{\text{surf}} \left[ \frac{\varphi_{\text{surf}}^* - \varphi_{\text{int}}^*}{2k_B T} + \ln \frac{v_{f,\text{int}}}{v_{f,\text{surf}}} \right] = \frac{4}{3} \pi R_e^2 \frac{\sigma}{k_B T} \left[ 2 \left( \frac{R_e}{R_s} \right) + \left( \frac{R_s}{R_e} \right)^2 \right] \quad [70]$$

which, in the bulk surface limit, becomes

$$(3\sqrt{10}i)^{2/3} \left[ \frac{\varphi_{\text{surf}}^*|_{\text{planar}} - \varphi_{\text{int}}^*}{2k_B T} + \ln \frac{v_{f,\text{int}}}{v_{f,\text{surf}}|_{\text{planar}}} \right] = \frac{4\pi R_e^2 \sigma_\infty}{k_B T} \quad [71]$$

Equation [64] has been used to obtain Eq. [71]. The "effective surface tension ratio" of our present theory is therefore the ratio of the left-hand sides of Eqs. [70] and [71]. Figure 10a shows the calculated effective surface tension ratio from the present theory as a function the size of the cluster,  $i$ , with  $c\epsilon/k_B T$  as a parameter. Again, f.c.c. packing is assumed. We find that the smaller the cluster the lower the surface tension from the bulk. Our theory predicts that for clusters smaller than 20-mer (down to the smallest icosahedron 13-mer) the surface tension increases when size decreases. For clusters smaller than a 13-mer, however, the present theory is not applicable because there does not exist a full covered surface.

The reason for the minimum around  $i = 20$  is as follows: The effective surface tension ratio, by taking the ratio of the left-hand sides of Eqs. [70] and [71], is the product of  $i_{\text{surf}}/(3\sqrt{10}i)^{2/3}$  and the ratio of the surface energies per molecule of a cluster and of a planar surface. The former, which stands for the ratio of the actual number of surface molecules to that in the bulk limit, monotonically decreases as  $i$  decreases. On the other hand, the ratio of the surface energies per molecule of a cluster and of a planar surface, from Figure 9, monotonically increases as  $i$  decreases since the surface energy per molecule of a cluster is higher than that of a planar surface. Because of these contrary  $i$  dependencies, the product of the aforementioned two ratios possesses a minimum which occurs at  $i = 20$ . From Figure 10a, we see that the former ratio,  $i_{\text{surf}}/(3\sqrt{10}i)^{2/3}$ , predominates over the range for  $i$  greater than 20, and the decrease of the surface tension from the bulk in this size range, therefore, is mainly due to the variation of the number of surface molecules from the bulk limit.

The effective surface tension ratio, the ratio of the right-hand sides of Eqs. [70] and [71], can also be obtained once an expression of the surface tension variation,  $\sigma/\sigma_\infty$ , is known. In this regard, Tolman (43) showed, from classical thermodynamics, that the variation of surface tension as a function of size is governed by

$$\frac{1}{\sigma} \frac{d\sigma}{dR_s} = \frac{\frac{2\delta_T}{R_s^2} \left[ 1 + \frac{\delta_T}{R_s} + \frac{1}{3} \left( \frac{\delta_T}{R_s} \right)^2 \right]}{1 + \frac{2\delta_T}{R_s} \left[ 1 + \frac{\delta_T}{R_s} + \frac{1}{3} \left( \frac{\delta_T}{R_s} \right)^2 \right]} \quad [72]$$

Bartell (44) used a different thermodynamic route to obtain Eq. [72]. The expression for  $\sigma/\sigma_\infty$  can be obtained once one integrates Eq. [72]. This was accomplished analytically by Plesner (45). The Tolman delta,  $\delta_T$ , was assumed not to be a function of size. From Plesner's result, the "effective surface tension ratio" can be written as (notice that in Eq. [42] of Plesner's work (45), an integration

constant 1.3115 was still missing; see equation below)

$$\begin{aligned} \frac{1}{3} \left[ 2 \left( \frac{R_e}{R_s} \right) + \left( \frac{R_e}{R_s} \right)^2 \right] \frac{\sigma}{\sigma_\infty} = \\ \frac{1}{3} \left[ 2 \left( \frac{R_e}{R_s} \right) + \left( \frac{R_e}{R_s} \right)^2 \right] \exp \left\{ 1.3115 - 1.691 \tan^{-1} \left[ \frac{0.804 + \frac{4}{3} \left( \frac{\delta_T}{R_s} \right)}{0.918} \right] \right\} \\ \times \left[ 1.794 + \left( \frac{\delta_T}{R_s} \right) \right]^{0.557} \left[ 0.558 + 0.804 \left( \frac{\delta_T}{R_s} \right) + \frac{2}{3} \left( \frac{\delta_T}{R_s} \right)^2 \right]^{0.721} \\ \left/ \left\{ 1 + 2 \left( \frac{\delta_T}{R_s} \right) \left[ 1 + \left( \frac{\delta_T}{R_s} \right) + \frac{1}{3} \left( \frac{\delta_T}{R_s} \right)^2 \right] \right\} \right. \end{aligned} \quad [73]$$

The determination of  $\delta_T$  is given in the Appendix, based on a theory of Kirkwood and Buff (46) and with the use of the Lennard-Jones potential, Eq. [20], together with solving Eq. [56] of the present work. We have, for the first time, determined that the Tolman delta,  $\delta_T/r_1$ , is a unique function of  $c\epsilon/k_B T$ . The size dependence of  $\delta_T$  is still unknown; this quantity is ill-defined for small clusters in Tolman's theory and in Kirkwood and Buff's work.

With the use of Eq. [73] and the  $\delta_T$  calculated in the Appendix, the ratio of the right-hand sides of Eq. [70] and Eq. [71], *i.e.*, the effective surface tension ratio, is shown in Figure 10b as a function of the cluster size  $i$ . This result is termed the "Tolman approach" since the concept of  $\delta_T$  and Tolman's original formulation, Eq. [72], have been used. Again, as in Figure 10a from the cell theory, the cluster surface tension is smaller than the bulk value. Comparing Figures 10a and 10b in the range of  $c\epsilon/k_B T = 25$  and 35, the predictions from the two totally different approaches agree well with each other when the cluster is larger than about 100. The two theories, however, predict different trends in the temperature dependence of the effective surface tension ratio.



*Bulk Surface Tension Prediction and Reconciliation with Measured Value —*

We will now show the comparison between the predicted bulk surface tension and measured values. We start from Eq. [71] that relates the work needed for creating a large surface predicted by the cell theory and macroscopic classical thermodynamics. We first recognize that the relation between the cluster size,  $i$ , and the equilmolar dividing surface radius,  $R_e$ , is

$$\left(\frac{R_e}{r_1}\right)^3 = i \quad [74]$$

where  $r_1$  is the monomer radius. Equation [74] states that an  $i$ -mer is defined within a sphere of radius  $R_e$  which divides the gas phase from the liquid phase; that is, the cluster radius should be the equilmolar dividing surface radius. An expression that is commonly used,  $(R_s/r_1)^3 = i$ , is erroneous because  $R_s$  is only related to the surface tension and there is no direct relation to  $i$ . With the use of Eq. [74], Eq. [71] can be rewritten as

$$\sigma_\infty = \frac{(3\sqrt{10})^{2/3}}{4\pi r_1^2} \left[ \frac{1}{2} (\varphi_{\text{surf}}^*|_{\text{planar}} - \varphi_{\text{int}}^*) + k_B T \ln \frac{v_{f,\text{int}}}{v_{f,\text{surf}}|_{\text{planar}}} \right]. \quad [75]$$

Table II shows the predicted surface tension of six substances by using Eq. [75] with the measured surface tension values. The predicted surface tensions are within about 35% of the measured values for these substances. This comparison shows promise for the present theory because the calculation is based only on the microscopic Lennard-Jones intermolecular potential.

It is not, however, our purpose to calculate a correct bulk surface tension based on the cell model of liquids, but rather the surface tension variation is of interest. Secondly, we *expect* the predicted surface tension to differ from the measured value because we have employed the nearest-neighbor interaction approxi-

mation throughout the calculation. A reconciliation of the present theory with the measured bulk surface tension value is therefore necessary. In other words, the prediction of bulk surface tension by Eq. [75] will not be used further. Instead we will use the *measured bulk surface tension* and the *prediction of surface tension variation* from the present theory (*i.e.*, Figure 10a) in order to predict the micro-cluster surface tension. Thus, upon combining Eqs. [71] and [75], the expression for free energy change incorporating the bulk surface tension is

$$\begin{aligned} \frac{\Delta F_i^\dagger}{k_B T} = & - \ln \left[ \left( \frac{\sqrt{2\pi m_1 i k_B T}}{h} \right)^3 \frac{k_B T}{p_1} \right] - i \ln S \\ & + i_{\text{surf}} \left[ \frac{4\pi r_1^2 \sigma_\infty}{(3\sqrt{10})^{2/3} k_B T} + \frac{\varphi_{\text{surf}}^* - \varphi_{\text{surf}}^*|_{\text{planar}}}{2k_B T} + \ln \left( \frac{v_{f,\text{surf}}|_{\text{planar}}}{v_{f,\text{surf}}} \right) \right]. \end{aligned} \quad [76]$$

Equation [76] is our final expression for  $\Delta F_i^\dagger$  to be compared with other theories in the next section.

## PREDICTION OF THE FREE ENERGY CHANGE

The goals of this final section are first to summarize the equations to be used in the comparison of free energy change in the formation of microclusters, and then to use an example to show the influence in the free energy change, as well as in the nucleation rate, by considering cluster translational and rotational motion and the cluster surface tension variation. The theories to be compared are: (A) classical nucleation theory with constant surface tension, (B) classical nucleation theory with surface tension variation due to Tolman, (C) Lothe-Pound nucleation theory with constant surface tension, (D) Lothe-Pound nucleation theory with surface tension variation due to Tolman, (E) the atomistic theory of Kulmala, Eq. [28], and (F) the present cell model, Eq. [76]. We first briefly summarize the equations to be used for each of the theories.

### *Classical Nucleation Theory with $\sigma_\infty$ —*

$$\frac{\Delta F_i^\dagger}{k_B T} = 4\pi \left( \frac{\sigma_\infty r_1^2}{k_B T} \right) i^{2/3} - i \ln S . \quad [77]$$

The two terms are the “volume term” and “surface tension term.”

### *Classical Nucleation Theory with $\sigma$ —*

$$\frac{\Delta F_i^\dagger}{k_B T} = 4\pi \left( \frac{\sigma_\infty r_1^2}{k_B T} \right) i^{2/3} \left[ \frac{1}{3} \left\{ 2 \frac{R_e}{R_s} + \left( \frac{R_s}{R_e} \right)^2 \right\} \frac{\sigma}{\sigma_\infty} \right] - i \ln S . \quad [78]$$

The bracketed term in Eq. [78] is the “effective surface tension ratio” discussed in the previous section. The Tolman approach, as in Figure 10b, will be used.

*The Lothe-Pound Theory (5–7) with  $\sigma$  and  $\sigma_\infty$  —*

$$\begin{aligned} \Delta F_i^\dagger / k_B T = & 4\pi \left( \frac{\sigma_\infty r_1^2}{k_B T} \right) i^{2/3} \times [\text{with or without multiplication of } \sigma \text{ variation}] \\ & - i \ln S - \ln \left[ \left( \frac{2\pi m_1 i k_B T}{h^2} \right)^{3/2} \frac{k_B T}{p^{\{\text{sat}\}} S} \right] \\ & - \ln \left[ \frac{64\pi^2}{\eta_i} \left( \frac{\pi}{5} \right)^{3/2} \left( \frac{k_B T}{h^2} \right)^{3/2} i^{5/2} m_1^{3/2} r_1^3 \right] \\ & - \ln \left[ \left( \frac{\exp(-h\nu/2k_B T)}{1 - \exp(-h\nu/k_B T)} \right)^{-6} \exp(-4) \right]. \end{aligned} \quad [79]$$

The terms of Eq. [79] are the contributions from volume creation, surface tension, cluster translation, cluster rotation, and the Lothe-Pound replacement factor. We have used the expression of the replacement factor by Abraham and Pound (28) based on an Einstein model of normal mode vibrations. We will use Eq. [23] for the calculation of the normal mode vibration frequency  $\nu$ . The surface tension variation, if included, is again due to the Tolman approach as in Figure 10b.

*The Atomistic Theory* — For interpretation and comparison, Eq. [28] can be rewritten as

$$\begin{aligned} \Delta F_i^\dagger / k_B T = & - i \ln S - \ln \left[ \left( \frac{2\pi m_1 i k_B T}{h^2} \right)^{3/2} \frac{k_B T}{p^{\{\text{sat}\}} S} \right] \\ & - \ln \left[ \frac{64\pi^2}{\eta_i} \left( \frac{\pi}{5} \right)^{3/2} \left( \frac{k_B T}{h^2} \right)^{3/2} i^{5/2} m_1^{3/2} r_1^3 \right] \\ & + \frac{E_{\text{vib}} - \epsilon}{k_B T} (4.3217 \times 10^{-2} i^2 + 2.6975 i - 5.4814) \\ & + i \ln \left[ \left( \frac{2\pi m_1 k_B T}{h^2} \right)^{3/2} \frac{k_B T}{p^{\{\text{sat}\}}} \right]. \end{aligned} \quad [80]$$

The first three terms are, again, the volume, cluster translation, and cluster rotation terms; the fourth term is the vibrational and binding term, and the fifth term arises from the deactivation of the free translation of  $i$  monomers. In comparison to other theories, the sum of the last two terms can be interpreted as the “surface energy contribution” in the atomistic theory.

*The Present Cell Model of Liquids* — Eq. [76].

In order to demonstrate the effect of the inclusion of cluster translational, rotational motion, as well as the surface tension variation due to Tolman and the present work, we choose water at a saturation ratio  $S = 3$  at 293K as an illustration. The results for different values of  $S$  would look qualitatively the same because all the equations contain the same volume term,  $-i\ln S$ , and therefore comparisons for different  $S$  will not be considered. For water at 293K, the  $\epsilon/k_B$  value is 809.1K, and from Figure 12, the Tolman delta is  $\delta_T = 0.64r_1$ . Water saturation vapor pressure is  $p^{\text{sat}} = 2.3378 \times 10^3$  Pa, and the bulk surface tension is  $72.88 \times 10^{-3} \text{ J m}^{-2}$ .

Figure 11 and Table III show the predictions of the free energy change from various theories for water at 293K at  $S = 3$ . Two values of the rotational symmetry factor  $\eta_i$  are used in the calculation of the cluster rotation term in both the atomistic theory and the Lothe-Pound theory;  $\eta_i = 1$  for a cluster that does not have any rotational symmetry, and  $\eta_i = 60$  for a cluster with an icosahedron configuration (26). The maxima in the curves of Figure 11 are interpreted as the critical sizes, and we find that different theories can predict different critical sizes. The number of monomers contained in a critical cluster,  $g^*$ , is shown in the 6th column of Table III for each of the theories. The free energy change associated with these critical sizes are given in the 7th column in Table III. The critical free energy change is decomposed into the volume term, surface tension term, translational term, rotational term, and the Lothe-Pound replacement factor term, and the numerical values of these terms are given in columns 1-5 of Table III, respectively.

We find that, in Figure 11, Kulmala's atomistic theory overestimates the free energy change of a critical cluster for  $i > 20$  as compared to the predictions of other

theories, though the atomistic theory is perhaps more appropriate for  $i$  smaller than 20 (region not shown). For the present situation considered ( $g^* > 30$  for all cases, see Table III), the large discrepancies in comparison to other theories may result from the fact that the atomistic theory fails to provide for the nature of a surface. The Lothe-Pound theory and the present work, Eq. [76], in Figure 11, on the other hand, predict much lower free energy change at the critical cluster size than the classical theory does. We find that with an increase of the rotational symmetry factor  $\eta_i$  from 1 to 60, the free energy change curves shift upward by about  $4.1k_B T$  for both the atomistic and Lothe-Pound theories, which would decrease the nucleation rate by about a factor of 100.

In Table III, we find that the cluster translational term is approximately constant and has a value of about  $-24k_B T$  for the case considered. The rotational contributions, on the other hand, have a value of about  $-20k_B T$  for  $\eta_i = 1$  and a value of about  $-16k_B T$  for  $\eta_i = 60$  for the Lothe-Pound theory. Kulmala's atomistic theory predicts the rotational contribution about  $3.3k_B T$  different from the Lothe-Pound prediction for both the  $\eta_i = 1$  and  $\eta_i = 60$  cases, because the critical cluster sizes predicted from Kulmala's theory are smaller. The present work predicts a zero rotational contribution because we have considered the cluster rotation by assuming the cells can freely interchange their positions. That is, for relatively large  $i$ , the cluster is not rigid and the rotational contribution should become insignificant. The volume and surface contributions, shown by the first two columns in Table III, are both strong functions of the critical cluster size  $g^*$ , and they vary dramatically for different theories because  $g^*$  varies when predicted by different theories. Thus, despite the inclusion or exclusion of the cluster translational and/or rotational contributions, a major cause in the discrepancies of the total free energy change prediction is the sum of the volume term and surface term.

For example, the sum of the first two columns in Table III is about  $73k_B T$  both for classical and Lothe-Pound theories without surface tension variation, and is about  $27k_B T$  for the above two theories with Tolman's surface tension variation and for the present theory.

In the comparison of the total free energy change and nucleation rate, the last two columns in Table III, we find that the Lothe-Pound theory predicts a  $10^{17}$  enhancement of the nucleation rate in comparison to the classical rate. Allowing for a surface tension variation, on the other hand, the classical rate itself predicts a  $10^{19}$  enhancement (see the first and second rows). The Lothe-Pound theory and surface tension variation together lead to a  $10^{36}$  enhancement over the classical rate (compare the first and fifth rows). The Lothe-Pound theory with surface tension variation, however, predicts the free energy change at the critical size as a negative value (rows 5 and 6 of Table III); this means that the free energy change over the entire cluster range is negative (see also the lower two dotted curves in Figure 11). In the present cell theory (the last row of Table III), the cluster translation and the surface tension variation (through the cell theory approach) are also considered, however, a nucleation rate enhancement of  $10^{30}$  is predicted as compared to the  $10^{36}$  of the Lothe-Pound theory. A major difference between the present prediction and the Lothe-Pound theory with surface tension variation, despite the fact that the predictions of surface tension variation in both approaches are different, is that the Lothe-Pound theory *does* include the cluster rotational contribution which will cause an underestimation of free energy change (as pointed out earlier, the free energy change in the entire range may become negative) and an overestimation of the nucleation rate.

## SUMMARY AND CONCLUDING REMARKS

In this work, we have applied the cell model of liquids to predict the free energy change of cluster formation in homogeneous nucleation. In particular, the surface tension (or surface energy) of a microcluster can be appropriately defined by the statistical mechanical formulation. We have compared the surface tension variation as a function of cluster size with that predicted by the Tolman approach, and the results agree well with each other. Unlike the Tolman approach which lacks a microscopic or molecular basis, the present model provides a better understanding of the cause of the surface tension decrease from the bulk for clusters.

The classical nucleation free energy change expression has been criticized for its failure to include the energy correction due to external degrees of freedom (translational, rotational, etc.). The Lothe-Pound theory, the atomistic theory, and the present work provide different approaches to recalculate the free energy change in a nucleation process. We summarize our findings in the comparison of these theories: (A) The atomistic theory estimates the free energy change for small clusters. When the critical clusters become larger and possess surfaces, unless all the intra-cluster vibrational frequencies are obtainable, the atomistic theory is less appropriate. (B) The Lothe-Pound theory overpredicts the cluster rotational contribution. For clusters larger than a certain size, liquid-like properties should appear, and the cluster rotational motion may become much less important as a contribution to the free energy. For example, the Lothe-Pound theory with a surface tension variation with cluster size may predict a negative free energy change for the critical cluster formation, which is an incorrect prediction; (C) In the Lothe-Pound and atomistic theories, the cluster rotational symmetry factor that varies from 1 to 60 can only increase the free energy change by  $5k_B T$ , which is not a major factor in the enhancement or retardation of the nucleation rate.



The present theory is not intended to replace the atomistic theory. The atomistic theory and the present work practically cover different size ranges; the former is a better theory for smaller clusters when a surface does not exist or the surface is small, and the latter for larger clusters when a surface is present and liquid-like properties appear. The surface tension variation with size, the cluster translational contribution, and/or rotational contribution all decrease the total free energy change prediction and, in consequence, predict many orders of magnitude increase in the nucleation rate in comparison to the classical theory. Therefore, one must conclude that if classical nucleation theory overestimates measured nucleation rates, the most likely explanation is kinetic reasons, such as the sticking probability between monomer and clusters.

#### **ACKNOWLEDGEMENTS**

This work was supported by National Science Foundation Grant ATM-9003186.

## APPENDIX

### Determination of the Tolman $\delta_T$

Kirkwood and Buff (46) were the first to give a statistical mechanical expression to calculate  $\delta_T$ , though Tolman (47) himself obtained a formula to estimate the order of magnitude of  $\delta_T$  through the use of the van der Waals equation of state. We will calculate  $\delta_T$  as a function of the Lennard-Jones potential parameters based on Kirkwood and Buff's theory. Their expression for  $\delta_T$  is

$$\delta_T = \frac{4}{15} \frac{\int_0^{\infty} r^5 \frac{du(r)}{dr} g(r) dr}{\int_0^{\infty} r^4 \frac{du(r)}{dr} g(r) dr} \quad [A1]$$

in which  $u(r)$  is the intermolecular potential,  $g(r)$  is the radial distribution function defined as the mean local density at  $r$  deviating from that of the bulk. It can be shown that for a dilute surrounding gas  $g(r)$  can be related to  $u(r)$  as (48)

$$g(r) = \exp\left(-\frac{u(r)}{k_B T}\right). \quad [A2]$$

If  $u(r)$  obeys the Lennard-Jones 6-12 potential (Eq. [20]), Eq. [A1] can be written as

$$\frac{\delta_T}{r_1} = \frac{4}{15} \frac{z^{1/2} (4\pi\gamma/3)^{1/3}}{Z^{1/6}} \left[ \frac{\int_0^{Z^{1/6}} (2ZX^6 - 1) \exp(X^6 - ZX^{12}) dX}{\int_0^{Z^{1/6}} X(2ZX^6 - 1) \exp(X^6 - ZX^{12}) dX} \right] \quad [A3]$$

where

$$X = \left(\frac{4\epsilon}{k_B T}\right)^{1/6} \frac{\delta}{r} \quad ; \quad Z = \frac{k_B T}{4\epsilon}. \quad [A4]$$

In obtaining Eq. [A3], the following relations of the cell theory in this paper have been used:  $a^3 = \gamma v$  (Eq. [50]),  $z = \delta^2/a^2$  (Eq. [44]), and Eq. [51] which relates  $r_1$  and  $v$ .  $\delta$  and  $\epsilon$  are the Lennard-Jones 6-12 potential parameters, and  $r_1$  is the radius of a molecule. Also in Eq. [A3], we have changed the limits of integration in both the denominator and numerator from that of Eq. [A1]; that is,  $r = 0 \rightarrow \infty$  is changed to  $r = r_1 \rightarrow \infty$ . The latter is nondimensionalized according to Eq. [A4]. This change of integration arises from the fact that for the distance  $r \leq r_1$ ,  $u(r) \rightarrow \infty$  and  $g(r) = 0$ .

Because  $\delta/a = z^{1/2}$  is uniquely related to  $c\epsilon/k_B T$  by Eq. [57] according to the cell model,  $\delta_T/r_1$ , given by Eq. [A3], is also a function of  $c\epsilon/k_B T$  only; the calculated result is shown in Figure 12, where the number of nearest neighbors,  $c = 12$ , is used. The value of  $\delta_T/r_1$  determined lies between 0.51 and 0.77 in the  $c\epsilon/k_B T$  range of interest; that is,  $\delta_T$  is of the order of magnitude of a molecular radius.

## REFERENCES

1. Volmer, M., and Weber, A., *Z. Phys. Chem. (Leipzig)* **119**, 277 (1926).
2. Farkas, L., *Z. Phys. Chem.* **125**, 236 (1927).
3. Becker, R., and Doering, W., *Ann Phys.* **24**, 719 (1935).
4. Zeldovich, Y. B., *Zh. Eksp. Teor. Fiz.* **12**, 525 (1942).
5. Lothe, J., and Pound, G. M., *J. Chem. Phys.* **36**, 2080 (1962).
6. Lothe, J., and Pound, G. M., *J. Chem. Phys.* **45**, 630 (1966).
7. Lothe, J., and Pound, G. M., *J. Chem. Phys.* **48**, 1849 (1968).
8. Reed, S. G., *J. Chem. Phys.* **20**, 208 (1952).
9. McGinty, D. J., *J. Chem. Phys.* **55**, 580 (1971).
10. McGinty, D. J., *Chem. Phys. Lett.* **13**, 525 (1972).
11. McGinty, D. J., *J. Chem. Phys.* **58**, 4733 (1973).
12. Burton, J. J., *J. Chem. Phys.* **52**, 345 (1970).
13. Lee, J. K., Barker, J. A., and Abraham, F. F., *J. Chem. Phys.* **58**, 3166 (1973).
14. Nishioka, K., Shawyer, R., Bienenstock, A., and Pound, G. M., *J. Chem. Phys.* **55**, 5082 (1971).
15. Hoare, M. R., and Pal, P., *Adv. Phys.* **20**, 161 (1971).
16. Kobraei, H. R., *J. Chem. Phys.* **81**, 6051 (1984).
17. Kobraei, H. R., and Anderson, B. R., *J. Chem. Phys.* **88**, 4451 (1988).
18. Kulmala, M., "Nucleation as an Aerosol Physical Problem," Ph.D. Thesis. University of Helsinki, Finland, 1988.
19. Kulmala, M., Olin, M., and Raunemaa, T., *J. Aerosol Sci.* **18**, 615 (1987).
20. Hill, T. L., "An Introduction to Statistical Thermodynamics," Chapt. 16. Dover Publications, New York, 1986.
21. Hirschfelder, J. O., Curtiss, C. F., and Bird, R. B., "Molecular Theory of Gases and Liquids," Chapt. 4, pp. 271-296. Wiley, New York, 1963.

22. Lennard-Jones, J. E., and Devonshire, A. F., *Proc. Roy. Soc. (London)* **A163**, 53 (1937).
23. Lennard-Jones, J. E., and Devonshire, A. F., *Proc. Roy. Soc. (London)* **A165**, 1 (1938).
24. Pruppacher, H. R., and Klett, J. D., "Microphysics of Clouds and Precipitation," pp. 163–164. Reidel Publishing, 1980.
25. Huang, D. D., and Seinfeld, J. H., *J. Statist. Phys.*, (submitted).
26. Hoare, M. R., and Pal, P., *Adv. Phys.* **24**, 645 (1975).
27. Lothe, J., and Pound, G. M., in "Nucleation," (A. C. Zettlemoyer Ed.), Chapt. 3. Marcel Dekker, New York, 1969.
28. Abraham, F. F., and Pound, G. M., *J. Chem. Phys.* **48**, 732 (1968).
29. Salk (Suck), S. H., Lutrus, C. K., and Hagen, D. E., *J. Atmos. Sci.* **45**, 2979 (1988).
30. Plummer, P. L. M., and Hale, B. N., *J. Chem. Phys.* **56**, 4329 (1972).
31. Daee, M., Lund, L. H., Plummer, P. L. M., Kassner Jr., J. L., and Hale, B. N., *J. Colloid Interface Sci.* **39**, 65 (1972).
32. Burton, J. J., and Briant, C. L., *Adv. Colloid Interface Sci.* **7**, 131 (1977).
33. Salk (Suck), S. H., and Lutrus, C. K., *J. Chem. Phys.* **87**, 636 (1987).
34. Salk (Suck), S. H., Chen, T. S., Hagen, D. E., and Lutrus, C. K., *Theor. Chim. Acta* **70**, 3 (1986).
35. Hoare, M. R., *Adv. Chem. Phys.* **40**, 49 (1979).
36. Hoare, M. R., and McInnes, J. A., *Adv. Phys.* **32**, 791 (1983).
37. Andres, R. P., *Ind. Eng. Chem.* **57**, 25 (Oct, 1965).
38. Herschbach, D. R., Johnson, H. S., and Rapp, D., *J. Chem. Phys.* **31**, 1652 (1959).
39. Hirschfelder, J. O., Curtiss, C. F., and Bird, R. B., "Molecular Theory of Gases and Liquids," Chapt. 5, pp. 342–347. Wiley, New York, 1963.

40. Lennard-Jones, J. E., and Corner, J., *Trans. Faraday Soc.* **36**, 1156 (1940).
41. Corner, J., *Trans. Faraday Soc.* **44**, 1036 (1948).
42. Mackay, A. L., *Acta. Cryst.* **15**, 916 (1962).
43. Tolman, R. C., *J. Chem. Phys.* **17**, 333 (1949).
44. Bartell, L. S., *J. Phys. Chem.* **91**, 5985 (1987).
45. Plesner, I. W., *J. Chem. Phys.* **40**, 1510 (1964).
46. Kirkwood, J. G., and Buff, F. P., *J. Chem. Phys.* **17**, 338 (1949).
47. Tolman, R. C., *J. Chem. Phys.* **17**, 118 (1949).
48. Hill, T. L., "An Introduction to Statistical Thermodynamics," Chapt. 17.  
Dover Publications, New York, 1986.

Table I. Comparison between the Atomistic Theory and Present Work

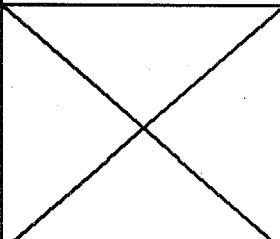
approach $q_i$ contri- bution	Atomistic Theory	Present Work	
translation	The movement of clusters is in the gas-cluster system.	Same as left	
rotation	The cluster rotates as a rigid body.	Cells that contain one molecule are allowed to interchange their relative positions, hence the cluster rotation is accounted for.	The cell theory of liquid is applied to describe the motion of molecules in a liquid-like microcluster.
vibration	Molecules in the cluster vibrate in the vicinity of their minimum energy positions.	Molecules are allowed to vibrate within their cells.	
binding	The motion of molecules is under a constant potential energy throughout the entire cluster volume.	Same as left	
surface molecules		Surface molecules are considered as a different group from the interior molecules.	

Table II. Comparison between Measured Surface Tensions and the Present Predictions

substance	Temp. (°C)	$\epsilon/k_B$ (K)	$c\epsilon/k_B T$	surface energy per molecule/ $k_B T$	$T_1$ (Å)	$\sigma^s$ (10 <sup>-3</sup> J/m <sup>2</sup> ) calculated	$\sigma^s$ (10 <sup>-3</sup> J/m <sup>2</sup> ) measured	error (%)
water	20	809.1	33.14	2.153	1.927	83.64	72.88	14.76
methanol	20	481.8	19.73	1.154	2.523	26.15	22.50	16.22
carbon disulfide	0	488.0	21.45	1.282	2.858	21.10	32.32	-34.72
n- propanol	20	576.7	23.62	1.446	3.094	21.79	23.71	-8.10
methyl acetate	20	469.8	19.24	1.117	3.158	16.18	23.97	-32.50
ethyl acetate	20	531.0	21.75	1.305	3.384	16.44	25.37	-35.20



Table III. Comparison of Free Energy Change of Water S=3 and T=293K Predicted from Various Theories.

$\Delta F^\ddagger/k_B T$ Theory	-g ins. volume term	surface tension term	cluster trans- lation	cluster rotation	replace- ment factor	critical size, g <sup>*</sup>	total $\Delta F/k_B T$ at g <sup>*</sup>	log <sub>10</sub> (J/J <sub>class.</sub> )
classical $\sigma = \text{const.}$	-146.12	219.05	—	—	—	133	72.94	0
classical $\sigma = \sigma(R_e)$	-90.09	117.63	—	—	—	82	27.55	19.71
Lothe-Pound $\sigma = \text{const.}, \eta_i = 1$	-134.03	206.80	-24.75	-21.25	6.53	122	33.30	17.21
Lothe-Pound $\sigma = \text{const.}, \eta_i = 60$	-134.03	206.80	-24.75	-17.15	8.53	122	37.39	15.44
Lothe-Pound $\sigma(R_e), \eta_i = 1$	-74.71	101.87	-23.87	-19.79	6.53	68	-9.97	36.01
Lothe-Pound $\sigma(R_e), \eta_i = 60$	-74.71	101.87	-23.87	-15.69	6.53	68	-5.87	34.23
atomistic (Kulmala) $\eta_i = 1, \text{Eq. (28)}$	-35.16	198.37 <sup>†</sup>	-22.74	-17.90	—	32	122.57	-21.55
atomistic (Kulmala) $\eta_i = 60, \text{Eq. (28)}$	-35.16	198.37 <sup>†</sup>	-22.74	-13.81	—	32	126.67	-23.33
This Work Eq. (76)	-61.52	89.63	-23.58	—	—	58	3.53	30.14

<sup>†</sup>Including intrachuster vibration, binding, and monomer translation energies

## LIST OF FIGURES

- Figure 1. Coordinates of a surface cell.
- Figure 2. Interior cell potential as a function of the radial distance with  $z$  as a parameter.
- Figure 3. Interior cell minimum potential and its location as functions of  $z^3$ .
- Figure 4.  $z^{1/2}$  as a function of  $c\epsilon/k_B T$ .  $\gamma = \sqrt{2}$ .
- Figure 5. Relations between the half open angle of a cluster,  $\chi$ , and that of a planar surface,  $\chi|_{\text{planar}}$ .
- Figure 6. Surface cell profiles: (a) cross-sectional view of a surface cell; (b) planar surface situation; (c) 55-mer situation; (c) 13-mer situation.  $c\epsilon/k_B T = 25$ . f.c.c. packing is assumed.
- Figure 7. Minimum potentials of a surface cell and an interior cell as functions of  $c\epsilon/k_B T$  and particle size. f.c.c. packing is assumed.
- Figure 8. Effective volumes of a molecule present in a surface cell or an interior cell as functions of  $c\epsilon/k_B T$  and particle size. f.c.c. packing is assumed.
- Figure 9. Surface energy per molecule as a function of  $c\epsilon/k_B T$  and particle size. f.c.c. packing is assumed.
- Figure 10. Effective surface tension ratio as a function of the cluster size with  $c\epsilon/k_B T$  as a parameter. (a) present theory; (b) Tolman approach.
- Figure 11. Comparison between the free energy change of formation of water clusters at 293 K and saturation ratio  $S = 3$  predicted by various theories.
- Figure 12. Tolman delta as a function of  $c\epsilon/k_B T$ .

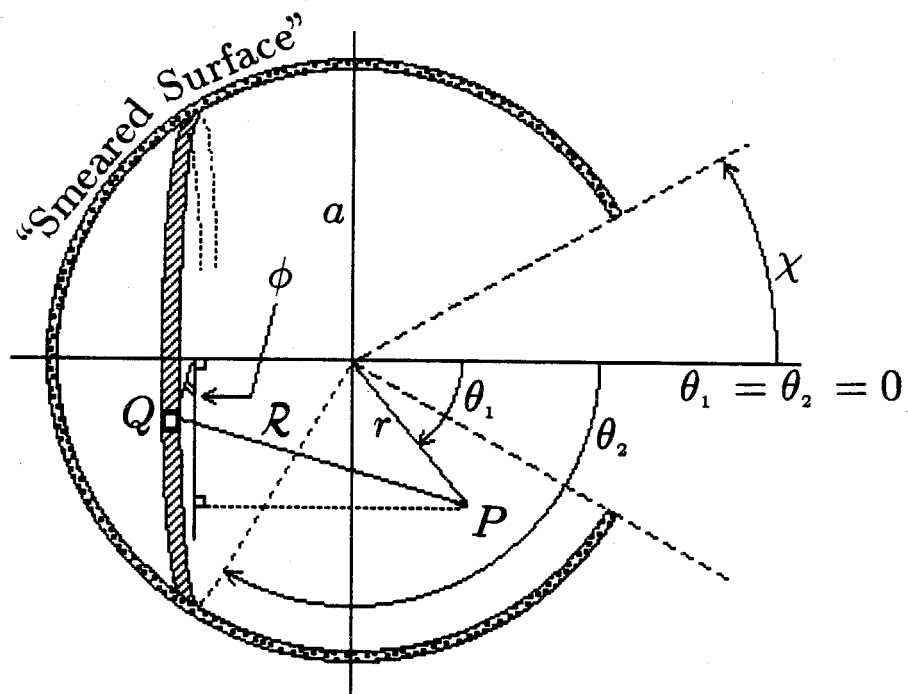


Figure 1

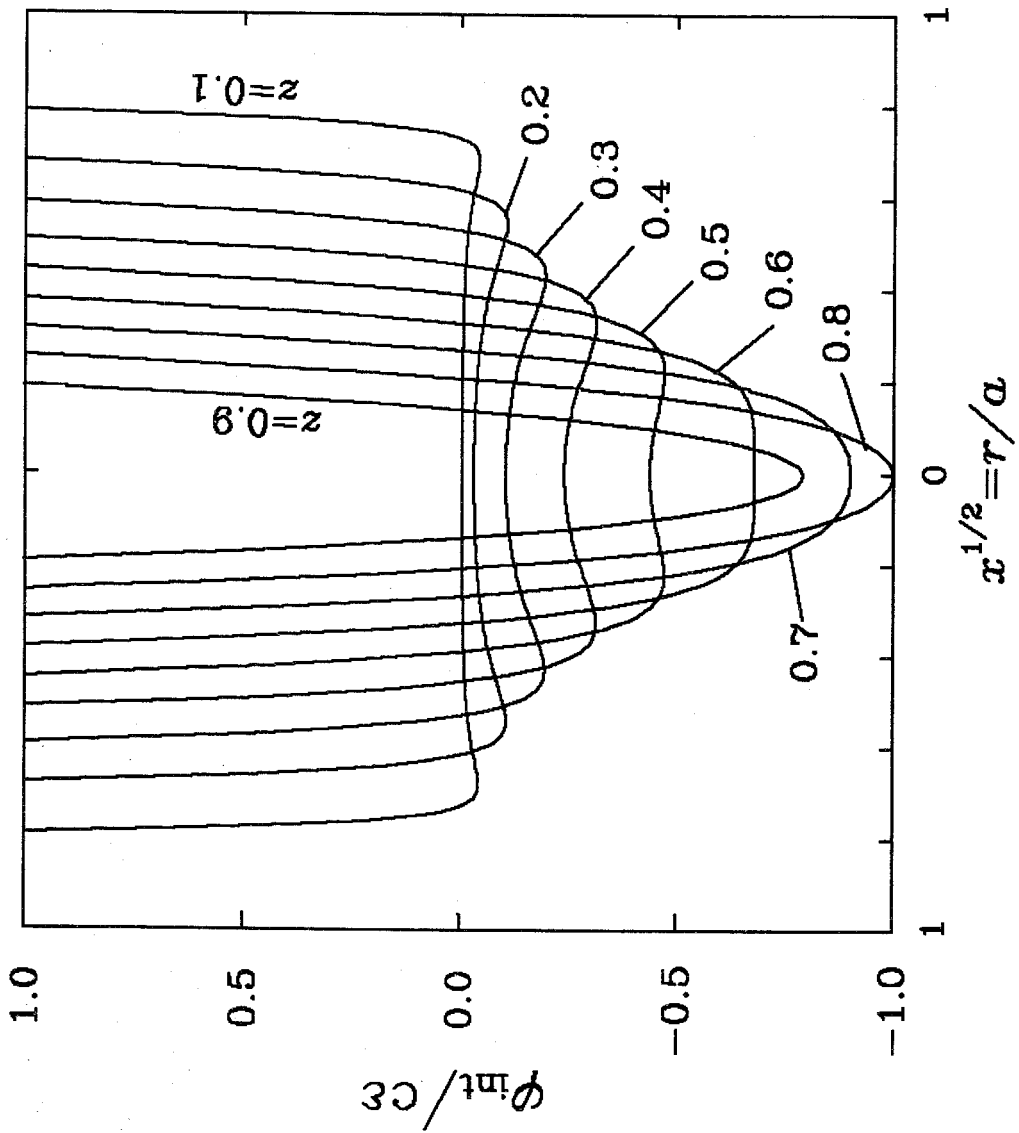


Figure 2

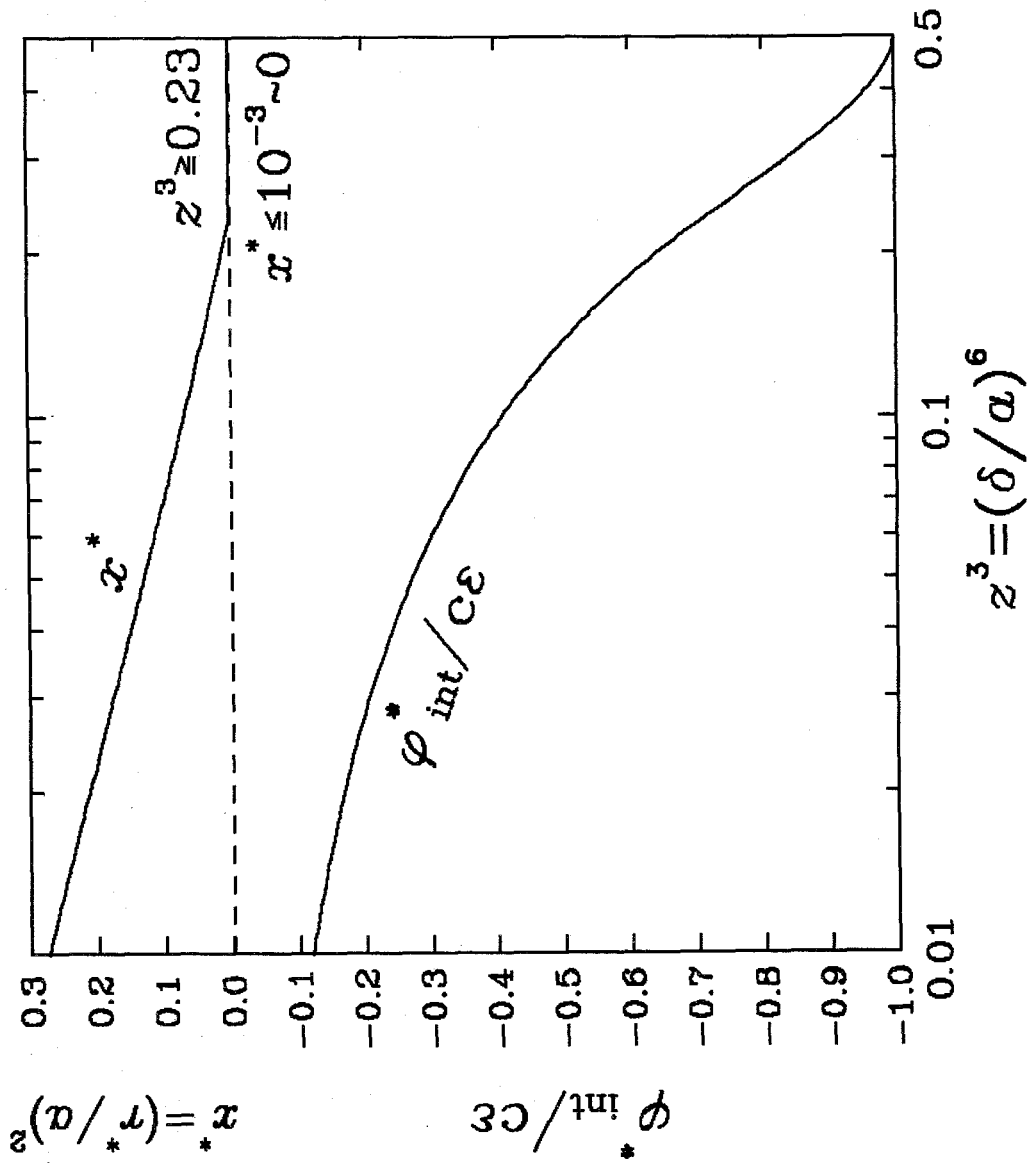


Figure 3

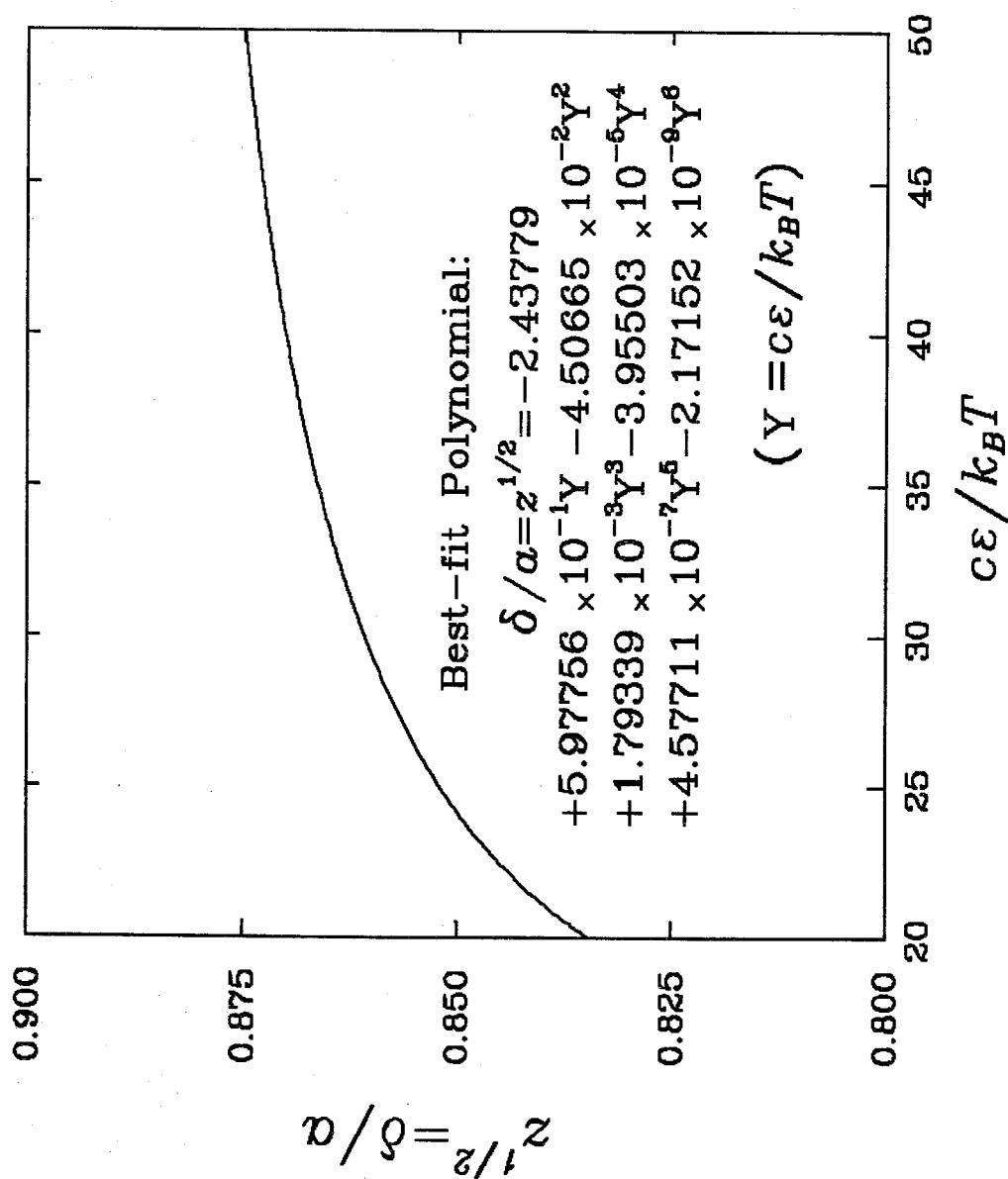


Figure 4

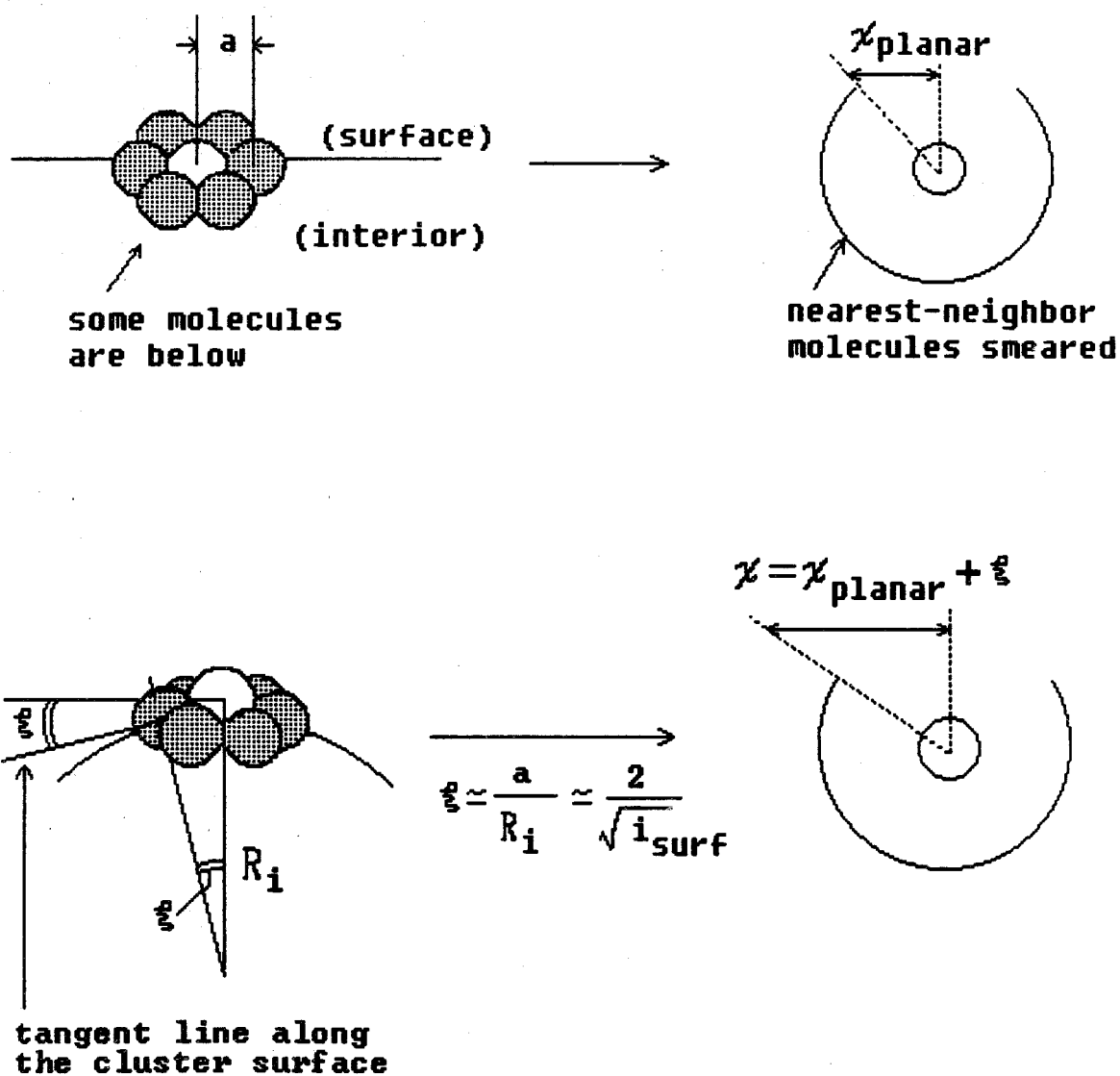


Figure 5

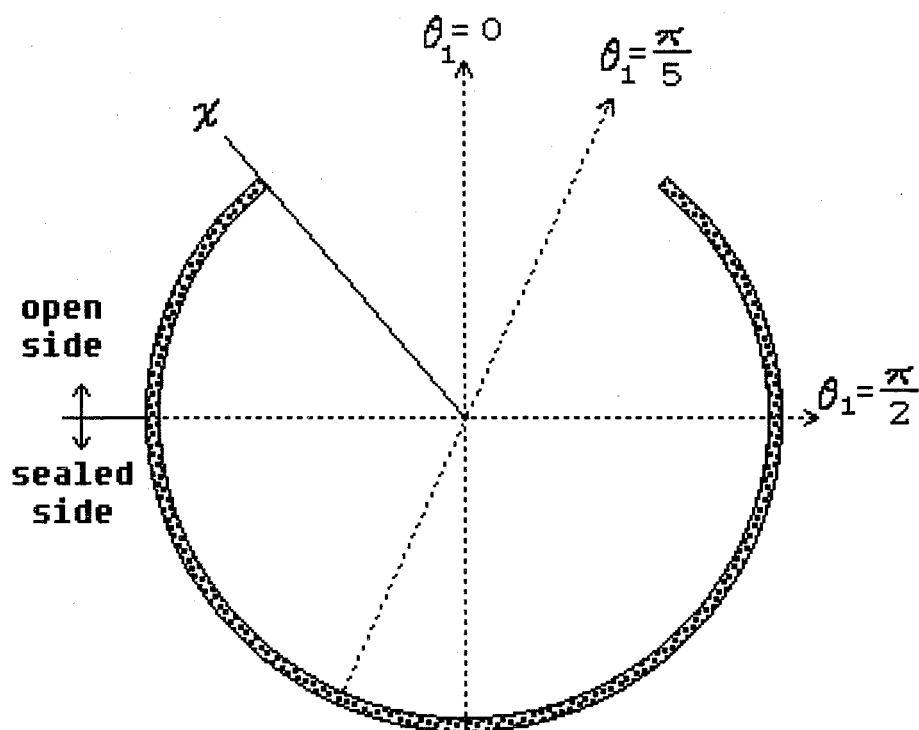


Figure 6a



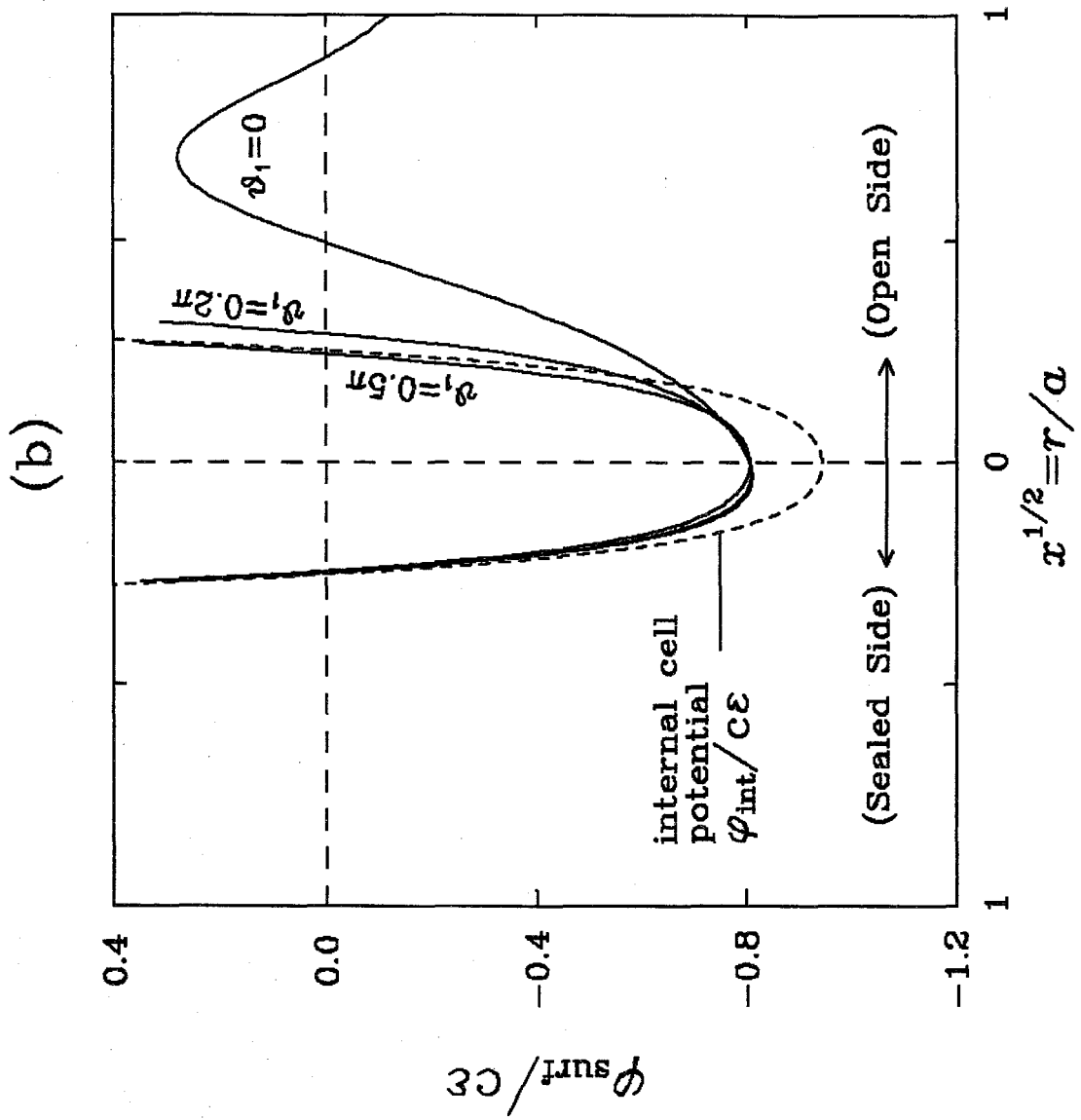


Figure 6b

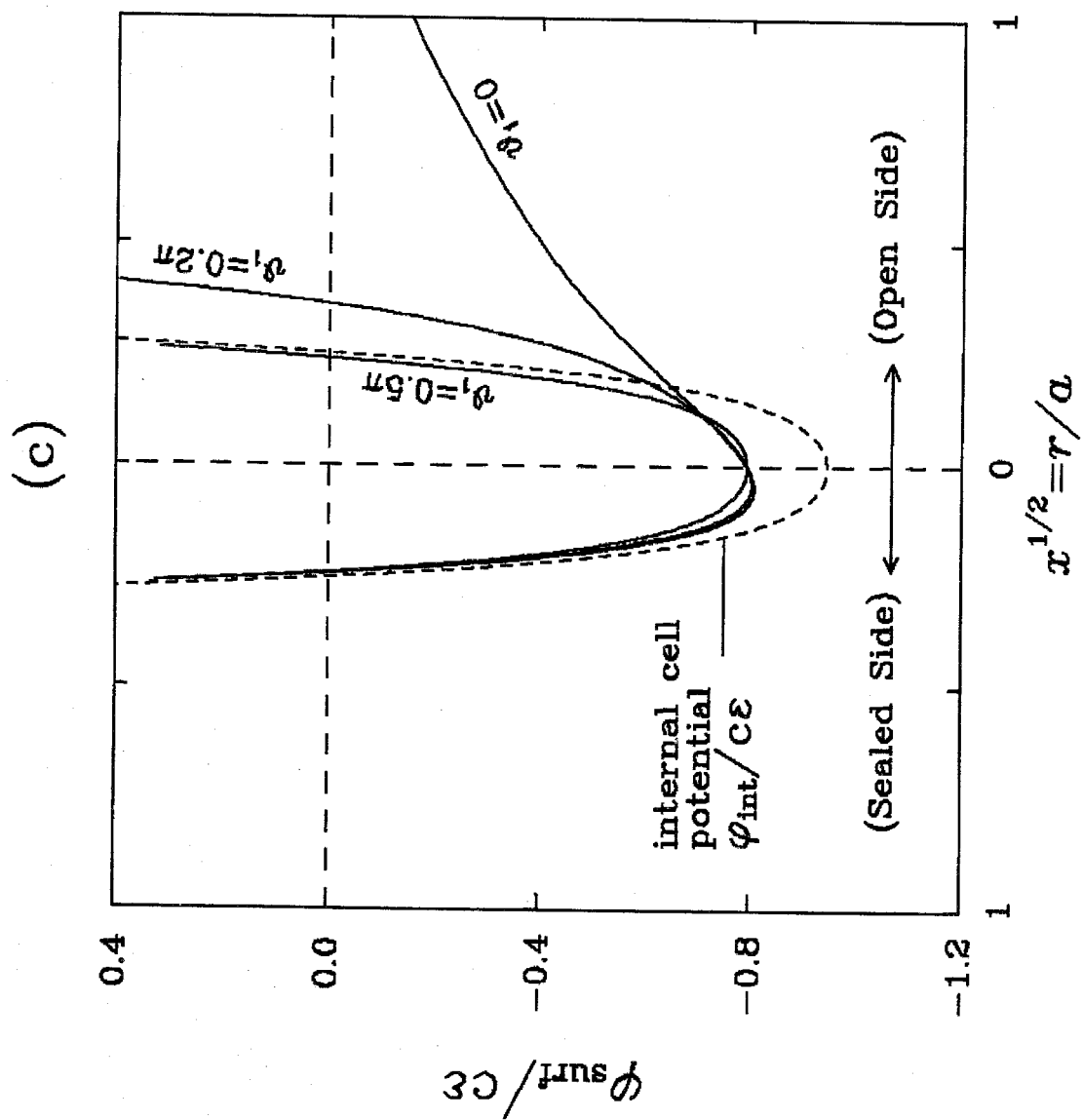


Figure 6c

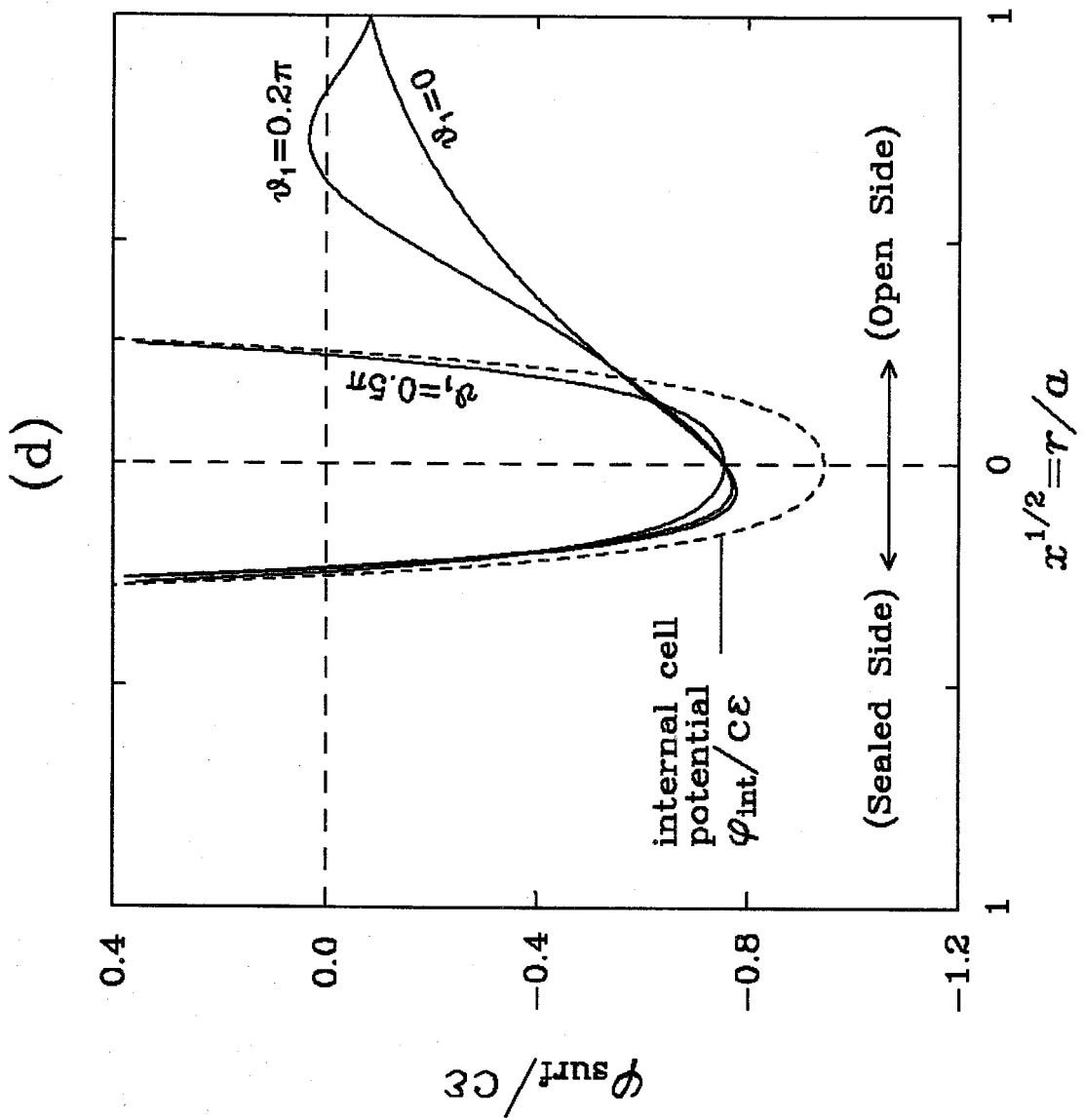


Figure 6d

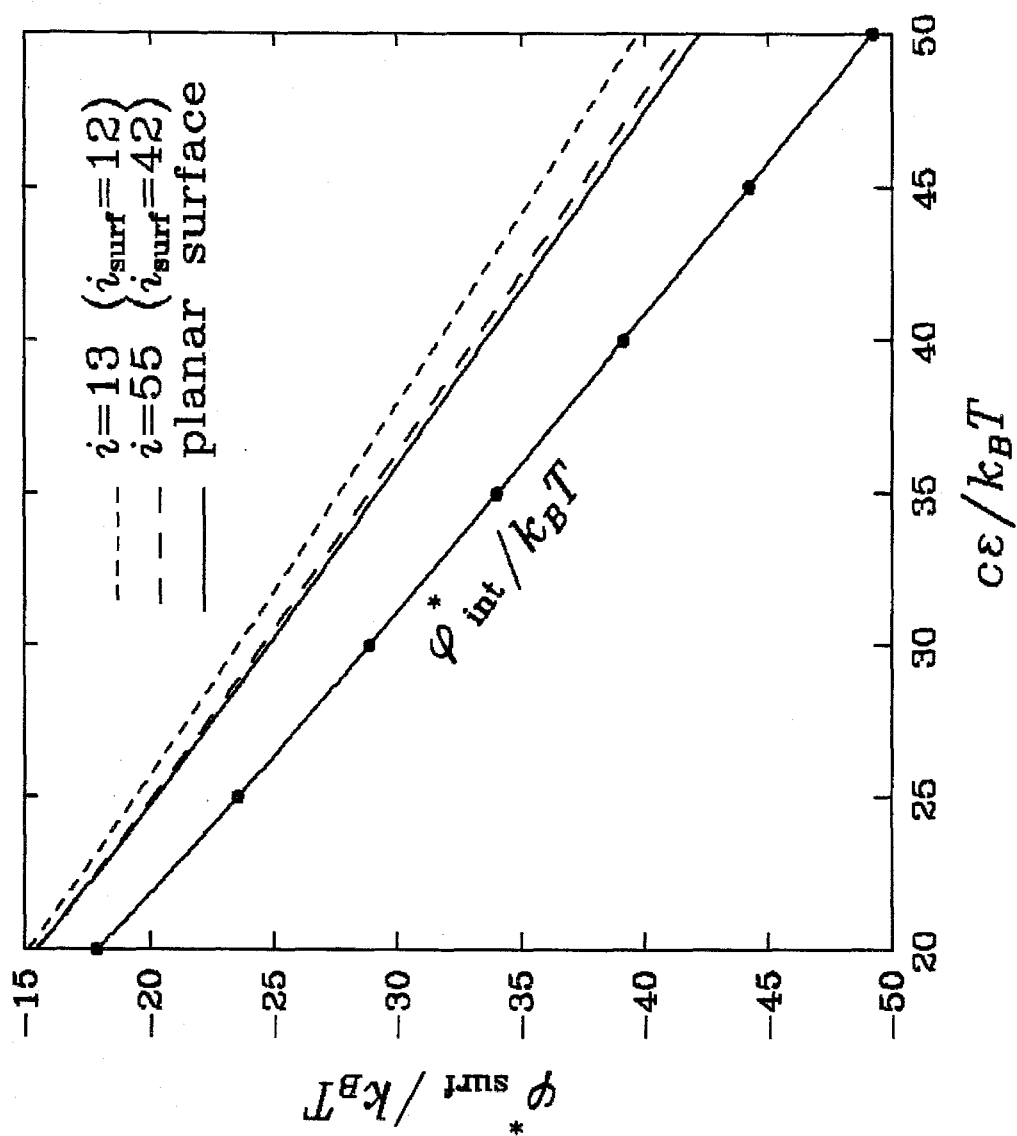


Figure 7

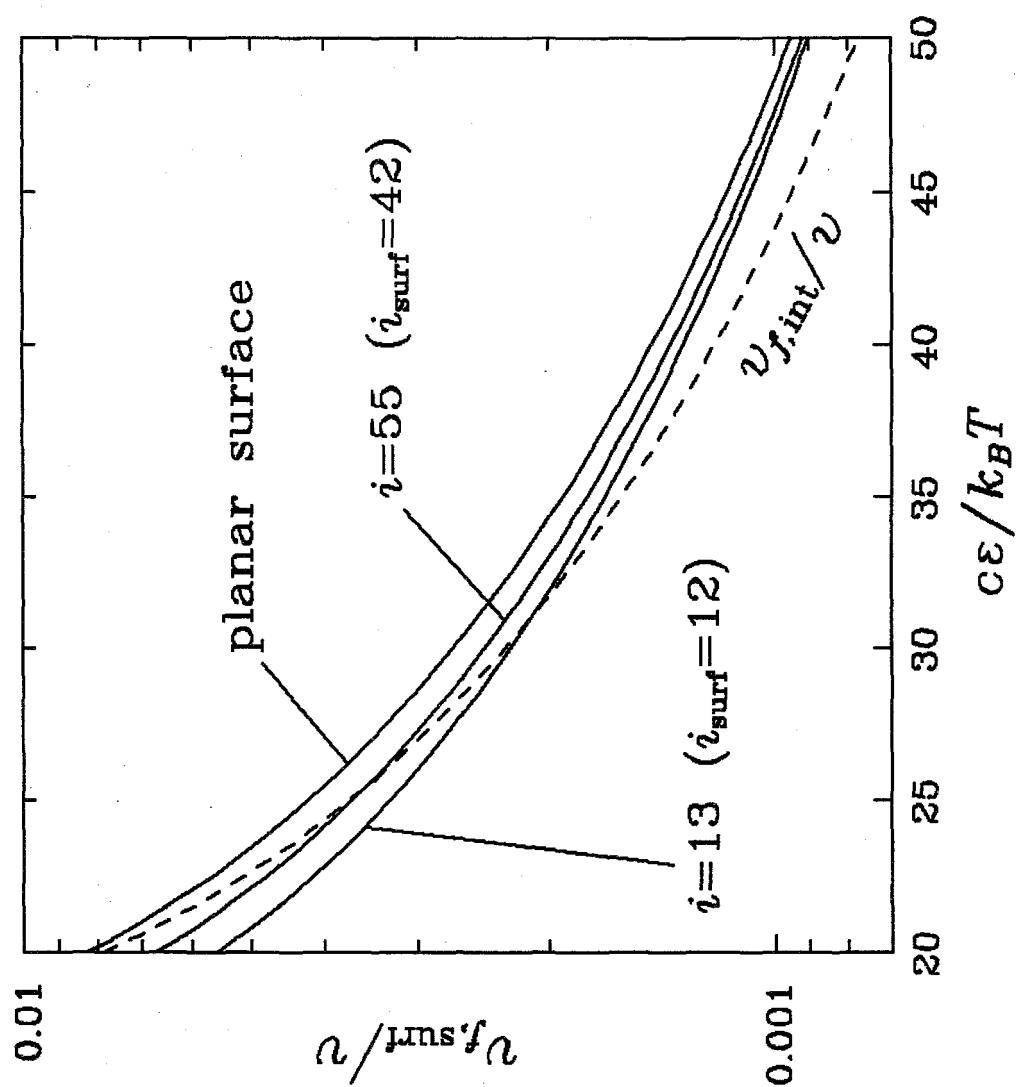


Figure 8

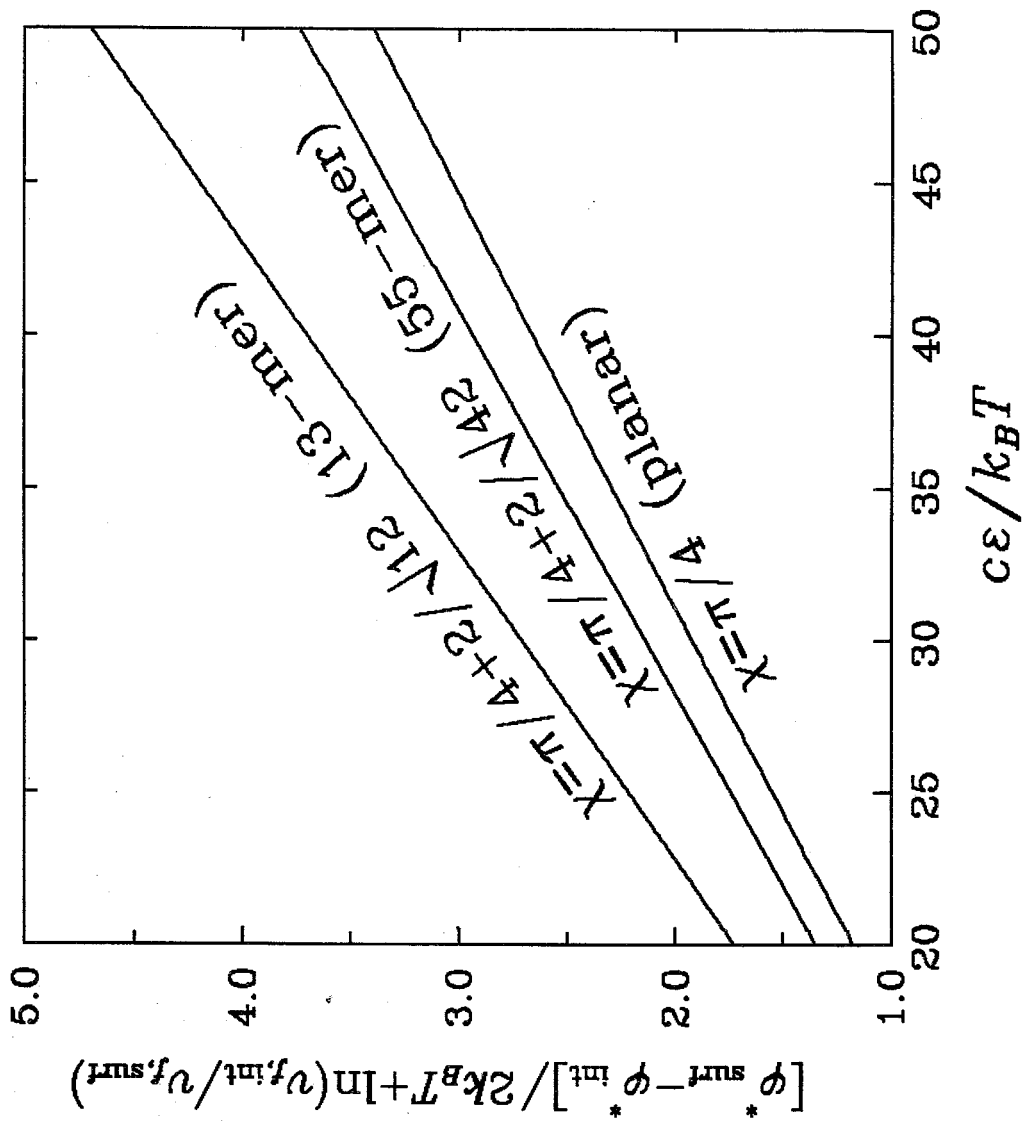


Figure 9

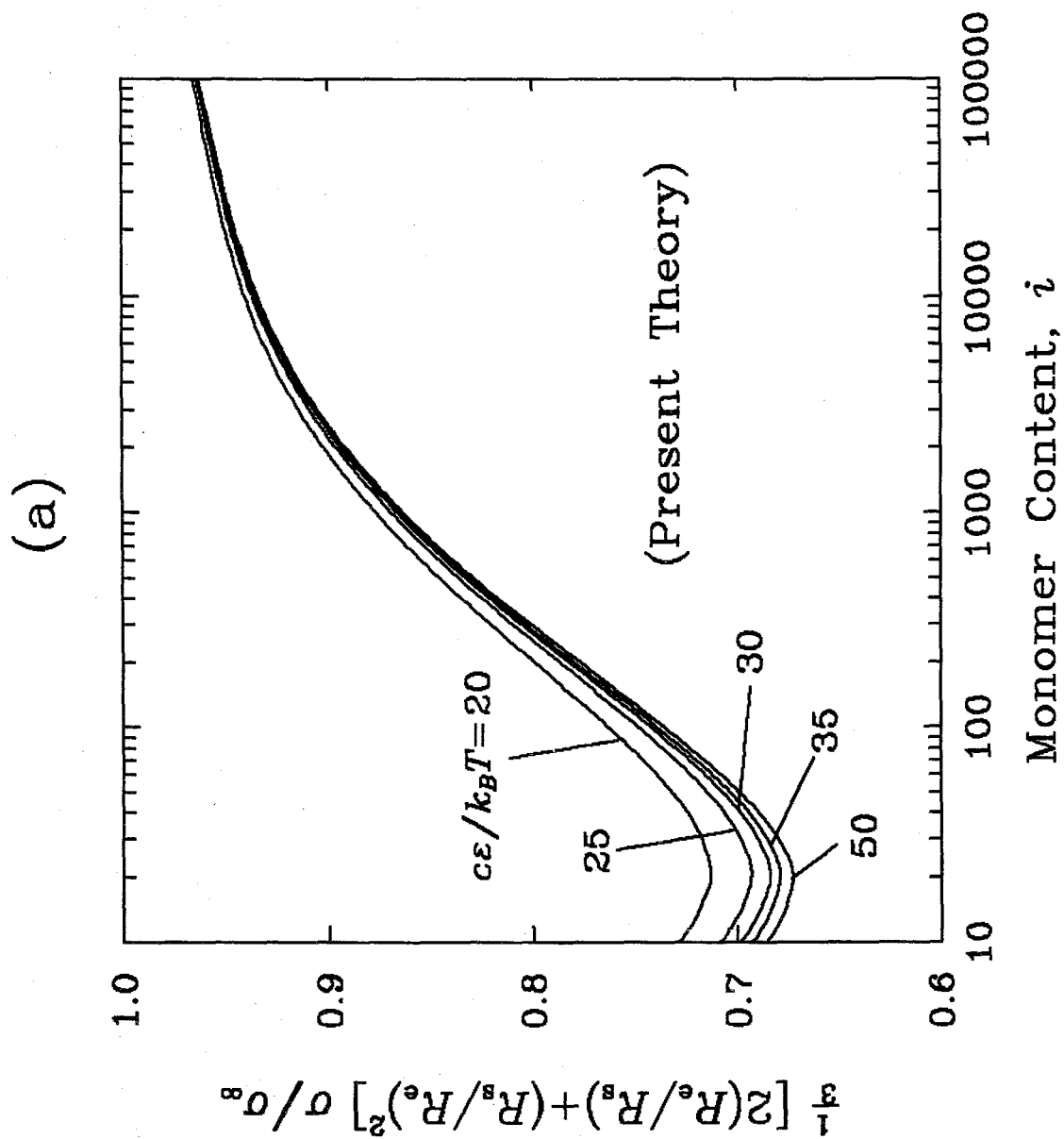


Figure 10a

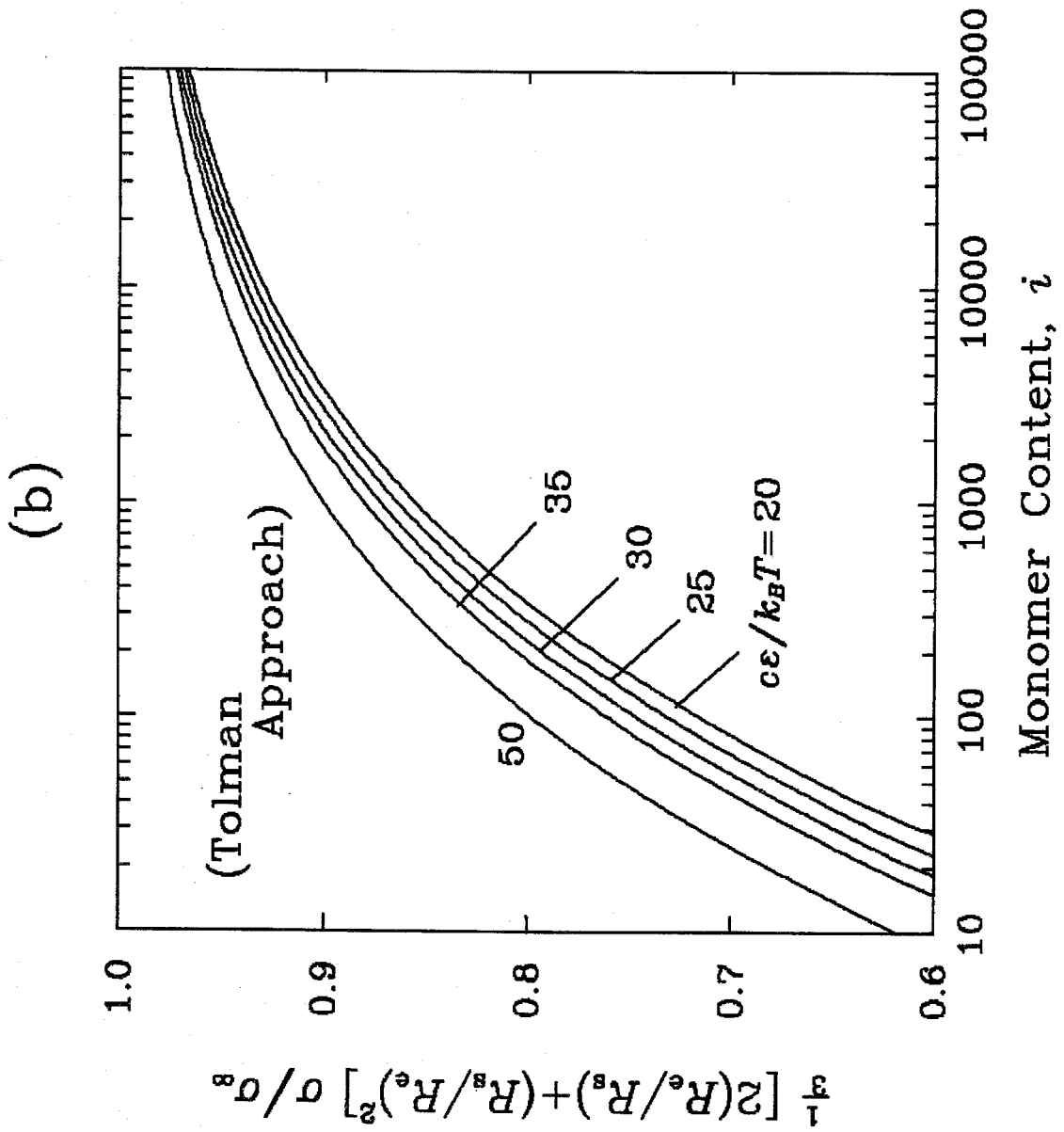


Figure 10b



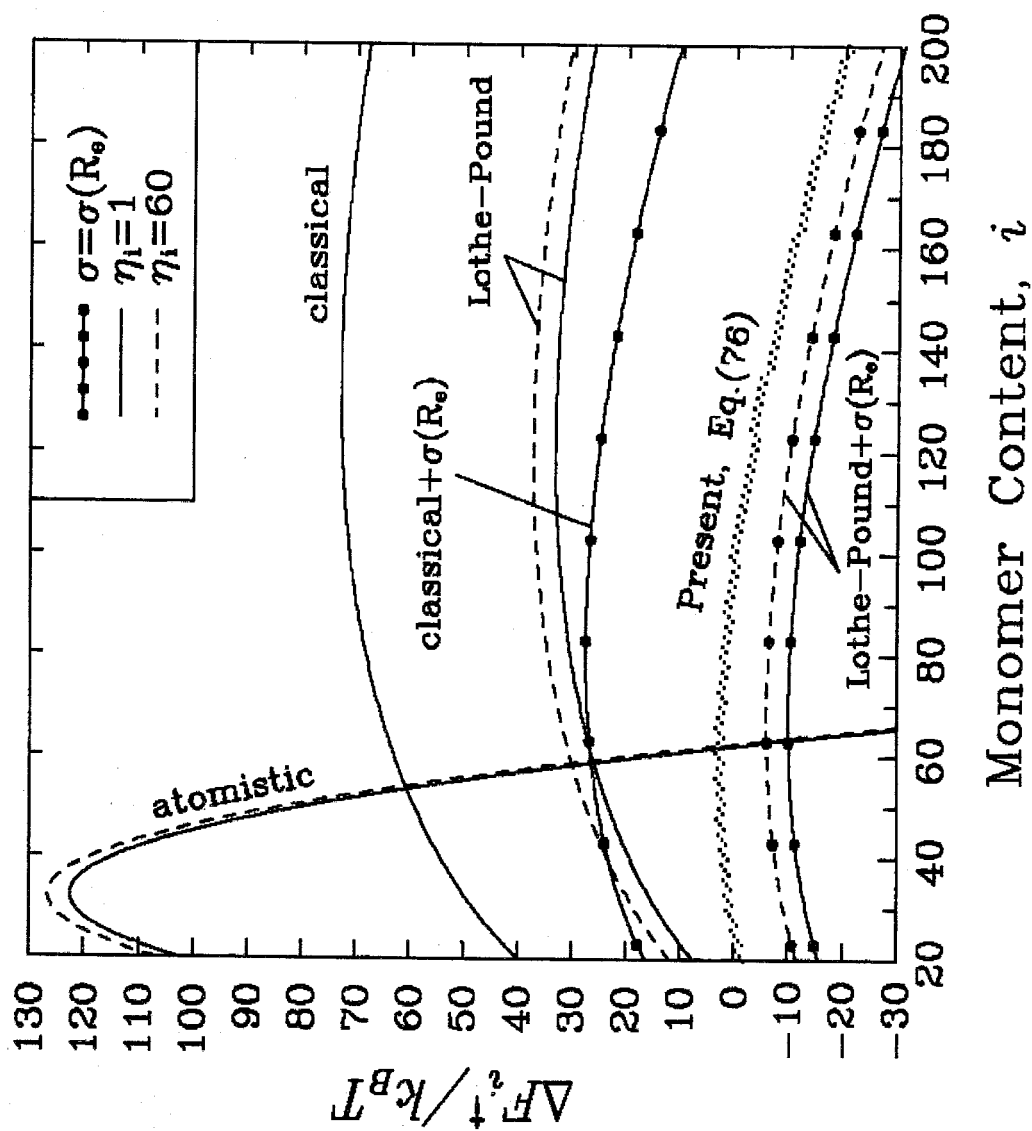


Figure 11

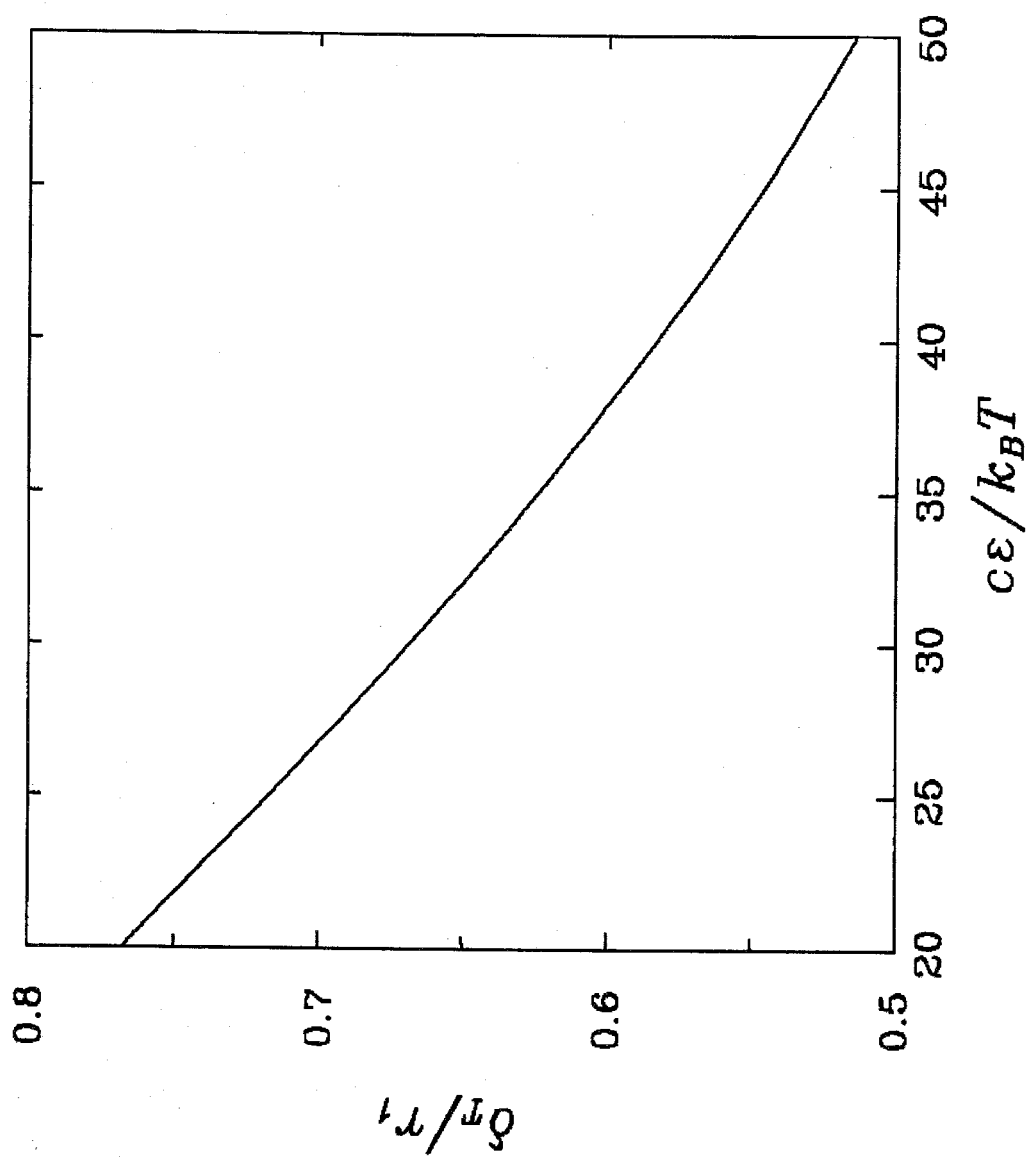


Figure 12

## **CHAPTER 9**

### **SUMMARY AND CONCLUDING REMARKS**

## THESIS SUMMARY

In the first few chapters, we have addressed issues on Brownian coagulation and the role played by an interparticle potential in coagulation. This nonequilibrium process is studied both analytically and numerically. The present research provides a fundamental and first-principle based theoretical routine for calculating aerosol particle coagulation in the presence of an interparticle potential. The application of a coagulation process is also demonstrated in a simulation of a chemical vapor deposition reactor.

In the latter part of the thesis, we have focused on the issue of the cluster formation free energy change in a nucleation process. We have shown that the inclusion of cluster translational and rotational motion is necessary in the formulation of free energy change, and we have been able to provide an explanation of the microcluster surface tension. The new theory that fulfills several aspects lacking in earlier theories reveals important information about the properties of a microcluster such as the surface tension.

## RECOMMENDATIONS FOR FUTURE RESEARCH

- A. For charged particle coagulation in the presence of an external field, a situation that commonly occurs in many aerosol instruments, the FPE or BGK equation as well as the interparticle image potential derived in Chapter 4 can be applied to obtain either the interparticle coagulation rate or the ion-particle charging rate for a situation in which one of the colliding particles is an ion.
- B. Numerical simulation can be further pursued for the ion nucleation situation. The coagulation between an uncharged monomer and a charged cluster, in

this case, is of interest. The simulation result can be compared with the earlier experiments and can continue to open new opportunities in experimental developments.

- C.* Investigation of the sticking probability between microclusters is the most important issue remaining in the nucleation field. The sticking probability is often taken as unity, however, one expects particles of molecular sizes will have a sticking probability close to zero. It is necessary in future nucleation research to express the sticking probability as a function of both the material properties, such as the intermolecular potential, and the cluster sizes.
- D.* Evaluation of the importance of aerosol coagulation and nucleation in chemical vapor deposition processes, including manufacturing semiconductor thin films and superconductor powders, is required.

## **THESIS APPENDIX**

### **ON THE RELATION BETWEEN BINARY DIFFUSIVITY AND MEAN FREE PATH**

**Appeared in Journal of Colloid and Interface Science  
Vol. 125, No. 2, pp. 733–735, June 1988**

In problems of the diffusion of a vapor species  $A$  through a background gas  $B$  (e.g., air) the relation between the binary mixture diffusivity,  $\mathcal{D}_{AB}$ , the mean free path,  $\lambda_{AB}$ , and the mean thermal speed,  $\bar{c}_A$  is of interest.

From so-called zeroth-order kinetic theory of gases it can be argued that (1)

$$\mathcal{D}_{AB} = \frac{1}{3} \lambda_{AB} \bar{c}_A . \quad [1]$$

Fuchs and Sutugin (2) called Eq. [1] Meyer's formula. In the same article Fuchs and Sutugin used another formula for the ion diffusivity in a neutral gas,

$$\mathcal{D}_{AB} = \frac{3\pi}{16\sqrt{2}} (1+z)^{1/2} \lambda_{AB} \bar{c}_A , \quad [2]$$

where  $z = m_A/m_B$ ,  $m_A$  and  $m_B$  are the ion and carrier gas molecule mass, respectively.

Fuchs (3) suggested yet another relation

$$\mathcal{D}_{AB} = \frac{\pi}{8} \lambda_{AB} \bar{c}_A \quad [3]$$

and Davis (4, 5) used the following equation from a hard sphere model:

$$\mathcal{D}_{AB} = \frac{3\pi}{32} (1+z) \lambda_{AB} \bar{c}_A . \quad [4]$$

Loyalka (6) has used

$$\mathcal{D}_{AB} = \frac{\sqrt{\pi}}{4} \lambda_{AB} \bar{c}_A . \quad [5]$$

Equation [2] was also used by Bricard and Pradel (7) and by Liu and Yeh (8). Based on Kennard (9), Pui (10) added a correction factor,  $(1 + \epsilon_{AB})$ , to Eq. [2],

$$\mathcal{D}_{AB} = (1 + \epsilon_{AB}) \frac{3\pi}{16\sqrt{2}} (1 + z)^{1/2} \lambda_{AB} \bar{c}_A, \quad [6]$$

where  $\epsilon_{AB} = 0.132$  for  $z \ll 1$  and  $0.016$  for  $z \gg 1$ . This formula was consequently used by Liu and Pui (11) and by Adachi *et al.* (12).

The purpose of the present note is to attempt to clarify the relationship between the binary diffusivity and the mean free path. Starting from Chapman (13), Enskog (14), and Chapman and Cowling (15), the *first-order* Chapman-Enskog approximation of the binary mixture diffusivity is

$$\mathcal{D}_{AB}^{<1>} = \frac{3}{8\sqrt{\pi}} \frac{\sqrt{k^3 T^3 (1 + z) / 2m_A}}{p \sigma_{AB}^2 \Omega_{AB}^{(1,1)*}}, \quad [7]$$

where the superscript " $< 1 >$ " indicates the *first-order* approximation,  $p = (N_A + N_B)kT$  is the system pressure,  $\sigma_{AB}$  is the binary collision diameter between A and B, and  $\Omega_{AB}^{(1,1)*}$  is the normalized collision integral having the form (16)

$$\Omega_{AB}^{(1,1)*} = \frac{2}{\sigma_{AB}^2} \int_0^\infty \int_0^\infty e^{-\gamma^2} \gamma^5 (1 - \cos \chi) b db d\gamma \quad [8]$$

in which

$$\chi = \pi - 2b \int_{r_m}^\infty \frac{dr/r^2}{\sqrt{1 - b^2/r^2 - \Phi_{AB}/kT\gamma^2}} \quad [9]$$

is the collision solid angle,  $b$  is the collision impact parameter,  $\gamma^2 = m_A m_B |v_A - v_B|^2 / 2kT(m_A + m_B)$ ,  $r_m$  is the distance of closest approach of the colliding particles, and  $\Phi_{AB}$  is the potential between A and B.

In many aerosol studies, we are interested in the diffusion of vapor molecules (A) in a background gas (B), and the interaction between A and B is usually assumed to be potential-free ( $\Phi_{AB} = 0$ ) and  $r_m = \sigma_{AB}$ . Thus from Eq. [9] we immediately have, in this case,



$$\chi = \begin{cases} 2 \cos^{-1}(b/\sigma_{AB}) ; & b \leq \sigma_{AB} \\ 0 ; & b > \sigma_{AB} \end{cases} \quad (\text{hard sphere}) . \quad [10]$$

Using Eqs. [9] and [10], Eq. [8] leads to

$$\Omega_{AB}^{(1,1)*} = 1 \quad (\text{hard sphere}) . \quad [11]$$

One must keep in mind two points: (A) when using Eq. [7], we are dealing with the *first-order Chapman-Enskog approximation*, which does not imply  $\Omega_{AB}^{(1,1)*} = 1$ , and (B) when using Eq. [11], a hard sphere model is implicit. *It is not a consequence of the first-order approximation.*

By combining the first-order approximation, Eq. [7], and the hard sphere model, Eq. [11], one obtains

$$\mathcal{D}_{AB}^{<1>} = \frac{3}{8\sqrt{\pi}} \frac{\sqrt{k^3 T^3 (1+z)/2m_A}}{p\sigma_{AB}^2} . \quad [12]$$

The next step is to employ a formula relating  $\sigma_{AB}$  and the mean free path  $\lambda_{AB}$ . Jeans (17) theoretically showed that

$$\lambda_{AB} = \frac{1}{\sqrt{2\pi} N_A \sigma_{AA} + \pi(1+z)^{1/2} N_B \sigma_{AB}^2} . \quad [13]$$

Because the vapor concentration  $N_A$  is generally diluted, Eq. [13] becomes

$$\lambda_{AB} = \frac{1}{\pi(1+z)^{1/2} N_B \sigma_{AB}^2} . \quad [14]$$

Combining Eqs. [12] and [14], one has

$$\mathcal{D}_{AB}^{<1>} = \frac{3\pi}{32} (1+z) \lambda_{AB} \bar{c}_A . \quad [15]$$

where  $\bar{c}_A = (8kT/\pi m_A)^{1/2}$ , and we have used  $p \approx N_B kT$ . Equation [15] is identical to Eq. [4]. It is the *first-order* hard sphere approximation. Equations [2] and [6] apparently arise from misinterpreting the  $\sigma_{AB}^2$  term, i.e.,  $\lambda_{AB} = (\sqrt{2}\pi N_B \sigma_{AB}^2)^{-1}$ , which leads to incorrect expressions for  $\mathcal{D}_{AB}^{<1>}$ .

We proceed to the second-order approximation of the binary diffusivity. Enskog (14, 18) obtained, for a hard sphere model,

$$\begin{aligned}\mathcal{D}_{AB}^{<2>} &= \mathcal{D}_{AB}^{<1>} / (1 - \xi) ; \\ \xi &= \frac{a^2(\delta_A N_A / N_B + 1) + b^2(\delta_B N_B / N_A + 1) - 2abc}{(\delta_A N_A / N_B + 1)(\delta_B N_B / N_A + 1) - c^2} ; \\ a &= \frac{z}{\sqrt{13z^2 + 16z + 30}} ; \quad b = \frac{1}{\sqrt{30z^2 + 16z + 13}} ; \quad c = 27ab ; \\ \delta_A &= \left(\frac{\sigma_{AA}}{\sigma_{AB}}\right)^2 \sqrt{\frac{1+z}{2}} \frac{8(1+z)^2}{30z^2 + 16z + 13} ; \\ \delta_B &= \left(\frac{\sigma_{BB}}{\sigma_{AB}}\right)^2 \sqrt{\frac{1+z}{2z}} \frac{8(1+z)^2}{13z^2 + 16z + 30} .\end{aligned}\tag{16}$$

Letting  $N_A/N_B = 0$ , Eq. [16] becomes

$$\mathcal{D}_{AB}^{<2>} = \frac{\mathcal{D}_{AB}^{<1>}}{1 - b^2}$$

or

$$\mathcal{D}_{AB}^{<2>} = \frac{3\pi}{64} (1+z) \left( \frac{30z^2 + 16z + 13}{15z^2 + 8z + 6} \right) \lambda_{AB} \bar{c}_A .\tag{17}$$

This is a closed form of  $\mathcal{D}_{AB}^{<2>}$  as a function of  $z$ .

Let us examine the limiting cases,  $z \ll 1$ ,  $z = 1$ , and  $z \gg 1$ . From Eqs. [15] and [17], we have

$$\frac{D_{AB}^{<i>}}{\lambda_{AB}\bar{c}_A} = \begin{cases} \frac{3\pi}{32}, & i = 1; & \frac{13\pi}{128}, & i = 2 & (z \ll 1) \\ \frac{3\pi}{16}, & i = 1; & \frac{177\pi}{928}, & i = 2 & (z = 1) \\ \frac{3\pi z}{32}, & \text{for both } i = 1 \text{ and } i = 2 & (z \gg 1). \end{cases} \quad [18]$$

For other higher-order approximations, Chapman (13, 19) obtained the asymptotic values

$$\frac{D_{AB}^{<i>}}{D_{AB}^{<1>}} = \begin{cases} 1.083, i = 2; & 1.107, i = 3; & 1.117, i = 4 \dots \\ \text{converges to } 32/9\pi \text{ or } 1.132, i = \infty & (z \ll 1) \\ 1.015, i = 2 \dots \text{converges to } 1.016, i = \infty & (z = 1) \\ 1, & \text{for all } i & (z \gg 1). \end{cases} \quad [19]$$

Although there is no closed form expression available for approximations higher than the second order, we suggest that one can use either Eq. [15] or [17]. The final value of  $D_{AB}^{<i>}/D_{AB}^{<1>}$  is not altered by further approximations by more than 0.001 or 0.002 (19).

In Eq. [19], the infinite approximations correspond to the *exact*  $D_{AB}$  values. therefore,

$$D_{AB}^{\text{exact}} = D_{AB}^{<\infty>} = \begin{cases} \frac{32}{9\pi} D_{AB}^{<1>} & (z \ll 1) \\ 1.016 D_{AB}^{<1>} & (z = 1) \\ D_{AB}^{<1>} & (z \gg 1). \end{cases} \quad [20]$$

By using Eq. [15], this leads to,

$$D_{AB}^{\text{exact}} = \begin{cases} \frac{1}{3} \lambda_{AB} \bar{c}_A & (z \ll 1) \\ 0.5985 \lambda_{AB} \bar{c}_A & (z = 1) \\ \frac{3\pi z}{32} \lambda_{AB} \bar{c}_A & (z \gg 1). \end{cases} \quad [21]$$

It is noteworthy that the rigorous solution Eq. [21] coincides with the result from zeroth-order kinetic theory of gases, Eq. [1], for  $z \ll 1$ .

## CONCLUSIONS

In this work, we have clarified ambiguities in the relations linking  $\mathcal{D}_{AB}$ ,  $\bar{c}_A$ , and  $\lambda_{AB}$ . It is shown that the formula used by Fuchs and Sutugin, Eq. [1], is an *exact* result for  $z \ll 1$ . For other cases ( $z = 1$  and  $z \gg 1$ ), Eq. [21] can be used. We suggest that one can use Eq. [15] or [17] as either the first- or second-order approximations of Chapman-Enskog solution, for arbitrary  $z$ .

## REFERENCES

1. McQuarrie, D. A., "Statistical Mechanics," p. 363. Harper & Row, New York, 1976.
2. Fuchs, N. A., and Sutugin, A. G., in "Topics in Current Aerosol Research" (G. M. Hidy and J. R. Brock, Eds.), Vol. 2, pp. 34, 42. Pergamon, New York, 1971.
3. Fuchs, N. A., "The Mechanics of Aerosols," p. 292. Pergamon, New York, 1964.
4. Davis, E. J., and Ray, A. K., *J. Aerosol Sci.* **9**, 411 (1978).
5. Davis, E. J., *Aerosol Sci. Technol.* **2**, 121 (1983).
6. Loyalka, S. K., *J. Chem. Phys.* **58**, 354 (1973).
7. Bricard, J., and Pradel, J., in "Aerosol Science" (C. N. Davies, Ed.), p. 190. Academic Press, New York, 1966.
8. Liu, B. Y. H., and Yeh, H. C., *J. Appl. Phys.* **39**, 1396 (1968).
9. Kennard, E. H., "Kinetic Theory of Gases," p. 195. McGraw-Hill, New York, 1938.
10. Pui, D. Y. H., "Experimental Study of Diffusion Charging of Aerosols," Ph.D. thesis, University of Minnesota, 1976.

11. Liu, B. Y. H., and Pui, D. Y. H., *J. Colloid Interface Sci.* **58**, 142 (1977).
12. Adachi, M., Kousaka, Y., and Okuyama, K., *J. Aerosol Sci.* **16**, 109 (1985).
13. Chapman, S., *Philos. Trans. R. Soc. London, Ser. A* **217**, 115 (1918).
14. Enskog, D., "Kinetische Theorie der Vorgänge in mässig verdünnten Gasen," Dissertation, Uppsala, 1917.
15. Chapman, S., and Cowling, T. G., "The Mathematical Theory of Non-uniform Gases," pp. 149, 165. Cambridge Univ. Press, London/New York, 1939.
16. Hirschfelder, J. O., Curtiss, C. F., and Bird, R. B., "Molecular Theory of Gases and Liquids," pp. 526–527, Wiley, New York, 1963.
17. Jeans, J. H., "The Dynamical Theory of Gases," 4th ed., p. 252. Dover, New York, 1925.
18. Enskog, D., in "Kinetic Theory" (S. G. Brush, Ed.), Vol. 3, pp. 184–187. Pergamon, New York, 1972.
19. Chapman, S., in "Kinetic Theory" (S. G. Brush, Ed.), Vol. 3, p. 115. Pergamon, New York, 1972.